Early Warning for Earthquakes with Large Rupture Dimension

Thesis by

Masumi Yamada

In Partial Fulfillment of the Requirements

for the Degree of

Doctor of Philosophy

California Institute of Technology

Pasadena, California

2007

(Defended February 15, 2007)

Acknowledgements

I would like to thank my advisor, Tom Heaton, for his great guidance on this project over the past 4 years. He was always enthusiastic and supportive of his students like a real father. Whenever I asked simple questions, he answered really sincerely and taught me something from his enormous knowledge of seismology.

The members of my advisory and defense committees, Jim Beck from Civil Engineering, Hiroo Kanamori and Rob Clayton from Seismolab, and Yih-Min Wu from Taiwan National University, were all very generous with their time and ideas. I especially thank Dr. Beck for giving me a guidance of probability theory. His contribution was very important for incorporating the Bayesian approach. Many thanks for Kanamori sensei, who talked me in a friendly and frank way whenever I visited his office. He gave me a lot of helpful advice for the physics of earthquakes.

I also appreciate people who provided me with seismic data and their research results, Brad Aagaard at the USGS, Chen Ji at UC Santa Barbara, Hiroo Kanamori, Jing Liu-Zeng at Institute of Tibetan Plateau Research, David Wald at the USGS, and Yih-Min Wu.

My thanks go to my fellow graduate students, Sai Hung Cheung, Anna Olsen, and Alexandros Taflanidis for helping me with research, exams, course work, and making the life in Thomas very enjoyable. Georgia Cua, who developed the Virtual Seismologist method, provides a lot of advice and support. I learned many things from her high-quality Ph.D. thesis. Support from Carolina Oseguera and all the members in Civil Engineering and Seismolab were also indispensable. Special thanks for all members in Caltech Japanese Association, I enjoyed life Caltech with them.

Above all, I am very thankful to my family in Japan. They are very patient and always support my decisions. It was a big adventure for me to go to US and get a Ph.D. degree. My dream is accomplished thanks to their understanding.

Abstract

Earthquake early warning systems have become popular these days, and many seismologists and engineers are making research efforts for their practical application. The existing earthquake early warning systems provide estimates of the location and size of earthquakes, and then ground motions at a site are estimated as a function of the epicentral distance and site soil properties. However, for large earthquakes, the energy is radiated from a large area surrounding the entire fault plane, and the epicenter indicates only where rupture starts.

In this project, we focus on an earthquake early warning system considering fault finiteness. We provide a new methodology to estimate rupture geometry and slip size on a finite fault in real time for the purpose of earthquake early warning.

We propose a new model to simulate high-frequency motions from earthquakes with large fault dimension: the envelope of high-frequency ground motion from a large earthquake can be expressed as a root-mean-squared combination of envelope functions from smaller earthquakes. We parameterize the fault geometry with an epicenter, a fault strike, and two along-strike rupture lengths, and find these parameters by minimizing the residual sum of squares of errors between ground motion models and observed ground motion envelopes.

To provide the information on the spatial extent of rupture geometry, we present a methodology to estimate a fault dimension of an earthquake in real time by classifying seismic records into near-source or far-source records. We analyze peak ground motions and use Bayesian model class selection to find a function that best classifies near-source and far-source records based on these parameters. This discriminant function is useful to estimate the fault rupture dimension in real time, especially for

large earthquakes.

In order to characterize slip on the fault in real time, we construct an analytical function to estimate slip on the fault from near-source ground displacement observations. In real-time analysis, we back project the recorded displacement data onto the fault line to estimate the size of the slip on the fault. The simulation results show that the slip size estimation predicts the observed GPS static displacement on the fault quite well. This current slip size on the fault is used for a probabilistic prediction of additional rupture length in the near future. We characterize the distribution of additional rupture length conditioned on the current slip on the fault for the ongoing rupture from the simulation with a 1-D slip model. The probability density of additional rupture length can be approximated by a lognormal distribution conditioned on the current slip size.

Contents

Acknowledgements **iii**

Abstract **v**

1 Introduction **1**

1.1 Motivation 1

1.2 Background on seismic early warning system 3

1.2.1 History of research efforts in seismic early warning system . . 3

1.2.2 Seismic early warning systems in the world 5

1.2.2.1 Earthquake early warning system in Japan 6

1.2.2.2 Seismic Alert System (SAS) of Mexico city 7

1.2.2.3 Early warning system in Taiwan 8

1.2.2.4 Early warning system in the United States 8

1.2.2.5 Early warning systems in other countries 9

1.3 Objectives and road map for this thesis 10

2 General Virtual Seismologist Method **11**

2.1 Bayes' theorem for seismic early warning system 12

2.2 Defining the prior $\boldsymbol{prob(M,R)}$ 14

2.2.1 Location of known faults 14

2.2.2 Previously observed seismicity 15

2.2.3 Geometric consideration of stations 17

2.2.4 Gutenberg-Richter law 20

2.3 Defining the likelihood function $\boldsymbol{prob(A|M,R)}$ 21

2.3.1 Magnitude ground motion relationships 21

2.3.2 P-wave and S-wave discriminant 23

2.3.3 Ground motion models 24

2.3.4 Complete form of the likelihood function 28

2.4 Finding the best estimates 30

2.5 Summary 31

3 Extended Virtual Seismologist Method 32

3.1 Road map for Virtual Seismologist Finite-Source method 32

3.2 Statistics of observed high-frequency and low-frequency ground motions 36

3.2.1 Data 37

3.2.2 Statistics of observed high-frequency ground motions 38

3.2.3 Statistics of observed low-frequency ground motions 40

3.2.4 Comparison of high-frequency and low-frequency ground motions 43

3.2.5 Definitions of the horizontal component 45

3.3 Summary 49

4 Estimating the Location of Fault Rupture Using Envelopes of Acceleration 50

4.1 Ground motion models for large earthquakes 51

4.2 Finding the best estimates 58

4.3 Example from the Chi-Chi earthquake 60

4.3.1 Data used for the VS-FS method 60

4.3.2 Results from the analysis of the VS-FS method 67

4.3.3 Comparison between predicted envelopes and observed envelopes 68

4.3.3.1 Result of model 1 (horizontal and vertical data) . . . 77

4.3.3.2 Result of model 2 (horizontal data) and model 3 (vertical data) 78

4.3.3.3 Result of model 4 (effect of area weight) 78

4.3.3.4 Result of model 5 and model 6 (the effect of station distribution) 79

4.3.4 Geometry of the parameter space . . . 79
4.3.5 Effects of different misfit functions . . . 85
4.4 Summary . . . 87

5 Near-Source versus Far-Source Classification Analysis 89
5.1 Strong motion data . . . 90
5.1.1 Data sources . . . 91
5.1.2 Data processing . . . 92
5.1.3 Data classification . . . 94
5.2 Near-source versus far-source discriminant function . . . 99
5.2.1 Fisher's linear discriminant analysis . . . 100
5.2.2 Bayesian approach . . . 103
5.2.2.1 Asymptotic approximation . . . 107
5.2.2.2 Stochastic simulation using Metropolis algorithm . . . 109
5.2.3 Comparison between traditional LDA and Bayesian approach 113
5.3 Bayesian model class selection . . . 116
5.3.1 Method . . . 116
5.3.2 Results of Bayesian model class selection . . . 118
5.3.3 Effect of the choice of prior . . . 120
5.4 Results and discussion . . . 122
5.5 Summary . . . 123

6 Estimating the Slip on the Fault from Low-Frequency Ground Motion 127
6.1 Data . . . 128
6.2 Estimating the slip on the fault from low-frequency ground motion . . . 132
6.2.1 Constructing a slip function as a function of fault distance . . . 132
6.2.2 Estimating the slip on the fault and predicting the additional rupture extent . . . 134
6.3 Predicting the probability of the additional rupture extent . . . 136
6.3.1 Generating 1-D slip models . . . 137

6.3.2 Characteristics of the 1-D slip models 139
6.3.3 Statistical distribution of the additional rupture length 142
6.4 Summary 153

7 Conclusions **154**

A An Article in the *San Francisco Daily Evening Bulletin* **169**

B Peak Ground Motion Database **171**

List of Figures

2.1 A block diagram to compute the posterior pdf from the prior information and ground motion data. 13

2.2 An example of the prior pdf for the known faults. 15

2.3 An example of the prior pdf for the previously observed seismicity. . . 16

2.4 An example of the prior pdf for the geometric consideration of stations (at the first P detection). 17

2.5 An example of the prior pdf for the geometric consideration of stations (at 3 seconds after the first P detection). 18

2.6 An example of the prior pdf for the geometric consideration of stations (at the second P detection). 19

2.7 Histogram of the magnitude of the earthquakes in Southern California during 2000∼2006. 20

2.8 Linear discriminant analysis of P-wave log(acc) and log($disp$) as indicators of magnitude. 22

2.9 P/S wave discriminant using vertical and horizontal ground motion acceleration and velocity. 24

2.10 Observed envelope for accelerogram and P-wave and S-wave envelopes for the ground motion model. 26

3.1 The algorithm of the VS method for finite source (VS-FS method). . . 33

3.2 A plot of near-source PGA as a function of moment magnitude. 39

3.3 A histogram of the near-source PGA. 39

3.4 A plot of near-source PGD as a function of moment magnitude. 41

3.5 A histogram of the near-source PGD. 42

3.6 A comparison of near-source PGA and PGD as a function of moment magnitude. 44

3.7 A histogram of the near-source PGA and PGD. 44

3.8 Comparison of the srss horizontal PGA and magnitude of horizontal accelerations as a function of magnitude. 46

3.9 Comparison of the srss horizontal PGD and magnitude of horizontal displacements as a function of magnitude. 47

3.10 A histogram of the srss horizontal PGA and magnitude of horizontal accelerations. 47

3.11 A histogram of the srss horizontal PGD and magnitude of horizontal displacements. 48

4.1 Near-source accelerations in the vertical component. 52

4.2 Envelopes of near-source accelerations in the vertical component. 53

4.3 Near-source accelerations in the EW component. 54

4.4 Envelopes of near-source accelerations in the EW component. 55

4.5 Schematic diagram of the multiple source model. 56

4.6 Envelopes of vertical acceleration recorded at the station C024 for the Chi-Chi earthquake. 58

4.7 The fault geometry and the station distribution of the Chi-Chi earthquake. 60

4.8 Topographic map of Taiwan. 63

4.9 Strong motion stations in the southern part of Taiwan. 64

4.10 Strong motion stations in the northern part of Taiwan. 65

4.11 Strong motion stations in the central part of Taiwan. 66

4.12 The estimated parameters, N1 and N2, for different rupture velocities. 68

4.13 Predicted and observed envelopes in the horizontal component. 70

4.14 Predicted and observed envelopes in the vertical component. 71

4.15 Predicted and observed envelopes in the horizontal component with different scaling. 72

4.16 Predicted and observed envelopes in the vertical component with different scaling. 73
4.17 Enlarged map of figure 4.13. 74
4.18 Enlarged map of figure 4.14. 75
4.19 Time series of the estimated parameters, θ, N1, and N2, for each model. 76
4.20 Error surface of θ and N1 for model 1 80
4.21 Error surface of N1 and N2 for model 1 81
4.22 Contour maps of the error surface of N1 and N2 for model 1 82
4.23 Posterior probability for the parameter θ. 83
4.24 Posterior probability for the parameter N1. 83
4.25 Posterior probability for the parameter N2. 84
4.26 Two-dimensional posterior probability for the parameters N1 and N2. . 84
4.27 Effects of different error functions. 86

5.1 An example of baseline correction for a velocity record from the Chi-Chi earthquake. 94
5.2 Maps of the fault projections and station distributions. 96
5.2 Maps of the fault projections and station distributions (continued). . . 97
5.3 Histograms and Gaussian densities of the log of ground motions for the near-source and far-source records. 98
5.4 Histogram of the near-source and far-source data to which the discriminant function obtained from traditional LDA is applied. 104
5.5 Logistic sigmoid function $\phi(x) = 1/(1 + e^{-x})$. 106
5.6 Samples generated by the Metropolis algorithm plotted in the parameter space. 112
5.7 Mean and standard deviation of samples plotted against the number of samples included. 112
5.8 Distribution of samples for 3 parameters generated by the Metropolis algorithm. 113

5.9 Correlation plot of posterior samples of the model parameters generated by the Metropolis algorithm. 114

5.10 Probabilities of near-source based on the optimal discriminant function obtained by the Bayesian approach. 124

5.10 Probabilities of near-source based on the optimal discriminant function obtained by the Bayesian approach (continued). 125

5.11 Snapshots of the probabilities of near-source for the Chi-Chi earthquake, based on the optimal discriminant function from the Bayesian approach. 126

6.1 Distribution of the static displacements for the Chi-Chi earthquake (EW component). 129

6.2 Distribution of the static displacements for the Chi-Chi earthquake (NS component). 130

6.3 Distribution of the static displacements for the Chi-Chi earthquake (UD component). 131

6.4 A peak displacement per unit slip as a function of fault distance obtained from ground motion simulations. 133

6.5 A slip on the fault can be obtained by backprojecting the displacement data onto the fault line. 135

6.6 Slip distribution for the Chi-Chi earthquake. 136

6.7 Cross section of the slip distribution in figure 6.6. 137

6.8 An example of the 1-D slip models. 138

6.9 The effect of the low-pass filter with different orders α on the slip models. 139

6.10 Plot for the average slip ($\bar{D}$) and rupture length (L) for the slip models with different α. 140

6.11 Plot for the average slip ($\bar{D}$) and rupture length (L) for the observed earthquake data. 141

6.12 Plot for the slope of $\log \bar{D}/\log L$ and α. The value of α that corresponds to the observed slope (0.85) is 1.33. 141

6.13 Plot for the average slip ($\bar{D}$) and rupture length (L) for the observed data and simulation results from the slip model with $\alpha = 1.33$. 142

6.14 Plot for the average slip ($\bar{D}$) and rupture length (L) for the slip models with different parent series size n. 143

6.15 3-D histogram of the additional rupture length (L_a) as a function of current slip (D). 143

6.16 Histogram of the additional rupture length (L_a) as a function of current slip (D). 147

6.17 Probability density of the additional rupture length (L_a) as a function of current slip (D) by the kernel smoothing method. 147

6.18 The parameters μ and σ for the lognormal distribution which is an approximation of the probability density of the additional rupture length (L_a). 148

6.19 Probability density of lognormal distribution which is the approximation of the additional rupture length (L_a). 149

6.20 Probability density of lognormal distribution with mean from the formula $\mu(D) = 1.16 \ln(D) + 4.94$ and constant σ. 149

6.21 Histogram of the additional rupture length (L_a) as a function of current slip (D). The bin size of the histogram is 10 km. 150

6.22 Probability density of the additional rupture length (L_a) as a function of current slip (D) by the kernel smoothing method. 150

6.23 Probability density of lognormal distribution which is the approximation of the additional rupture length (L_a). 151

6.24 Probability density of lognormal distribution with mean from the formula $\mu(D) = 1.16 \ln(D) + 4.94$ and constant σ. 151

6.25 The probability that the additional rupture length exceeds a certain value conditioned on the current slip size D. 152

List of Tables

1.1 On-site and regional approaches for the earthquake early warning system. 5

2.1 Coefficients for the envelope attenuation relationships for horizontal and vertical acceleration on a soil site in equation 2.16. 28

3.1 Earthquake data set used for the near-source ground motion analysis. . 38

4.1 P-wave and S-wave velocity model in central Taiwan. 62

4.2 Model parameters for estimating a fault geometry. 67

5.1 The earthquake dataset used for the classification analysis. 90

5.2 Eight measurements of peak ground motions. 95

5.3 Estimated model parameters. 102

5.4 The confusion matrix for the cross-validation analysis with the Bayesian method with asymptotic approximation. 109

5.5 The confusion matrix for near-source versus far-source classification. . 115

5.6 Results of leave-one-out cross-validation for LDA and Bayesian approach. 116

5.7 Results for Bayesian model class selection when fifteen combinations of the ground motion parameters are examined. 118

5.8 The best five model classes in the Bayesian model class selection when 255 combinations of the ground motion parameters are examined. . . . 119

5.9 The posterior probability of the model class selection with different types of prior distribution for parameters. 121

5.10 The estimated parameters from Bayesian approach with different types of prior distribution for parameters. 121

B.1 Earthquake data set used for the near-source ground motion analysis. . 171
B.2 Peak values of the strong motion records for ten earthquakes. 172
B.2 Continued. 173
B.2 Continued. 174
B.2 Continued. 175
B.2 Continued. 176
B.2 Continued. 177
B.2 Continued. 178
B.2 Continued. 179
B.2 Continued. 180
B.2 Continued. 181
B.2 Continued. 182
B.2 Continued. 183
B.2 Continued. 184
B.2 Continued. 185
B.2 Continued. 186
B.2 Continued. 187
B.2 Continued. 188
B.2 Continued. 189
B.2 Continued. 190
B.2 Continued. 191
B.2 Continued. 192
B.2 Continued. 193
B.2 Continued. 194
B.2 Continued. 195
B.2 Continued. 196
B.2 Continued. 197

Chapter 1

Introduction

1.1 Motivation

Recently, with advances in data analysis and increased awareness of the seismic hazard, the topic of earthquake early warning has attracted more research attention, and various early warning methods have been proposed from seismologists and engineers (Nakamura and Tucker, 1988; Allen and Kanamori, 2003; Odaka et al., 2003; Wu and Kanamori, 2005a). Currently, the most ambitious system is the earthquake early warning system provided by the Japan Meteorological Agency, which is in a testing phase. The news of the system was broadcasted widely and attracted considerable public attention in Japan. The goal of seismic early warning is to initiate optimal mitigating actions based on the arrival time and amplitude of seismic waves predicted at a given location. To achieve this, an earthquake early warning system must collect and quickly analyze seismic data in a manner that can be used to predict future shaking. In principle, this could be achieved by using the present value of an approximately known wavefield as a boundary condition to predict future wavefields using Navier's equation (Baker et al., 2005). However, from a practical viewpoint, there are advantages to data analysis schemes that involve characterization of the earthquake source. Predictions of future shaking can be achieved by utilizing the extensive existing work on predicting ground shaking from seismic sources. Ideally, an early warning system would provide the best estimate of slip in time and space that can be deduced from seismic data available at any given instant in time.

Cua and Heaton developed the Virtual Seismologist (VS) method (Cua, 2005; Cua and Heaton, 2006). It is a Bayesian approach to seismic early warning designed for modern seismic networks, and is proposed for small to moderate earthquakes with ruptures that can be approximately modeled as a point source. The VS algorithm uses an envelope attenuation relationship and the predominant frequency content from the first few seconds after the P-wave arrival. The advantage of the VS method is its capacity to assimilate different types of information that may be useful to find quick and reliable estimates of magnitude and location (Cua, 2005). It gives the best estimate of an earthquake property in terms of a probability density function. The Bayesian approach is a scheme to emulate human capabilities to judge complex information by modeling uncertainty in a probabilistic way.

Our goal is to extend the VS method to large earthquakes where fault finiteness is important. Most other earthquake early warning systems focus on estimating epicenters and magnitudes of earthquakes, not the fault geometry (Nakamura and Tucker, 1988; Allen and Kanamori, 2003). However, for large earthquakes, rupture length can be on the order of tens to hundreds of kilometers, and the inhomogeneous slip distribution significantly affects the ground motion amplitude at a site. For example, the fault rupture in the 1999 Chi-Chi earthquake was longer than 80 km, and the largest slip was recorded at the northern end of the fault. It would be difficult, if not impossible, to predict such large shaking at large distances from the epicenter when using a scheme that only characterizes the earthquake as a point source.

Early warning for large earthquakes provides two types of predictions: 1) At a given instant, it recognizes the present geometry of an ongoing earthquake, and predicts the shaking from waves that are traveling to another site; 2) Given the present dimensions of a rupture, what is the probability distribution for the final dimensions of the rupture?

We introduce a two-step strategy to accomplish the first type of predictions; 1) we determine the spatial and temporal extent of an ongoing rupture by analyzing waveform envelopes of high-frequency shaking, 2) we determine approximate slip from simple projections of long-period shaking onto the approximately known location of the rupture. Based on the current configuration of the fault, the second type of prediction can be accomplished.

1.2 Background on seismic early warning system

1.2.1 History of research efforts in seismic early warning system

Lee and Espinosa-Aranda (2003) and Kanamori (2005) provide a recent review and history of research efforts in seismic early warning. According to the quotation in Nakamura (1988), the concept of a seismic early warning system dates as far back as 140 years ago. Cooper (1868) proposed to "arrange a very simple mechanical contrivance at various points from 10 to 100 miles from San Francisco," and "instantaneously ring an alarm bell, which should be hung in a high tower near the center of the city" when the "very simple mechanical contrivance" detects an earthquake. This article explains the fundamentals of a seismic early warning system. It refers to the automation of the system, danger of false alarms, and weakness of the system for very near-source earthquakes (see Appendix A for the quotation). Unfortunately, Cooper's concept was never implemented. A hundred years later, a railway company, Japan Railways (JR) designed an earthquake warning system in 1965 and started operation the next year (Nakamura and Tucker, 1988; Nakamura, 1988).

In the United States, Heaton (1985) developed a model for a seismic computerized alert network (SCAN), which is a system to provide short-term warning for imminent strong ground motion from large earthquake in southern California. By using this model, the relationship between the size of the ground motions, warning time, and area where the warning is issued was analyzed. According to the results, although warning times are likely to be short for areas greatly damaged by relatively small to moderate earthquakes, large areas that experience very strong shaking during large earthquakes would receive longer warning times. He also comments that large earthquakes have a long rupture length, so the system can provide substantial warning times. Toksöz et al. (1990) described a prototype earthquake warning system for strike-slip earthquakes whose slip can be approximated by only horizontal displacement. As the first practical application in US, a prototype early warning system for aftershocks was operated by the United States Geological Survey (USGS) in the San Francisco Bay area after the 1989 Loma Prieta earthquake, M_w=6.9 (Bakun et al., 1994).

The concept of amplitude-based location estimate was introduced by Kanamori (1993). In his method, an attenuation relationship is fit to the observed peak acceleration data, and parameters of magnitude, latitude, and longitude are determined by minimizing the error between observations and predictions. This technique is the fundamental principle used in VS method. Kanamori et al. (1997) describe examples of seismic early warning system developed in several parts of the world. They discussed the current configuration of the seismic network in California and technical issues for providing real-time information. In the paper, they pointed out an issue that the energy is radiated from a large area for major earthquakes, and estimating the epicenter location is not enough to determine the ground motion at a site. It is proposed to locate not only the traditional hypocenter, but the center of the energy radiation, which is referred to as the ground motion centroid.

Kanamori (2005) classifies early warning approaches as either on-site or regional. An on-site approach uses available ground motions at a given site to predict the later-arriving main shock at the same site. This method is suitable for the region close to the epicenter. The regional approach predicts the ground motion at a site based on an estimate of the size and magnitude of the event from the near-source records. This approach is more reliable and provides more accurate information for stations relatively distant from the epicenter. The on-site approach can make a more rapid warning for the region close to the epicenter, since there is no need to compute the magnitude or location of the earthquake. On the other hand, the regional approach is useful for issuing a regional warning for the relatively distant stations. The merits and demerits of these approaches are shown in table 1.1.

Allen and Kanamori (2003) introduced the Earthquake Alarm System (ElarmS),

Table 1.1: On-site and regional approaches for the earthquake early warning system. Examples of each approach are explained in Section 1.2.2.

Type	On-site EWS	Regional EWS
Data to be used	Records of a station whose ground motion is estimated.	All the current available records.
Output information	Peak ground motion at a site. (additionaly, magnitude and epicenter location)	Source information. (ground motion at a site can be estimated from attenuation relationships)
Merits	Simple and quick.	Reliable and acculate.
Demerits	Large uncertainty.	Taking time for data collection and computation.
Suitable for	Regions close to the epicenter.	Relatively distant regions.
Examples	-UrEDAS (Nakamura, 1988) -ElarmS (Allen and Kanamori, 2003) -Taiwan EWS (Wu and Kanamori, 2005b)	-Mexico city SAS (Espinosa-Aranda et al., 1995) -Japan EWS (Odaka et al., 2003) -VS method (Cua, 2005)

which is an on-site approach for the California Integrated Seismic Network (CISN). This algorithm determines the magnitude of events from the predominant period of the first few seconds of the P-wave, based on the assumption that the seismic magnitude has a linear relationship with the predominant period of the ground motion. Wu and Kanamori (2005a) introduced an approach based on a predominant period and displacement amplitude for the Taiwan early warning system. The regional approach for seismic early warning is employed in Japan and Mexico (Odaka et al., 2003; Espinosa-Aranda et al., 1995, respectively). The VS method is also categorized as a regional approach.

1.2.2 Seismic early warning systems in the world

We review earthquake early warning systems that are currently in operation around the world (Normile, 2004).

1.2.2.1 Earthquake early warning system in Japan

1) Urgent Earthquake Detection and Alarm System (UrEDAS)

The Bullet Train, or Shinkansen, of the Japan Railways (JR) started operation in 1964. The next year, Shizuoka earthquake (M6.1) hit the route of the train and damaged the train track. From the concern for the potential of serious damage from large earthquakes, the earthquake early warning system began operation in 1966 (Nakamura and Tucker, 1988). The system consists of accelerometers installed at the transforming stations along the train route, each separated by about 20 km (Nakamura and Tucker, 1988; Saita and Nakamura, 2003). When acceleration exceeds 40 gals, the electric power to the Bullet Train is automatically shut off and the brakes are applied (Nakamura and Tucker, 1988; Saita and Nakamura, 2003).

Starting from 1983, an intelligent earthquake warning system called UrEDAS (Urgent Earthquake Detection and Alarm System) was implemented (Nakamura, 1996b,a). In this upgraded system, the accelerometers are installed on the coastal line, which is closer to the Japanese subduction zone, to provide more warning time (Nakamura and Tucker, 1988). When the accelerometers record a strong ground motion, each station estimates the epicentral azimuth, magnitude, and hypocentral distance of the earthquake from the first few seconds of the records (Nakamura, 1996a). Based on this information, it then issues an alarm and automatically shuts off the electric power for trains which are running at high speed. The system worked during the Niigata Chuetsu earthquake in 2004. It immediately detected the P-wave arrival and shut off the train's power in less than 3 seconds (Nakamura et al., 2006).

2) Early Warning System in Japan (extended Nowcast system)

The Japan Meteorological Agency (JMA) and National Research Institute for Earth Science and Disaster Prevention (NIED) recently implemented a prototype emergency earthquake warning system in Japan (Doi, 2003; Odaka et al., 2003; Horiuchi et al., 2005).

It uses a method of estimating the epicentral distance from a single seismic record in a short amount of time (Odaka et al., 2003). They fit a function $Bt \cdot \exp(-At)$ to the initial part of the waveform envelopes of the past earthquakes and determine A and B by the least-squares method. It is found that the $\log B$ is inversely proportional to log of epicentral distance. Therefore, in real-time analysis, the observed envelopes are fit to the empirical function to estimate the epicentral distance.

After deciding distance estimate, they estimate the magnitude from the maximum amplitude observed within a given short time interval after the P-wave arrival by using an empirical magnitude-amplitude relation that includes the epicentral distance as a parameter. Using epicentral location, depth, and magnitude as input data, the amplitude of the maximum velocity on local site bedrock and the arrival time are estimated from a velocity attenuation relationship (Si and Midorikawa, 1999). In order to obtain the peak ground velocity estimate from the site bedrock velocity estimate, the latter is multiplied by a site amplification factor from an available database called the digital national land information. Currently, this early warning system is under going a testing phase, and the distribution of the early warning information is limited to the people in charge of emergency services.

1.2.2.2 Seismic Alert System (SAS) of Mexico city

Seismic Alert System (SAS) is a seismic early warning system for Mexico city (Espinosa-Aranda et al., 1995, 1996; Lee and Espinosa-Aranda, 2003). From the lesson of the aftermath of the 1985 Michoacan earthquake, the SAS was implemented to detect subduction earthquakes occuring in the Mexican subduction zone located several hundred kilometers south-west of Mexico city. The system consists of a seismic detector on the Pacific coast, telecommunications, central control, and radio warning. The local magnitude is estimated from an empirical relation embedded in each seismic detector, and a warning message is sent via the telecommunications unit if the estimated magnitude is greater than 6. The system is effective since Mexico city is located 300 km from the coast line and it takes about 1 minute for seismic waves to travel from the coast to the central city. The characteristics of the seismic damage in the Mexico city is the collapse of high-rise buildings because of the very soft soil structure. The SAS would be more useful if the warning information is effectively used for those high-rise buildings.

1.2.2.3 Early warning system in Taiwan

Taiwan has established several research programs that are actively pursuing earthquake early warning and rapid reporting systems (e.g., Teng et al., 1997; Wu et al., 1998). The early warning system established by the Taiwan Central Weather Bureau (CWB) uses a real-time strong-motion accelerograph network consisting of 86 stations distributed around Taiwan (Wu and Kanamori, 2005b). The system takes an on-site approach and the predominant period (τ_c) and peak amplitude of displacement in the first 3 seconds after the P-wave arrival (Pd) determine the seismic magnitude (Wu et al., 2006). Wu and Kanamori (2005a) also found that Pd correlates well with the peak ground displacement (PGD) and peak ground velocity (PGV) at the same site. Therefore, P-wave arrival time, τ_c, and Pd can jointly be used to determine the hypocenter, magnitude, and the ground motion intensity at the site. For an event with the same location as the 1999 Chi-Chi earthquake, the Taipei metropolitan area, at 145 km from the epicenter, would have more than 20 sec of early warning time with this early warning system (Wu and Kanamori, 2005b).

1.2.2.4 Early warning system in the United States

The U. S. Geological Survey (USGS) has sponsored the development of a telemetered earthquake monitoring system in California to provide rapid earthquake information for the benefit of public safety, emergency response, and loss mitigation.

In Southern California, the CUBE (Caltech-USGS Broadcast of Earthquakes) project, started in 1991, had a goal to develop near real-time earthquake information systems (Kanamori and Hauksson, 1991). The seismic network in the original CUBE system used digital data from a seismic network with analog telemetry, which severely limited the dynamic range of the data. The increasing demand of rapid earthquake information after the 1994 Northridge earthquake led to the deployment of 24-bit digital communications as a part of the TriNet project (Heaton et al., 1996).

In northern California the REDI (Rapid Earthquake Data Integration) system was operated by the University of California at Berkeley in collaboration with the USGS. Since 1994, the CUBE and REDI systems have been upgraded to the California Integrated Seismic Network (CISN). Recently, Allen and Kanamori (2003) demonstrated the feasibility of a short-term earthquake warning using the extensive data set from CISN. The proposed system, ElarmS (Earthquake Alarm Systems), could issue a warning a few to tens of seconds ahead of damaging ground motion (Lockman and Allen, 2005; Simons et al., 2006; Allen, 2006). Currently, universities, federal and state government agencies, and the private sector are collaborating for the practical implementation of an early warning system on CISN.

1.2.2.5 Early warning systems in other countries

As a result of increased public perception of the benefits of earthquake early warning systems, such systems are being developed all over the world. Southern Europe is an earthquake-prone zone and their national and local governments have a great interest in mitigating seismic damage by installing seismic early warning systems.

In Campania Region, southern Italy, a prototype system for seismic early warning and rapid shake map evaluation is being developed and tested (Zollo et al., 2006).

In Istanbul, Turkey, one hundred strong motion accelerometers have been placed in populated areas, and ten strong motion stations are sited at locations as close as possible to the main fault (Great Marmara Fault) in on-line data transmission mode to provide earthquake early warning information (Zschau et al., 2003; Erdik et al., 2003).

Seismicity in Bucharest, Romania, has special properties such as the invariability of the location of epicenters and the stability of radiation patterns (Wenzel et al., 2003). A Mexico city-type SAS system would be adequate for those kinds of areas.

The city of Yerevan, Armenia, is planning to install 13-15 seismic detectors around the city with a radius of 30 km. Approximately 3 to 8 seconds of warning time is expected (Balassanian et al., 2003).

1.3 Objectives and road map for this thesis

In order to construct an early warning system for large earthquakes, we characterize the rupture extent and the slip on the fault in real time and predict ground motions at a given site based on the current rupture configuration. The objectives of this thesis are:

- Characterize the present rupture extent from high-frequency ground motions
- Characterize the present slip on the fault from low-frequency ground motions
- Predict the rupture extent from the on-going rupture.

The thesis is organized as follows: In chapter 1 we outline the research area of earthquake early warning systems and look at the previous research in this area. In chapter 2 we briefly discuss the basic procedures of the Virtual Seismologist (VS) method, a seismic early warning system developed by Cua and Heaton (Cua, 2005; Cua and Heaton, 2006). In chapter 3 we discuss a strategy to extend the VS method to large earthquakes. To work this problem, we first recognize the statistical observations of high-frequency and low-frequency ground motions for large earthquakes with magnitude greater than 6.0. In chapters 4 and 5 we introduce two different methodologies that can estimate the rupture geometry from acceleration envelopes. In the first method the rupture geometry can be characterized with three parameters, an azimuthal direction, and two rupture lengths, one in the positive direction and one in the negative direction, as measured from the epicenter. These parameters can be estimated from acceleration envelopes in real time. In chapter 5 we propose a technique to classify near-source and far-source stations. In chapter 6 we propose a methodology to determine the slip on the fault and predict the total length of the rupture propagation possible conditioned on the current slip. Finally, in chapter 7 we provide conclusions and future work.

Chapter 2

General Virtual Seismologist Method

In this chapter, we briefly discuss the basic procedures of the Virtual Seismologist (VS) method developed by Cua and Heaton (Cua, 2005; Cua and Heaton, 2006), which forms a foundation for the work in this thesis. The VS method is a Bayesian approach for seismic early warning systems. The Bayesian framework provides a means to incorporate previous experiece and judgment that is not traditionally and explicitly incorporated into automated decision making. When making a decision, a human processes many kinds of information, combines and analyzes them simultaneously, and makes a judgment based on the analyzed information. The Bayesian approach is a scheme to emulate human capabilities to judge multiple pieces of information comprehensively and make judgements from limited information.

One component of the VS method is a method to estimate: 1) magnitude from observed ground motion ratios between vertical acceleration and vertical filtered displacement; and 2) magnitude and location from P- and S-wave amplitudes of vertical and horizontal acceleration, velocity, and filtered displacement. Any seismic early warning system estimates the earthquake information from the sparse set of available observations immediately after the initial P wave detection. What differentiates the VS method from other proposed seismic early warning systems is the use of prior information. Prior information (i.e. the state of health of the seismic network, fault locations, and previously observed seismic activity) can help to reduce the uncertainty of the initial estimate of the event information.

2.1 Bayes' theorem for seismic early warning system

Bayes' Theorem is a simple mathematical formula to calculate conditional probabilities. The probability of event A conditioned on the occurrence of event B is called a posterior probability for the event A. This can be expressed as a normalized product of a prior probability density function (pdf) and a likelihood function:

$$\underbrace{prob(A|B)}_{posterior} = \frac{\overbrace{prob(B|A)}^{likelihood} \times \overbrace{prob(A)}^{prior}}{\underbrace{prob(B)}_{normalizing\ constant}} \tag{2.1}$$

The posterior probability for the earthquake early warning system is the probability of the parameter we would like to estimate (e.g., magnitude, location of the epicenter) given observed ground motion data (e.g., accelerograms, GPS displacement). For the VS method, Bayes' Theorem can therefore be expressed as:

$$\begin{aligned}\underbrace{prob(M,R|A)}_{posterior} &= \frac{prob(A|M,R) \times prob(M,R)}{prob(A)} \\ &\propto \underbrace{prob(A|M,R)}_{likelihood} \times \underbrace{prob(M,R)}_{prior},\end{aligned} \tag{2.2}$$

where A is the observed ground motion amplitude, M is the magnitude of the earthquake, and R is the location (i.e., latitude and longitude) of the epicenter. The posterior pdf, $prob(M,R|A)$, is proportional to the product of the prior pdf, $prob(M,R)$, and the likelihood function, $prob(A|M,R)$, since the constant, $prob(A)$, is independent of the magnitude and the location of the earthquake. The posterior pdf represents the conditional probability of magnitude and location when we observe the ground motion amplitude. The best estimation of the magnitude and location can be obtained by maximizing the posterior to give the most probable values (see Figure 2.1).

The likelihood function is the probability of the ground motion amplitude ob-

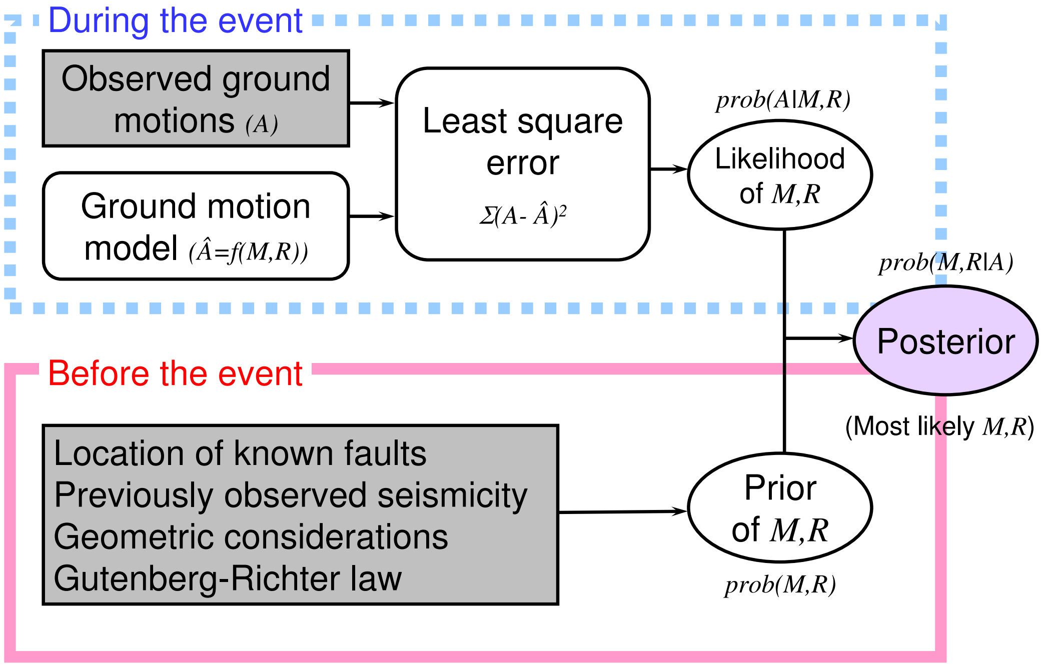

Figure 2.1: A block diagram to compute the posterior pdf of Bayes' theorem from the prior information and real-time ground motion data.

servation given the magnitude and distance. It is defined using a ground motion attenuation relationship for ground motion amplitudes in terms of magnitude and distance. The sum of square errors ($\Sigma(A - \hat{A})^2$) is often used to define the likelihood function which corresponds to taking a Gaussian probability model for each prediction error, the error between the observation (A) and prediction ($\hat{A}$) based on the models. The Bayesian approach reduces to some other geophysical inverse methods if the prior information is not considered; then it is the same as the maximum likelihood method and corresponds to a least-square approach in the case of Gaussian prediction errrors.

The prior pdf expresses information known before examining waveform data for the ongoing earthquake rupture. Station geometry, location of faults, or previously observed seismicity can be expressed as probability density functions and used as prior information. For example, the regions where earthquakes were observed on previous days have a higher probability of producing additional earthquakes. Therefore, the prior pdf is higher for regions that are near events on previous days. The prior pdf is also higher for areas near known faults. Other prior information (e.g., station geometry, Gutenberg-Richter law) can be included in the same way.

2.2 Defining the prior $prob(M, R)$

The prior pdf is a probability of magnitude (M) and location (R) based only on the information obtained before an earthquake occurs. If there is no prior information, the magnitude and location of an earthquake are treated as equally likely to be any size and at any place, and so a uniform prior is used. However, generally speaking, there is usually some information before the initiation of an earthquake rupture, and that information can be used to constrain the magnitude and location estimates in seismic early warning. The following information is considered as prior information:

- Location of known faults
- Previously observed seismicity
- Geometric consideration of stations
- Gutenberg-Richter law

2.2.1 Location of known faults

Recognized active faults are more likely sources of future large earthquake than regions without recognized faults. Even though there are many faults hidden underground which are too small to extend from earthquake depths to ground level, the information of active faults helps to confine the source location. The prior pdf, considering the location of known faults, can be defined as an exponential function of the distance from fault lines (Felzer and Brodsky, 2006):

$$prob(r) = cr^{-1.34}, \tag{2.3}$$

where

r =the shortest distance between fault lines and a station,

c =constant.

An example of the prior pdf for the known faults is shown in Figure 2.2.

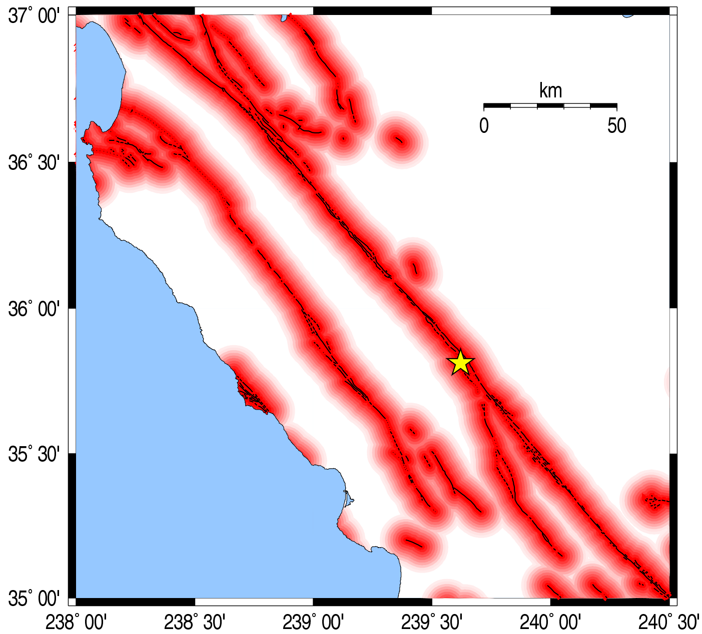

Figure 2.2: An example of the prior pdf for the known faults for the 2004 Parkfield earthquake. Solid lines indicate the location of the fault lines in California and darkness of the shade around the lines show higher prior pdf values. The star symbol shows the epicenter of the Parkfield earthquake.

2.2.2 Previously observed seismicity

Since observations of foreshocks preceding large earthquakes are significantly related to subsequent earthquakes, the regions where an earthquake was observed on the previous day have a higher probability of an earthquake occurrence (Abercrombie and Mori, 1996). Abercrombie and Mori (1996) found that 44% of the earthquakes in their California dataset had foreshocks. Therefore, the prior pdf is higher at regions near the source of events on the previous day. The prior pdf considering the previously observed seismicity is expressed by the exponential function (Felzer and Brodsky, 2006):

$$prob(r) = cr^{-1.34}, \tag{2.4}$$

where

$$\begin{aligned} r &= |\boldsymbol{x} - \boldsymbol{x_i}|, \\ \boldsymbol{x} &= \text{location of the station}, \\ \boldsymbol{x_i} &= \text{location of the foreshock epicenter}(i = 1, ..., n), \\ c &= \text{constant}. \end{aligned}$$

An example of the prior pdf for the known faults is shown in Figure 2.3.

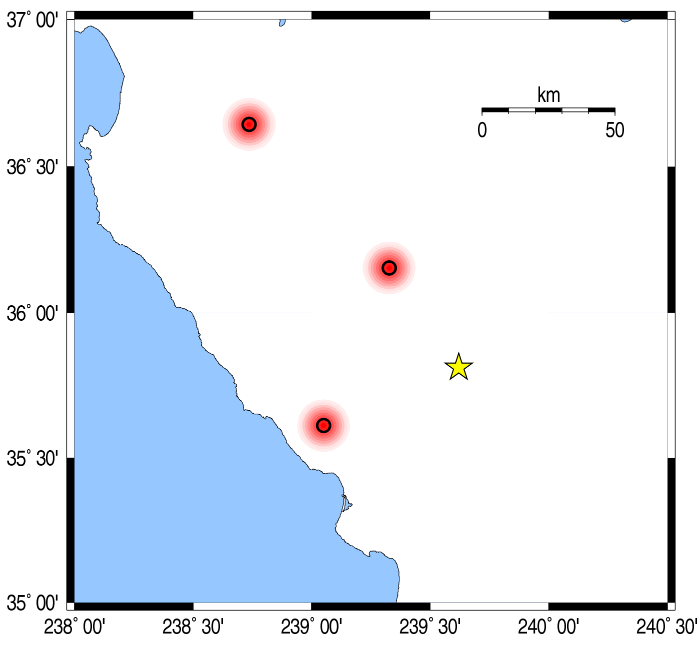

Figure 2.3: An example of the prior pdf for the previously observed seismicity of the 2004 Parkfield earthquake. Open circles indicate the location of the previously observed seismicity and darkness of the shade around the circle show higher prior pdf values. The star symbol shows the epicenter of the Parkfield earthquake.

2.2.3 Geometric consideration of stations

Station geometry also provides a geometric constraint to the location of an earthquake epicenter. Rydelek and Pujol (2004), Cua (2005), and Horiuchi et al. (2005) developed a new technique to constrain the location of an earthquake from the P-wave arrival time using the Voronoi cell concept (Sambridge, 1999a,b). The Voronoi cell of a station is a convex polygon around the station, which is a set of all points closer to a station than to any other stations. The location of the earthquake epicenter must be inside of the Voronoi cell of the station first triggered by a P-wave arrival (Figure 2.4).

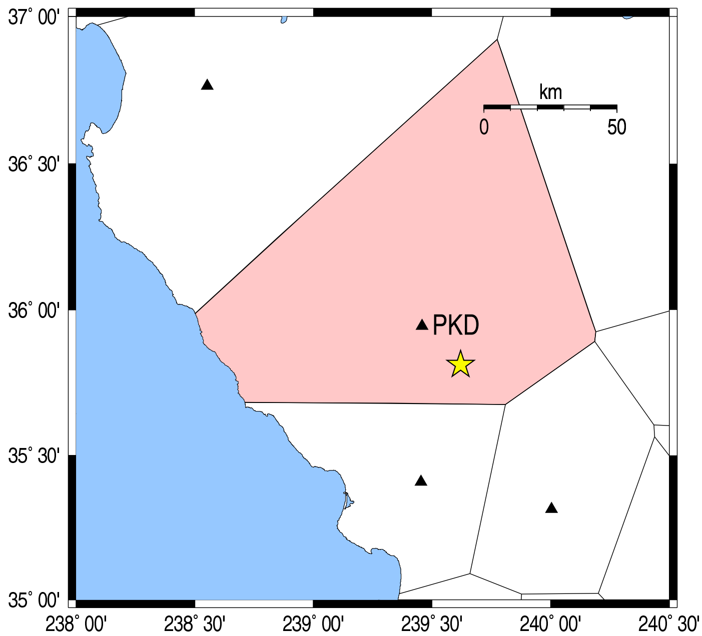

Figure 2.4: Voronoi cells of strong motion stations for 2004 Parkfield earthquake. Triangles denote strong motion station locations. The shaded region is that of possible location of epicenter when the closest station PKD detects the first P-wave arrival. The star symbol shows the epicenter of the Parkfield earthquake.

After the first P-wave arrives at the first station, not-yet-arrived data can shrink the probable region of the epicenter location inside the Voronoi cell (Figure 2.5). From Rydelek and Pujol (2004), the region of likely location of the epicenter based on the first two P-wave arrivals forms a hyperbola, which is a set of points the difference of whose distances from the first and the second arrival stations is a given positive

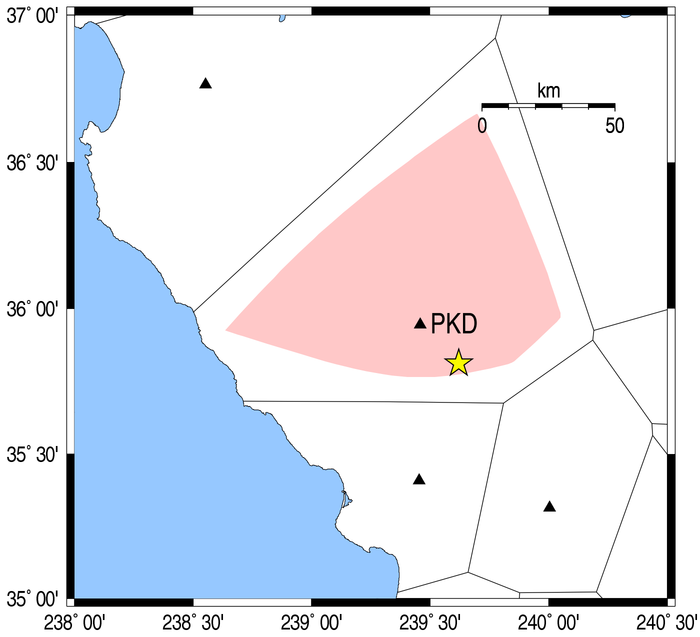

Figure 2.5: Voronoi cells of strong motion stations for 2004 Parkfield earthquake. Triangles denote strong motion station locations. The shaded region is that of possible location of epicenter at the 3 seconds after the first P-wave detection. The star symbol shows the epicenter of the Parkfield earthquake.

constant k (Figure 2.6). Furthermore, the use of not-arrived data after the first two P-wave arrivals can provide continuously evolving constraints on the region of likely location.

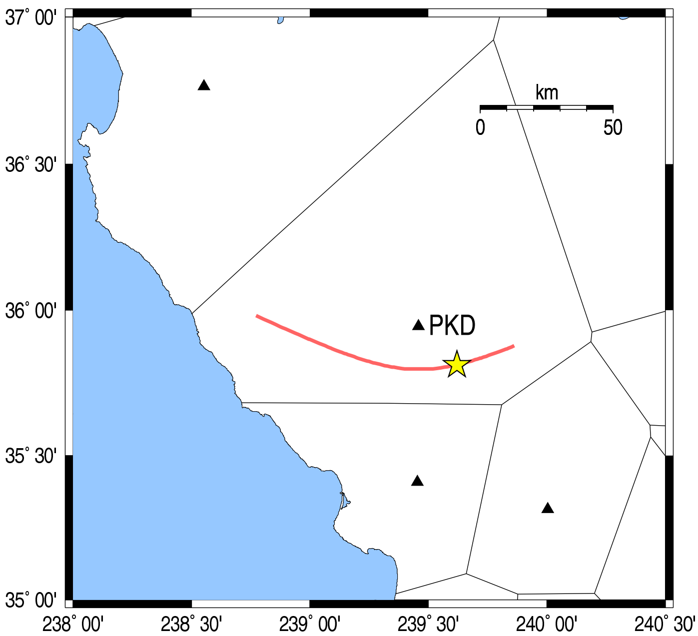

Figure 2.6: Voronoi cells of strong motion stations for 2004 Parkfield earthquake. Triangles denote strong motion station locations. The shaded region is that of possible location of epicenter at the second P-wave detection. The star symbol shows the epicenter of the Parkfield earthquake.

2.2.4 Gutenberg-Richter law

The Gutenberg-Richter law states that the number of earthquakes per year, N, of Richter magnitude M is statistically proportional to 10^{-bM} (see Figure 2.7). This relationship is mathematically expressed as:

$$N(M) = 10^{a-bM}, \tag{2.5}$$

where a and b are constant, and the size of the constant b is typically around 1.

According to the Gutenberg-Richter law, there are a lot more small earthquakes than large ones. Therefore, the prior pdf corresponding to the Gutenberg-Richter law is defined as:

$$prob(M) \propto 10^{a-bM}. \tag{2.6}$$

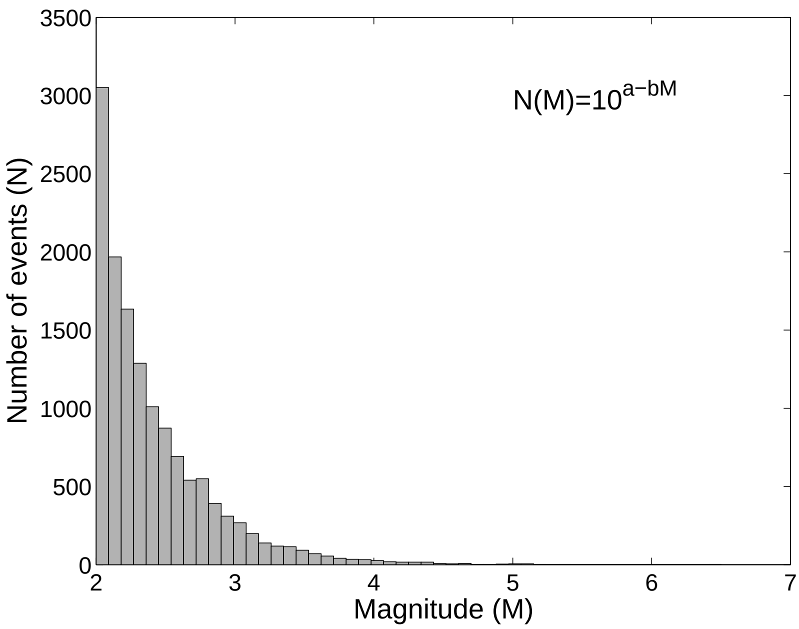

Figure 2.7: Histogram of the magnitude of the earthquakes in Southern California during 2000∼2006. The distribution follows the Gutenberg-Richter law.

2.3 Defining the likelihood function $prob(A|M, R)$

The likelihood function is the probability of the ground motion amplitude observation (A) given the magnitude (M) and distance (R). Cua (2005) defined a likelihood function in terms of the ratio between vertical acceleration and displacement amplitudes, and the envelope attenuation relationships for vertical acceleration and horizontal acceleration, velocity, and displacement. This section describes the magnitude ground motion relationships, P-wave and S-wave discriminant, and ground motion models as components of the likelihood function.

2.3.1 Magnitude ground motion relationships

Magnitude ground motion relationship is one of the measurements to find magnitude of an earthquake from the ground motion. Many seismologists have pointed out that the P-wave predominant period is linearly correlated with the ultimate magnitude (Nakamura and Tucker, 1988; Allen and Kanamori, 2003). Cua and Heaton (2006) use ratios of the ground motion as indicative of the predominant frequency of the seismograms. Since the acceleration is equal to the square of frequency (ω^2) times displacement in the frequency domain, the magnitude is proportional to the ratio between acceleration and displacement.

$$
\begin{aligned}
M &\propto \omega_0^{-1} \\
&= c_1 \log(acceleration) + c_2 \log(displacement) + c_3,
\end{aligned}
\tag{2.7}
$$

where ω_0 is the predominant frequency of the ground motion, and c_1, c_2, and c_3 are coefficients. Cua (2005) performed a linear discriminant analysis with over 30,000 seismograms in Southern California to determine these coefficients. Figure 2.8 shows the dataset and the most probable linear discriminant function which classifies the dataset with different magnitudes. The best magnitude ground motion relationship is:

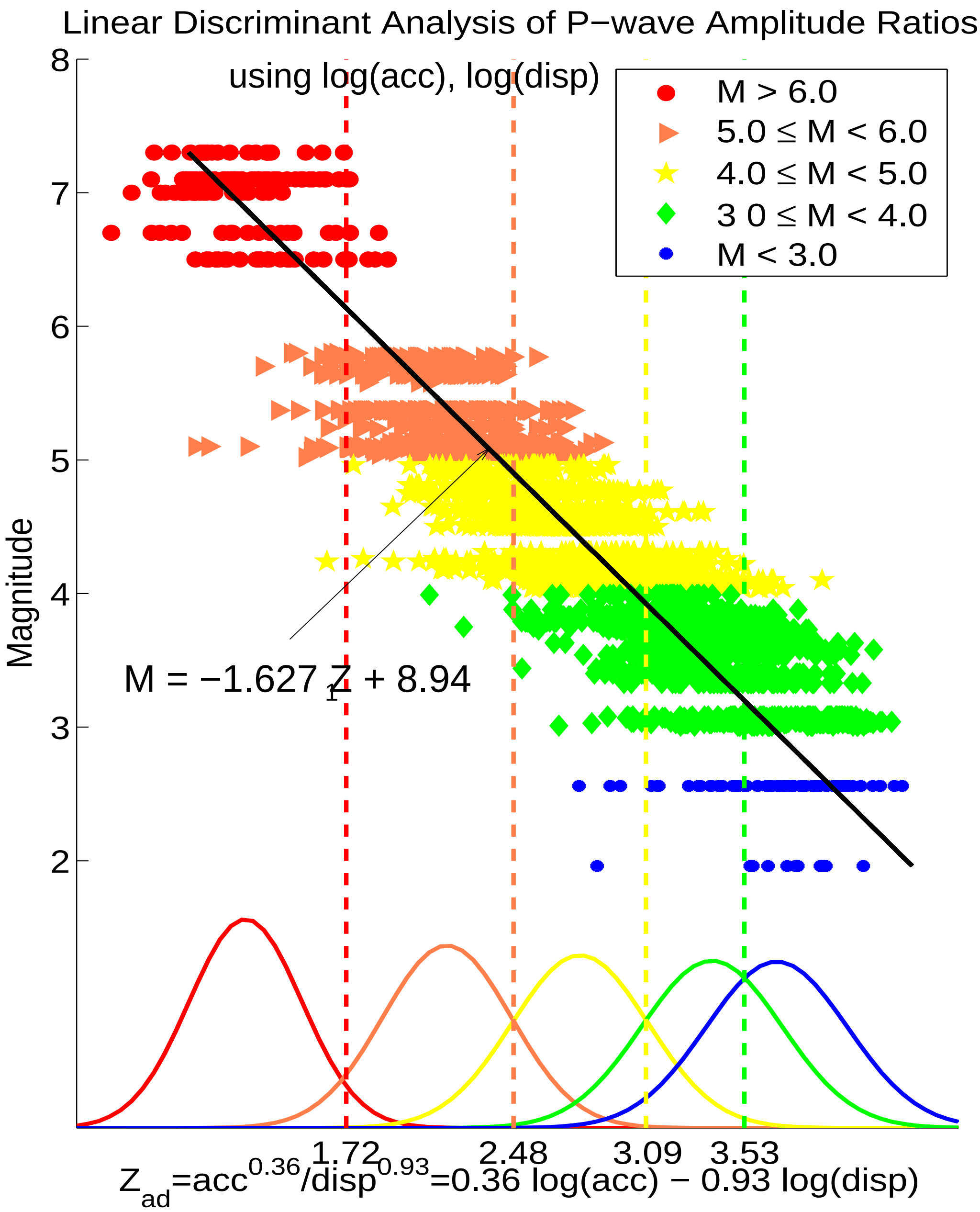

Figure 2.8: Linear discriminant analysis of P-wave $\log(acc)$ and $\log(disp)$ as indicators of magnitude. $Z = X_2 \cdot u = 0.36\log(acc) - 0.93\log(disp)$ (Cua, 2005).

$$\hat{M} = \begin{cases} -1.627(0.36\log(Zacc) - 0.93\log(Zdisp)) + 8.94 & : \quad \text{if P-wave,} \\ -1.459(0.36\log(Zacc) - 0.93\log(Zdisp)) + 8.05 & : \quad \text{if S-wave,} \end{cases} \tag{2.8}$$

where $Zacc$ and $Zdisp$ are vertical acceleration and vertical displacement, respectively and standard deviations are:

$$\sigma = \begin{cases} 0.45 & : \text{ if P-wave,} \\ 0.41 & : \text{ if S-wave.} \end{cases} \tag{2.9}$$

By using this relationship, the observed and predicted ground motion ratios in equation 2.19 are expressed as follows:

$$Z_i = 0.36\log(Zacc) - 0.93\log(Zdisp), \tag{2.10}$$

$$\hat{Z}_i(M) = \begin{cases} (-M + 8.94)/1.627 & : \text{ if P-wave,} \\ (-M + 8.05)/1.459 & : \text{ if S-wave.} \end{cases} \tag{2.11}$$

2.3.2 P-wave and S-wave discriminant

In equation 2.11, the magnitude ground motion relationship is defined separately for P-wave and S-wave. Although it is not significantly sensitive to whether the observed amplitudes are P- or S-wave (see equation 2.11), we can obtain better source estimates if we can identify phases (Cua, 2005). Cua (2005) defined a discriminant function as a linear combination of ground motion measures, and found the best combinations and coefficients for seismograms in Southern California by linear discriminant analysis. The result of the P/S wave discriminant is shown in figure 2.9. The most probable discriminant function is:

$$\begin{aligned} PS &= 0.44\log(Zacc) + 0.55\log(Zvel) - 0.46\log(Hacc) - 0.55\log(Hvel) \\ &= \log(\frac{Zacc^{0.44}}{Hacc^{0.46}}) + \log(\frac{Zvel^{0.55}}{Hvel^{0.55}}), \end{aligned} \tag{2.12}$$

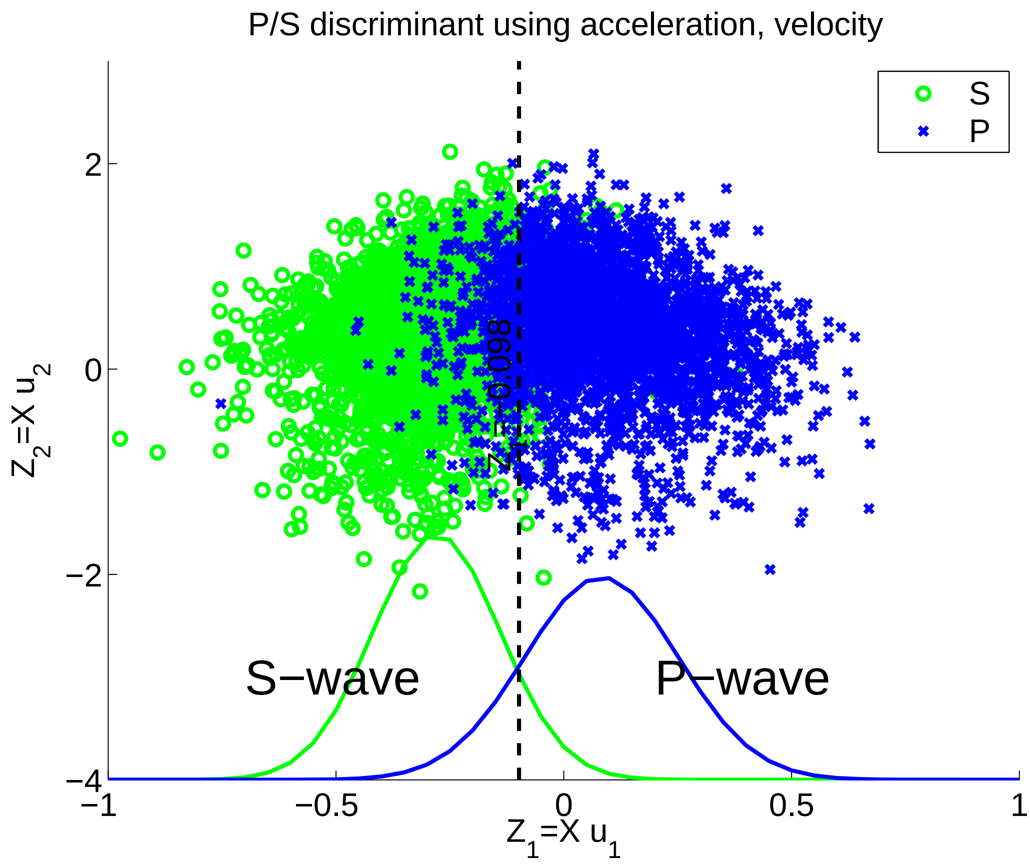

Figure 2.9: P/S wave discriminant using vertical and horizontal ground motion acceleration and velocity (Cua, 2005).

$$
if \begin{cases} PS > 0 : \text{ P-wave,} \\ PS < 0 : \text{ S-wave,} \end{cases}
$$

where $Zacc$, $Zvel$, $Hacc$, and $Hvel$ are vertical acceleration and velocity, and horizontal acceleration and velocity, respectively.

2.3.3 Ground motion models

Cua and Heaton examined over 30,000 seismograms in Southern California and developed relationships that predict waveform envelopes as a function of magnitude, distance and station corrections (Cua, 2005; Cua and Heaton, 2006). First, the envelopes of the ground motions are modeled as a combination of the envelopes of P-wave, S-wave, and ambient noise.

$$E_{observed}(t) = \sqrt{E_P^2(t) + E_S^2(t) + E_{ambient}^2} + \epsilon, \tag{2.13}$$

where

$$\begin{aligned}
E_{observed}(t) &= \text{envelope of observed ground motion,} \\
E_P(t) &= \text{envelope of P-wave,} \\
E_S(t) &= \text{envelope of S-wave and later-arriving phases,} \\
E_{ambient} &= \text{ambient noise at the site,} \\
\epsilon &= \text{difference between predicted and observed envelope.}
\end{aligned}$$

The ambient noise, $E_{ambient}$, for a given time history is modeled as a station constant. The P- and S-wave envelopes, $E_P(t)$ and $E_S(t)$, are defined by a rise time (t_{rise_P} and t_{rise_S}), a constant amplitude (A_P and A_S), a duration (Δt_P and Δt_S), and two decay parameters (γ_P and γ_S) and (τ_P and τ_S) respectively. See figure 2.10 for the physical interpretation of these parameters.

The general form of the envelope function is:

$$E_{ij}(t) = \begin{cases} 0 & ; \quad t < T_i, \\ \frac{A_{ij}}{t_{rise_{ij}}}(t - T_i) & ; \quad T_i \leq t < T_i + t_{rise_{ij}}, \\ A_{ij} & ; \quad T_i + t_{rise_{ij}} \leq t < T_i + t_{rise_{ij}} + \Delta t_{ij}, \\ A_{ij} \frac{1}{(t - T_i - t_{rise_{ij}} - \Delta t_{ij} + \tau_{ij})^{\gamma_{ij}}} & ; \quad t \geq T_i + t_{rise_{ij}} + \Delta t_{ij}, \end{cases} \tag{2.14}$$

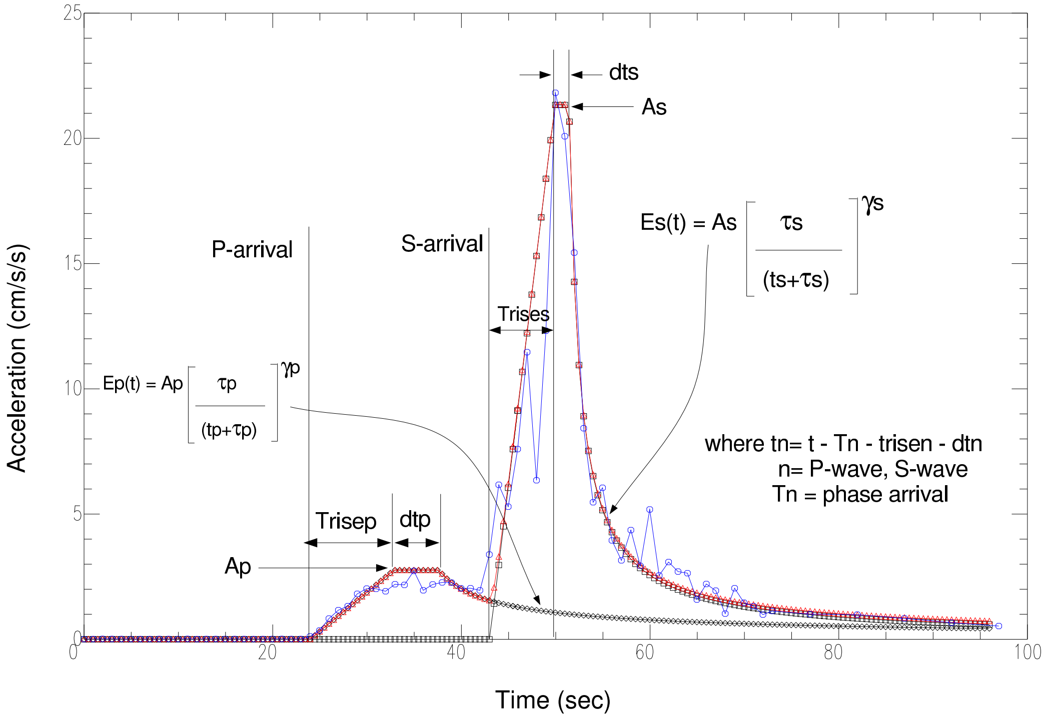

Figure 2.10: Observed envelope for accelerogram and P-wave and S-wave envelopes for the ground motion model defined in equation 2.14 (Cua, 2005).

where

i =P-, S-wave,

T_i =P-, S-wave arrival times,

j =horizontal and vertical acceleration, velocity, and displacement.

Cua and Heaton parameterized each seismogram as a set of eleven parameters (five for the P-wave envelope, five for the S-wave envelope, and one for the ambient noise). Furthermore, each parameter is described by magnitude, distance, log of distance, and site dependent constants based on the traditional strong motion attenuation relationships (Campbell, 1981; Boore and Joyner, 1982; Boore et al., 1993). The functional forms which describe the P- and S- wave envelope functions are given below:

$$\log_{10} A_{ij} = a_{ij} M + b_{ij}(R_1 + C_{ij}(M)) + d_{ij} \log_{10}(R_1 + C_{ij}(M)) + e_{ij} + \epsilon_{ij}, \tag{2.15}$$

$$\log_{10} B_{ij} = a_{ij} M + b_{ij} R_1 + d_{ij} \log_{10} R_1 + e_{ij} + \epsilon_{ij}, \tag{2.16}$$

where

$$\begin{aligned}
i =& \text{P-, S-wave},\\
j =& \text{horizontal and vertical acceleration, velocity, and displacement},\\
A_{ij} =& \text{ground motion envelope amplitude},\\
B_{ij} =& \text{rise time } (t_{rise}), \text{ duration } (\Delta T), \text{ and decay parameters } (\tau,\ \gamma),\\
M =& \text{local magnitude } (M_w \text{ for } M > 5.0),\\
R =& \text{ epicentral distance in km for } M < 5,\\
& \text{ closest distance to fault for } M > 5.0 \text{ (when available)},\\
R_1 =& \sqrt{(R^2 + 9)},\\
C_{ij}(M) =& (\arctan(M - 5) + 1.4)(c_{1ij} \exp(c_{2ij}(M - 5))),\\
a_{ij}, b_{ij}, c_{1ij}, c_{2ij}, d_{ij}, e_{ij} =& \text{regression constants},\\
\epsilon_{ij} =& \text{statistical (or prediction) error}, \sim NID(0, \sigma^2).
\end{aligned}$$

The A_{ij}s are the ground motion envelope amplitudes (P- or S-wave) from fitting equations 2.13 and 2.14 to the observed ground motion envelopes in the database. The B_{ij}s are the parameters characterizing the envelope function (t_{rise}, ΔT, τ, and γ). Coefficients in equations 2.15 and 2.16 are determined by regression analysis of the database using the Neighborhood Algorithm (described later in Section 4.2). An example of set of coefficients (for horizontal and vertical accelerations on soil sites) are shown in table 2.1. Table 2.1 and equations 2.13 – 2.16 can determine the envelope function of ground motions with magnitude M and epicentral distance R. Figure 2.10 shows an observed ground motion envelope and the best P-wave, S-wave, and ambient noise envelopes based on equations 2.13 – 2.16.

Table 2.1: Coefficients for the envelope attenuation relationships for rms horizontal and vertical acceleration on a soil site in equation 2.16. All attenuation relationships model $\log_{10}$ of the envelope parameter as functions of magnitude and distance (Cua, 2005).

Coefficients for rms horizontal acceleration on soil sites

	a (M)	b (R)	d (log(R))	c1	c2	e	σ
A_P	0.740	-3.30×10^{-3}	-1.26	2.41	0.95	-0.90	0.29
A_S	0.840	-2.30×10^{-3}	-1.56	2.42	1.05	-0.19	0.31
$T_{rise,P}$	0.070	1.25×10^{-3}	0.24	-	-	-0.38	0.26
ΔT_P	0.030	2.37×10^{-3}	0.39	-	-	-0.59	0.36
τ_P	0.087	-1.89×10^{-3}	0.58	-	-	-0.77	0.31
γ_P	-	-	-	-	-	0.07	0.21
$T_{rise,S}$	0.055	1.21×10^{-3}	0.34	-	-	-0.66	0.25
ΔT_S	0.028	-	0.07	-	-	-0.10	0.23
τ_S	0.056	-8.30×10^{-4}	0.51	-	-	-0.58	0.24
γ_S	-	-	-	-	-	0.07	0.13
noise	-	-	-	-	-	-2.50	-

Coefficients for vertical acceleration on soil sites

	a (M)	b (R)	d (log(R))	c1	c2	e	σ
A_P	0.739	-4.13×10^{-3}	-1.20	2.03	0.97	-0.62	0.32
A_S	0.751	-2.47×10^{-3}	-1.47	1.59	1.02	-0.21	0.30
$T_{rise,P}$	0.057	5.86×10^{-4}	0.23	-	-	-0.37	0.23
ΔT_P	0.000	1.76×10^{-3}	0.36	-	-	-0.48	0.41
τ_P	0.057	-1.36×10^{-3}	0.63	-	-	-0.89	0.28
γ_P	-	-	-	-	-	0.05	0.18
$T_{rise,S}$	0.060	2.18×10^{-3}	0.26	-	-	-0.66	0.25
ΔT_S	0.029	-	0.31	-	-	-0.31	0.24
τ_S	0.060	-1.45×10^{-3}	0.51	-	-	-0.54	0.22
γ_S	-	-	-	-	-	0.05	0.09
noise	-	-	-	-	-	-1.96	-

2.3.4 Complete form of the likelihood function

As we discussed at the top of this section, the likelihood function is defined in terms of the ground motion ratio between vertical acceleration and displacement amplitudes, and the envelope attenuation relationships for vertical acceleration and horizontal acceleration, velocity, and displacement.

The ground motion ratio estimates the magnitude of earthquakes. To find the best estimate, the error between the observation and prediction from the magnitude ground motion relationships is minimized.

$$prob(Z_i|M) = \frac{1}{\sqrt{2\pi}\sigma_{Z_i}} \exp\left(-\frac{(Z_i - \hat{Z}_i(M))^2}{2\sigma_{Z_i}^2}\right), \tag{2.17}$$

where

$i =$1, . . . , n, where n is the number of stations with P detections,

$\sigma_{Z_i} =$ standard deviation in equation 2.9,

$Z_i =$ observed ground motion ratio in equation 2.10,

$\hat{Z}_i =$ ground motion ratio predicted by the magnitude ground motion, relationship in equation 2.11.

The amplitude of the ground motion envelopes estimate the magnitude and location of earthquakes. The errors between the observed envelopes and predicted envelopes from the ground motion models are also approximated by a Gaussian distribution.

$$prob(Y_{ijk}|M,R) = \frac{1}{\sqrt{2\pi}\sigma_{ijk}} \exp\left(-\frac{(Y_{ijk} - \hat{Y}_{ijk}(M,R))^2}{2\sigma_{ijk}^2}\right), \tag{2.18}$$

where

$j =$1, . . . , 4, for peak amplitudes of vertical velocity, and horizontal acceleration, velocity, and displacement,

$k =$1, . . . , nt, time in 1-second intervals from the event onset,

$\sigma_{ijk} =$ standard deviation of j channels and time k at station i

$Y_{ijk} = \log_{10}$ of peak observed amplitude of j channels and time k at station i

$\hat{Y}_{ijk} = \log_{10}$ of peak amplitude of k channels and phase j at station i predicted by ground motion models in equations 2.13 – 2.16

The vertical acceleration and displacement are used to estimate the magnitude, and the amplitudes of the vertical velocity and three horizontal components solve the trade-off between the magnitude and location of the epicenter. From equations 2.17 and 2.18, the likelihood function of 1-second-interval ground motion envelopes (A) conditioned on the magnitude (M) and location (R) is:

$$\begin{aligned} prob(A|M,R) &= \prod_{i=1}^{n}\prod_{j=1}^{4}\prod_{k=1}^{nt} prob(Z_i|M) prob(Y_{ijk}|M,R) \\ &\propto \exp\left[-\sum_{i=1}^{n}\left(\frac{(Z_i-\hat{Z}_i(M))^2}{2\sigma_{Z_i}^2}+\sum_{j=1}^{4}\sum_{k=1}^{nt}\frac{(Y_{ijk}-\hat{Y}_{ijk}(M,R))^2}{2\sigma_{ijk}^2}\right)\right]. \end{aligned} \tag{2.19}$$

2.4 Finding the best estimates

In order to operate the VS method in real time, we first assume that seismic waveform data are transmitted to a central processor by a seismic network with sufficient station density to quickly characterize the seismic wave field. The central processing station processes currently available seismic records and produces updates as additional data are received. The prior probability incorporated in the real-time Bayesian analysis includes information about magnitude likelihood (e.g., Gutenberg-Richter frequency magnitude) and location likelihood (e.g., known faults, or previously observed seismicity). This prior pdf has been calculated before the occurrence of any earthquake which the VS method is intended to provide a warning for. As the seismic data arrives, the processor can use it to evaluate the likelihood function for any location and size of the earthquake in order to maximize the posterior in equation 2.2 to get the best estimate of magnitude and location of the earthquake; this is done using updated information every second. The predicted ground motion at any site can be computed by the ground motion model in equations 2.13 and 2.14, since a magnitude and distance define the ground motion envelope uniquely in the model. This strategy assumes a point-source model and works for small to moderate earthquakes (magnitude < 6.5).

2.5 Summary

In this chapter, we briefly discussed the basic procedures of the VS method developed by Cua and Heaton (Cua, 2005; Cua and Heaton, 2006).

The VS method is a Bayesian approach for seismic early warning systems. It incorporates prior information which can be obtained before an event and a likelihood function computed from the ground motion data available after the initial P-wave detection, and finds the most probable estimate for magnitude and location by maximizing the posterior, which is equivalent to maximizing the product of prior pdf and likelihood function.

We discussed how to define prior pdf and likelihood function from available set of data in this chapter. The location of known faults, and previously observed seismicity, geometric consideration of stations, and Gutenberg-Richter law are considered as the prior information. Likelihood function is defined in terms of the magnitude ground motion relationship and envelope ground motion amplitudes. More detail about the VS method and examples of the application of the VS method are shown in Cua's Ph.D. thesis (Cua, 2005).

Chapter 3

Extended Virtual Seismologist Method

This chapter discusses a strategy to extend the Virtual Seismologist method to large earthquakes. We obtain the finite-rupture information by inverting high-frequency and low-frequency ground motions respectively. To understand this procedure, it is important to recognize the characteristics of high-frequency and low-frequency ground motions. This chapter also analyzes the statistical features of observed high-frequency and low-frequency ground motions for large earthquakes with magnitude greater than 6.0.

3.1 Road map for Virtual Seismologist Finite-Source method

The previous chapter briefly discusses the general VS method. In its current level of development, this methodology seems effective for earthquakes (M $<$ 6.5), where rupture can be modelled with a point source. However, for large earthquakes, rupture length can be on the order of tens to hundreds of kilometers, and the heterogeneous slip distribution significantly affects the ground motion amplitude expected at a site. For example, the fault rupture in the 1999 Chi-Chi earthquake was longer than 80 km, and the largest slip was recorded near the end of the rupture at the northern end of the fault. It would be difficult, if not impossible, to predict such large shaking at large distances from the epicenter when using a scheme that only characterizes the earthquake as a point source.

In order to extend the VS method to earthquakes with M > 6.5, we need to consider the fault rupture geometry and the size of slip on the fault. To differentiate the VS method considering the fault finiteness, we call the general VS method described in the previous chapter "VS Point-Source (PS) method" and the VS method for large earthquakes "VS Finite-Source (FS) method."

Our strategy for large earthquakes is as follows. (See also figure 3.1.)

01

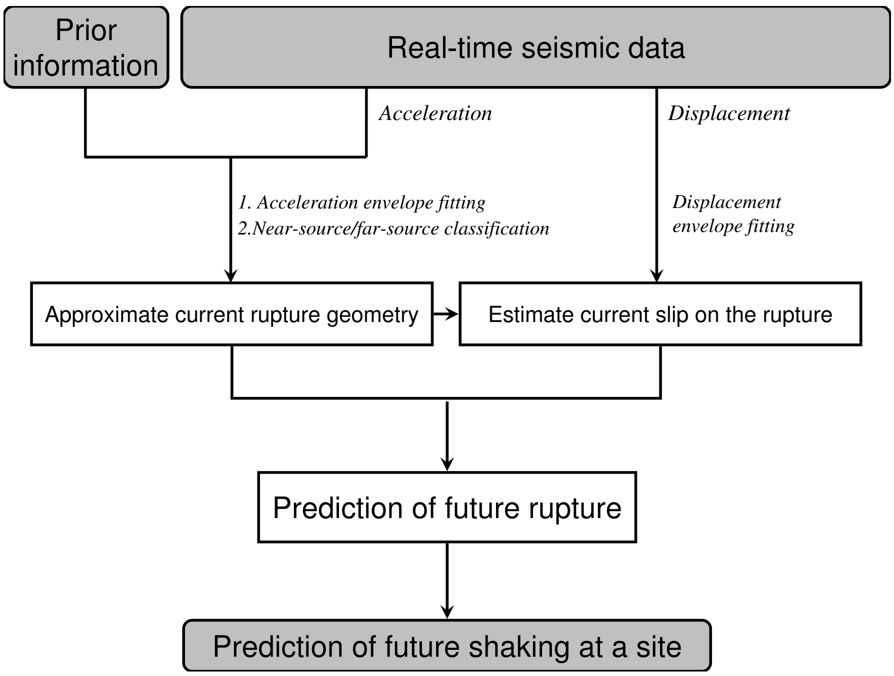

Figure 3.1: The algorithm of the VS method for finite source (VS-FS method). First, we estimate the rupture geometry from the accelerations by the methods discussed by Yamada and Heaton (2006) and Yamada et al. (2006). Based on this geometry, slip on the fault can be estimated from displacement records. By combining current rupture information and prior information, the predicted probability of rupture extent can be obtained.

1) Apply the VS-PS method

First, apply the VS-PS method to the ongoing rupture. Estimate the epicenter and magnitude of an event when the closest stations record the P-waves. If the magnitude is less than a certain threshold (e.g. $M < 5.5$), the estimated location and magnitude of the earthquake is accepted. If it exceeds the threshold, then there is a reasonable possibility that the earthquake is large, and it might not be adequately modeled as a point source. In this case, we apply VS Finite-Source (FS) method to find the location of the finite fault.

2) Estimating the current rupture extent

The VS-FS method determines the ongoing rupture geometry in real time from high frequency ground motions. Acceleration records are used to estimate the temporal and spatial evolution of the rupture front. Use of Bayes' theorem in equation 2.1 is also helpful here. The posterior pdf of the problem of estimating a rupture extent is the probability of the rupture location (S) given observed ground motion data (A). Bayes' Theorem for the problem to estimate rupture geometry is:

$$prob(S|A) \propto prob(A|S) \times prob(S). \tag{3.1}$$

The prior $prob(S)$ is information known before examining waveform data, such as the location of known faults. Large earthquakes often occur on recognized active faults, and information about the location and activity of these faults is potentially a valuable set of prior information. After an earthquake initiates and ground motion data becomes available, the likelihood function will be computed.

The likelihood function $prob(A|S)$ is the probability of the ground motion amplitude observation given the rupture location. Two separate methodologies have been developed to estimate the evolving rupture geometry:

i) the multiple source model described in chapter 4 determines the rupture geometry that best predicts the envelopes of high-frequency ground motions (Yamada and Heaton, 2006); and

ii) a near-source versus far-source station discriminator in chapter 5 has been developed which allows us to map the location of an ongoing rupture front (Yamada et al., 2006).

These techniques are used to characterize the likelihood function. They are also valuable for predicting the future ground motions.

3) Estimating size of the current slip on the fault

We determine the slip on the fault that is compatible with both the observed low-frequency motions and also with the rupture geometry determined from high-frequency motions. Aagaard et al. (2004) simulated near-source ground motions and investigated the near-source displacement as a function of distance from the fault. We use the result of their simulations to characterize the slip on the fault, and construct an analytical function to estimate slip on the fault from observations of displacement away from the fault.

The probability of the slip on the fault (D) given the rupture geometry and real-time seismic data is also written by Bayes' Theorem:

$$prob(D|A,S) \propto prob(A|D,S) \times prob(A|S). \tag{3.2}$$

The likelihood function $prob(A|D,S)$ is the probability of the ground motion amplitude observation given rupture location and size of the slip. Substituting $prob(A|S)$ from equation 3.1, the probability is expressed as:

$$prob(D|A,S) \propto prob(A|D,S) \times prob(A|S) \times prob(S). \tag{3.3}$$

Currently, the displacement data is obtained from the double integration of strong motion accelerations, and it can be difficult to remove erroneous baselines in real-time analysis. However, quite a few high-frequency GPS—which record displacement directly—are installed these days, so we assume displacement data will be available in real time. In real-time analysis, we back project the recorded displacement data onto the fault line to estimate the size of the slip on the fault. The fault slip makes it possible to predict long-period seismic waves, which is important to estimate seismic damage. The current size of the slip on the fault allows for a probabilistic prediction of additional rupture in the near future.

4) Predicting the probability of rupture extent

We also create a methodology to predict the total length of the rupture propagation conditioned on the current slip size. Liu-Zeng et al. (2005) created a methodology to generate simple 1-D models of spatially heterogeneous slip. By using this methodology, we compute the probability of the final rupture length (L) conditioned on the current slip on the fault (D) in a statistical way. Intuitively, a rupture is much more likely to terminate in the near future if its present value is small. Our final goal is to predict final rupture extent from ground motion data available in real time.

3.2 Statistics of observed high-frequency and low-frequency ground motions

The ground motions at a site could be different for different earthquakes of the same magnitude at the same distance, because of differences in source mechanisms, path effect, or site conditions. One of the most commonly used ground motion parameters is peak ground acceleration (PGA), and Campbell (1981) found that the uncertainty of peak ground acceleration can be modeled using a lognormal distribution. In other words, the distribution of the amplitude of ground motions with constant magnitude and distance follows a lognormal distribution.

Studies of near-source records show that the high frequency ground motion saturates as a function of magnitude for large earthquakes, and it weakly depends on the magnitude in the near-source (Hanks and Johnson, 1976; Joyner and Boore, 1981; Hanks and Mcguire, 1981). Therefore, if we constrain the size of the magnitude greater than a certain number, the distribution of the near-source PGA of those earthquakes can be assumed to be a lognormal distribution.

However, the low frequency ground motion has a strong correlation with the magnitude of an earthquake, as we see in the formula of the seismic moment and average slip on the fault. We use power law distributions to describe the statistics of near-source peak ground displacement (PGD). Gutenberg-Richter Law of earthquake magnitudes obeys a power law. The number of earthquakes per year of magnitude M is proportional to the base-ten exponential of the magnitude M. The relationship between magnitude and the PGD is expected to be a power law distribution, i.e., the PGD increases as seismic magnitude becomes large.

In this section, we analyze near-source PGA and PGD of 10 major earthquakes with magnitude greater than 6.0 and show the near-source ground motion distributions.

3.2.1 Data

We investigate strong motion datasets of ten earthquakes with magnitude greater than 6.0 and containing records of near-source stations. The earthquakes are shallow crustal earthquake with focal depths less than 25 km. The selected earthquake dataset is shown in table 3.1. Here, we defined the near-source station as a station with fault distance less than 10 km. Fault models used to determine the fault distance are also shown in table 3.1. 147 near-source records are used in total.

Those near-source accelerograms are processed according to the following method. The DC offset of accelerograms is corrected by subtracting the mean of the pre-event portion. This process sets the initial velocity and displacement to zero, which is important because a small DC offset has a large effect when the record is integrated. This process is used for all accelerograms.

The horizontal peak ground motions are calculated by the square root of the sum of the squares of the peak value of the EW and NS components. The vertical peak ground motions are the peak value of the UD component. The following processes are completed for all the data.

Table 3.1: Earthquake data set used for the near-source ground motion analysis. Moment magnitude (M_w) and focal depth are cited from Harvard CMT solution. The preliminary determination of epicenter is used for the focal depth. The definition of the near-source station is a station with fault distance less than 10 km. The numbers of near-source data for each earthquake are also shown. The fault models are used as selection criteria to classify near-source stations.

Earthquake	M_w	Records	Focal Depth	Fault Model
Imperial Valley (1979)	6.5	14	12.0	Hartzell and Heaton (1983)
Loma Prieta (1989)	6.9	8	19.0	Wald et al. (1991)
Landers (1992)	7.3	1	15.0	Wald and Heaton (1994)
Northridge (1994)	6.6	17	16.8	Wald et al. (1996)
Hyogoken-Nanbu (1995)	6.9	4	20.3	Wald (1996)
Izmit (1999)	7.6	4	17.0	Sekiguchi and Iwata (2002)
Chi-Chi (1999)	7.6	42	21.2	Ji et al. (2003)
Denali (2002)	7.8	1	15.0	Tsuboi et al. (2003)
Parkfield (2004)	6.0	47	12.0	Ji et al. (2004)
Niigataken-Chuetsu (2004)	6.6	9	13.0	Honda et al. (2005)
Total		147		

Acceleration: The accelerograms from which the DC offset is corrected are used to compute the PGA.

Displacement: The accelerograms from which the DC offset is corrected are integrated twice in the time domain and high-pass filtered using a forth-order Butterworth filter with a corner frequency of 0.075 Hz, avoiding most complications due to baseline shifts. However, the computed PGD from filtered displacement records can be significantly smaller than actual PGD.

Since it is difficult to compute the actual peak displacement, the filtering process is performed. The computed PGD from filtered displacement records are much smaller than actual PGD.

3.2.2 Statistics of observed high-frequency ground motions

Based on the collected near-source ground motion data (i.e., horizontal and vertical components of the PGA and PGD), we examine the statistical features of the near-source ground motions for large earthquakes.

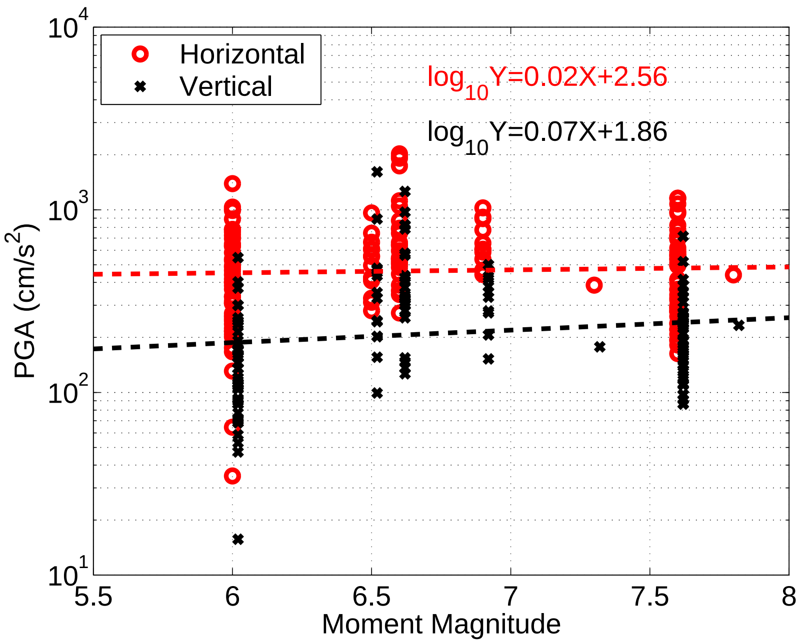

Figure 3.2: A plot of near-source (fault distance less than 10 km) PGA as a function of moment magnitude. The dashed lines are trendlines for the horizontal and vertical component and the regression equations are shown on the plot.

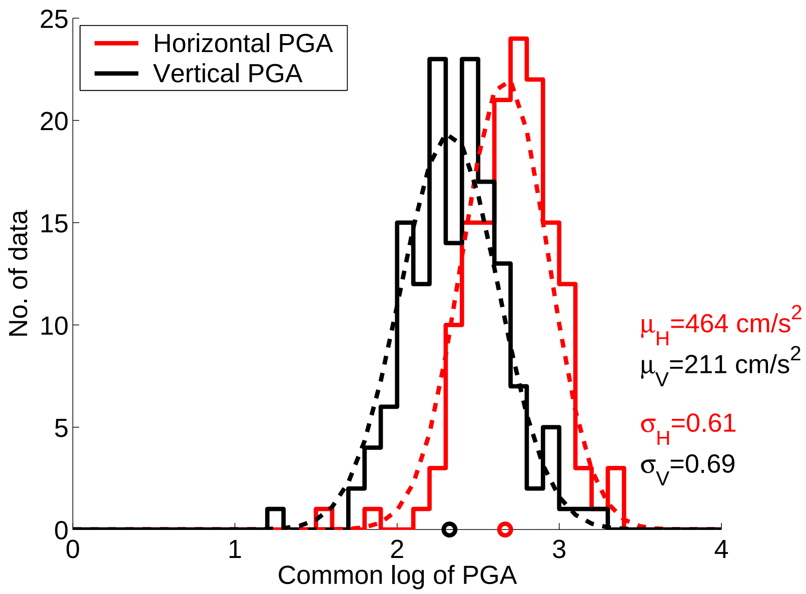

Figure 3.3: A histogram of the near-source (fault distance less than 10 km) PGA for earthquakes with magnitude ≥ 6.0. The dashed lines are lognormal distribution fitting to the histograms. The circles on the x-axis indicate the geometric mean of each component. The values of the geometric means and natural log of the geometric standard deviations are shown on the plot (μ and σ).

Figure 3.2 shows horizontal and vertical near-source PGA in this dataset as a function of moment magnitude. Even though data from the same earthquake are scattered, the slope of regression line is almost equal to zero. Based on the two tailed Student's t-test, these slopes fall inside of the 95% confidence interval of the zero slope. This is consistent with past studies which indicate the high frequency ground motion at near-source region saturate as a function of magnitude for large earthquakes.

We also examine the marginal distribution of PGA. Figure 3.3 show histograms of horizontal and vertical PGA. The horizontal and vertical acceleration histograms show a good fit to the lognormal distribution. This is reasonable since the uncertainty of PGA for earthquakes of the same magnitude at the same distance can be modeled using a lognormal distribution. Also, the PGA of near-source stations weakly depends on the magnitude for large earthquakes. Therefore, all the PGA data with magnitude greater than 6.0 are approximately independent of magnitude and lognormally distributed.

3.2.3 Statistics of observed low-frequency ground motions

The distributions of horizontal and vertical PGD as a function of moment magnitude are shown in figure 3.4. The log of PGD is proportional to the magnitude. The high frequency motion does not depend on magnitude for large earthquake and observed PGA do not exceed 2g. However, low frequency motion is highly correlated with magnitude, and the amplitude seems to follow a power law. There is evidence that average fault slip ($\bar{D}$) scales with rupture length (L), even for large earthquake (Scholz, 1982; Liu-Zeng et al., 2005). In this case we expect that seismic moment $M_0 \propto L\bar{D} \propto \bar{D}^2$ for large crustal earthquakes. Since moment magnitude $M \propto 2/3 \log M_0$, we expect that $\log \bar{D} \propto 3/4M$. If near-source ground displacement is a linear function of the fault slip and rupture length (L) $\gg$ rupture width (W), then we expect that near source displacement should scale as $3/4M$. The slopes of the near-source ground displacement in figure 3.4 are 0.6 and 0.71 for horizontal and vertical components, respectively. These numbers are consistent with this theoretical interpretation.

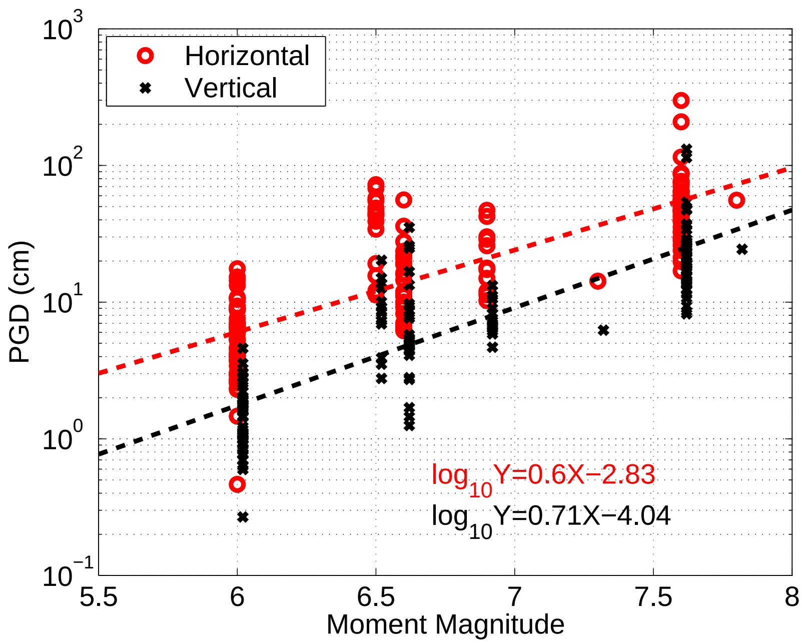

Figure 3.4: A plot of near-source (fault distance less than 10 km) PGD as a function of moment magnitude. The dashed lines are trendlines for the horizontal and vertical component and the regression equations are shown on the plot.

The histogram of PGD does not follow a lognormal distribution. We discuss the theoretical form of the PGD distribution.

From the Gutenberg Richter Law, N_E, the number of earthquakes having magnitude greater than M, is proportional to the base-ten exponential of $-M$.

$$N_E \propto 10^{-M}, \tag{3.4}$$

$$\frac{dN_E}{dM} \propto 10^{-M}. \tag{3.5}$$

Since the moment scales as $2/3$ of log of the product of average slip ($\bar{D}$) and fault rupture area (S), equation 3.5 becomes:

$$\begin{aligned} N_E &\propto 10^{-\log(\bar{D}S)^{2/3}} \\ &\propto (\bar{D}S)^{-2/3}. \end{aligned} \tag{3.6}$$

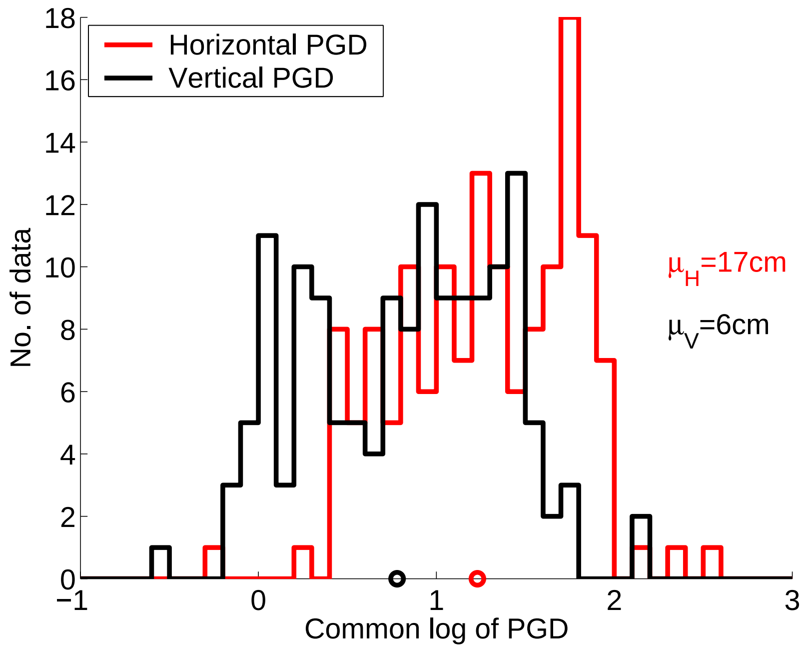

Figure 3.5: A histogram of the near-source (fault distance less than 10 km) PGD for earthquakes with magnitude ≥ 6.0. The circles on the x-axis indicate the geometric mean of each component and their values are shown on the plot (μ).

We assume the number of the near-source stations is proportional to the fault rupture area (S) times station distribution density (ρ_s). The number of records (N_r) of earthquakes with magnitude M is:

$$\begin{aligned} N_r \propto & N_E \times S \times \rho_s \\ \propto & (\bar{D}S)^{-2/3} S \rho_s \\ \propto & \bar{D}^{-2/3} S^{1/3} \rho_s. \end{aligned} \tag{3.7}$$

Assuming homogeneous station distribution (ρ_s=constant), equation 3.7 is:

$$N_r \propto \bar{D}^{-2/3} S^{1/3}. \tag{3.8}$$

The fault rupture surface is equal to the product of fault rupture length (L) and fault rupture width (W). For large earthquakes, $L \gg W$, and W has an upper limit (Scholz, 1982). Assuming constant stress drop, the average slip scales as the fault rupture area, which is proportional to the rupture length ($\bar{D} \propto S \propto L$). Substituting this relationship into equation 3.8,

$$N_{ns} \propto \bar{D}^{-2/3} S^{1/3} \tag{3.9}$$
$$\propto \bar{D}^{-2/3} \bar{D}^{1/3} \tag{3.10}$$
$$\propto \bar{D}^{-1/3}. \tag{3.11}$$

This shows that the number of records of earthquakes with a certain amplitude slowly decays with its amplitude. Our observations of large earthquakes are too few to verify this theory experimentally, and there are some assumptions which do not hold in our dataset (e.g., homogeneous station distribution). However, this simple derivation considering the Gutenberg Richter Law and fault rupture dimension shows that the probability that a site will experience large ground displacement is not as small as we can ignore. In figure 3.5, the distribution of PGD does not seem to follow the distribution in equation 3.11, but it shows records of large ground displacements as many as those of small ground displacements. This observation is important for high-rise buildings, telling us there are high probability that buildings are subjected to large ground displacements.

3.2.4 Comparison of high-frequency and low-frequency ground motions

We compare horizontal PGA and PGD distributions in figures 3.6 and 3.7. Figure 3.6 shows the moment magnitude versus PGA and PGD. The amplitudes of the PGA and PGD are normalized by the geometric mean of each. The PGA saturate as a function of moment magnitude, and the slope of the trendline is about zero. On the other hand, the PGD trendline is log proportional to the moment magnitude.

Figure 3.7 shows the histogram of horizontal PGA and PGD normalized by the geometric mean of each component. The PGA follows a lognormal distribution centered at 464 cm/s^2. The variance for the high-frequency motions is smaller than that

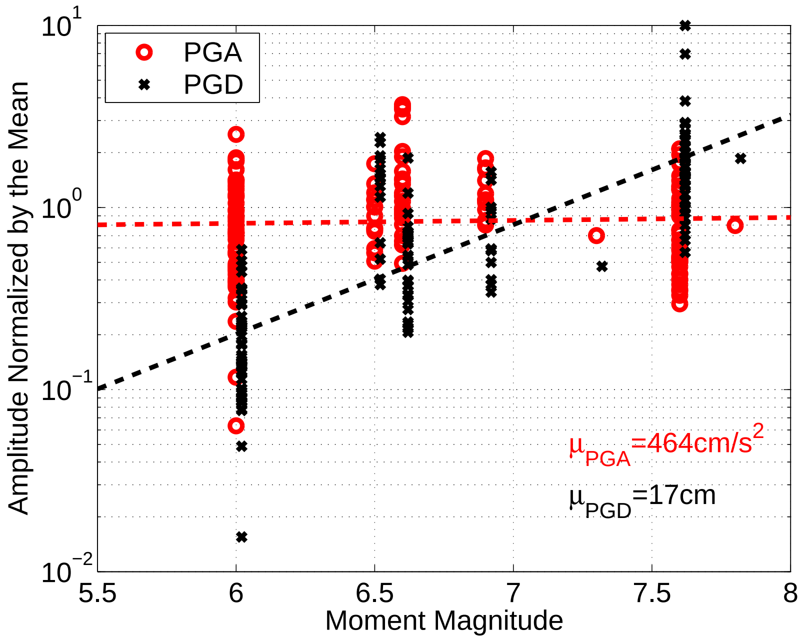

Figure 3.6: A comparison of near-source PGA and PGD as a function of moment magnitude. The dashed lines are trendlines for each component. The numbers on the plot (μ) are the geometric mean of each component.

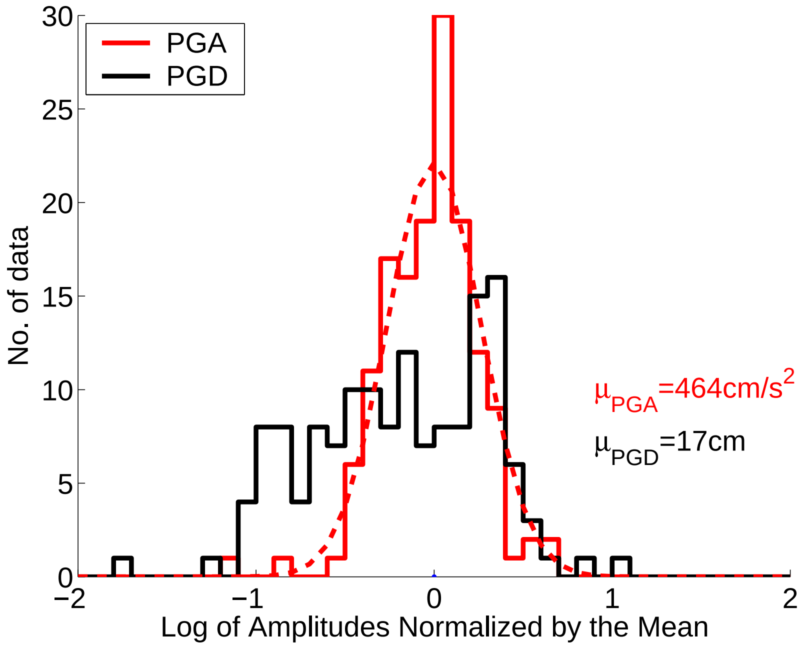

Figure 3.7: A histogram of the near-source PGA and PGD for earthquakes with magnitude ≥ 6.0. The numbers on the plot (μ) are the geometric mean of each component.

of the low-frequency motions. This is reasonable since the high-frequency ground motions saturate as a function of magnitude, the variance of PGA is not as large as that of PGD.

3.2.5 Definitions of the horizontal component

The horizontal component in this thesis is computed by the square root of the sum of squares of peak EW component and peak NS component. However, there are other definitions for the horizontal acceleration.

For example, in some cases, a peak value over time of the largest of the two accelerations from each of the recorded horizontal channel is also used. We compared the three different definitions of horizontal components.

(1) square root of sum of squares (srss) horizontal components = $\sqrt{\max(EW)^2 + \max(NS)^2}$: the square root of sum of squares of peak EW component and peak NS component.

(2) magnitude of horizontal vector = $\max(\sqrt{EW^2 + NS^2})$: peak over time of the amplitude of the srss horizontal acceleration vector.

(3) root mean squares (rms) horizontal components = $\sqrt{\frac{1}{2}(\max(EW)^2 + \max(NS)^2)}$: the root mean squares of peak EW component and peak NS component.

It is obvious that the rms horizontal components in definition (3) is $\sqrt{1/2}$ as large as the srss horizontal components in definition (1), so the horizontal components only in definition (1) and (2) are compared.

Figures 3.8 and 3.9 show the PGA and PGD as a function of magnitude, and figures 3.10 and 3.11 show the distributions of PGA and PGD. For both PGA and PGD, the definition (1) is a little larger than definition (2). The geometric means of PGA for definition (1) and (2) are 464 cm/s^2 and 393 cm/s^2, and the geometric means of PGD for definition (1) and (2) are 17.0 cm and 15.3 cm. Therefore, the definition (2) is 85% smaller for PGA, and 90% smaller for PGD, than the definition (1). This means it is easy to estimate the horizontal component of one definition from that of the other definition.

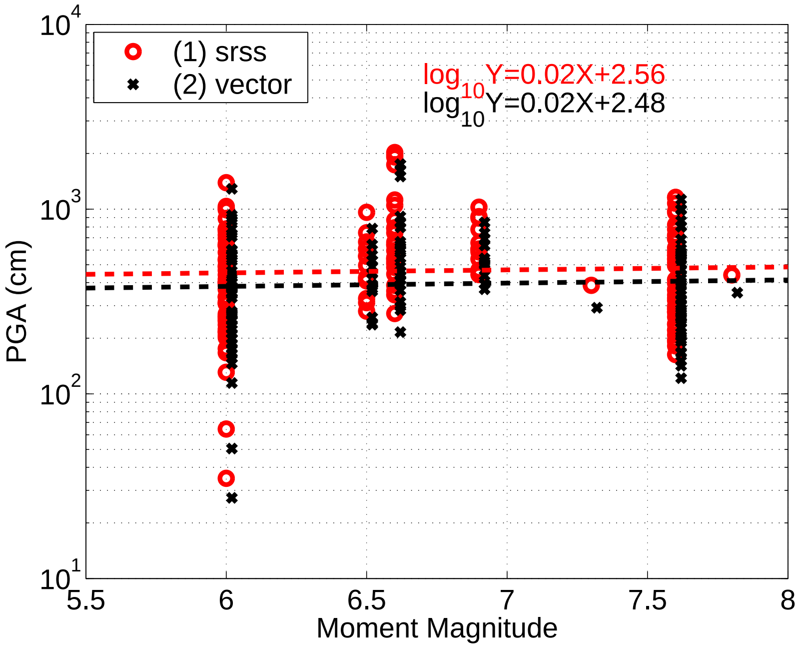

Figure 3.8: Comparison of the srss horizontal PGA (definition (1)) and magnitude of horizontal accelerations (definition (2)) as a function of magnitude.The regression curves and regression equations are also shown in the plot.

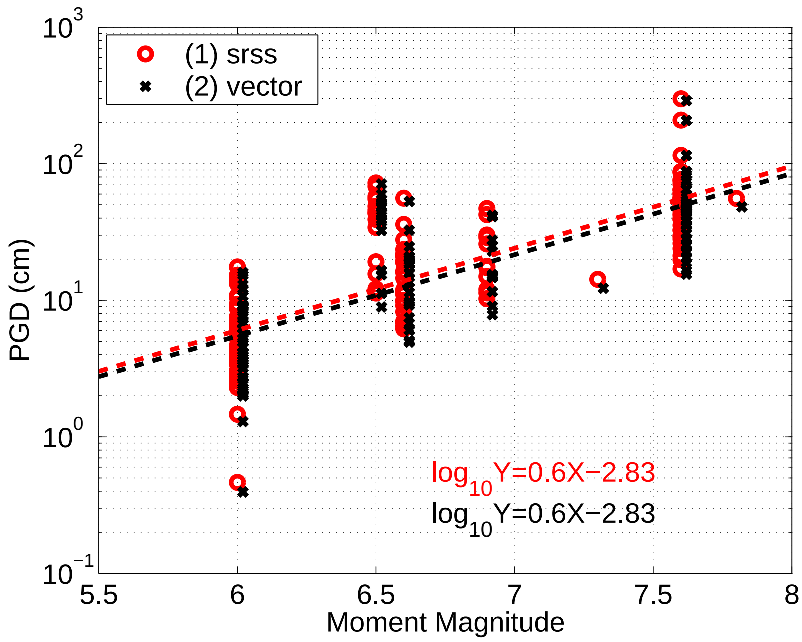

Figure 3.9: Comparison of the srss horizontal PGD (definition (1)) and magnitude of horizontal displacements (definition (2)) as a function of magnitude.The regression curves and regression equations are also shown in the plot.

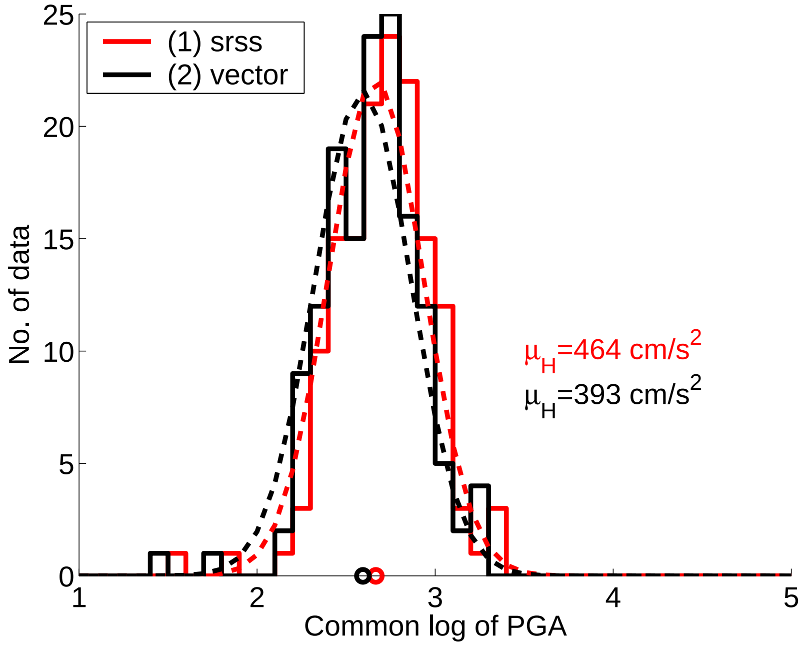

Figure 3.10: A histogram of the srss horizontal PGA (definition (1)) and magnitude of horizontal accelerations (definition (2)) for earthquakes with magnitude ≥ 6.0. The numbers on the plot (μ) are the geometric mean of each acceleration.

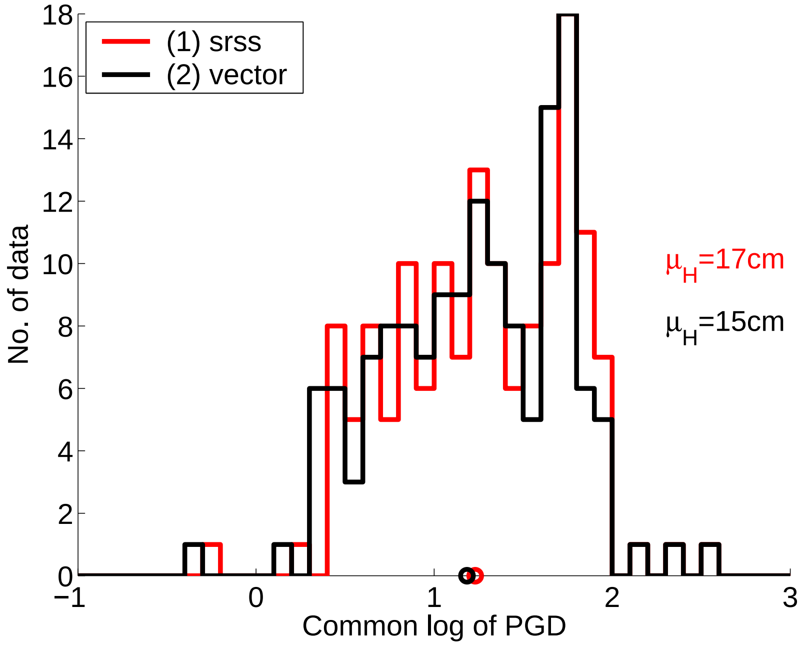

Figure 3.11: A histogram of the srss horizontal PGD (definition (1)) and magnitude of horizontal displacements (definition (2)) for earthquakes with magnitude ≥ 6.0. The numbers on the plot (μ) are the geometric mean of each displacement.

3.3 Summary

In this chapter, we explained a strategy to extend the VS-PS method to large earthquakes. For large earthquakes, the rupture length can be on the order of tens to hundreds of kilometers, and the heterogeneous slip distribution significantly affects the ground motion amplitude at a site. In order to estimate the size and location of an earthquake or the expected ground motion at a given site, we need to characterize the fault geometry and size of the slip on the fault in real time.

The statistical features of high-frequency and low-frequency ground motions for large earthquakes with magnitude greater than 6.0 were analyzed. The observations show that the near-source peak ground accelerations saturate as a function of magnitude for large earthquakes, and is almost independent of magnitude if the magnitude is greater than 6.0. The marginal distribution of PGA follows the lognormal distribution with mean 464 and 211 cm/s^2 for the horizontal and vertical acceleration, respectively. On the other hand, the near-source low frequency ground motion for large earthquakes has strong correlation with the magnitude of an earthquake, and the PGD scales by a power law with the magnitude.

We compute the horizontal components of ground motion from three definitions and compare the results. The three definitions (srss horizontal components, magnitude of horizontal vector, and rms horizontal components) are linear scale of each other. The horizontal component of one definition can be estimated from that of the other definition.

For early warning of large earthquakes, we use high-frequency seismic radiation to determine ongoing fault rupture geometry in real-time and low-frequency ground motion to estimate the slip on the fault. In chapters 4 and 5, we propose two approaches to determine the ongoing fault rupture geometry from accelerograms in real time. In chapter 7, we focus on estimating slip on the fault in real time and the probabilistic prediction of additional rupture in the near future.

Chapter 4

Estimating the Location of Fault Rupture Using Envelopes of Acceleration

Early warning information based on a point-source model may underestimate the ground motion at a site, if a station is close to the fault and distant from the epicenter. This occurs because, for large earthquakes, the peak characteristics of ground motion, such as peak ground acceleration, have stronger correlation with the fault rupture distance rather than with the epicentral or hypocentral distance (Campbell, 1981). (The definition of the fault rupture distance in this paper is the shortest distance between the station and the surface projection of the fault rupture surface.)

In order to construct an early warning system that is more reliable for large earthquakes, it is necessary to estimate the fault rupture extent and slip on the fault in real time. The VS-FS method uses high-frequency ground motions to estimate the temporal and spatial evolution of the rupture. Two separate methodologies have been developed to estimate the evolving rupture geometry:

i) the multiple source model described in this paper determines the rupture geometry that best predicts the envelopes of high-frequency ground motions (Yamada and Heaton, 2006) and

ii) a near-source versus far-source station discriminator has been developed which allows us to map the location of an ongoing rupture front (Yamada et al., 2006).

In this chapter, we introduce a methodology that can estimate the rupture geometry from acceleration envelopes. The second methodology will be introduced in the next chapter. In this analysis, we characterize the rupture geometry with three parameters, an azimuthal direction, and two rupture lengths, one in the positive direction and one in the negative direction as measured from the epicenter. These parameters can be estimated from acceleration envelopes in real time.

4.1 Ground motion models for large earthquakes

As we saw in the previous chapter, accelerations recorded close to a rupture saturate at magnitudes larger than 6, whereas distant sites do not demonstrate comparable saturation as a function of magnitude. Examples of the near-source accelerations and their envelopes are shown in figures 4.1 - 4.4 The envelope functions (Cua, 2005) are made from the dataset including earthquakes with magnitudes ranging between 2 and 7, assuming point-source model. Therefore, we need a new envelope function which can fit the acceleration envelopes of large earthquakes.

We introduce a multiple source model to express the fault finiteness. The fault surface is divided into subfaults, and each subfault is represented by a single point source, called "subsources" (figure 4.5). To simplify the problem, we assume that the dimensions of all subsources are uniform. Each source nucleates, and the P- and S-waves are radiated when the rupture front arrives at the subsource.

The ground motion at a site is modeled as the combination of the responses of each subsource. For high-frequency motions with approximately random phase, we found that the square root of the sum of the squares of the envelope amplitudes from each subsource provides a good estimation of an acceleration envelope.

$$E_{total}(t) = \sqrt{\sum_{i=1}^{n} E_i(t)^2}, \tag{4.1}$$

where $E_{total}(t)$ is the estimated envelope as a function of time, $E_i(t)$ is the envelope of the ith source, and n is the total number of subsources. $E_i(t)$ is actually a fairly complex function of time, magnitude, distance, and station corrections, although its

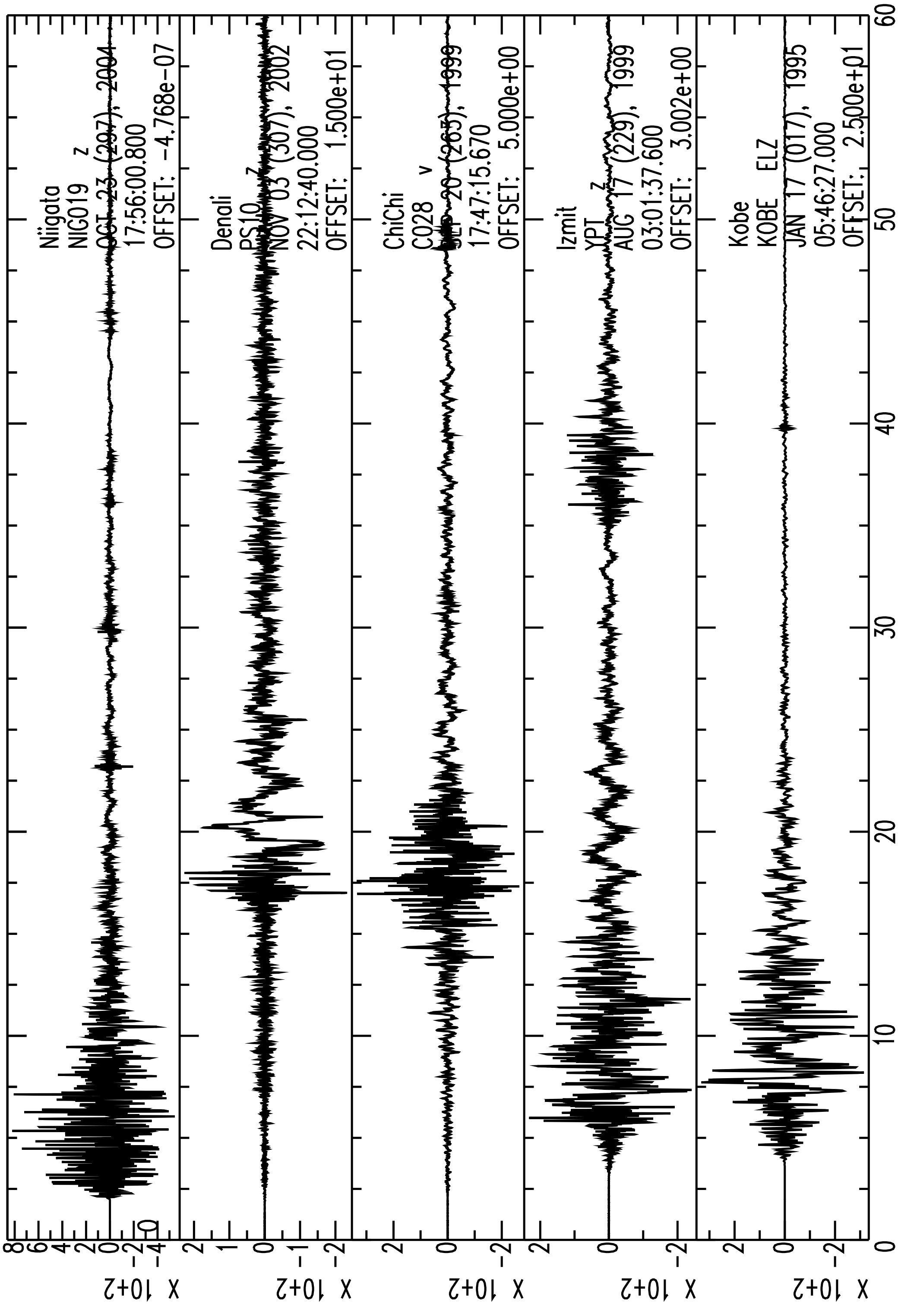

Figure 4.1: Near-source accelerations in the vertical component.

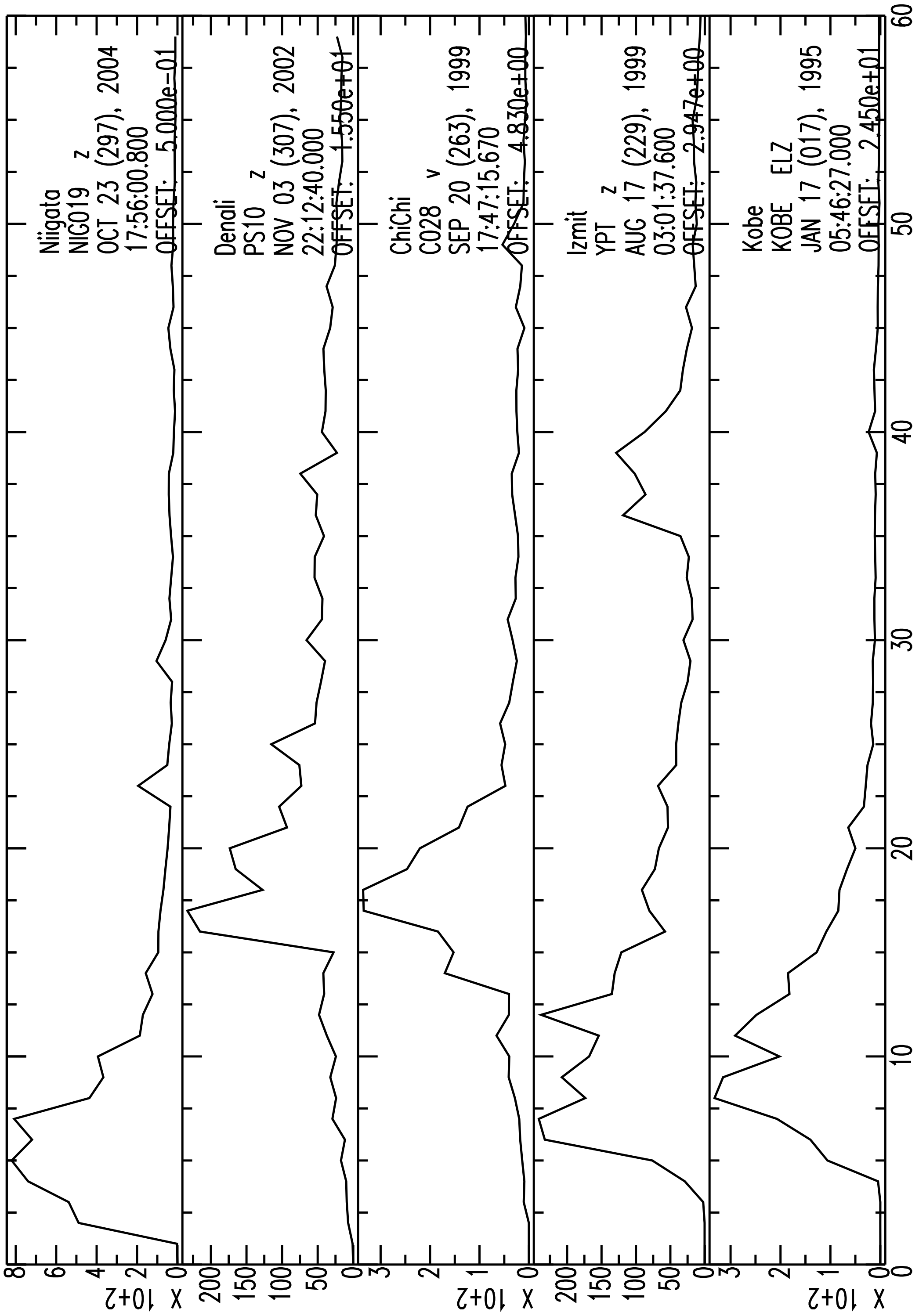

Figure 4.2: Envelopes of near-source accelerations in the vertical component.

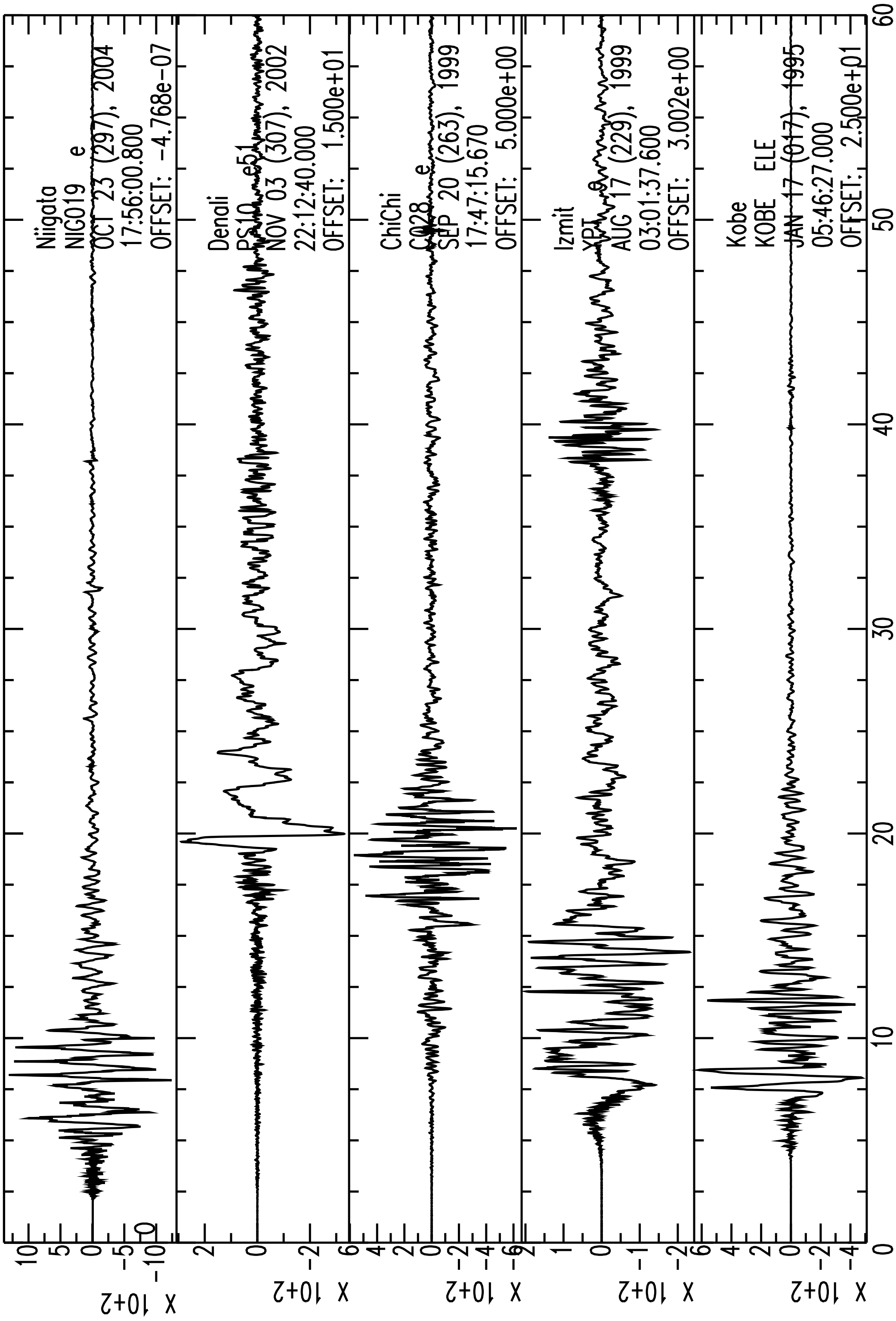

Figure 4.3: Near-source accelerations in the EW component.

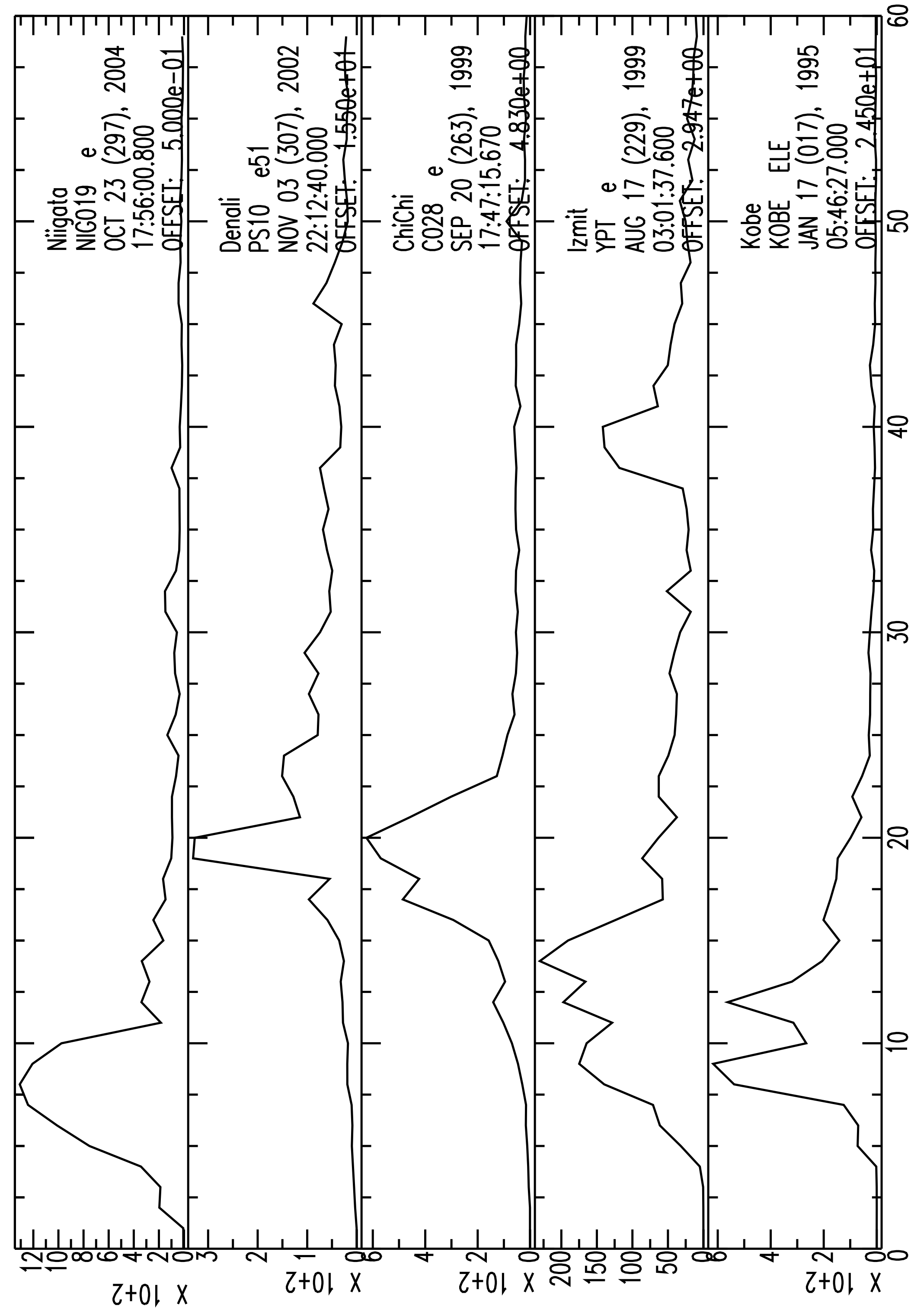

Figure 4.4: Envelopes of near-source accelerations in the EW component.

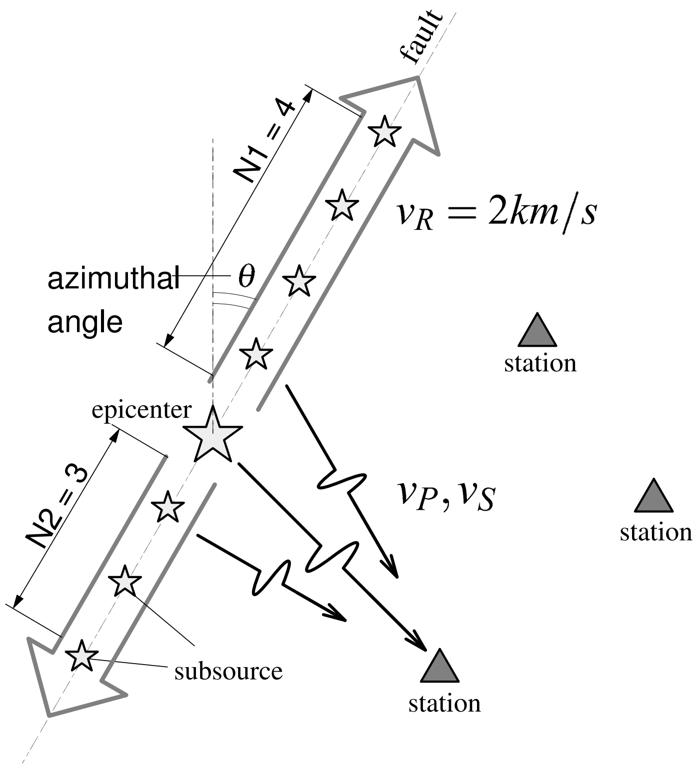

Figure 4.5: Schematic diagram of the multiple source model. The fault rupture is assumed to propagate from the epicenter at the constant velocity v_R. The fault is parameterized by θ, N1, and N2, where θ is the azimuthal angle of the fault, N1 and N2 are the number of subsources north and south of the epicenter, respectively. The ground motion at a station is expressed as a combination of the envelope from each subsource.

forward calculation is very fast since it only involves analytic functions (Cua, 2005; Cua and Heaton, 2006).

This model only works for high-frequency ground motions. Unlike longer-period ground motions, high-frequency motions seem to be insensitive to either radiation pattern (Liu and Helmberger, 1985) or directivity (Boatwright and Boore, 1982). Furthermore, near-source high-frequency motions saturate as a function of magnitude. That is, near-source high-frequency ground motions are independent of the amplitude of the slip for large earthquakes (Kanamori and Jennings, 1978; Cua and Heaton, 2006).

Heaton and Hartzell (1989) pointed out that the assumptions of a Brune (1970) source spectrum combined with constant stress drop leads to high-frequency energy radiated from a subfault that is independent of the slip on the subfault. A consequence of the fact that high-frequency near-source ground motions can be modeled as random noise whose amplitude is independent of slip is that the high-frequency radiated energy in earthquakes is proportional to the rupture surface area. This is consistent with the observation of Boatwright (1982), who showed that high-frequency spectral acceleration amplitudes are proportional to the root-mean-square (rms) dynamic stress drop and the square root of the rupture area. Our simple model for simulating high-frequency motions is also compatible with the observation of Hanks and Mcguire (1981) that high-frequency ground accelerations are remarkably similar from one event to another. Subsources for our multiple source model are evenly spaced, so the surface area and high-frequency radiated energy corresponding to each subsource are also constant. Based on this theoretical interpretation, we estimated the ground motion envelopes with the multiple source model for the 1999 Chi-Chi earthquake.

Figure 4.6 (top) shows an example of predicted envelopes for vertical accelerations using the multiple source model. It shows the envelopes of the vertical acceleration record for each subsource with magnitude 6.0. Figure 4.6 (bottom) shows the time history envelope of the accelerogram (vertical component) at the station C024, a station on the foot wall side and 10 km from the Chelungpu faultline (shown in figure 4.7, southwest of the epicenter). Figure 4.6 also shows that the vertical acceleration envelopes predicted by the multiple source model for the VS-FS method fit the observed envelopes much better than the envelopes predicted by the single source model for the VS-PS method.

Even though the Ch-Chi rupture has large spatial variations in the amplitude of the slip, it appears that the high-frequency accelerations can be modeled as a sum of the radiation from a uniform tiling of the magnitude 6.0 subfaults, based on the random-phase assumption and saturation with regard to magnitude.

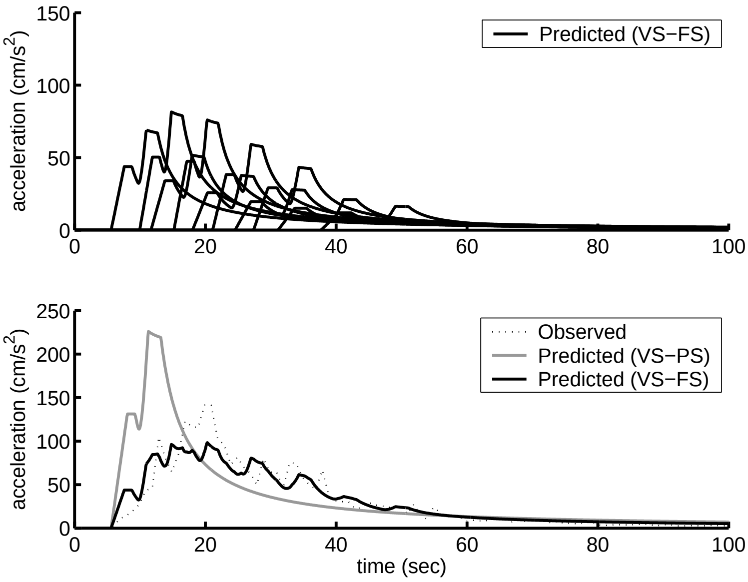

Figure 4.6: Envelopes of vertical acceleration recorded at the station C024 for the Chi-Chi earthquake. Top: predicted envelopes of the vertical acceleration record for each subsource with magnitude 6.0. Bottom: Observed envelope (in dotted black line), and predicted envelopes of the point-source model in VS-PS method (in solid gray line) and of the multiple source model in VS-FS method (in solid black line).

4.2 Finding the best estimates

We assume that the location of the epicenter is already estimated from the VS-PS method, and that the fault ruptures bilaterally from the epicenter with constant rupture velocity. Thus, the time delay for each subsource rupture is the distance from the epicenter divided by the rupture velocity. Therefore, parameters that we need to estimate from the observed data are the azimuthal angle (θ) of the rupture direction, and N1 and N2, that are used to simulate each of the segments of the bilateral rupture.

The best estimate of the model parameters minimizes the residual sum of the squares (RSS) between observed ground motion envelopes and predicted envelopes from the multiple source model. The misfit function as a measure of goodness of fit is defined as follows:

$$RSS(t) = \sum_{i=1}^{ns}\sum_{j=1}^{2}\sum_{k=1}^{t}(A_{ijk} - \hat{A}_{ijk})^2, \tag{4.2}$$

where ns is the number of stations, t is the time in 1 second intervals ($\Delta t = 1$) from the event onset, and A_{ijk} and $\hat{A}_{ijk}$ are observed and predicted envelopes of component j at station i at time $k\Delta t$.

This form of the misfit function tends to emphasize the importance of fitting stations with large accelerations. That is, distant stations have small observed and predicted accelerations and even if there are serious discrepancies in the ratio of the predicted and observed amplitudes, they will have little impact on the inversion. The results of different misfit functions are shown in Section 4.3.5.

Our parameterization scheme has the advantage that we characterize the source with relatively few parameters (θ, N1, N2), none of which require high-precision estimates. However, for this strategy to be effective, we will need to solve a nonlinear inverse problem in real time. In this study, we solve this nonlinear inverse problem by using the Neighborhood Algorithm (Sambridge, 1999a,b). We recognize that other inverse techniques may ultimately be chosen for real-time applications. However, since the purpose of this study is to determine the effectiveness of our parameterization, we use the Neighborhood Algorithm to characterize and solve this nonlinear inverse problem.

The Neighborhood Algorithm is a direct search method for finding models of acceptable data fit in a multidimensional parameter space. We generate samples in the parameter space and draw the Voronoi cells for these samples. Voronoi cells are nearest neighbor regions defined under a suitable distance norm, and the shape and the size of each Voronoi cell is determined by the sample distribution in the parameter space. See figure 4.7 as an example of Voronoi cells that are used to define the nearest neighbors to seismic stations. We calculate the misfit function for each sample and choose the model with the lowest misfit. New samples are generated by performing a uniform random walk in the chosen Voronoi cell. By repeating these steps, we will

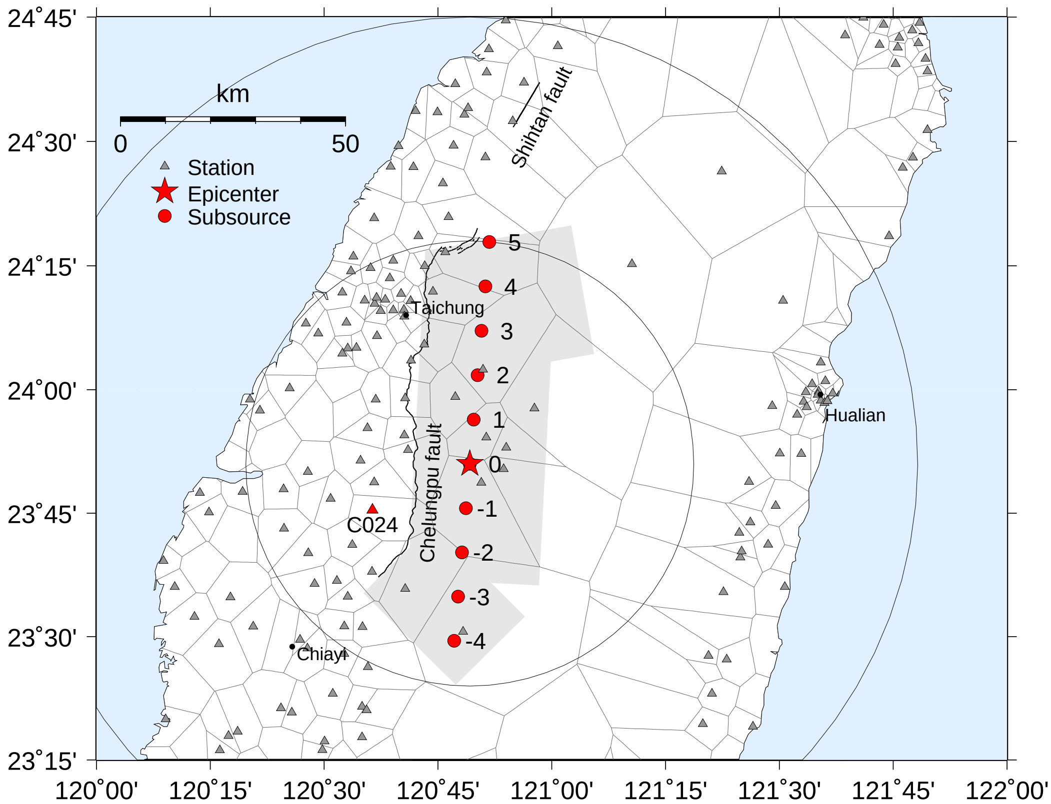

Figure 4.7: The fault geometry and the station distribution of the Chi-Chi earthquake. The shaded area around the epicenter displays the map projection of the fault geometry proposed by Ji *et al.* (2003). Small circles indicate the location of subsources determined based on the fault model. The area within 50 km and 100 km from the epicenter is shown by large circles. Stations used in this analysis are shown by solid triangles. The polygon surrounding each station is the Voronoi cell for the station.

find a set of samples that identifies those regions of the parameter space that provide the best fit to the data. This is an approach for constructing the posterior probability density function from the ensemble samples based on the Voronoi cell concept.

4.3 Example from the Chi-Chi earthquake

4.3.1 Data used for the VS-FS method

The data for this analysis is the strong motion dataset from the 21 September 1999 Chi-Chi Earthquake that occurred in central Taiwan (Lee et al., 2001). The epicenter was located at 120.82 N, 23.85 E, with a focal depth of 8 km according to the Central Weather Bureau (CWB) of Taiwan (Shin and Teng, 2001). It is currently the largest well-recorded earthquake with moment magnitude 7.6. 441 strong motion stations recorded the main event, and 69 of those were at distances of less than 50 km from the epicenter. We use three component (NS, EW, and UD) strong motion records from the data set collected by CWB. They classified the recorded accelerograms into four quality groups based on the existence of absolute timing, pre-events, and defects. For this analysis, we use QA-class data (best for any studies), QB-class data (next best but no absolute timing) and a part of QC-class data (covering the principal strong motions but not having pre-event or post-event data) which includes the pre-event. Stations of which we use the records are shown in 4.8. The color code of each station indicates soil condition. Cua (2005) classified those station classes into a binary rock-soil classes. Class A and B are classified as "rock," and class C, D, and E as "soil." Most of the stations in Taiwan are class C and below, so we use the ground motion model for soil only. Figure 4.8 shows that the soil conditions of the stations corresponds to the geographical formation. Western part of the Taiwan island is soft soil basin, where most of the major cities are located. Eastern part of the island is mountainous area, and there are not many stations. On the east coast, there are cities such as Yilan or Hualien where station distribution is very high. The Chi-Chi earthquake occurred at the boundary of western basin and eastern mountains. Around the epicenter the station distribution is very inhomogeneous (see figure 4.11): there are many stations on the west side (foot-wall side of Chelungpu fault) and few stations on the east side (hanging-wall side of Chelungpu fault).

Figures 4.9 – 4.11 are closer looks of figure 4.8 with station code. The station code has four characters: the first alphabet is an abbreviation of the district, and the last three numbers are a sequencing number. Prefix "C" indicates Chiayi, "H," Hualien, "I," Yilan, "N," Taitung, "P," Taipei, and "T," Taichung.

Table 4.1 describes the crustal model for P-wave and S-wave velocity in central Taiwan (Ma et al., 1996). P-wave and S-wave arrival time for the predicted envelope are computed with this 1-D layered crustal model. Since the original seismic records

Table 4.1: P-wave and S-wave velocity model in central Taiwan (Ma et al., 1996).

Thickness(km)	V_p(km/s)	V_s(km/s)
1.0	3.50	2.00
3.0	3.78	2.20
5.0	5.04	3.03
4.0	5.71	3.26
4.0	6.05	3.47
8.0	6.44	3.72
5.0	6.83	3.99
0.0	7.28	4.21

reported incorrect universal time, we use the data modified by Lee et al. (2001). They compared picked P-wave arrival times with computed theoretical P-wave arrival times. If the P-time residual was larger than 1 second for accelerograms at the distance within 50 km, they corrected the P-wave arrival time (Lee et al., 2001). Therefore, the error of the time stamp of the modified data is less than 1 second.

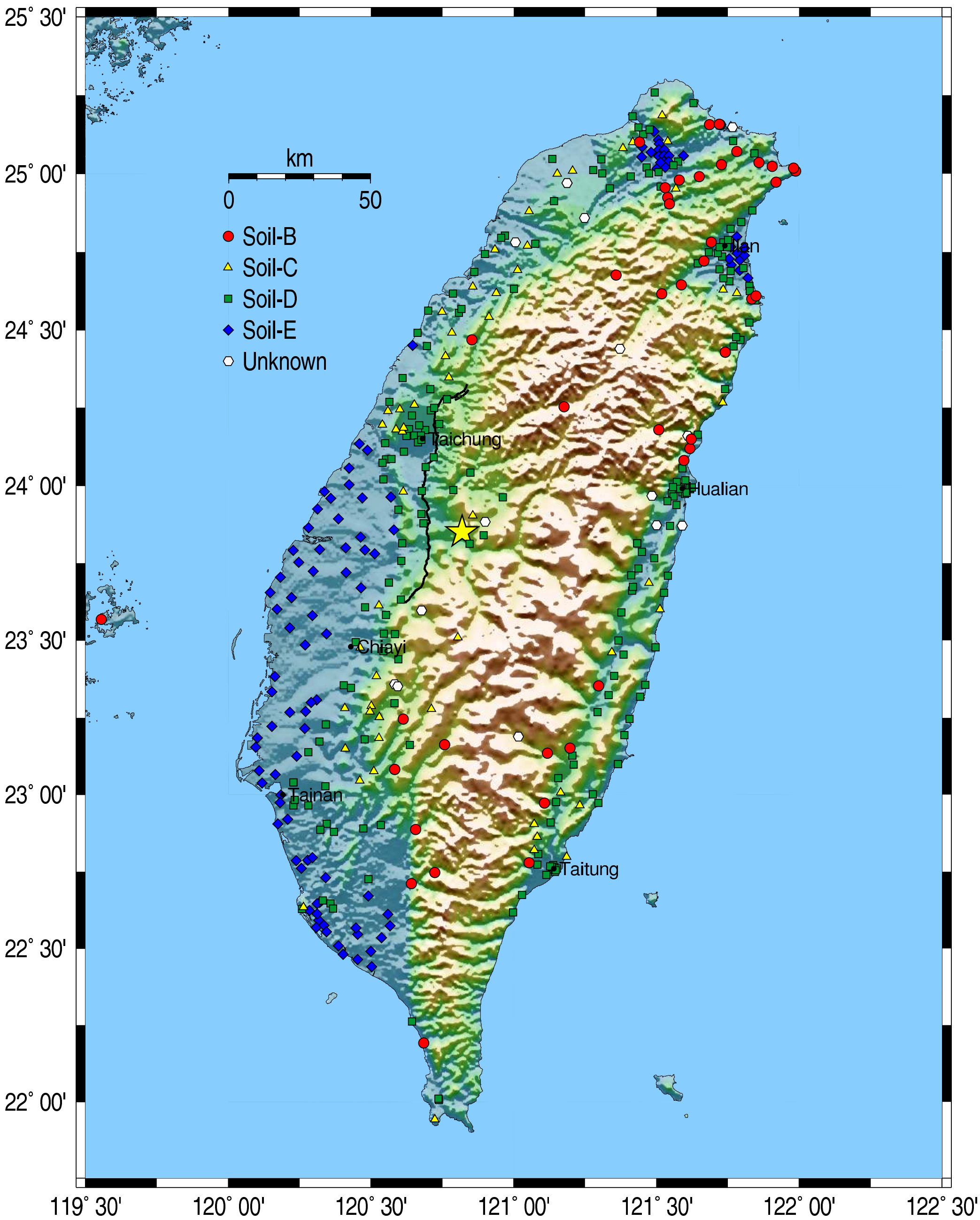

Figure 4.8: Topographic map of Taiwan. Soil condition of each station are shown in colored symbols. The Chelungpu fault lines are shown in the solid lines. The star symbol denotes the epicenter of the earthquake.

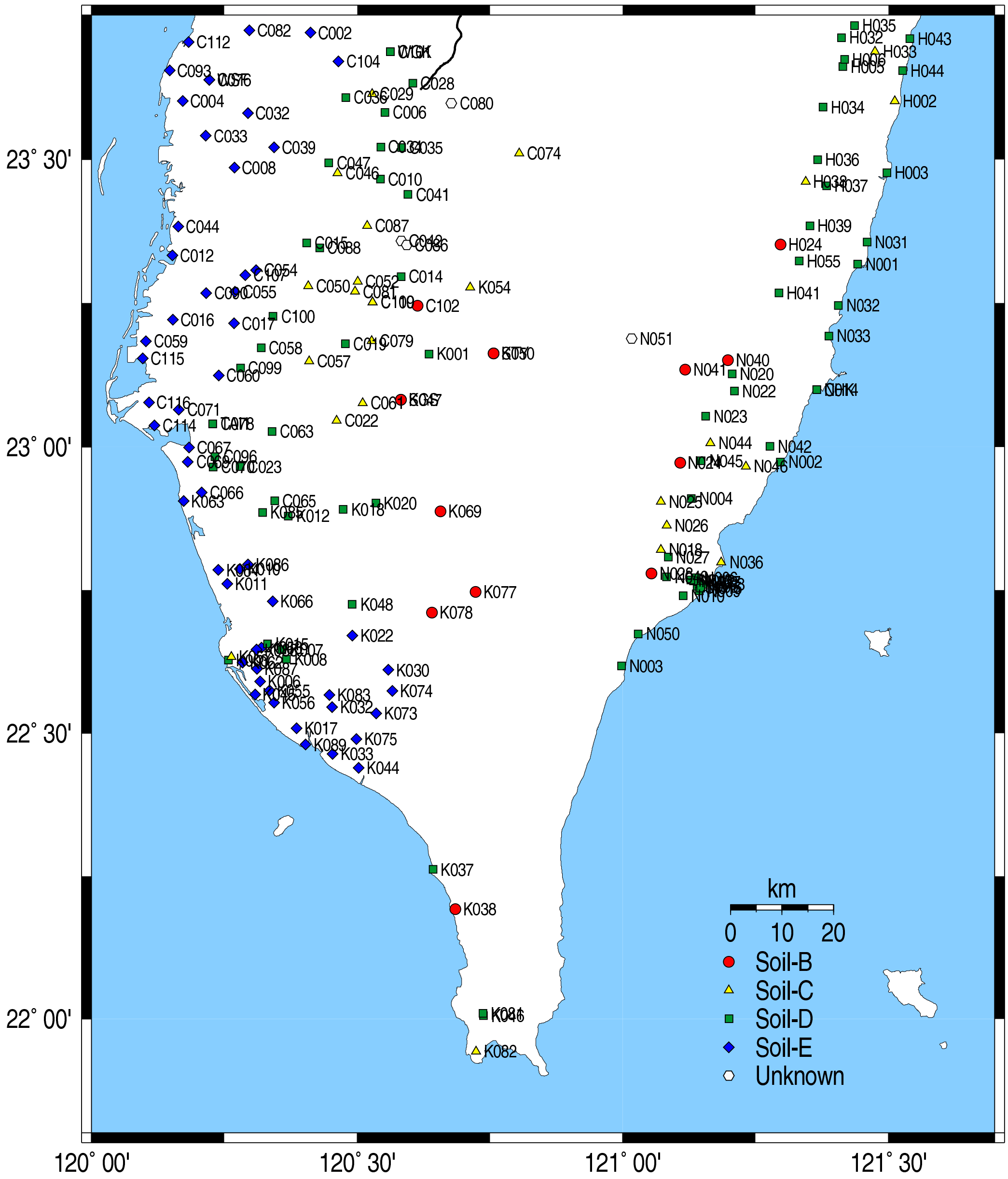

Figure 4.9: Station code and soil conditions of the strong motion stations in the southern part of Taiwan. The symbols are in the same format as in figure 4.8.

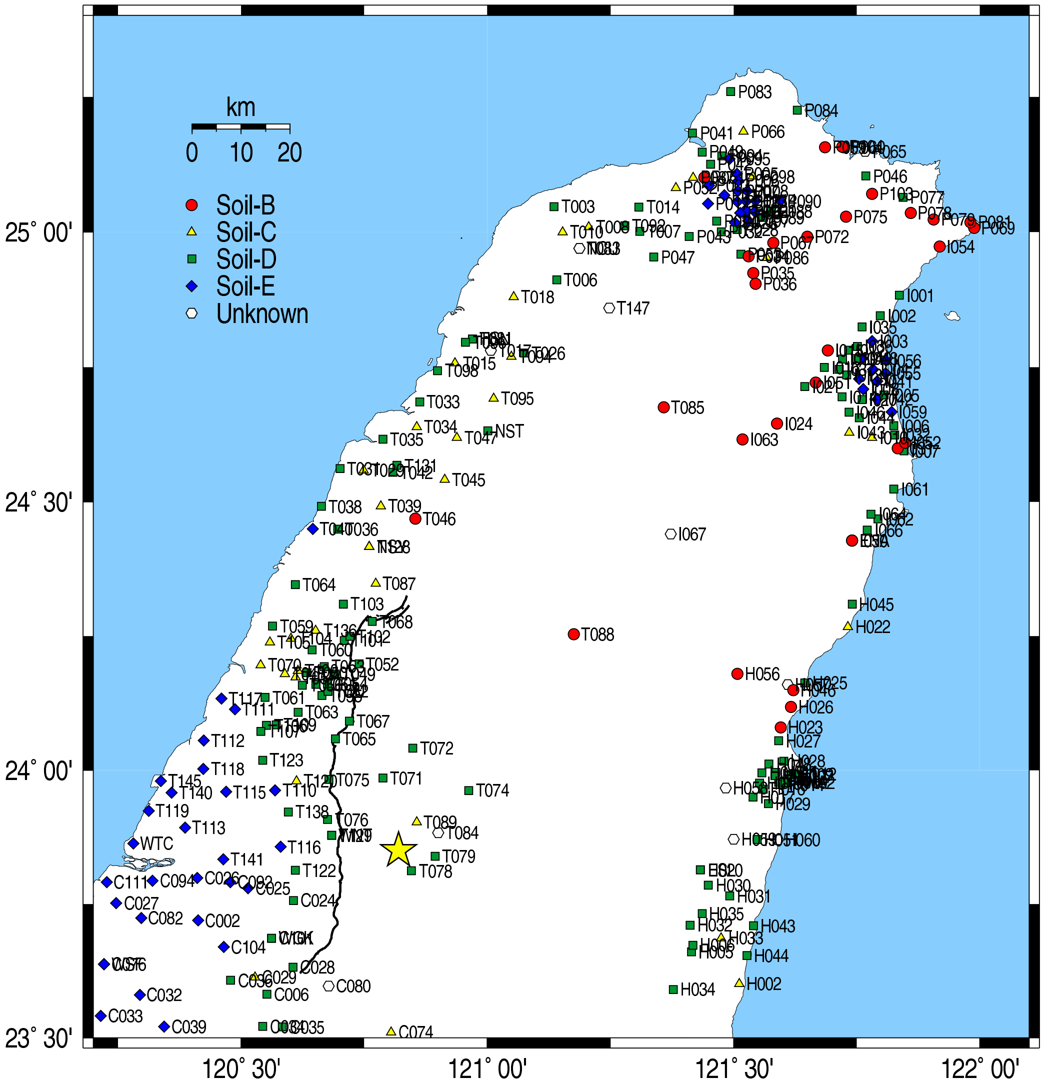

Figure 4.10: Station code and soil conditions of the strong motion stations in the northern part of Taiwan. The symbols are in the same format as in figure 4.8.

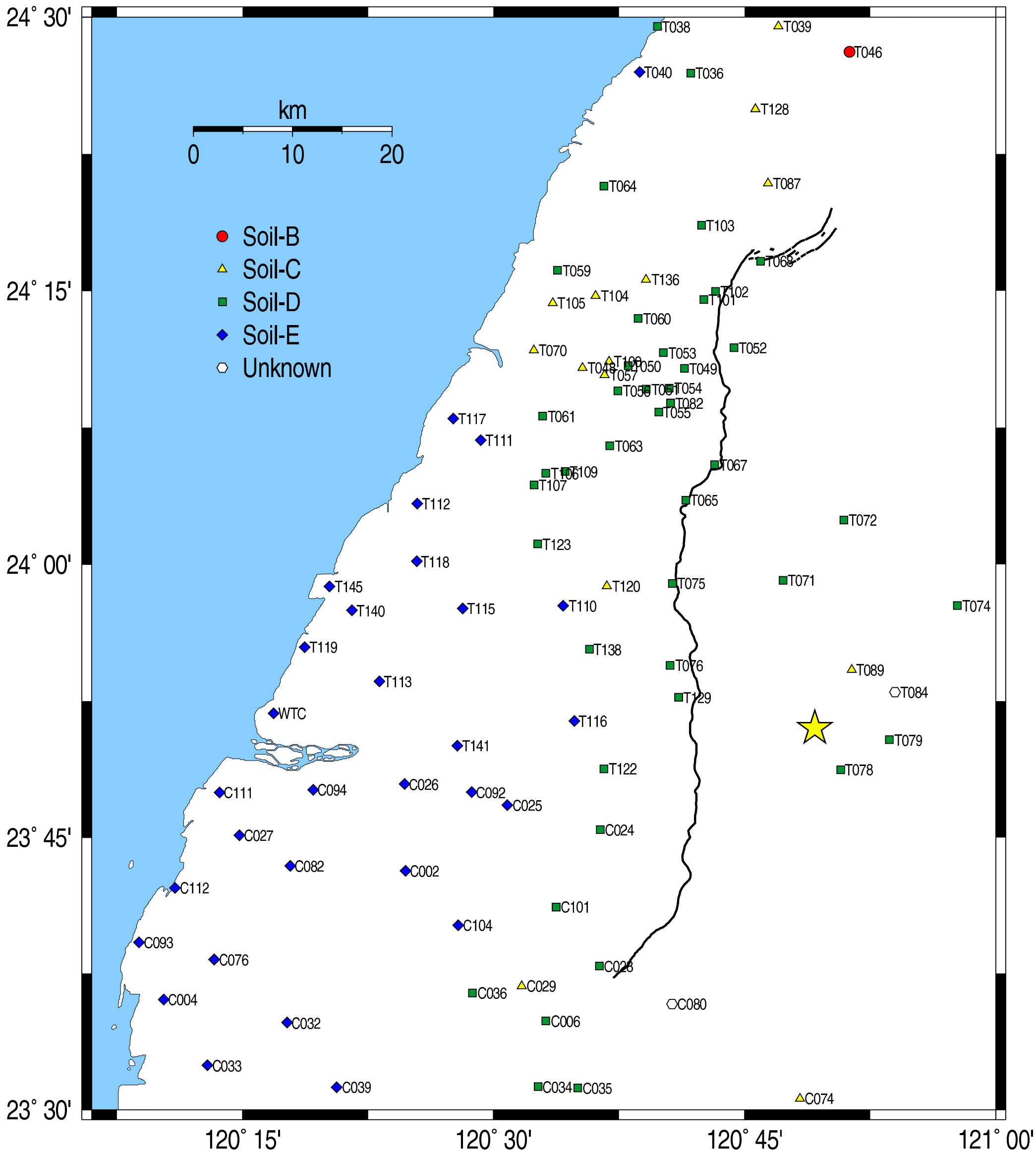

Figure 4.11: Station code and soil conditions of the strong motion stations in the central part of Taiwan. The symbols are in the same format as in figure 4.8.

4.3.2 Results from the analysis of the VS-FS method

We have run many different inversions by varying both the inversion parameters and the data sampling, such as the number of records used for the inversion, the components of the records, etc. Table 4.2 contains a list of the models investigated. We consider model 1 as a standard against which all other models are compared. It uses the horizontal and vertical records of the stations within 120 km of the epicenter.

Table 4.2: Model parameters for estimating a fault geometry. Distance is the maximum epicentral distance of the records used for the inversion. Component H and V stand for the horizontal and vertical component respectively. See the text for the area weight and data sampling.

Model	No. of stations	Distance(km)	Component	Area weight	Data sampling
1	239	120	H + V	-	-
2	239	120	H	-	-
3	239	120	V	-	-
4	239	120	H + V	X	-
5	126	120	H + V	-	even only
6	56	120	H + V	-	6 and 8 only

To simplify the problem, we assume each subsource has the same magnitude 6.0 and is located at the same depth, 8 km. The distance between each virtual source is 10 km. We assume constant rupture velocity to construct the predicted envelopes from subsources. In order to check the sensitivity of the parameter estimate to the rupture velocity, we run four simulations for model 1 with different rupture velocities. Figure 4.12 shows the estimated parameters, N1 and N2, for the rupture velocities from 2.0 km/s to 3.5 km/s. Even though we let the rupture velocity be faster than the real rupture velocity 2.0 km/s (Ji et al., 2003), N1 and N2 do not increase faster than 2 km/s (one per 5 seconds). In other words, the way that N1 and N2 change with the duration of the data tells us the rupture velocity. For the following simulations, we use the constant rupture velocity 2.0 km/s.

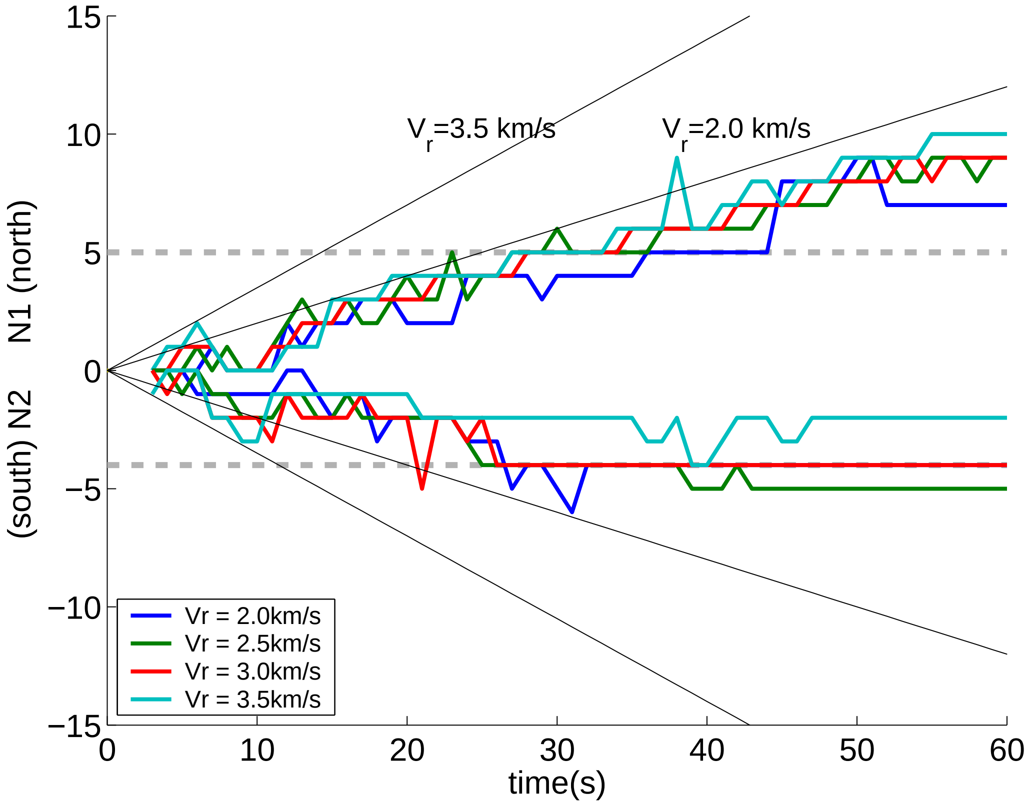

Figure 4.12: The estimated parameters, N1 and N2, for different rupture velocities. The solid thin lines are the upper limits for N1 and N2 for the rupture velocity 2 km/s and 3.5 km/s. The broken lines are the best estimates based on the fault model proposed by Ji et al. (2003). Time is relative to the origin. The parameters are computed at each second using only the data available at that time.

4.3.3 Comparison between predicted envelopes and observed envelopes

Figures 4.13 and 4.14 are a comparison of observed envelopes and predicted envelopes for model 1. Figures 4.15 and 4.16 are the same waveforms as figures 4.13 and 4.14 with different scaling (the waveforms are scaled so that the peak amplitude of the predicted envelopes becomes a unit length). The best-fit source model for model 1 consists of 14 subsources distributed along a line trending 17 degrees clockwise from north; there are 7 subsources north of the epicenter and 4 subsources to the south. That is, the best fitting model 1 is given by (θ=17 degrees, N1=7, N2=4). The predicted acceleration envelopes for this model agree well with the observed envelopes.

Predicted envelopes of near-source stations have some discrepancy depending on the source process, but predicted envelopes of far-source stations fit the observation well.

The vertical predicted envelopes of the stations in the epicentral region (e.g., stations T078, T079, T084, and T089; see 4.17 and 4.18) are of particular interest. Model 1 overestimates these observed envelopes for the first 10 seconds, but then underpredicts the observed records 20 seconds after the earthquakes origin. The fact that the largest accelerations in the epicentral region occurred 20 seconds after the origin time seems to indicate that there may have been some rupture complexity in the hypocentral region; perhaps there was an early aftershock in the epicentral region 20 seconds after the first rupture. Although this feature is noteworthy, it does not have a significant effect on the inversions since the epicentral stations are less important for estimating azimuthal angle and length of the fault.

Note that there is a discrepancy between the predicted and observed horizontal envelopes of the stations along the east coast of Taiwan, especially near Hualien around 40 seconds after the origin time (see figures 4.15 and 4.16). The observed envelopes of those stations have large amplitudes which cannot be captured by the predicted envelopes. The P-wave and S-wave should arrive at Hualien about 15 and 26 seconds after the origin time, respectively, based on the velocity structure in central Taiwan (table 4.1). That is, the large amplitude at Hualien is neither a first arrival P-wave or S-wave. While critically reflected shear waves off the Moho discontinuity have been suggested for large amplitude high-frequency phases at similar distances (Somerville and Yoshimura, 1990), the large amplitude waves on the east coast of Taiwan seem too late to be Moho critical reflections. Perhaps a secondary triggered event occurred east of the epicenter.

Another major discrepancy is the sharp pulse that appears about 40 seconds after the event onset in the records of stations located about 40 km north of the recognized northern terminus of the Chelungpu fault rupture (e.g., stations T045, T047, and T095). Shin and Teng (2001) suggested that these large accelerations were generated by a secondary rupture, perhaps on the Shihtan fault.

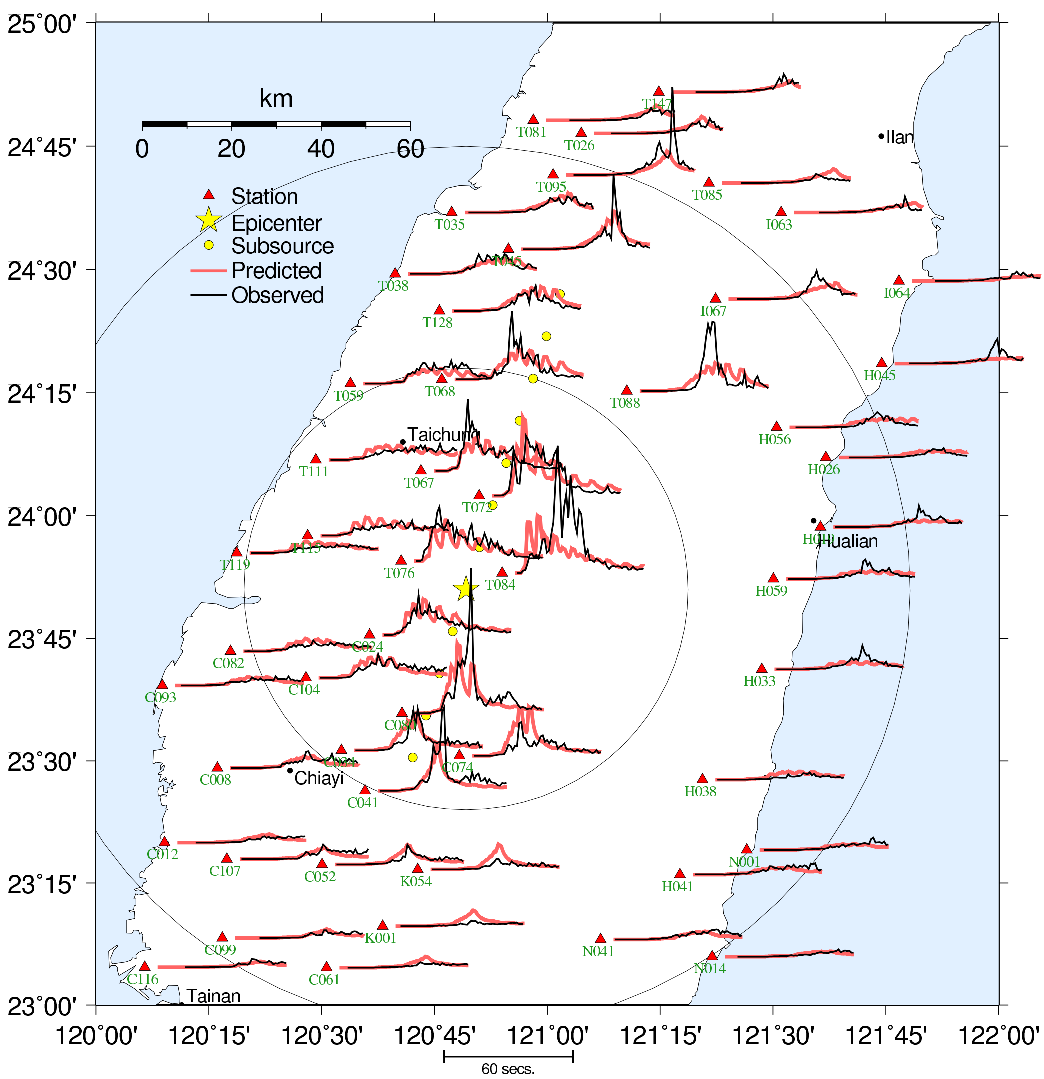

Figure 4.13: Predicted and observed envelopes in the horizontal component. The red and black lines are the predicted and observed envelopes, respectively. The locations of the subsources estimated from model 1 are shown in a small yellow circles. The area within 50 km and 100 km from the epicenter are shown by large circles. Only characteristic records of the stations are shown in this figure.

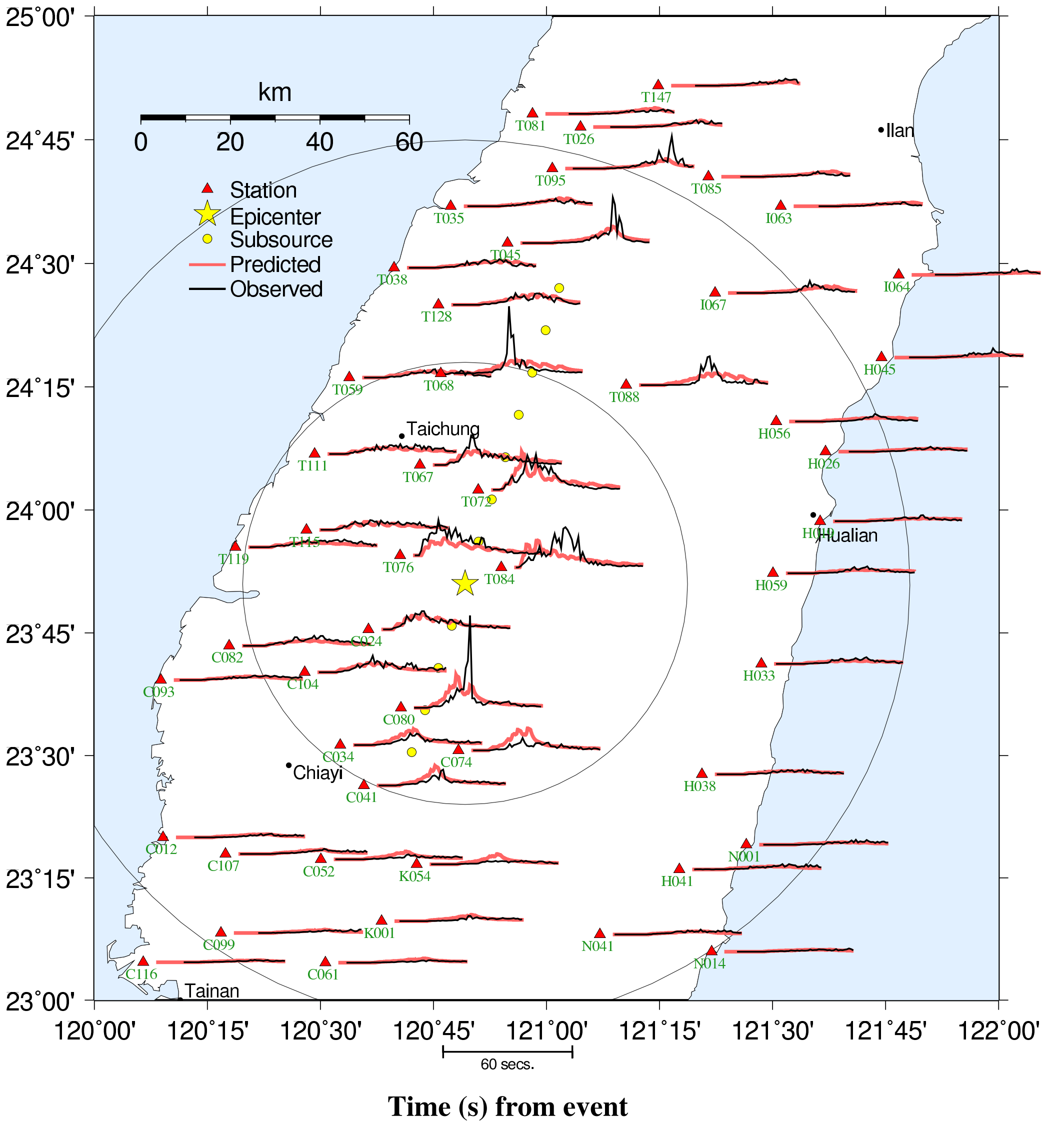

Figure 4.14: Predicted and observed envelopes in the vertical component. The symbols are in the same format as in figure 4.13.

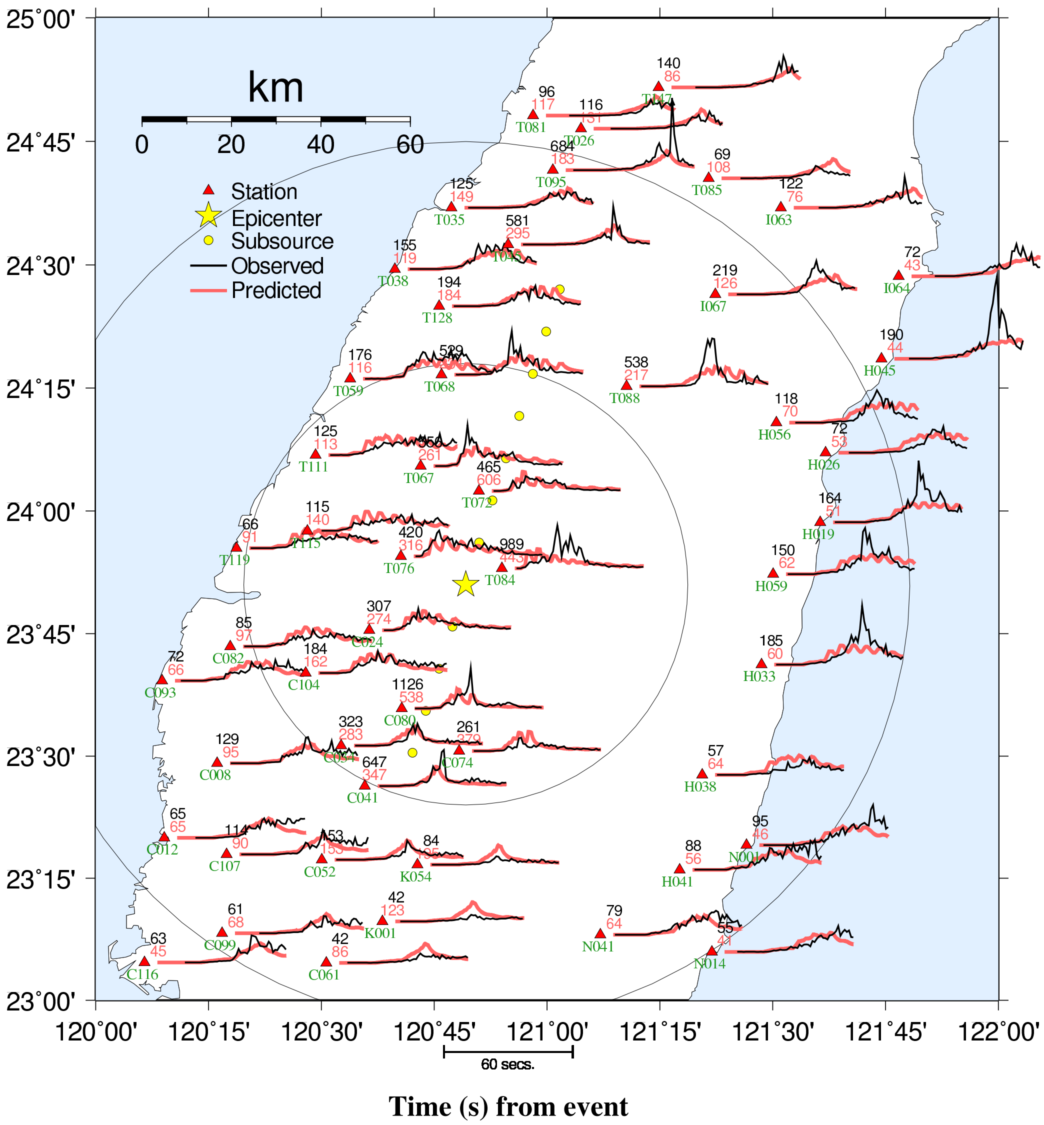

Figure 4.15: Predicted and observed envelopes in the horizontal component with different scaling. The waveforms are scaled so that the peak amplitude of the predicted envelopes becomes a unit length. The predicted and observed envelopes of the same station have the same scaling. The peak values are shown at the upper right of each station. The symbols are in the same format as in figure 4.13.

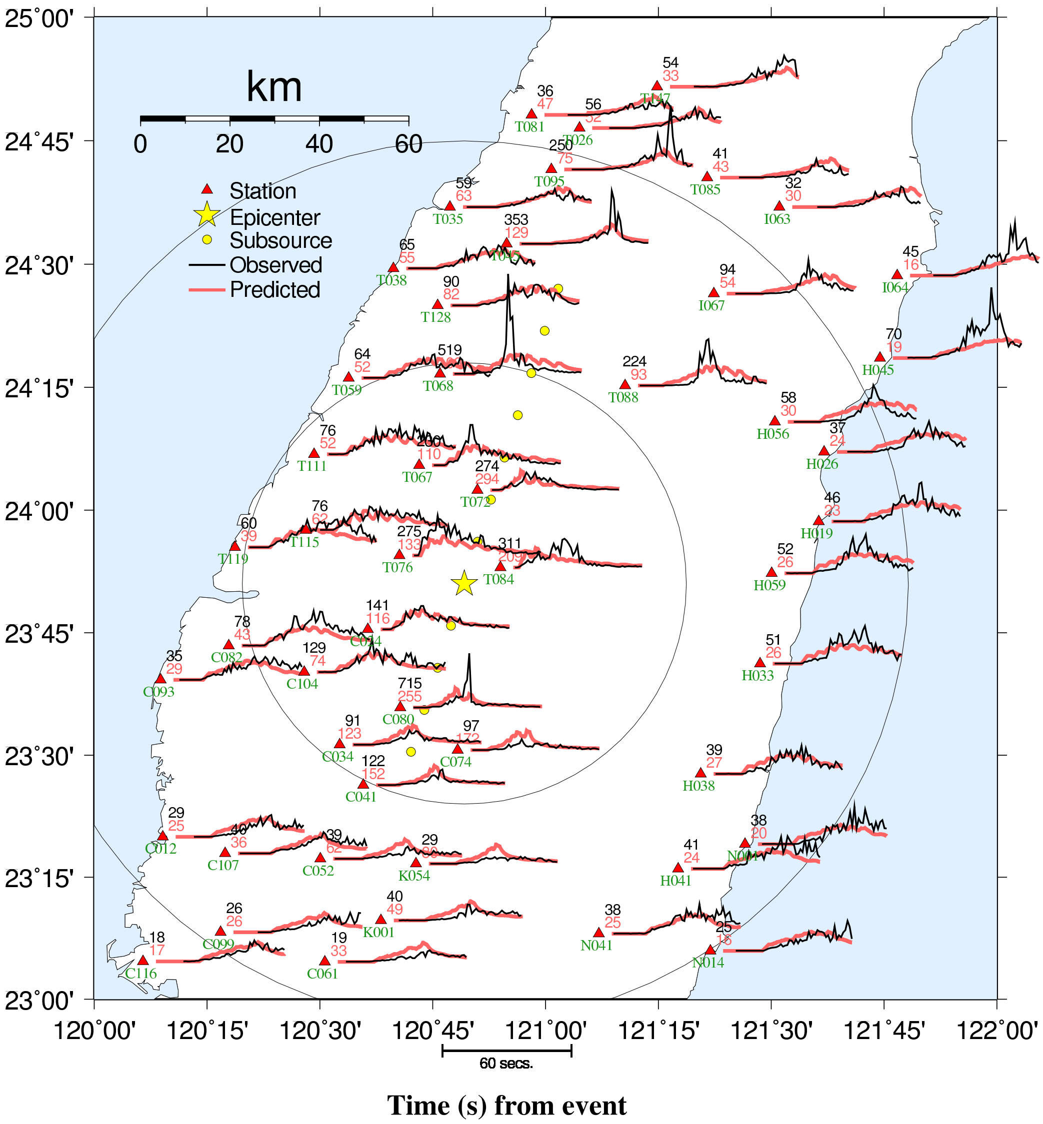

Figure 4.16: Predicted and observed envelopes in the vertical component with different scaling. The scalings are the same as in figure 4.15 The symbols are in the same format as in figure 4.13.

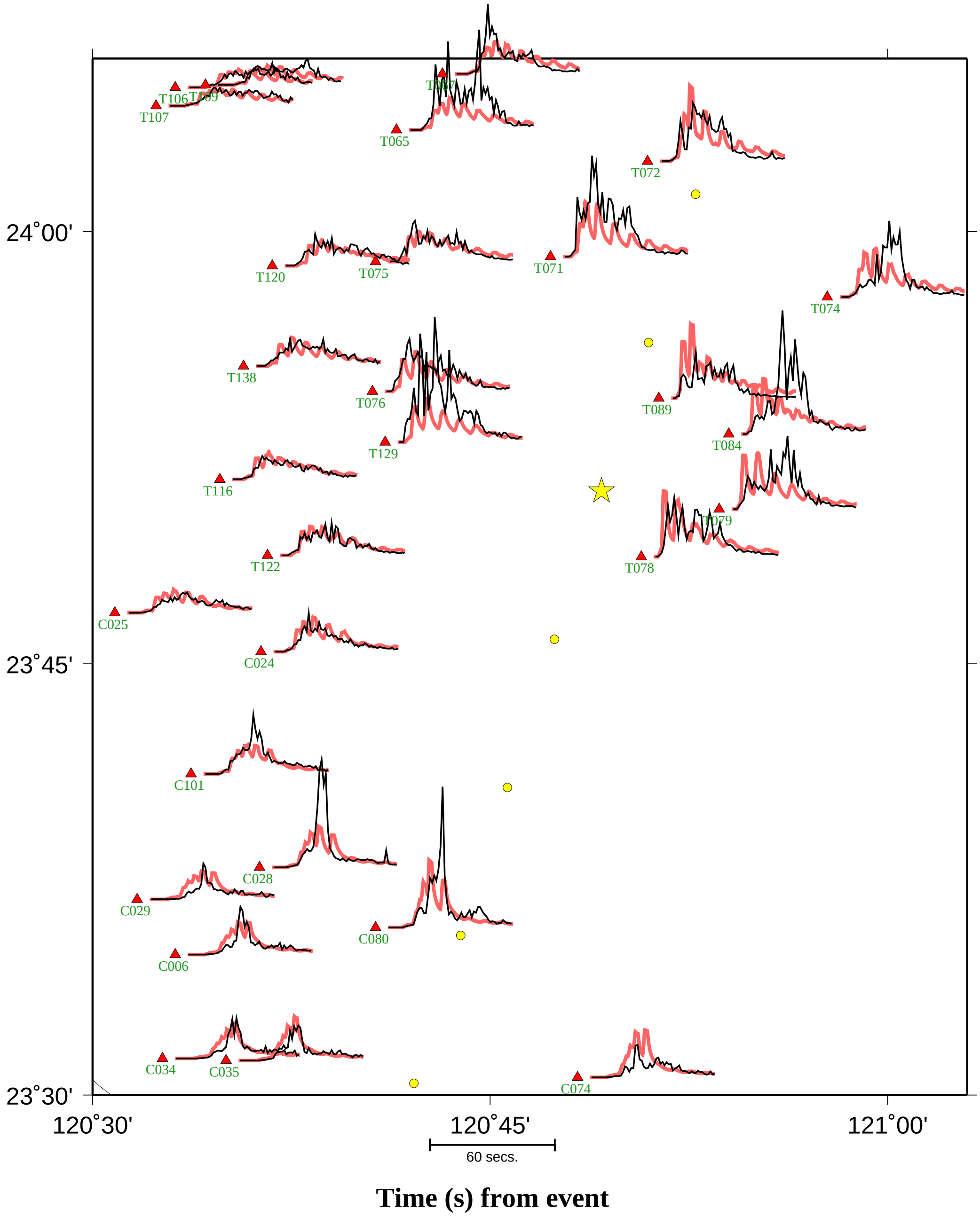

Figure 4.17: Enlarged map of figure 4.13. All of the stations near the epicenter are shown in this figure.

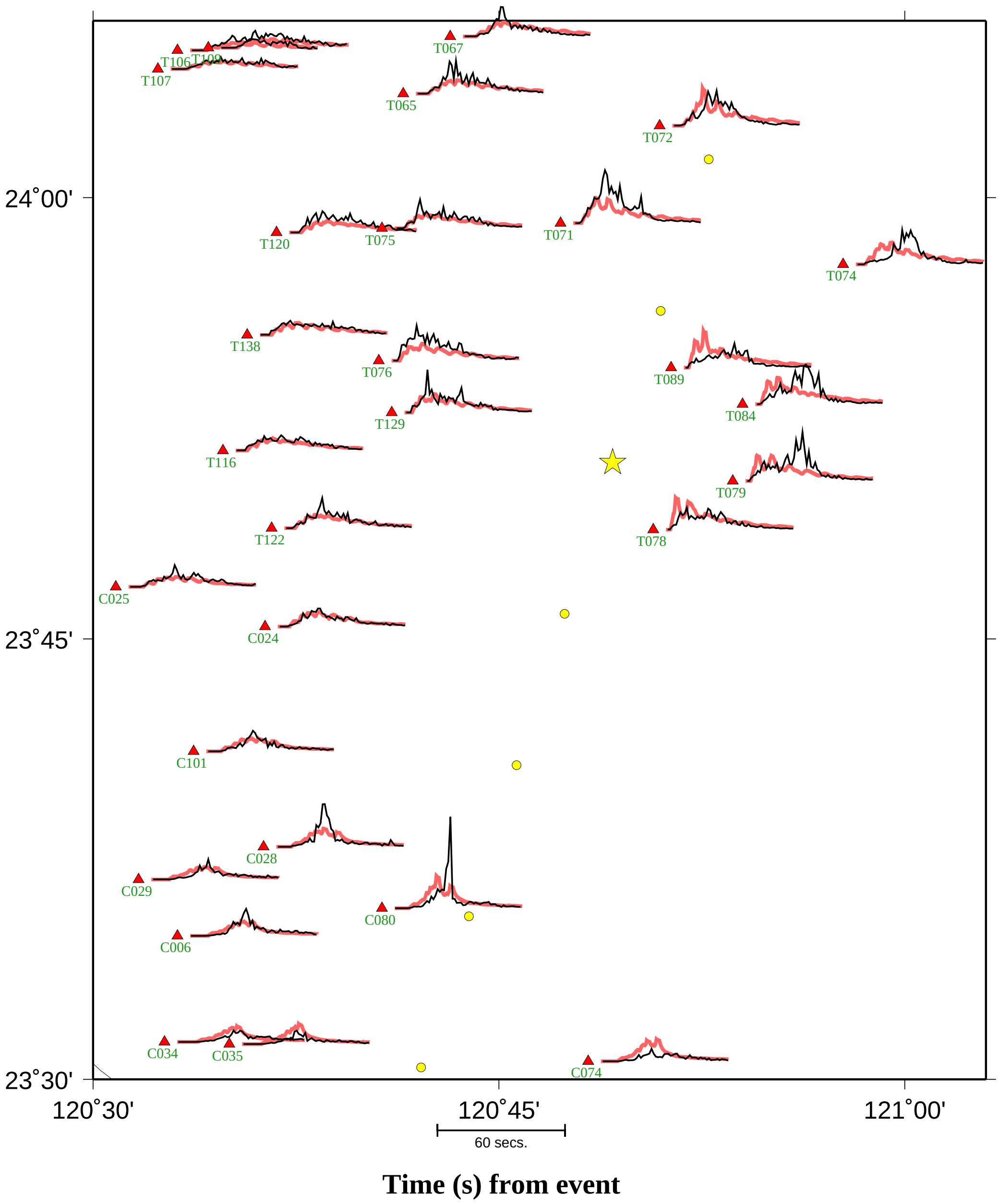

Figure 4.18: Enlarged map of figure 4.14. All of the stations near the epicenter are shown in this figure.

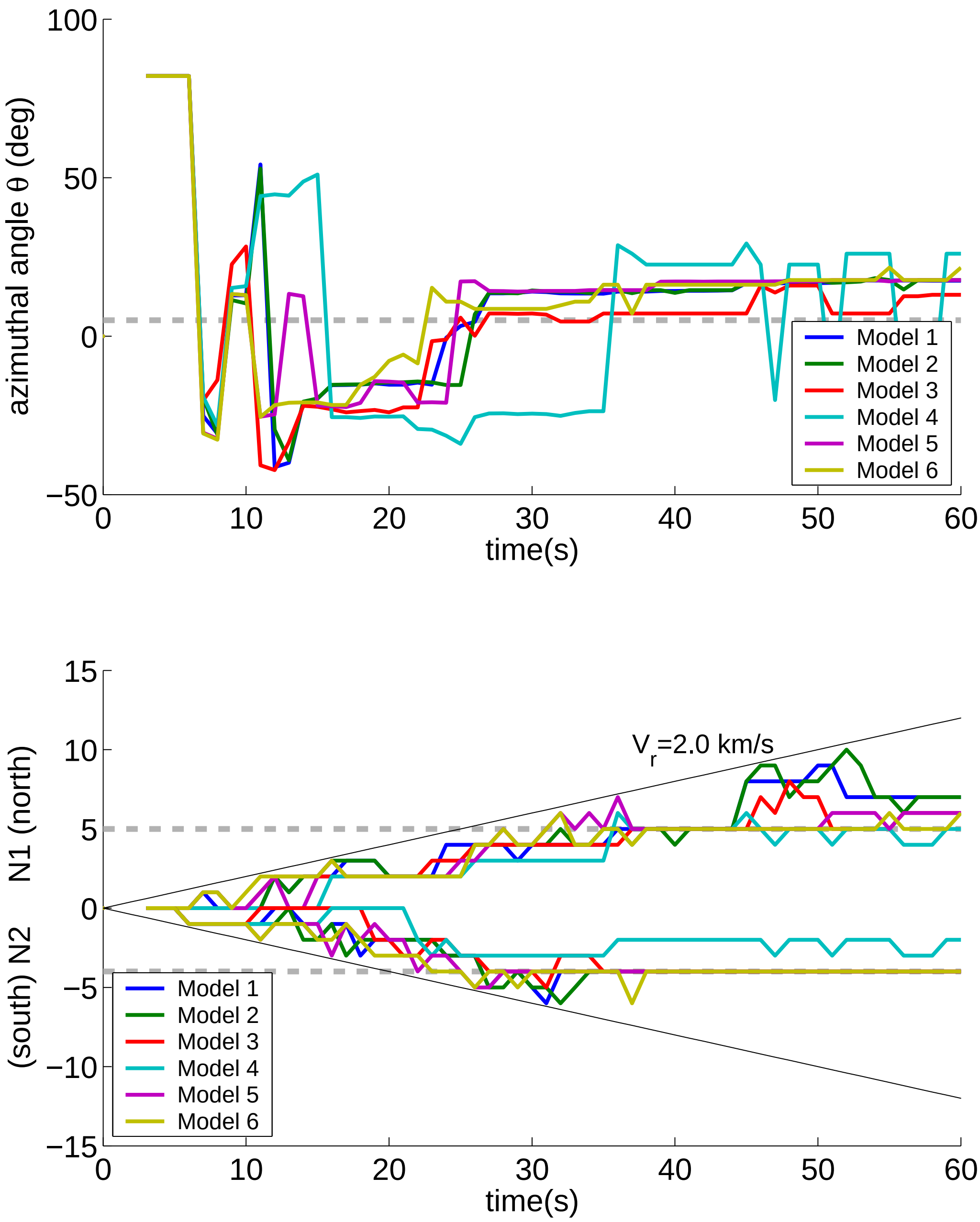

Figure 4.19: Time series of the estimated parameters, θ, N1, and N2, for each model. The model numbers correspond to the numbers in table 4.2. Time is relative to the origin. The parameters are computed at each second using only the data available at that time. The broken lines are the best estimates based on the fault model proposed by Ji et al. (2003). Top: time series estimations for θ. Bottom: time series estimations for for N1 and N2. The solid thin lines are the upper limits for N1 and N2 for the rupture velocity 2 km/s.

Figure 4.19 shows the estimation results of three parameters (azimuthal angle of fault line (θ), number of the point sources to the north (N1) and to the south (N2)). Three parameters are computed at each second using only the data available at that time. The estimation is updated every second as the ground motion data are observed.

4.3.3.1 Result of model 1 (horizontal and vertical data)

Model 1 includes all of the data considered in this study. Although it does a good job at characterizing the rupture length and timing, we see that it is difficult to resolve θ until 15 seconds after the event onset since the event can be approximated as a point source at the beginning. The estimated θ at 15 seconds is about -20 degrees and it increases gradually after 20 seconds due to a impulsive acceleration arrival at station C080 which is located at the south of the epicenter. Estimates of θ stabilize at about 13 degrees with respect to additional data after 26 seconds. There is an additional small shift at 44 seconds, at which point the inversion achieves its final solution of 15 degrees, which compares favorably with the observed average fault strike of the Chelungpu fault rupture.

Since the subsources are equally spaced, the length of the fault is represented by the number of the point sources to the north (N1) and to the south (N2). Figure 4.19 (bottom) shows values of N1 and N2 as a function of time after the origin. From the figure, we can see the fault length grows bilaterally along the dashed black lines. At 26 seconds, the rupture stops growing to the south. It also stops to the north temporarily, but it grows again around 40 seconds. This is due to the delayed high-frequency radiation at stations north of the Chenlungpu surface rupture and may have been caused by rupture on the Shihtan fault. Even though the result of the simulation fits the actual location of the fault accurately, the multiple source model does not consider "rupture jumping dislocations" (i.e., the rupture at the adjacent active faults triggered by the main shock) (Shin and Teng, 2001). The final result shows 7 point sources to the north and 4 point sources to the south. This fault length is comparable to the total length from the Chelungpu fault to the Shihtan fault in figure 4.7.

4.3.3.2 Result of model 2 (horizontal data) and model 3 (vertical data)

Model 2 only uses the horizontal acceleration data for the analysis whereas model 3 only uses the vertical acceleration data. The azimuthal angles of the fault for models 2 and 3 are not significantly different from model 1. The estimation of the angle, N1 and N2 from the horizontal component data (model 2) is similar to the estimation of model 1. However, the estimation of rupture length from the vertical component data (model 3) is a little smaller than that of model 1. In particular, the inversion indicates unilateral rupture to the north (i.e., N2 is zero) until 18 seconds after the origin. The reason is that the predicted envelopes overestimate the observed envelopes in the epicentral region for the first 10 seconds (see figure 4.14). Overall, the predicted envelope is larger than the observed envelope for the vertical component and smaller for the horizontal component.

4.3.3.3 Result of model 4 (effect of area weight)

Model 4 considers the heterogeneity of station distribution and applies an area weight when we characterize the misfit function. The area weight is a coefficient applied for each station. Since the station distribution is not uniform for the Chi-Chi earthquake dataset, we attempt to normalize the effect of each station. We assume a station in a sparse area is more important than a station in a dense area. Therefore, when we compute the misfit function in equation 4.2, the misfit of each station is weighted by the area weight, which is proportional to the area of the Voronoi cell of each station (shown in figure 4.7).

There are quite a few differences between the estimates for N1 and N2 of model 1 and model 4. The real-time estimation of the azimuthal angle has unique characteristics. It stays around -20 degrees at the beginning of the rupture, and it jumps to 35 degrees suddenly at 36 seconds. The angle estimation is very unstable even after 40 seconds. Moreover, the estimate for N1 and N2 are a lot smaller than that of model 1. The reason for this sudden transition is that a few stations with large area weighting (e.g., T088, T074, C074) control the parameters. When the envelopes of those stations are weighted, the residual sum of squares changes greatly, and the Neighborhood Algorithm chooses the parameter to reduce the residuals. We would like to obtain accurate information of the fault location as soon as possible. For this purpose, model 1 is more robust than model 4. In a larger sense though, it means that it becomes difficult to determine the fault geometry if the station distribution is sparse and uneven.

4.3.3.4 Result of model 5 and model 6 (the effect of station distribution)

In models 5 and 6, the effect of station distribution is examined further. To sample the stations randomly, we use the records with an even station code number for model 5. For model 6, the records with a station code ending in 6 or 8 (e.g., T078) are used. Even though the station distribution is not homogeneous as shown in figure 4.7, the average station density is 214 km^2/station for model 5, and 482 km^2/station for model 6. The stations are located in an area of about 27,000 km^2. Even though the station density is different, the estimated parameters are quite similar. In figure 4.19, the time series of θ and N2 for models 1, 5, and 6 are almost the same. N1 for models 5 and 6 stays around 5 after 30 seconds, and the increase observed in Model 1 due to the Shihtan fault rupture does not appear. The reason is that several near-source stations of the Shihtan fault have an odd number station code and are not included in this analysis (e.g., T045, T047, and T095). Considering that the rupture of the Shihtan fault is quite small compared to that of the Chelungpu fault, model 5 and model 6 can express the Chi-Chi earthquake rupture well. The VS-FS method for large earthquakes works well even if the station density is reduced to a quarter of the original density, as long as the station distribution is uniform.

4.3.4 Geometry of the parameter space

We have solved the optimization problem in parameter space (θ, N1, and N2) by a Neighborhood Algorithm. Here, we discuss the geometry of the parameter space.

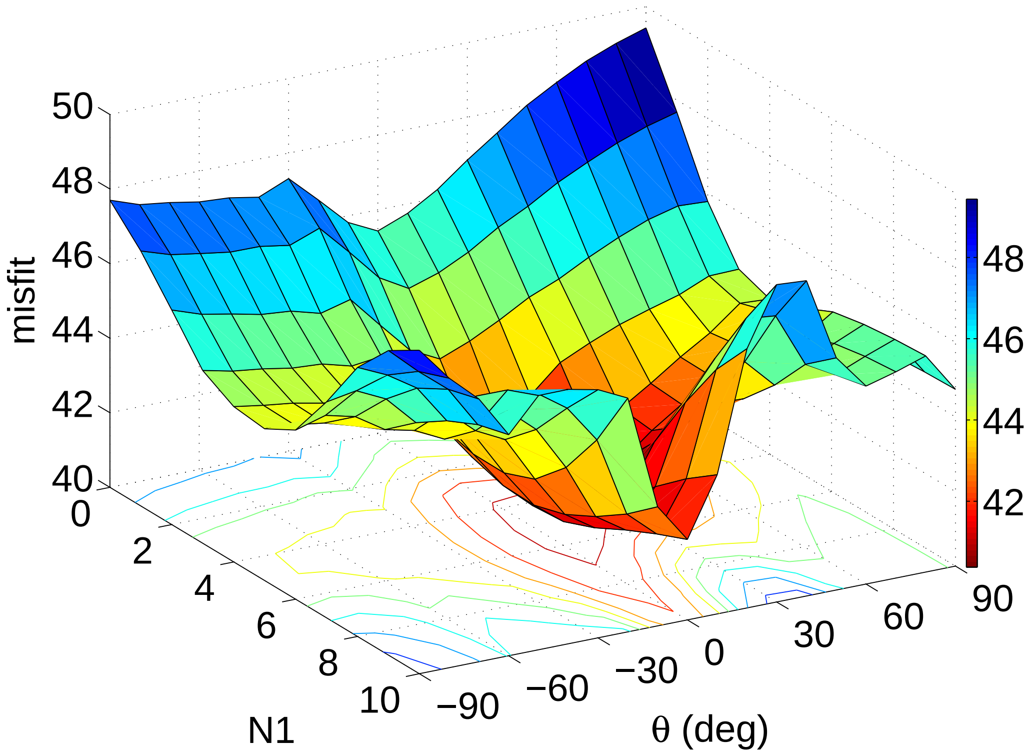

Figure 4.20: Error surface of θ and N1 for Model 1 at the fixed N2 = 5 at 60 seconds after the origin time. Since the surface is peaked around $\theta = 0$, it is easy to converge in θ. However, the optimal N1 will change easily depending on the misfit function (see equation 4.2).

Figure 4.20 shows the error surface of θ and N1 for model 1 at a fixed N2 of 5 and assuming that all data is used in the inversion. The surface is smooth and has a deep and narrow valley at $\theta = 10$. The solution easily converges to this minimum. Figure 4.21 shows the error surface of N1 and N2 for model 1 at a fixed θ of 10. The surface is very smooth in both N1 and N2 directions. The global minimum is very sensitive to the choice of the dataset, as shown in the results of model 5 and 6.

Contour maps of the error surface of N1 and N2 at 10 second intervals are shown in figure 4.22. θ is fixed at 10 degrees which is the optimal final solution. At 10 seconds, the minimum of this error surface is (N1, N2) = (0, 1). However, it is not the global minimum in the parameter space since $\theta = 10$ is not the optimal solution at 10 seconds. At 20 and 30 seconds, the minimum of the error surface is at the maximum N1 and N2 in the possible parameter space even though θ is not optimal.

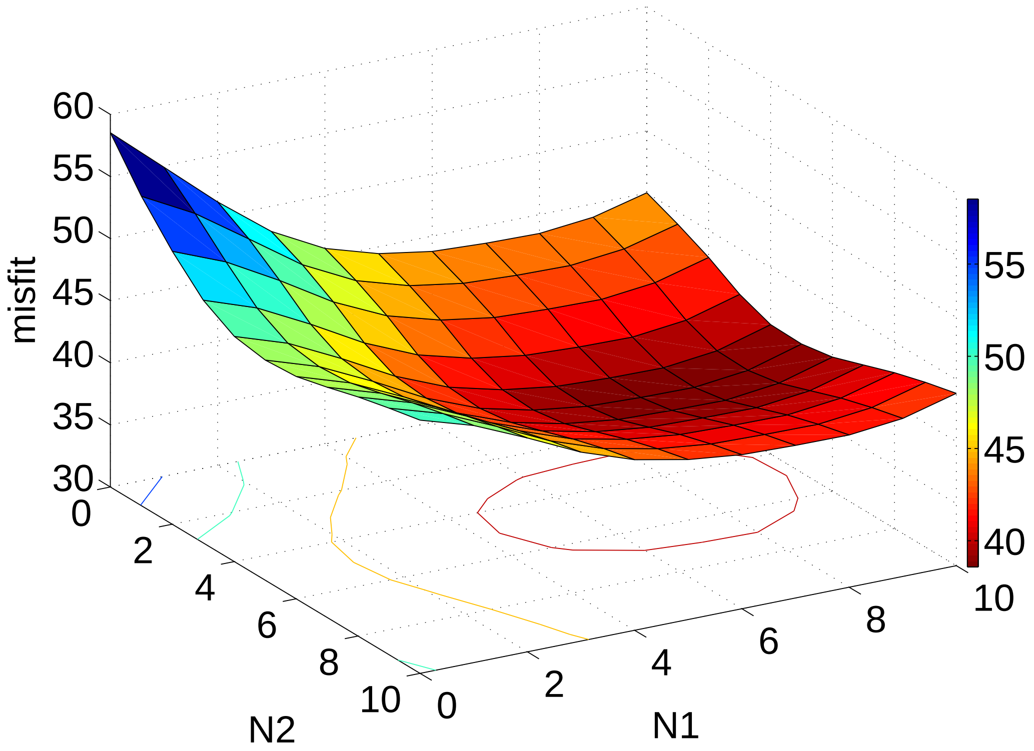

Figure 4.21: Error surface of N1 and N2 for model 1 at the fixed $\theta = 10$ at 60 seconds after the origin time. Since the surface is smooth in both N1 and N2 direction, the optimal solution is sensitive to a small disturbance.

There is high possibility that the rupture is still ongoing at this point. At 40 seconds, the minimum of the contour is around (N1, N2) = (6, 4) and it suggests that the rupture has stopped rupturing toward the south. After 40 seconds, the shape of contour map does not change much, and the elliptic shape of the smallest contour indicates that N2 is determined uniquely, but that considerable uncertainty about N1 remains.

The Neighborhood Algorithm generates samples in the parameter space and constructs the posterior probability density (ppd) from the ensemble samples. (In this simulation, the prior pdf is assumed to be uniform.) The 1-D marginal posterior ppd of parameter θ, N1, and N2 are shown in are shown in figures 4.23 – 4.25. The ppd for θ is more peaked than those for N1 and N2, and it is consistent with the geometry of the error surface which enables a solution to converge easily to the minimum. The more data is available as the rupture propagates, the smaller the deviations of the ppd

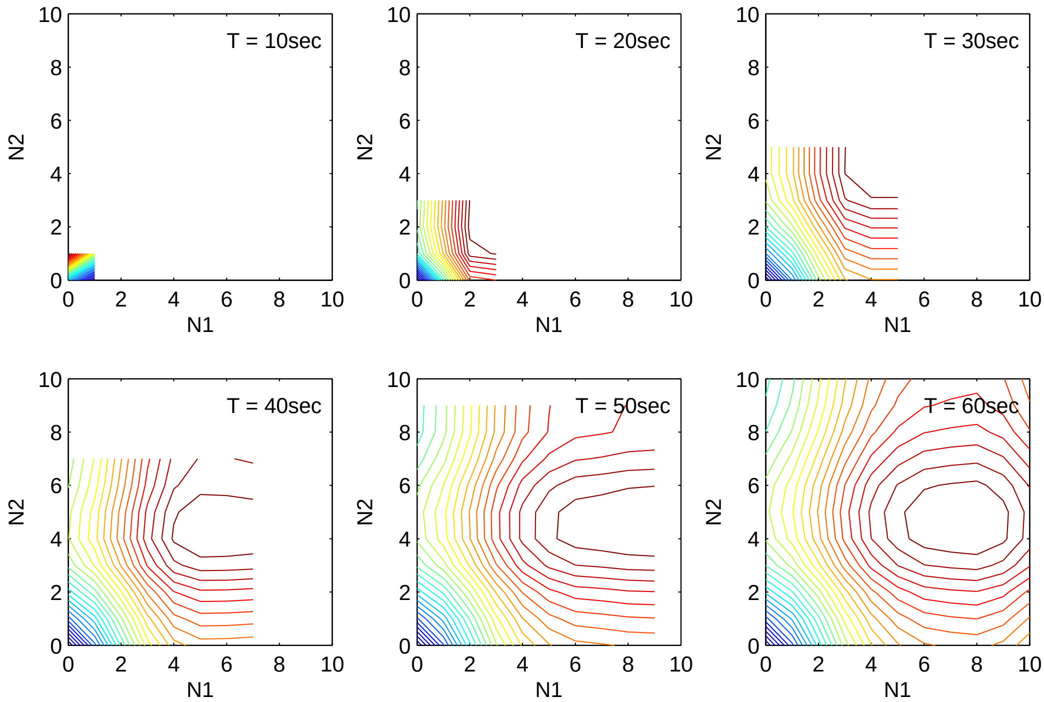

Figure 4.22: Contour maps of the error surface of N1 and N2 for model 1 at the fixed $\theta = 10$. The maps are shown in 10 second intervals. The blank area in the boxes is the region where there is no solution due to the constraint that the rupture velocity is less than 2 km/s.

becomes for all three parameters. Figure 4.26 is the 2-D marginal of parameters N1 and N2. The difference between figure 4.22 and figure 4.26 is as follows: figure 4.22 is the error surface where the misfit function (equation 4.2) is evaluated and figure 4.26 is the posterior probability density of the parameter space. The location of the most probable solution is almost identical between figure 4.22 and 4.26, but figure 4.26 shows the ppd which represents the probability for each value of the parameters. The maximum value of ppd becomes larger with time.

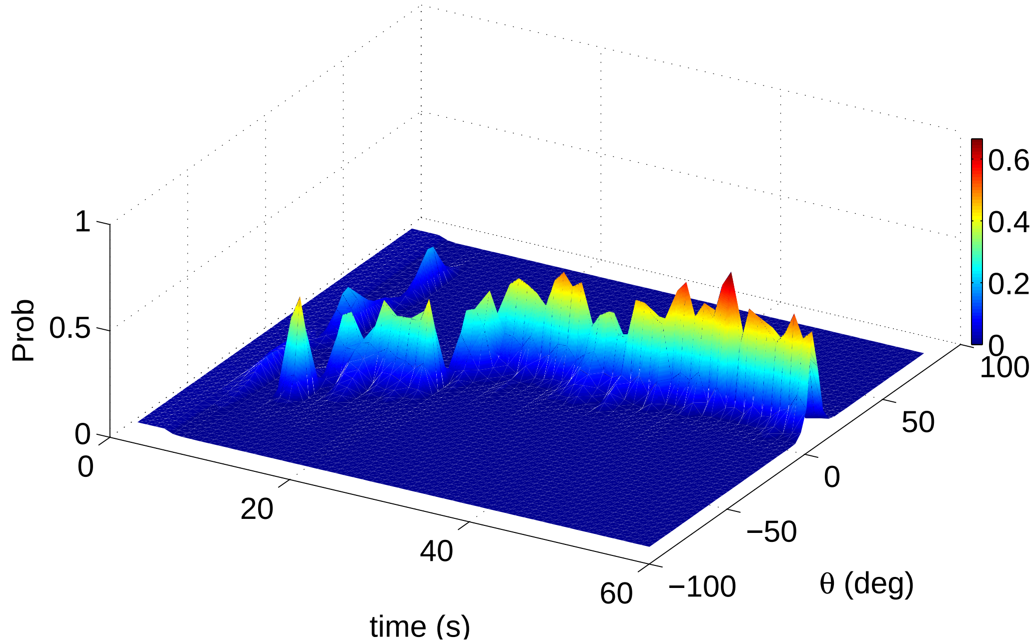

Figure 4.23: Posterior probability for the parameter θ.

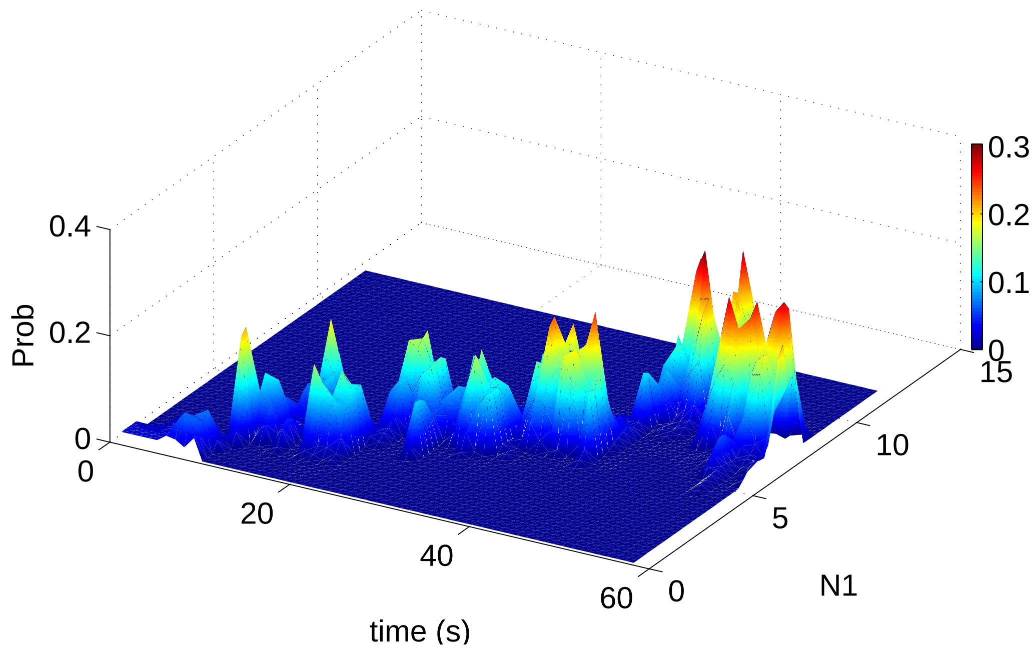

Figure 4.24: Posterior probability for the parameter N1.

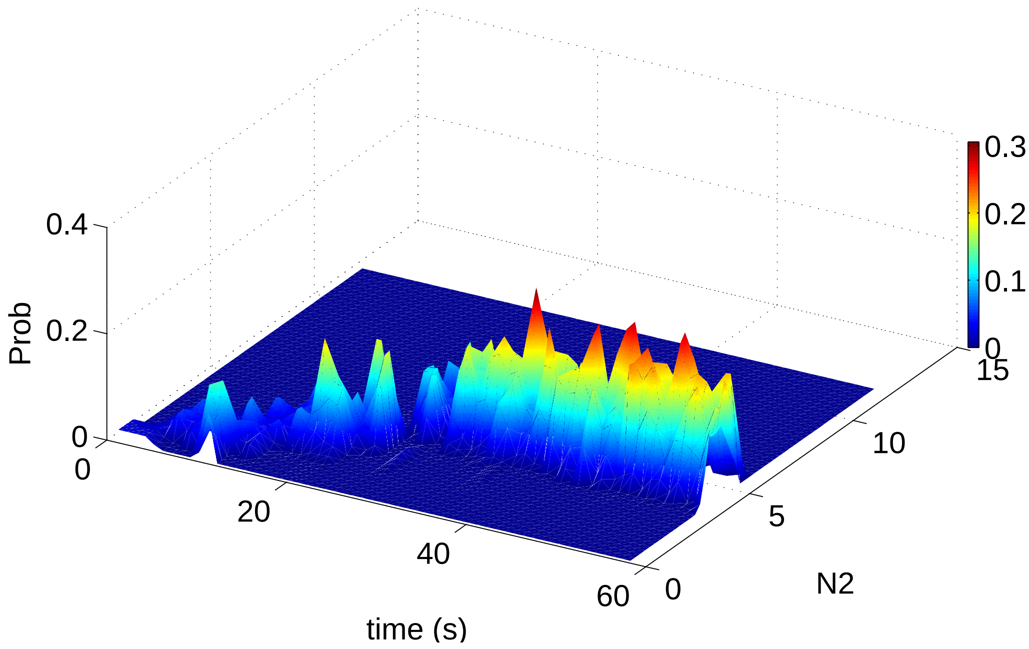

Figure 4.25: Posterior probability for the parameter N2.

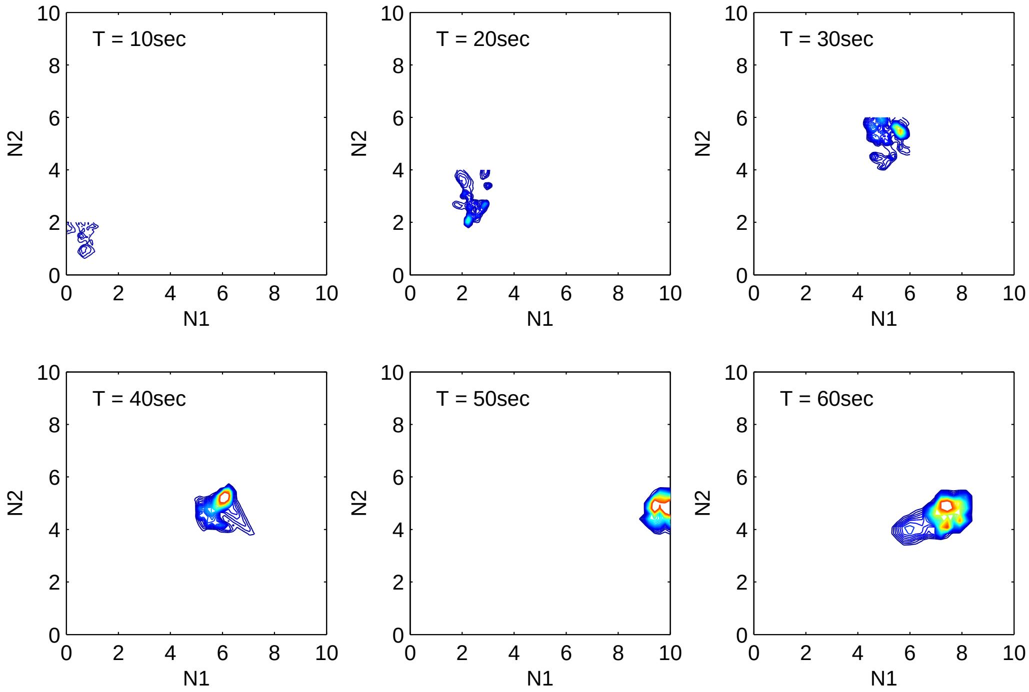

Figure 4.26: Two-dimensional posterior probability for the parameters N1 and N2. The plots are shown in 10-second intervals.

4.3.5 Effects of different misfit functions

In the course of this study, we also tried inversions in which we defined misfit function in terms of log of amplitudes and PGA. Figure 4.27 shows the simulation results with the same dataset as model 1 but different misfit functions. The misfit function used in the main analysis was:

$$RSS(t) = \sum_{i=1}^{ns}\sum_{j=1}^{2}\sum_{k=1}^{t}(A_{ijk} - \hat{A}_{ijk})^2. \tag{4.3}$$

In the ground motion analysis, the distribution of log of amplitude follows the Gaussian distribution, so the log of amplitudes is often used as a misfit function. The misfit function in terms of log of amplitudes is:

$$RSS_{log}(t) = \sum_{i=1}^{ns}\sum_{j=1}^{2}\sum_{k=1}^{t}(\log A_{ijk} - \log \hat{A}_{ijk})^2. \tag{4.4}$$

This misfit function emphasizes the ratio of predicted and observed amplitudes; large amplitude data is no more important than small amplitude data. However, we found that such a misfit function emphasized misfits in the coda for near-source data; furthermore, the distant data was often not well explained by our simple descriptions of wave envelopes that have been developed to explain the "average" effects of waves propagating through the crust. That is, it is important to emphasize the data from the near-source records and a logarithmic misfit function was not appropriate to recover the timing and location of the rupture.

We also tried the misfit function defined in terms of the error when the each ground motion records the peak value (PGA):

$$RSS_{max}(t) = \sum_{i=1}^{ns}\sum_{j=1}^{2}(\max\{A_{ijk}|k = 1, \ldots, t\} - \max\{\hat{A}_{ijk}|k = 1, \ldots, t\})^2. \tag{4.5}$$

The fault length estimate from this misfit function is very unstable even after most of the rupture terminated. This is because far-source stations which receive propagating seismic waves with delay affect the misfit function. As we mentioned in the

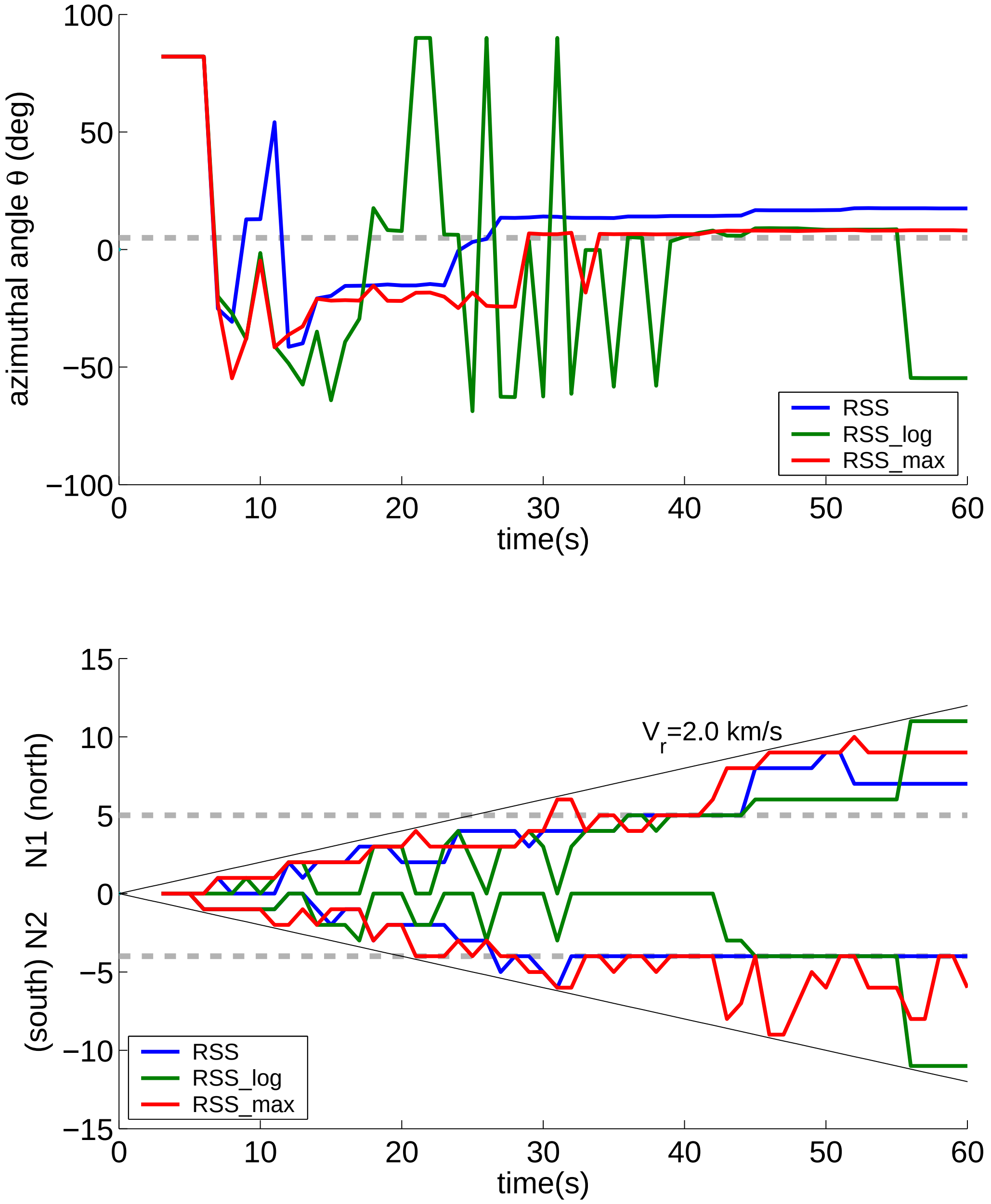

Figure 4.27: Effects of different error functions. RSS error function gives the best estimate of the model parameters.

logarithmic misfit function, it is important to emphasize the data from the near-source records, and so the best estimate of the model parameters minimizes the RSS between observed ground motion envelopes and predicted envelopes from the multiple source model.

4.4 Summary

We outlined a strategy to estimate slip in time and space for an ongoing earthquake rupture. A key aspect of this strategy is to map the location of the rupture using envelopes of high-frequency acceleration data. Once the location of the rupture is estimated, long-period displacement data can be projected back onto the fault to determine the slip in real time.

Our strategy for using high-frequency radiation to determine the timing and length of the rupture relies on the observation that high-frequency seismic waves can be modeled as random-phase waves whose total radiated energy scales linearly with the rupture area. By using this assumption, we show that we can simulate the ground motion of a large earthquake by tiling the surface of the large event with smaller events and then summing the random phase signals from the smaller events. In our example of the Chi-Chi earthquake, we showed that a sum of 10 km interval magnitude 6.0 subevents provided a good prediction of the acceleration envelopes for this earthquake. In order to turn this simulation into a real-time inverse, we parameterize the rupture with a linear alignment of magnitude 6.0 earthquakes. We then invert for the azimuth angle of the alignment as well as two integers, N1 and N2, which are the number of additional 10 km patches in the positive and negative directions from the epicenter, respectively.

The best estimate of the model parameters minimizes the residual sum of the squares between observed ground motion envelopes and predicted envelopes from the multiple source model (in equation 4.2). This misfit function with linear amplitudes of ground motions can provide better estimates than that of logarithmic amplitudes, since the linear misfit function tends to emphasize the importance of fitting stations with large amplitudes.

Our study of the Chi-Chi data set indicates that it is more difficult to determine rupture length than it is to determine rupture azimuth. Furthermore, for this method to work well, an adequate near-source station distribution is important. Real-time mapping of an on-going rupture using this strategy becomes a simple matter of tracking the spatial evolution of near-source seismic stations. Although this strategy appears promising, it requires adequate station coverage to track near-source stations.

Chapter 5

Near-Source versus Far-Source Classification Analysis

We introduced the methodology that can estimate the rupture geometry from acceleration envelopes in the previous chapter. In this chapter, we propose another approach to recognize the fault rupture extent. We develop a methodology to classify stations into near-source and far-source by using the Bayesian model selection analysis so that we can identify the fault geometry if there is a sufficiently dense seismic network. Peak ground motions recorded in past earthquakes are analyzed to predict whether a station recording ground motion is close to the earthquake fault area. This classification problem can be stated as follows: given ground motion data from past earthquake records, what is the probability that a station is near-source when a new observation is obtained?

To approach this problem, we:

1) Collect strong motion data from earthquake strong motion archives and classify these samples into two predefined groups: records from near-source stations and far-source stations. This particular set of data is called the training set.

2) Discover a discriminant function of the samples features (e.g., peak ground acceleration (PGA), velocity (PGV), displacement (PGD)) which provides the best performance in terms of near-source versus far-source classification.

3) Allocate new observations when they are obtained to one of the two groups based on the discriminant function.

The first step is quite straightforward; strong motion data from past earthquakes are collected based on certain selection criteria. The second step is the main topic of this paper; and we investigate linear discriminant functions by using the traditional Fisher method and two Bayesian methods. The third step can then be accomplished in a real-time analysis. Given a new ground motion observation from on-going rupture, the discriminant function gives the probability that the observation is located in the near-source.

5.1 Strong motion data

We used strong motion datasets from nine earthquakes with magnitude greater than 6.0 and containing records of near-source stations. The selected earthquake dataset is shown in table 5.1. Here, we define a near-source station as a station whose fault rupture distance is less than 10km. 695 three-component strong motion data are used for the classification analysis and 14% (100 stations) are from near-source stations.

Table 5.1: The earthquake dataset used for the classification analysis. Moment magnitude (M_w) is cited from Harvard CMT solution. The numbers of near-source (NS) and far-source (FS) data for each earthquake are also shown. The fault models are used as selection criteria to classify near-source and far-source stations.

Earthquake	M_w	NS	FS	Total	Fault Model
Imperial Valley (1979)	6.5	14	20	34	Hartzell and Heaton, 1983
Loma Prieta (1989)	6.9	8	39	47	Wald et al., 1991
Landers (1992)	7.3	1	112	113	Wald and Heaton, 1994
Northridge (1994)	6.6	17	138	155	Wald et al., 1996
Hyogoken-Nanbu (1995)	6.9	4	14	18	Wald, 1996
Izmit (1999)	7.6	4	13	17	Sekiguchi and Iwata, 2002
Chi-Chi (1999)	7.6	42	172	214	Ji et al., 2003
Denali (2002)	7.8	1	29	30	Tsuboi et al., 2003
Niigataken-Chuetsu (2004)	6.6	9	58	67	Honda et al., 2004
Total		100	595	695	

5.1.1 Data sources

We obtained the strong motion dataset for the Imperial Valley (October 15, 1979), Loma Prieta (October 18, 1989), Landers (June 28, 1992), Northridge (January 17, 1994), and Denali (November 3, 2002) earthquakes from the COSMOS Virtual Data Center (http://db.cosmos-eq.org) which includes data from the California Strong Motion Instrumentation Program (CSMIP) seismic network and the United States Geological Survey (USGS) seismic network. The Northridge earthquake dataset in the COSMOS Virtual Data Center also includes records from seismic networks of the California Institute of Technology, Los Angeles Department of Water and Power, Metropolitan Water District, Southern California Earthquake Center, and University of Southern California. All these data were recorded by accelerometers and processed appropriately before distribution to users. The correction process may apply baseline corrections, band-pass filters to remove noise contamination, and instrument correction to remove the effects of frequency-dependent instrument response (http://nsmp.wr.usgs.gov/processing.html).

Strong motion data from the Hyogoken-nanbu earthquake (January 16, 1995) are provided by Japan Meteorological Agency (JMA), the Committee of Earthquake Observation and Research in the Kansai Area (CEORKA) in Japan (Toki et al., 1995), and the Japan Railway Institute (JR) whose records were scanned and digitized by Wald (1996). Seismometers installed in the CEORKA network record velocity, and those records are differentiated once to obtain accelerograms.

The national strong-motion accelerograph network in Turkey recorded the strong motions during the Izmit earthquake (August 17, 1999) (Akkar and Gülkan, 2002). They can be downloaded from the ftp site of the Earthquake Research Department of General Directorate of Disaster Affairs, Ministry of Public Works and Settlement, Ankara, Turkey (ftp://angora.deprem.gov.tr/). The COSMOS Virtual Data Center archived the dataset of another network operated by Kandilli Observatory and Earthquake Research Institute, Earthquake Engineering Department, Bogaziçi University, Istanbul, Turkey. Stations with fault distance greater than 200 km are excluded since ground motion amplitudes of those stations are quite small which results in a low signal-to-noise ratio. We use four digital and six analog acceleration records from the national network and eight digital acceleration records from the Bogaziçi University network.

The Chi-Chi earthquake (September 20, 1999) is one of the best recorded earthquakes with a large number of stations and a dense station distribution both in the near-source and far-source. Strong motion records for the Chi-Chi earthquake are available on the attached CD in the Special Issue of the *Bulletin of the Seismological Society of America*, vol. 93, no. 5 (Lee et al., 2001). These records were produced by the Central Weather Bureau Seismic Network (CWBSN) and they are the largest set of strong motion data recorded from a major earthquake (Shin and Teng, 2001). Shin and Teng (2001) classified the recorded accelerograms into four quality groups based on the existence of absolute timing, pre-events, and defects. For this analysis, QA-class data (best for any studies) and QB-class data (next best but no absolute timing) are used.

Strong motion data from the Niigataken-chuetsu earthquake (October 23, 2004) were recorded by the K-NET and KiK-net seismic networks operated by the National Research Institute for Earth Science and Disaster Prevention in Japan. Those data are available at their websites (http://www.k-net.bosai.go.jp/ and http://www.kik.bosai.go.jp/). The stations with epicentral distance less than 100 km are used for this analysis.

5.1.2 Data processing

We processed the accelerograms obtained from the nine earthquakes according to the following method. The DC offset of the accelerograms is corrected by subtracting the mean of the pre-event portion. Because a small DC offset has a large effect when the record is integrated, this process is applied to all accelerograms.

The peak amplitude of the horizontal components is calculated by the square root of the sum of the squares of the peaks of NS and EW components. If one of the horizontal components (NS or EW) of a station has been clipped or is not well recorded, the square root of twice the other well-recorded horizontal component is used for the peak amplitude of the horizontal component.

The peak amplitude of UD (up-down) component is used directly for the peak vertical component. The station records that have defects in the vertical component are excluded.

The following processes are completed for all the data.

Jerk: The three-component accelerograms are differentiated in the time domain, using a simple finite-difference approximation. The peak value of each component is selected.

Acceleration: Original accelerograms are used to select the peak value.

Velocity: Some velocity records have a linear trend due to either tilting, the response of the transducer to strong shaking, or problems in the analog-to-digital converter. The baseline correction scheme applied to obtain appropriate velocity records is as follows (Iwan et al., 1985; Boore, 2001):

1) Determine the straight line to be subtracted from the velocity trace. The line is given by the equation:

$$v_f(t) = a_1 t + a_2, \tag{5.1}$$

where coefficients a_1 and a_2 are determined by least-squares fitting to the velocity trace after the strong shaking. The segment of the record used for least-squares fitting is from t_1 to t_2 (see figure 5.1). t_1 is the time when the strong shaking has subsided. The results of baseline correction are not very sensitive to the choice of t_1 (Boore, 2001). The second cut-off time, t_2, is generally chosen as the end of the record;

2) Remove this linear trend from the velocity record.

This baseline correction scheme assumes the baseline shift of the acceleration occurs only once. There may be records that have more than one baseline shift during strong shaking. However, our purpose is to get the peak value of each velocity record, and this does not require accurate integration of the entire record. After time-domain integration, the distortion is not very large in the first portion of the record where the peak value is generally recorded.

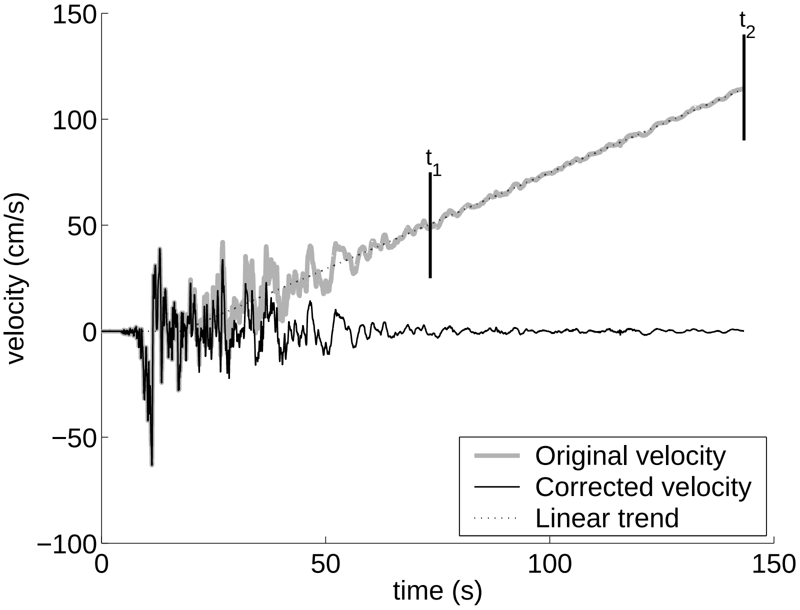

Figure 5.1: An example of baseline correction for a velocity record from the Chi-Chi earthquake. The corrected velocity trend is obtained by subtracting the linear trend from the original velocity record. The portion of the record from t_1 to t_2 is used for least-square fitting to obtain the linear trend.

Displacement: The corrected velocity records are integrated once in the time domain and high-pass filtered using a fourth-order Butterworth filter with a corner frequency of 0.075 Hz.

The peak features used for the classification analysis are shown in table 5.2. Several combinations of these 8 features are tried to find the best performance of the classification.

5.1.3 Data classification

The classification as near-source or far-source in the training set is based on rupture area models used for waveform inversions. These rupture area models are typically determined from the aftershock distribution (Sekiguchi et al., 1996), and the shape

Table 5.2: Eight measurements of peak ground motions are calculated from three component accelerograms. Codes and units of the components used in this paper are shown.

Code	Measurement	Unit
Hj	Horizontal Peak Ground Jerk	(cm/s^3)
Zj	Vertical Peak Ground Jerk	(cm/s^3)
Ha	Horizontal Peak Ground Acceleration	(cm/s^2)
Za	Vertical Peak Ground Acceleration	(cm/s^2)
Hv	Horizontal Peak Ground Velocity	(cm/s)
Zv	Vertical Peak Ground Velocity	(cm/s)
Hd	Horizontal Peak Ground Displacement	(cm)
Zd	Vertical Peak Ground Displacement	(cm)

of the rupture area is approximated by a rectangular box. Fault models used for classifying stations are shown in table 5.1 and figure 5.2. In figure 5.2, black solid lines indicate the surface projection of the fault rupture surface based on the fault models. Stations within 10 km of this fault projection (the white area in the figures) are classified as near-source, indicated by solid circles. Far-source stations are shown in open circles.

High-frequency near-source ground motions have long been researched by engineers and seismologists. High-frequency ground motions depend weakly on magnitude in the near-source (Hanks and Johnson, 1976; Joyner and Boore, 1981; Hanks and Mcguire, 1981). This helps to analyze ground motions with a wide range of magnitudes. Figure 3.2 shows horizontal and vertical PGA of near-source records in our training set as a function of moment magnitude. The slope of a regression line would be almost equal to zero, which is consistent with past studies. On the other hand, low-frequency motion has a strong correlation with magnitude. Figure 3.4 shows horizontal and vertical PGD as a function of moment magnitude. The PGD are log proportional to the magnitude. Based on such observations, we assume that high-frequency motion does not depend on magnitude for large earthquake and that accelerations do not exceed 2g, whereas low-frequency motion is highly correlated with magnitude, and its amplitude increases as the magnitude becomes large.

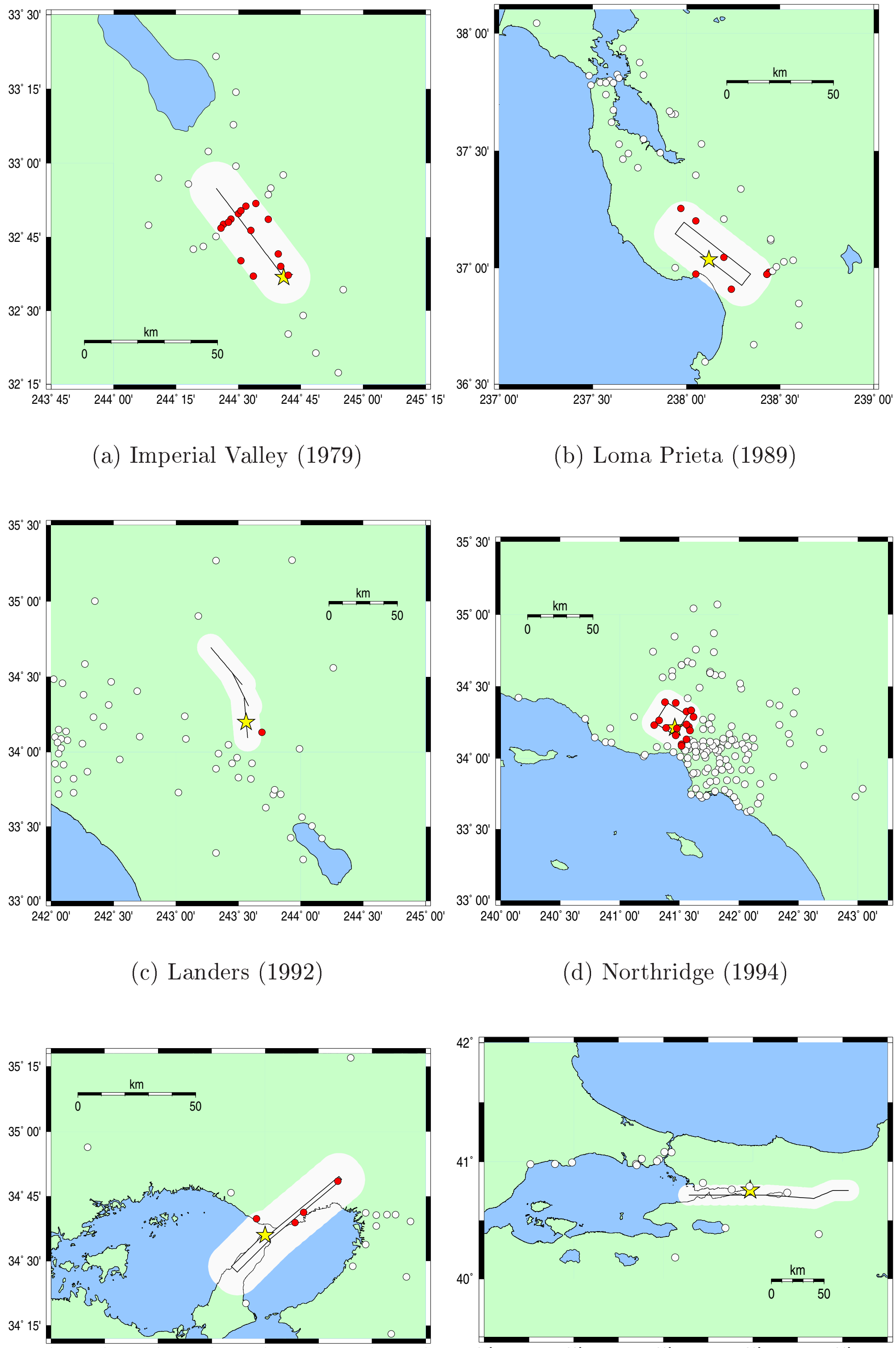

(a) Imperial Valley (1979)

(b) Loma Prieta (1989)

(c) Landers (1992)

(d) Northridge (1994)

(e) Hyogoken-Nanbu (1995)

(f) Izmit (1999)

Figure 5.2: Maps of the fault projections and station distributions. The fault projections are shown in the solid lines. The white area around the fault lines indicates the area with distance less than 10 km from the fault projections. The stations in this area are classified as near-source and marked as solid circles. Far-source stations are shown in open circles. The star symbol denotes the epicenter of the earthquake.

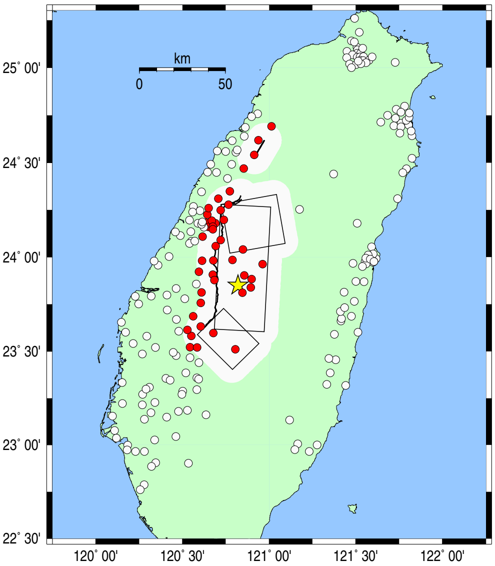

(g) Chi-Chi (1999)

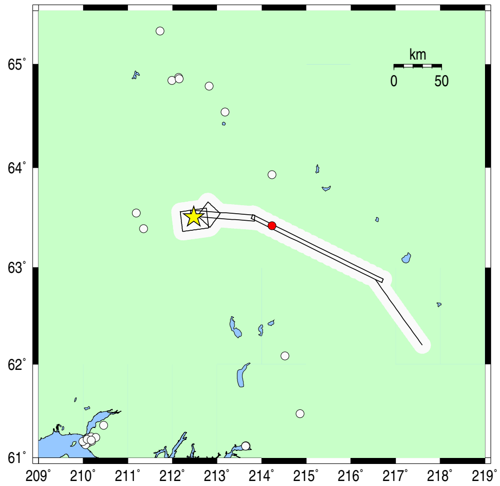

(h) Denali (2002)

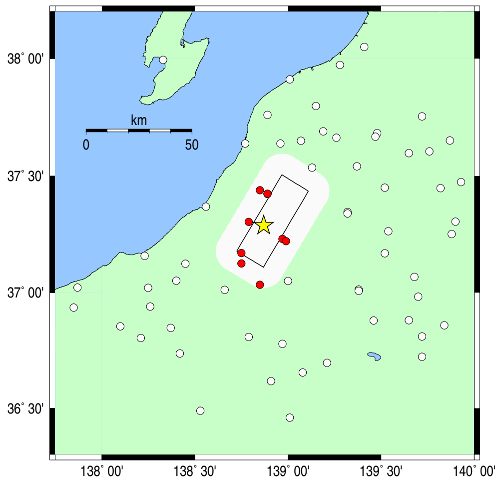

(i) Niigataken-Chietsu (2004)

Figure 5.2: Maps of the fault projections and station distributions (continued).

High-frequency ground motion decays in amplitude more rapidly with distance than low-frequency motion (Hanks and Mcguire, 1981). Therefore, high-frequency motions (e.g., acceleration, jerk) have high correlations with the fault distance. We compute the log of the ground motion amplitudes and find the means and standard deviations for the near-source and far-source records. Figure 5.3 shows the histograms and Gaussian densities given by the sample means and standard deviations for the near-source and far-source records. The Gaussian densities are good approximations of the histograms of the log of the ground motion data. Figure 5.3 also shows that the distance between means for the near-source and far-source datasets is larger in high-frequency than low-frequency motions. Therefore, we expect that the high-frequency motions is a good measure to classify near-source and far-source records.

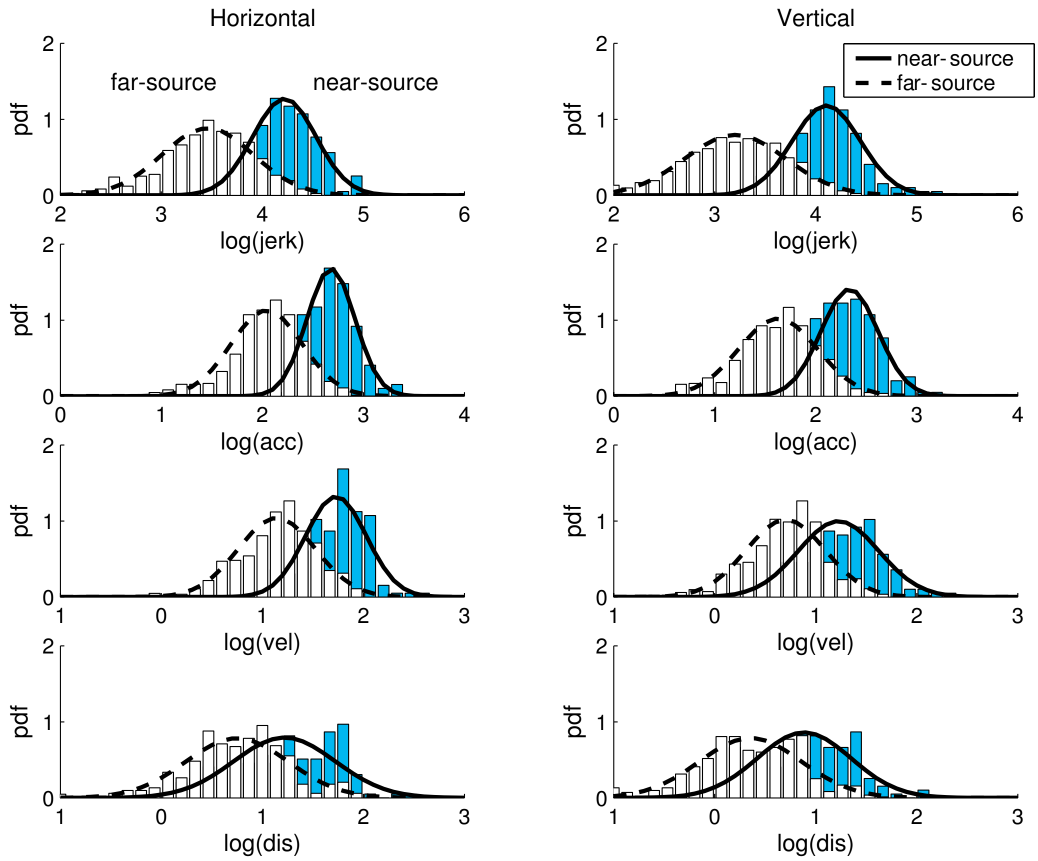

Figure 5.3: Histograms and Gaussian densities based on the sample means and standard deviations of the log of ground motions for the near-source and far-source records. These are distributions for jerk, acceleration, velocity, and displacement from the top.

5.2 Near-source versus far-source discriminant function

We assume the discriminant function to classify records into near-source and far-source is expressed as a linear combination of the log of ground motion amplitudes:

$$
\begin{aligned}
f(X_i|\theta) =& c_1 x_{i1} + c_2 x_{i2} + \ \dots \ + c_m x_{im} - d \\
=& \sum_{k=1}^{m} c_k x_{ik} - d \\
=& X_i \cdot c - d,
\end{aligned}
\tag{5.2}
$$

where

$$
\begin{aligned}
x_{ik} =& \ k\text{th feature parameter of the ground motion at the } i\text{th station,} \\
m =& \text{ the number of feature parameters,} \\
X_i =& [x_{i1},\ x_{i2}, \dots ,\ x_{im}] \\
=& [\log_{10}(component1),\ \log_{10}(component2), \dots,\ \log_{10}(component\mathrm{m})\ ], \\
c_1, \dots, c_m =& \text{the regression coefficients,} \\
d =& \text{ decision boundary constant,} \\
\theta =& [c_1,\ c_2, \dots,\ c_m,\ d]^T.
\end{aligned}
$$

We may use m components out of the eight ground motion components shown in table 5.2. The coefficients $c_1, \dots, c_m$, and d are determined from the training data set by two different approaches: Fisher's linear discriminant analysis and Bayesian analysis.

This discriminant function is used to allocate new observations to one of the near-source or far-source groups, where $f(X_i|\theta) = 0$ is the boundary between the two groups in the feature parameter space. The station with observation X_i is classified as near-source if $f(X_i|\theta)$ is positive. If $f(X_i|\theta)$ is negative, the station is classified as a far-source station. Note that the decision boundary may also be expressed using equation 5.2 as: $X_i \cdot c = d$.

5.2.1 Fisher's linear discriminant analysis

Fisher's Linear Discriminant Analysis (LDA) is a method to classify data by using a linear function (5.2) that best discriminates two or more naturally occurring groups. LDA was first described by Fisher (1936) to separate two groups optimally. In general, LDA requires placing objects (e.g., humans) in predefined groups (e.g., Caucasoid, Mongoloid, and Negroid) based on certain feature parameters (e.g., related to physical characteristics), and finding a function to distinguish the groups. The parameters c_k in the linear function (5.2) are selected to minimize the within-group variance (variance of the samples centered on the group mean) and maximize the between-group variance (variance between group means). The following is a brief discussion about the procedure of linear discriminant analysis (Venables and Ripley, 2002):

> Consider $n \times m$ data matrix X where n is the number of samples and m is the number of different features of samples. Each sample is assigned to one of g groups $N_j, j = 1, ..., g$, with n_j observations in each group. Let G denote the group indicator matrix, which indicates the group each sample is assigned to, and let M denote the group mean matrix, then within-group covariance matrix W and between-group covariance matrix B are:
>
> $$W = \frac{(X - GM)^T (X - GM)}{n - g}, \tag{5.3}$$
>
> $$B = \frac{(GM - \mathbf{1}\mu)^T (GM - \mathbf{1}\mu)}{g - 1}, \tag{5.4}$$

where

$$
\begin{aligned}
X =& [x_{ik}] : n \times m \text{ data matrix,} \\
G =& [g_{ij}] : n \times g \text{ group indicator matrix,} \\
M =& [m_{jk}] : g \times m \text{ group mean matrix,} \\
\mu =& [\mu_1,\ \mu_2, ...,\ \mu_m] : 1 \times m \text{ mean vector,} \\
\mathbf{1} =& n \times 1 \text{ column vector of 1s,} \\
x_{ik} =& \ k\text{th feature of the } i\text{th sample,} \\
g_{ij} =& 1 \iff X_i = [x_{i1},\ x_{i2}, ...,\ x_{im}] \text{ is assigned to group } j, \\
m_{jk} =& \frac{1}{n_j} \sum_{i \in N_j} x_{ik}, \\
\mu_k =& \frac{1}{n} \sum_{i=1}^{n} x_{ik}.
\end{aligned}
$$

We would like to find a linear combination $X \cdot c$ of the data such that the different groups are maximally separated, that is, maximizing the following separation ratio λ:

$$
\lambda = \frac{c^T Bc}{c^T Wc} = \frac{\text{between-group variance}}{\text{within-group variance}}. \tag{5.5}
$$

A necessary condition to maximize λ is $\frac{\partial \lambda}{\partial c} = 0$. By substituting equation 5.5 into this condition, we get:

$$
W^{-1}Bc = \lambda c, \tag{5.6}
$$

assuming W is invertible. This is an eigenvalue problem, and the weight vector c and the separation ratio λ are eigenvectors and eigenvalues of $W^{-1}B$, respectively. $X \cdot c$ is called a canonical variate, and the canonical variate of the eigenvector c which corresponds to the largest eigenvalue is called the first canonical variate.

For the near-source versus far-source classification problem, the data matrix X is the dataset of peak seismic ground motions, where n is the number of stations, and m is number of the object features (PGA, PGV, PGD, etc.). We have two groups: near-source group and far-source group ($g = 2$). LDA finds the optimal set of coefficients of ground motion amplitudes to classify near-source or far-source records.

Since the traditional LDA does not treat which choice of the ground motion parameters is the best, Bayesian model class selection is performed (the results are shown later). According to this analysis, the best selection is (Za and Hv), and their coefficients obtained from LDA are shown in table 5.3.

Table 5.3: Estimated model parameters by Fisher's LDA, Bayesian approach with asymptotic approximation, and Bayesian approach with the Metropolis algorithm. The standard deviations for each parameter are shown in brackets.

Method	c_1 (Za)	c_2 (Hv)	d
LDA	7.233	6.813	25.903
Bayesian-Asym.	6.046	7.886	27.090
(σ)	($\pm$ 0.903)	($\pm$ 1.206)	($\pm$ 3.163)
Bayesian-MA	6.194	8.150	27.872
(σ)	($\pm$ 0.946)	($\pm$ 1.224)	($\pm$ 3.330)

We choose the decision boundary constant d to maximize the classification performance for the set of coefficients obtained by the LDA. The classification performance is evaluated by the following function:

$$P_c(d) =(P(f(X_i|\theta) \geq 0|Y_i = 1) + P(f(X_i|\theta) < 0|Y_i = -1))/2, \tag{5.7}$$

where

$$f(X_i|\theta) =X_i \cdot c - d,$$
$$Y_i = \begin{cases} 1 & \text{if near-source,} \\ -1 & \text{if far-source.} \end{cases}$$

This is the average probability between the probability that a near-source station is classified correctly and the probability that a far-source is classified correctly. The parameter d which maximizes this function for the given coefficients (table 5.3) is 25.903, and the performance defined by the function above is 93.4%. Another way to compute d is to take the midpoint of the two group means of the first canonical variate. This method makes it easier to compute the value of d and it gives $d = 25.045$, a good approximation to $d = 25.903$ which shows maximum performance.

As a conclusion, the discriminant function computed from the LDA is:

$$f(X_i|\theta) = 7.233 \log_{10} Za + 6.813 \log_{10} Hv - 25.903, \tag{5.8}$$

$$\text{if} \begin{cases} f(X_i|\theta) \geq 0 & \text{near-source,} \\ f(X_i|\theta) < 0 & \text{far-source.} \end{cases}$$

This discriminant function is applied to all the dataset, and the values of $f(X_i|\theta)$ are shown in figure 5.4. The figure shows that most of the near-source data lie on the right side of the decision boundary, which means the classification performance is very good.

5.2.2 Bayesian approach

In this section, a Bayesian approach is applied to determine the coefficients of the discriminant function that classifies near-source and far-source data. The probability density function (pdf) of parameter θ conditioned on data D_n and model class M can be expressed using Bayes' theorem:

$$\begin{aligned} \underbrace{p(\theta|D_n, M)}_{posterior} &\propto \underbrace{p(D_n|\theta, M)}_{likelihood} \times \underbrace{p(\theta|M)}_{prior} \\ &\propto \prod_{i=1}^{n} P(Y_i|X_i, \theta) \times p(\theta|M), \end{aligned} \tag{5.9}$$

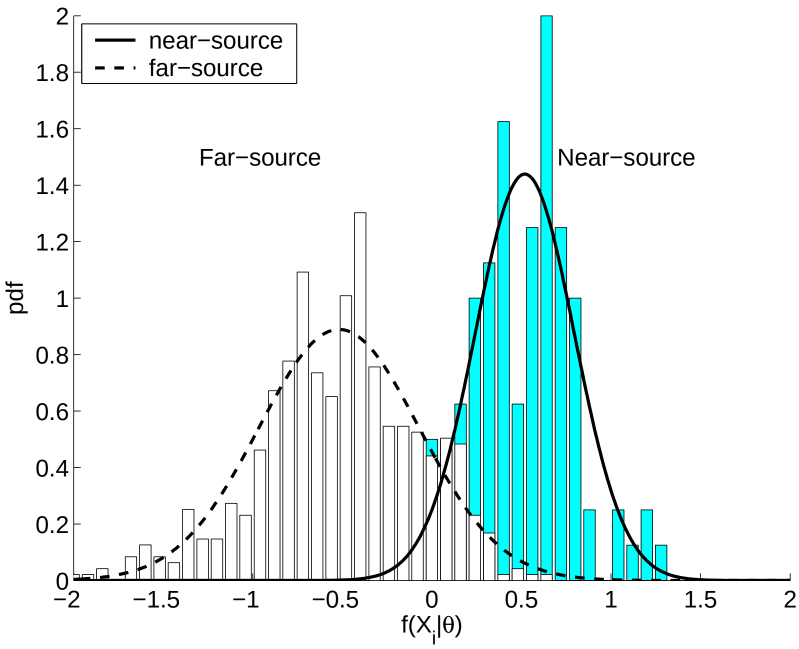

Figure 5.4: Histogram of the near-source and far-source data to which the discriminant function obtained from traditional LDA is applied. The column heights are normalized by the number of the data in each group. $f(X_i|\theta) = 0$ is the decision boundary between the two groups. The curves are the Gaussian distribution with the same mean and standard deviation as the values of $f(X_i|\theta)$ for each group.

where

$$
\begin{aligned}
\theta =& [c_1,\ c_2, ...,\ c_m,\ d]^T : \text{parameter vector},\\
D_n =& \{(X_i, Y_i) : i = 1, ...,\ n\} : \text{available set of data},\\
X_i =& [x_{i1},\ x_{i2}, ...,\ x_{im}] : \text{ground motion at the station } i\\
=& [\log_{10}(component1),\ \log_{10}(component2), ...,\ \log_{10}(component\mathrm{m})],\\
Y_i =& \begin{cases} 1 & ;\ \text{if near-source} \\ -1 & ;\ \text{if far-source} \end{cases} \text{ at the station } i,\\
m =& \text{ the number of object features},\\
n =& \text{ the number of data}.
\end{aligned}
$$

Note that the model class M defines the likelihood for each value of θ in some set of values and also the prior pdf $p(\theta)$.

We determine the parameters $c_1, ..., c_m, d$ based on a Bayesian approach using the same notation as the LDA. The goal of the Bayesian approach is to obtain the posterior pdf of the model parameters (θ) and determine the most plausible value of θ by maximizing this pdf.

Choice of Prior Distribution

Assume that the model class M is globally identifiable based on D_n (Beck and Katafygiotis, 1998), that is, there is a unique θ maximizing the likelihood $p(D_n|\theta, M)$. In this case, given a sufficiently large dataset D_n, the choice of prior pdf does not affect the resulting posterior pdf, and all posteriors with different priors will converge to the same answer (Sivia, 1996). Here, the prior is chosen to cover a wide range of the parameter space by selecting the prior of each model parameter to be a Gaussian pdf with zero mean and standard deviation σ=100, so:

$$p(\theta|M) = \frac{1}{(\sqrt{2\pi}\sigma)^{m+1}} \exp(-\frac{1}{2\sigma^2}\theta^T\theta) = \frac{1}{(\sqrt{2\pi}\sigma)^{m+1}} \exp(-\frac{1}{2\sigma^2}(\sum_{k=1}^{m} c_k^2 + d^2)). \tag{5.10}$$

Choice of Likelihood function

Let the predictive probability that station i is near-source be $P(Y_i = 1|X_i, \theta)$. The predictive probability that a station is far-source is then $P(Y_i = -1|X_i, \theta) = 1 - P(Y_i = 1|X_i, \theta)$. A standard approach in Bayesian classification is to define the predictive probability by applying the logistic sigmoid function $\phi(x) = 1/(1 + e^{-x})$ to the linear function $f(X_i|\theta)$ that is also used in the traditional LDA (Li et al., 2002). The logistic sigmoid function is a smooth, positive, and monotonically increasing function, as shown in figure 5.5. The predictive probability that the ith station is near-source is therefore defined here by:

$$P(Y_i = 1|X_i, \theta) = \phi(f(X_i|\theta)) = \frac{1}{1 + e^{-f(X_i|\theta)}}. \tag{5.11}$$

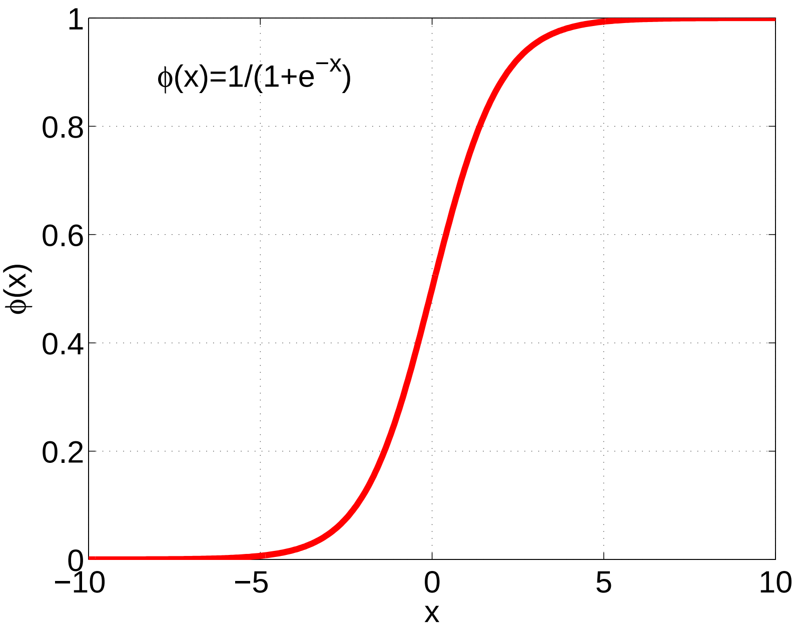

Figure 5.5: Logistic sigmoid function $\phi(x) = 1/(1+e^{-x})$ is used to express the predictive probability for classification. The function approaches zero as $x \to$ -∞, and one as $x \to \infty$. The function is 0.5 when x is zero.

As $f(X_i|\theta)$ becomes larger, the station is more likely to be near-source, and the probability that the station is near-source becomes closer to one. Note that the predictive probability that the station is far-source is then:

$$P(Y_i = -1|X_i, \theta) = 1 - \phi(f(X_i|\theta)) = \phi(-f(X_i|\theta)) = \frac{1}{1+e^{f(X_i|\theta)}}, \tag{5.12}$$

where, from equation 5.2,

$$f(X_i|\theta) = \sum_{k=1}^{m} c_k x_{ik} - d = X_i \cdot c - d.$$

From equations 5.11 and 5.12, the likelihood function can be expressed as:

$$p(D_n|\theta, M) = \prod_{i=1}^{n} P(Y_i|X_i, \theta) = \prod_{i=1}^{n} \phi(Y_i f(X_i|\theta)) = \prod_{i=1}^{n} \frac{1}{1+e^{-Y_i f(X_i|\theta)}}. \tag{5.13}$$

Posterior Distribution

By substituting equations 5.10 and 5.13 into equation 5.9, the posterior can be expressed as:

$$p(\theta|D_n, M) \propto \frac{1}{(\sqrt{2\pi}\sigma)^{m+1}} \exp(-\frac{1}{2\sigma^2}\theta^T\theta) \prod_{i=1}^{n} \frac{1}{1+e^{-Y_i f(X_i|\theta)}}. \tag{5.14}$$

Both an asymptotic approximation and stochastic simulation are performed to characterize the pdf defined by equation 5.14. In the asymptotic approach, the posterior is represented by a Gaussian distribution for θ with mean $\hat{\theta}$, the most probable value of θ, and a covariance matrix $\hat{\Sigma}$ defined later. Stochastic simulation uses the Metropolis algorithm to generate random samples of the parameter vector θ from the posterior pdf. It is noted that it is computationally challenging to evaluate the proportionality constant in equation 5.14 that normalizes the posterior pdf because it requires numerical integration over a high-dimensional parameter space. However, this evaluation can be avoided in both the asymptotic approximation and stochastic simulation methods.

5.2.2.1 Asymptotic approximation

We first find the optimal value $\hat{\theta}$ of θ that maximizes the posterior pdf. This multidimensional optimization problem is solved by a numerical optimization algorithm provided by Matlab.

Using Laplace's method of asymptotic approximation, Beck and Katafygiotis (1998) show that the posterior pdf for a set of model parameters θ for a globally identifiable model class M (which has a unique most probable value) may be approximated accurately by a Gaussian distribution with mean $\hat{\theta}$ and covariance matrix $\hat{\Sigma}$, given a large amount of data. Define $H(\theta)$ by:

$$H(\theta) = -\nabla\nabla \log[p(D_n|\theta, M)p(\theta|M)] = -\nabla\nabla \log[\prod_{i=1}^{n} P(Y_i|X_i, \theta)p(\theta|M)], \tag{5.15}$$

then $\hat{\Sigma} = H(\hat{\theta})^{-1}$. By substituting equations 5.10 and 5.13 into equation 5.15;

$$
\begin{aligned}
[H(\theta)]_{(\alpha,\beta)} =&[-\nabla\nabla \log \prod_{i=1}^{n} P(Y_i|X_i,\theta) - \nabla\nabla \log p(\theta|M)]_{(\alpha,\beta)} \\
=& - \frac{\partial^2}{\partial c_\alpha \partial c_\beta}(\log \prod_{i=1}^{n} \phi_i) + \frac{1}{\sigma^2}\delta_{\alpha\beta} \\
=& - \sum_{i=1}^{n} \frac{\partial^2}{\partial c_\alpha \partial c_\beta}(\log \phi_i) + \frac{1}{\sigma^2}\delta_{\alpha\beta} \\
=& - \sum_{i=1}^{n} \frac{\partial}{\partial c_\beta}[\frac{1}{\phi_i}\phi_i(1-\phi_i)\frac{\partial(Y_i f(X_i|\theta))}{\partial c_\alpha}] + \frac{1}{\sigma^2}\delta_{\alpha\beta} \\
=& \sum_{i=1}^{n} \phi_i(1-\phi_i) x_{i\alpha} x_{i\beta} + \frac{1}{\sigma^2}\delta_{\alpha\beta},
\end{aligned} \tag{5.16}
$$

where $\phi_i = \phi(Y_i f(X_i|\theta))$, and equation 5.2, along with $Y_i^2 = 1$, has been used. The optimal parameter values and their standard deviations for the selection of features Za and Hv are shown in table 5.3. Note that for large σ, the effect of the prior in equation 5.16 is negligible.

In order to examine the sensitivity of the Bayesian approach to the training dataset, we perform a cross-validation analysis. First, the training dataset is randomly divided into two datasets and the discriminant function is constructed from one dataset (training set). This discriminant function is applied to the other dataset (validation set) to check its classification performance. We then switch the testing set and validation set, and repeat this cross-validation analysis. We set the near-source versus far-source boundary so that the probability is a half that the station is near-source, that is, the station is classified as near-source if the probability that it is near-source is more than 1/2. The confusion matrices of these two analysis and the previous analysis which uses all of the dataset are shown in table 5.4. The classification error with half of the dataset is as small as that of the analysis which uses all of the dataset. Therefore, we confirm that the sensitivity to the training dataset is small, giving more confidence that the discriminant function from Bayesian analysis will perform well for future earthquake data.

Table 5.4: The confusion matrix for the cross-validation analysis with the Bayesian method with asymptotic approximation. “All dataset” is the analysis which uses the whole dataset as a training set and a validation set. “Half of dataset” is the analysis which uses half of dataset as a training set and the other half as a validation set. “Other half of dataset” is the analysis which switches the training and validation set. NS and FS stand for near-source and far-source, respectively.

Dataset	NS/FS	Near-source	Far-source
All dataset	NS	78 (78%)	22 (22%)
	FS	12 (2%)	583 (98%)
Half of dataset	NS	39 (74%)	14 (26%)
	FS	4 (1%)	291 (99%)
Other half of dataset	NS	37 (79%)	10 (21%)
	FS	8 (3%)	292 (97%)

5.2.2.2 Stochastic simulation using Metropolis algorithm

The asymptotic approximation is valid only if the posterior pdf for the model parameters can be approximated well with a Gaussian distribution. This requires a large sample size and that the class of models M is globally identifiable based on data D_n (Beck and Katafygiotis, 1998). On the other hand, a stochastic simulation algorithm can be applied to the problem which generates samples from a Markov Chain whose stationary pdf is the posterior pdf, that is, the samples are asymptotically distributed according to the posterior pdf for the parameters. The Metropolis algorithm is used to solve this high-dimensional problem, because it does not require evaluation of the normalizing constant for sampling the posterior pdf in equation 5.14.

The Metropolis algorithm is a Markov chain Monte Carlo (MCMC) method proposed by Metropolis et al. (1953). It is a simulation technique for generating random samples from any given probability distribution. The algorithm uses a proposal pdf Q which depends on the current sample of parameters, $\theta^{(t)}$ at tth iteration (MacKay, 1999). Here, we choose as the proposal density a Gaussian pdf centered on the current parameters $\theta^{(t)}$ with the covariance matrix Σ of the parameters in the asymptotic approximation. The optimal parameters estimated from direct optimization of the posterior pdf are used as an initial $\theta^{(t)}$. The expression for Q is:

$$Q(\theta'|\theta^{(t)}) = \frac{1}{(2\pi)^{m'/2}|\Sigma|^{1/2}} \exp(-\frac{1}{2}(\theta' - \theta^{(t)})^T\Sigma^{-1}(\theta' - \theta^{(t)})), \tag{5.17}$$

where $|\Sigma|$ is the determinant of the covariance matrix, and m' is the dimension of the parameter θ, which is $m + 1$. A candidate sample is drawn from $Q(\theta'|\theta^{(t)})$. The ratio of the posterior pdf in equation 5.9 at the current sample $\theta^{(t)}$and the candidate sample θ' determines whether to accept the candidate sample, according to:

$$r = \frac{p(\theta'|D_n, M)}{p(\theta^{(t)}|D_n, M)}, \tag{5.18}$$

$$\theta^{(t+1)} = \begin{cases} \theta' & \text{with probability} \min(1, r), \\ \theta^{(t)} & \text{with probability } 1 - \min(1, r). \end{cases} \tag{5.19}$$

If $r \geq 1$ then the candidate is accepted as the next sample in the Markov Chain. Otherwise, the candidate is accepted with probability r as follows; we generate a random number uniformly distributed between zero and one, and if it is less than r, the candidate is accepted, that is, $\theta^{(t+1)} = \theta'$. If it is not accepted, the current sample is repeated ($\theta^{(t+1)} = \theta^{(t)}$). This procedure is repeated until the desired number of samples are generated. There is a burn-in period at the beginning of the MCMC method until the probability distribution of the current sample $\theta^{(t)}$ is sufficiently close to the posterior pdf, which is the stationary pdf of the Markov chain, so judgment is used to discard initial samples.

Figure 5.6 shows 5000 parameter samples generated with the Metropolis algorithm for the optimal selection of features Za and Hv. This selection of the ground motion features comes from Bayesian model class selection explained later. After discarding the samples in the burn-in period (taken as the first 100 samples), the mean and standard deviation of the samples are shown in table 5.3. The average acceptance ratio of the candidate samples θ' is 44%, which indicates the method works well

(Roberts et al., 1997). The stability of the sample mean and standard deviation of each parameter is examined in figure 5.7. The mean and standard deviation of the samples converge after the first 1000 samples are added. The most probable values of the parameters from maximization of the posterior pdf are also shown in figure 5.7. Note that the means of the marginal pdf's and the most probable values of the joint posterior pdf need not agree if these pdf's are skewed.

The distribution of sample values for parameters θ and the resulting histogram of probability that a station is near-source calculated by the generated set of parameters are shown in figure 5.8. The distribution of parameter samples agrees well with the Gaussian distribution defined by the optimal parameters and standard deviations given by the asymptotic approximation. The standard deviations of c_1 and c_2 are similar to each other and the distribution is peaked close to the mean of the samples. The distribution of samples for the decision boundary constant d has a standard deviation almost three times as large as that of c_1 and c_2. However, in terms of coefficient of variation, the uncertainty in d is smaller than that of other parameters (11.7% compared with 14.9% and 15.3% for c_1 and c_2, respectively).

Figure 5.9 shows the correlation of samples of model parameters generated from the simulation. This is the result of the model class with all parameters corresponding to the eight ground motion parameters, not the result of the optimal model class. The figure shows that the parameter d is not correlated significantly with any other parameter. The combinations of parameters which have significant interaction are horizontal and vertical jerk (c_1 and c_2), horizontal and vertical acceleration (c_3 and c_4), and horizontal and vertical displacement (c_7 and c_8). Parameters with the same component and similar frequency range (e.g., jerk and acceleration (c_1 and c_3, and c_2 and c_4), acceleration and velocity (c_3 and c_5, and c_4 and c_6), velocity and displacement (c_5 and c_7, and c_6 and c_8)) are also strongly correlated. This result agrees with our intuition; horizontal and vertical components of the same quantity are correlated, and records with similar frequency ranges have similar attenuation relationships and so are correlated.

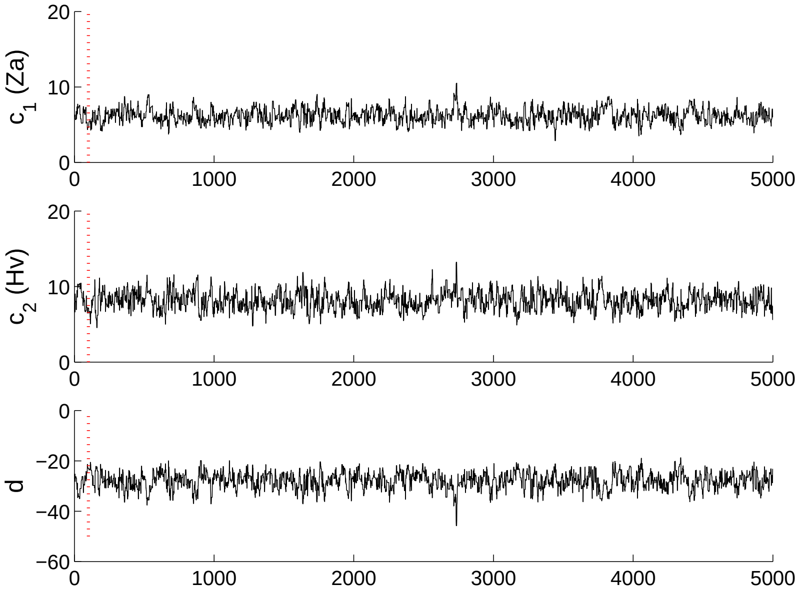

Figure 5.6: Samples generated by the Metropolis algorithm plotted in the parameter space. The x-axis denotes the sample number. The vertical dotted lines indicate the end of the burn-in period (100 samples).

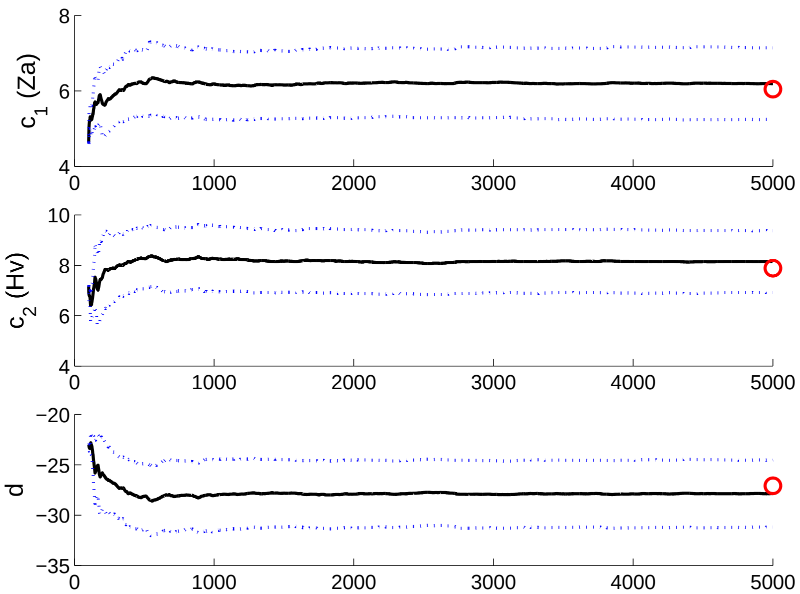

Figure 5.7: Mean and standard deviation of samples plotted against the number of samples included (excluding first 100 samples). The solid line is the sample mean, and the dashed lines represent the mean plus and minus one standard deviation. The small circle is the most probable values of the model parameters estimated from optimization.

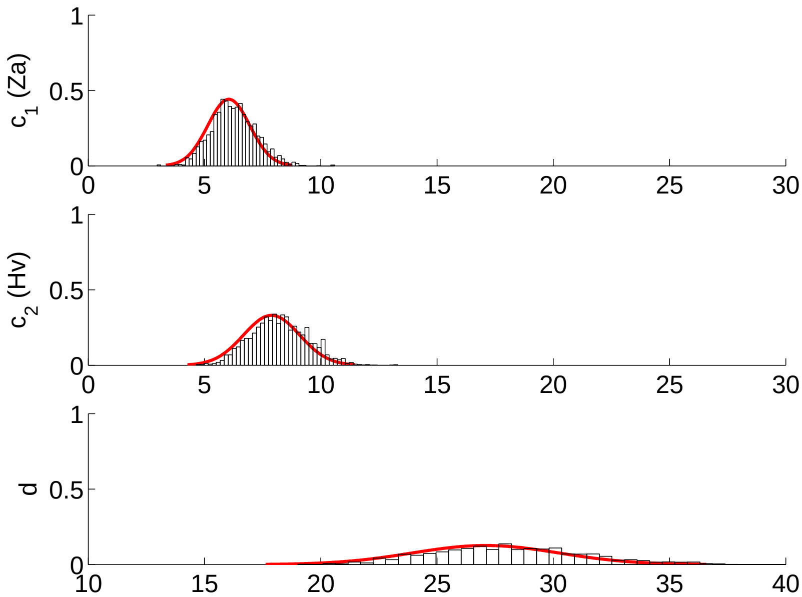

Figure 5.8: Distribution of samples for 3 parameters generated by the Metropolis algorithm. The Gaussian distributions obtained from the asymptotic approximation are added in the figure, and fit the histogram well.

5.2.3 Comparison between traditional LDA and Bayesian approach

Parameters for the linear discriminant function $f(X_i|\theta) = \sum_{k=1}^{m} c_k x_{ik} - d$ are estimated by traditional LDA and by the Bayesian approach with two different techniques to characterize the posterior pdf. The results are shown in table 5.3. The parameters for LDA are scaled such that the norm of the vector $c = [c_1,\ c_2]$ is equal to the norm of the vector from the asymptotic approximation. Note that the discriminant function $f(X_i|\theta)$ is a linear function, so for the traditional LDA, multiplying all c_k and d by an arbitrary positive constant does not change the result of classification. However, this is not true for the Bayesian approach, where the modulus of $f(X_i|\theta)$ affects the probability that a station is near-source.

The estimated parameters are close for the three methods. The coefficients from LDA are within one standard deviation of those from both Bayesian methods, except that c_1 from LDA is slightly over one standard deviation from the corresponding mean and most probable values from the Bayesian methods.

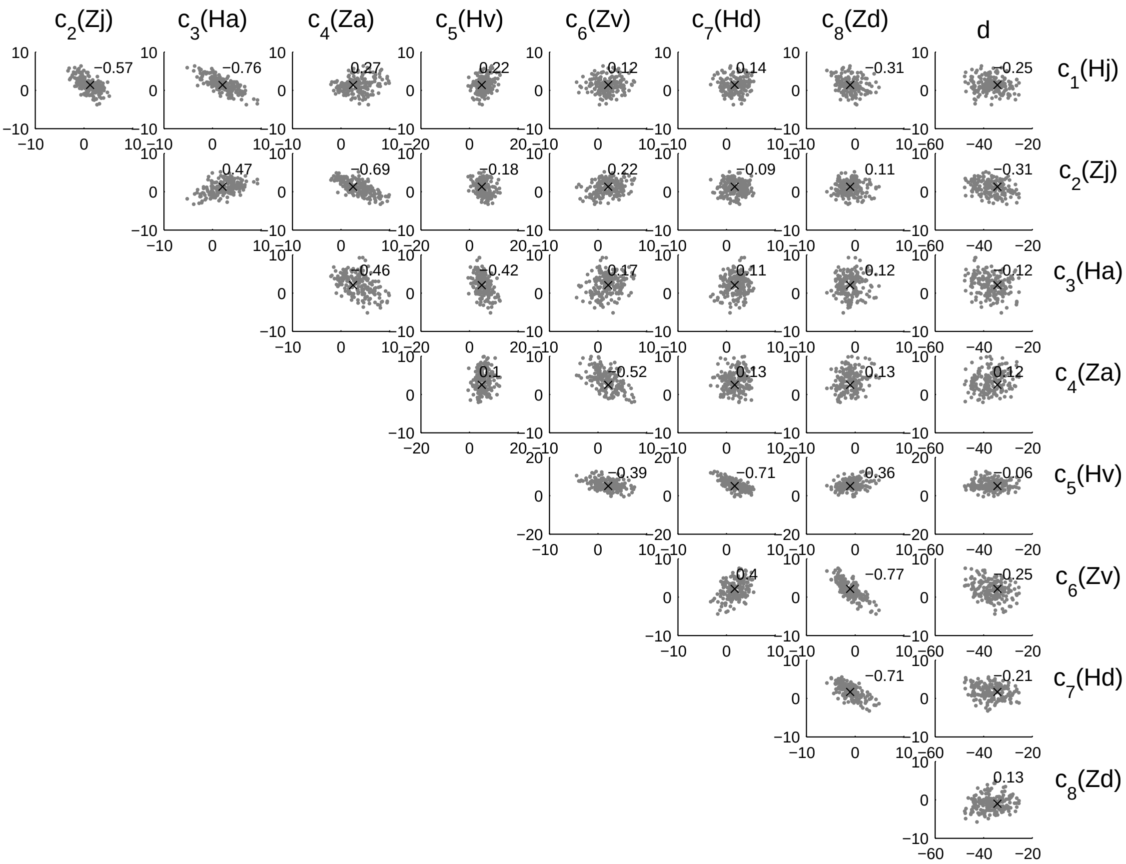

Figure 5.9: Correlation plot of posterior samples of the model parameters generated by the Metropolis algorithm. The most probable values of the parameters are shown as "x". The numbers in the figure are the correlation coefficient of parameters.

For the asymptotic approximation and Metropolis algorithm, the estimates and standard deviations for the posterior parameter distribution are very close. If the posterior is a skewed pdf, the mean is not necessarily equal to the most probable value (e.g., consider lognormal distribution), as mentioned before. However, figure 5.8 suggests that the posterior pdf is almost symmetric, and the means of the samples and the most probable values should show very good agreement. In this case, the Gaussian distribution is a good approximation for the posterior pdf of the parameters.

By using the discriminant functions defined by the values of the parameters in table 5.3, we performed a classification analysis using the whole dataset. The classification performance for the discriminant function from LDA and two Bayesian approaches are shown in table 5.5. The results for LDA show 100% of near-source data and 86% of far-source data are classified correctly, and the result of Bayesian approach shows 78% of near-source data and 98% of far-source data are classified correctly. This discriminant function is the function which has the smallest prediction error. To obtain this function, the misclassification of near-source data and that of far-source data are considered to be of equal importance. Generally speaking, the misclassifications of near-source data is more critical than that of far-source data, and we may want to decrease the misclassification rate of near-source data. This misclassification rate can be easily controlled by changing the decision boundary constant d. We also can control this by shifting the near-source versus far-source boundary in the Bayesian approach to correspond to some other probability than the 1/2 used in this classification analysis.

Table 5.5: The confusion matrix for near-source versus far-source classification by the discriminant function obtained from LDA, Bayesian approach with asymptotic approximation, and Bayesian approach with Metropolis algorithm.

Dataset	NS/FS	Near-source	Far-source
LDA	NS	100 (100%)	0 (0%)
	FS	82 (14%)	513 (86%)
Bayesian-Assym.	NS	78 (78%)	22 (22%)
	FS	12 (2%)	583 (98%)
Bayesian-MA	NS	78 (78%)	22 (22%)
	FS	12 (2%)	583 (98%)

We performed the leave-one-out cross-validation to compare the misclassification rate between LDA and the Bayesian method with asymptotic approximation. The idea of this method is to predict the probability of a station from the discriminant function constructed from the dataset from which that station is excluded. This process is repeated for all 695 data and the accuracy of prediction is computed. The percentage of misclassified data is shown in table 5.6. It shows the prediction error of the Bayesian approach is much smaller than that of LDA. In other words, the Bayesian approach is able to construct a more robust discriminant function. Therefore, we use the discriminant function obtained from the Bayesian method with asymptotic approximation for further analysis.

Table 5.6: Results of leave-one-out cross-validation for LDA and Bayesian approach.

Method	Prediction Error
LDA	82 / 695 (12%)
Bayesian approach	36 / 695 (5%)

5.3 Bayesian model class selection

5.3.1 Method

Bayesian model class selection determines which combination of the eight ground motion parameters gives the best classification for the near-source and far-source. The essential idea is to find the most probable model class based on data D_n within a set of candidate model classes M_j, $j = 1, ..., J$ (Beck and Yuen, 2004). Applying Bayes' theorem, the probability of model class M_j can be expressed as follows:

$$P(M_j|D_n, M) = \frac{\overbrace{p(D_n|M_j)}^{evidence}\overbrace{P(M_j|M)}^{prior}}{\underbrace{p(D_n|M)}_{normalizing\ constant}}, \tag{5.20}$$

where

$M = \{M_1, M_2, \ldots, M_J\}$: a set of candidate model classes,

$J =$number of the model classes.

The left-hand side of equation 5.20 is the probability of a particular model class M_j given the dataset and a set of candidate model classes. On the right-hand side, $p(D_n|M_j)$ is the evidence for each model class, $P(M_j|M)$ is the prior over the candidate model classes evaluated for M_j, and $p(D_n|M)$ is a normalizing constant given by:

$$p(D_n|M) = \sum_{j=1}^{J} p(D_n|M_j)P(M_j|M). \tag{5.21}$$

Assuming a uniform prior for the model class, $P(M_j|M)$ in the numerator and denominator of equation 5.20 cancel. By the total probability theorem, the evidence for M_j provided by the dataset D_n is given as:

$$p(D_n|M_j) = \int_{\theta_j} p(D_n|\theta_j, M_j)p(\theta_j|M_j)d\theta_j. \tag{5.22}$$

This is simply the integral of the likelihood of the data for a vector of parameters weighted by its prior probability integrated over the whole parameter set for θ_j for model class M_j.

An asymptotic approximation for large sample sizes n can be used to compute the evidence of the model (Papadimitriou et al., 1997):

$$p(D_n|M_j) \approx \underbrace{\frac{2\pi^{N_j/2} p(\hat{\theta}_j|M_j)}{\sqrt{|H_j(\hat{\theta}_j)|}}}_{Ockham\ factor} \times \underbrace{p(D_n|\hat{\theta}_j, M_j)}_{likelihood}, \tag{5.23}$$

where

$$\begin{aligned} H_j(\theta_j) =& -\nabla\nabla \log[p(D_n|\theta_j, M_j)p(\theta_j|M_j)], \\ \hat{\theta}_j =& \text{ optimal parameter vector (most probable value) for model class } M_j, \\ N_j =& \text{ number of parameters for model class } M_j. \end{aligned}$$

Here, $H_j(\theta_j)$ is given by equation 5.16 for the choice of parameters θ_j corresponding to model class M_j. $p(\hat{\theta}_j|M_j)$ is the prior defined in equation 5.10 and $p(D_n|\hat{\theta}_j, M_j)$ is the likelihood function defined in equation 5.13, evaluated at the optimal parameter vector for model class M_j. For the model class selection, the effect of the number of the parameters, N_j, in the Gaussian prior is significant if the standard deviation, σ, is large. However, the prior we chose is not affected by this issue (we demonstrate this later).

5.3.2 Results of Bayesian model class selection

We used Bayesian Model Class Selection to find the best combination of the eight ground motion parameters with the same dataset as the previous classification problem. First, we impose the condition that both horizontal and vertical components be included in the model for any selected ground motion quantity. Under this condition, there are four groups of ground motion parameters (peak jerk, acceleration, velocity, and filtered displacement) giving fifteen possible combinations. These fifteen candidate model classes are shown in table 5.7.

Table 5.7: Results for Bayesian model class selection when fifteen combinations of the ground motion parameters are examined under the condition that the horizontal and vertical components are used together. The most probable value of the decision boundary parameter corresponding to each ground-motion parameter is given first for each model class. The values for the Ockham factor (Ock.), likelihood (like.), and evidence (evi.) of each model class are log scaled. The last column is the posterior probability that measures how plausible the model class is. It is scaled such that the total probability of the fifteen model classes is 100%.

model	Hj	Zj	Ha	Za	Hv	Zv	Hd	Zd	d	Ock.	Like.	Evi.	P(%)
j	1.53	4.30	-	-	-	-	-	-	23.8	-17	-140	-156	0.0
a	-	-	4.38	4.37	-	-	-	-	21.4	-16	-117	-133	0.0
v	-	-	-	-	8.57	0.87	-	-	16.3	-16	-118	-134	0.0
d	-	-	-	-	-	-	2.49	1.44	5.8	-17	-192	-209	0.0
ja	-2.74	2.04	6.60	2.95	-	-	-	-	20.8	-25	-114	-139	0.0
jv	2.57	2.79	-	-	7.00	2.00	-	-	36.1	-25	-80	-105	32.4
jd	3.44	3.43	-	-	-	-	3.48	0.79	33.2	-26	-94	-120	0.0
av	-	-	2.54	4.38	7.01	0.91	-	-	29.5	-24	-80	-104	62.1
ad	-	-	4.93	5.02	-	-	3.89	0.22	29.4	-25	-82	-106	5.3
vd	-	-	-	-	12.55	2.30	-3.38	-0.25	20.0	-25	-106	-131	0.0
jav	1.36	1.47	1.36	2.28	6.93	1.50	-	-	33.8	-33	-78	-111	0.1
jad	0.55	0.43	4.35	4.49	-	-	3.89	0.27	30.7	-33	-81	-115	0.0
jvd	2.72	2.68	-	-	6.66	2.91	0.66	-1.12	36.7	-34	-80	-113	0.0
avd	-	-	3.47	4.50	4.58	1.06	1.80	-0.47	30.2	-33	-79	-112	0.0
javd	1.40	1.29	2.05	2.49	5.05	2.11	1.69	-1.0	34.3	-41	-78	-119	0.0

The results in table 5.7 indicate that the combination of acceleration and velocity is the model with highest probability, although the jerk and velocity combination also has significant probability. The log of prior $(p(\hat{\theta}_j|M_j))$ is simply a function of N_j and becomes smaller as the number of parameters increases. The factor $p(\hat{\theta}_j|M_j)(2\pi^{N_j/2})/\sqrt{|H_j(\hat{\theta}_j)|}$ in equation 5.23 is called the Ockham factor by Gull (Gull, 1988; Beck and Yuen, 2004). It penalizes a more complicated model and so makes a simpler model preferable. The Ockham factor is also shown in table 5.7. Although the coefficient $2\pi^{N_j/2}$ and $\sqrt{|H_j(\hat{\theta}_j)|}$ are included in the Ockham factor, the effect of prior $p(\hat{\theta}_j|M_j)$ is dominant.

The log of the likelihood function $p(D_n|\hat{\theta}_j, M_j)$ becomes larger as the number of the parameters in the model class increases because a more complicated model class will fit the data better than a less complicated one. However, the Bayesian model class selection automatically accounts for the trade-off between the complexity of the model (e.g., number of parameters) and the fit of the data to find a well-balanced model (Beck and Yuen, 2004).

To examine the possible model classes further, the constraint that horizontal and vertical components be used together is removed. We test all 255 model classes created from the combinations of 8 parameters. The results for the best five model classes are shown in table 5.8. The sum of the posterior probability of the five model classes is 95% out of all 255 model classes.

Table 5.8: The best five model classes in the Bayesian model class selection when 255 combinations of the ground motion parameters are examined. The columns are in the same format as in table 5.7.

model	Hj	Zj	Ha	Za	Hv	Zv	Hd	Zd	d	Ock.	Like.	Evi.	P(%)
1	-	-	-	6.05	7.89	-	-	-	27.1	-15	-81	-96	80.8
2	1.91	-	-	4.41	8.31	-	-	-	31.9	-20	-79	-99	6.6
3	-	-	1.86	4.88	7.86	-	-	-	29.2	-20	-80	-100	2.9
4	-	1.59	-	4.31	8.02	-	-	-	29.7	-20	-80	-100	2.5
5	-	4.43	-	-	8.52	-	-	-	32.2	-16	-84	-100	1.9

Model class 1, which has the coefficients of the vertical acceleration and horizontal velocity, is the most probable model within the set of 255 model classes. The discriminant function for the most probable model in model class 1 is:

$$f(X_i|\theta) = 6.046 \log_{10} Za + 7.885 \log_{10} Hv - 27.091, \tag{5.24}$$

where

$$P(Y_i = 1|X_i, \theta) = \frac{1}{1 + e^{-f(X_i|\theta)}}, \tag{5.25}$$

is the probability that station i is near-source. This result indicates that the amplitude of high-frequency components is effective in classifying near-source and far-source stations. Note that the probability that the station is near-source is higher, if f is larger.

5.3.3 Effect of the choice of prior

In this section, we examine the choice of prior for the parameters in the model class selection. As we stated, for the Gaussian prior distribution, the effect of the number of parameters, N_j, is significant if the prior standard deviation, σ, is large (Lindley, 1957; Muto, 2006). We demonstrate this feature by performing model class selection with a Gaussian prior with different values of σ and a uniform prior with different widths of boundary b. The posterior probabilities of the model class selections are shown in table 5.9.

In the table, we can see the effect of the prior standard deviation in the Gaussian prior. As we increase σ, it tends to bias the posterior probability toward simpler models (i.e., models with fewer parameters). For example, the probability of model jav slightly decreases as σ increases. The small probability of model jv with Gaussian prior (σ=10) is caused by the narrow prior range. If σ is too small, it restrict the range of parameters as shown in table 5.10. Therefore, the choice of σ=100 is reasonably wide enough to find the most probable parameters, so we chose it in the Bayesian approach.

For the uniform prior, we are able to choose the small width of the boundary

Table 5.9: The posterior probability of the model class selection with different types of prior distribution for parameters. σ is the standard deviation for the Gaussian distribution and $|b|$ is the width of the boundary for the uniform distribution.

Model	Gaussian prior			Uniform prior	
	σ=10	σ=100	σ=1000	$\|b\|$ <20	$\|b\|$ <100
j	0.0	0.0	0.0	0.0	0.0
a	0.0	0.0	0.0	0.0	0.0
v	0.0	0.0	0.0	0.0	0.0
d	0.0	0.0	0.0	0.0	0.0
ja	0.0	0.0	0.0	0.0	0.0
jv	7.2	32.4	33.0	31.5	32.9
jd	0.0	0.0	0.0	0.0	0.0
av	78.9	62.1	61.7	59.0	61.6
ad	7.3	5.3	5.3	5.0	5.3
vd	0.0	0.0	0.0	0.0	0.0
jav	3.3	0.1	0.0	3.0	0.1
jad	0.1	0.0	0.0	0.0	0.0
jvd	0.1	0.0	0.0	0.3	0.0
avd	3.0	0.0	0.0	1.1	0.0
javd	0.1	0.0	0.0	0.0	0.0

Table 5.10: The estimated parameters from Bayesian approach with different types of prior distribution for parameters.

Prior	c_1 (Za)	c_2 (Hv)	d
Gaussian(σ=10)	5.522	7.147	24.686
Gaussian(σ=100)	6.046	7.885	27.091
Gaussian(σ=1000)	6.053	7.895	27.122
Uniform Cases	6.053	7.895	27.122

since the uniform prior does not affect the most probable parameter if the parameter is inside the boundary. We show the results of model class selection of uniform prior with $|b| < 20$ and $|b| < 100$ ($|b| < 10$ is not wide enough to find the most probable parameters). They are almost the same, but the probability of model jav decreases a little as $|b|$ increases.

We conclude that in this problem, the effect of the choice of prior is small. In other words, the likelihood in equation 5.23 is very peaked and the prior pdf does not significantly affect the probability of the model.

5.4 Results and discussion

We apply the optimal discriminant function from Bayesian approach (in equations 5.24 and 5.25) to all the stations in the dataset. Figure 5.10 shows the classification results. The distribution of stations with a high probability of being in the near-source is consistent with the fault geometry. As mentioned before, the fault models that are used here are those from the source inversion, and they are not necessarily the best indicator of near-source and far-source stations.

To examine the application for real-time analysis, the optimal discriminant function in equations 5.24 and 5.25 is applied to the Chi-Chi earthquake strong motion records. We generated snapshots of the probability that a station is near-source from 10 to 40 seconds after the beginning of rupture. Peak ground motions used for this classification analysis are computed from the observed data every 10 seconds for each station and evaluated in the discriminant function. The results are shown in figure 5.11. A darker mark at a station in figure 5.11 indicates that the station is more likely to be near-source, and a lighter mark indicates that the station is more likely to be far-source.

Ten seconds after the rupture initiation, the map shows that stations with high probability of being in the near-source are located near the epicenter, and it indicates that the rupture area is propagating concentrically. At 20 seconds, the probability of being in the near-source at thirteen stations is computed to be greater than 50%, but the concentric station distribution makes it difficult to identify any directivity of rupture propagation. The average slip velocity is 2 km/s (Ji et al., 2003), and the rupture front propagates 40 km from the hypocenter at this point. We can see the North – South character of the rupture direction clearly after 30 seconds of rupture. At 40 seconds, the distribution of stations with high near-source probability agrees with the fault surface projection, and stations at the near-source and far-source boundary have around 50% probability. Even though the fault geometries used for the wave inversion are not necessarily the actual extent of the fault, to a first-order approximation, the classification results are in good agreement with them.

5.5 Summary

We presented a methodology to classify seismic records into near-source or far-source records as a prelude to estimating fault dimension in an earthquake early warning system. Ground motion records from some past earthquakes are analyzed to find a linear function that best discriminates near-source and far-source records. Peak values of jerk, acceleration, velocity, and displacement are used in a traditional LDA and in a Bayesian approach to find the linear combination of peak values which provides the best performance to classify near-source and far-source records. All methods gave similar discriminant functions. We also analyzed which combination of ground motion features had the best performance for classification using Bayesian model class selection, and the best discriminant function is:

$$f(X_i|\theta) = 6.046 \log_{10} Za + 7.885 \log_{10} Hv - 27.091, \tag{5.26}$$

$$P(Y_i = 1|X_i, \theta) = \frac{1}{1 + e^{-f(X_i|\theta)}}, \tag{5.27}$$

where Za and Hv denote the peak values of the vertical acceleration and horizontal velocity, respectively, and $P(Y_i = 1|X_i, \theta)$ is the probability that a station is near-source. This function indicates that the amplitude of high-frequency components is effective in classifying near-source and far-source stations.

The probability that a station is near-source obtained using this optimal discriminant function for all the earthquakes shows the extent of the near-source area quite well, suggesting that the approach provides a good indicator of near-source and far-source stations for real-time analyses. Note that this function is constructed by the training dataset with magnitude greater than 6.0, so it only works for large earth-

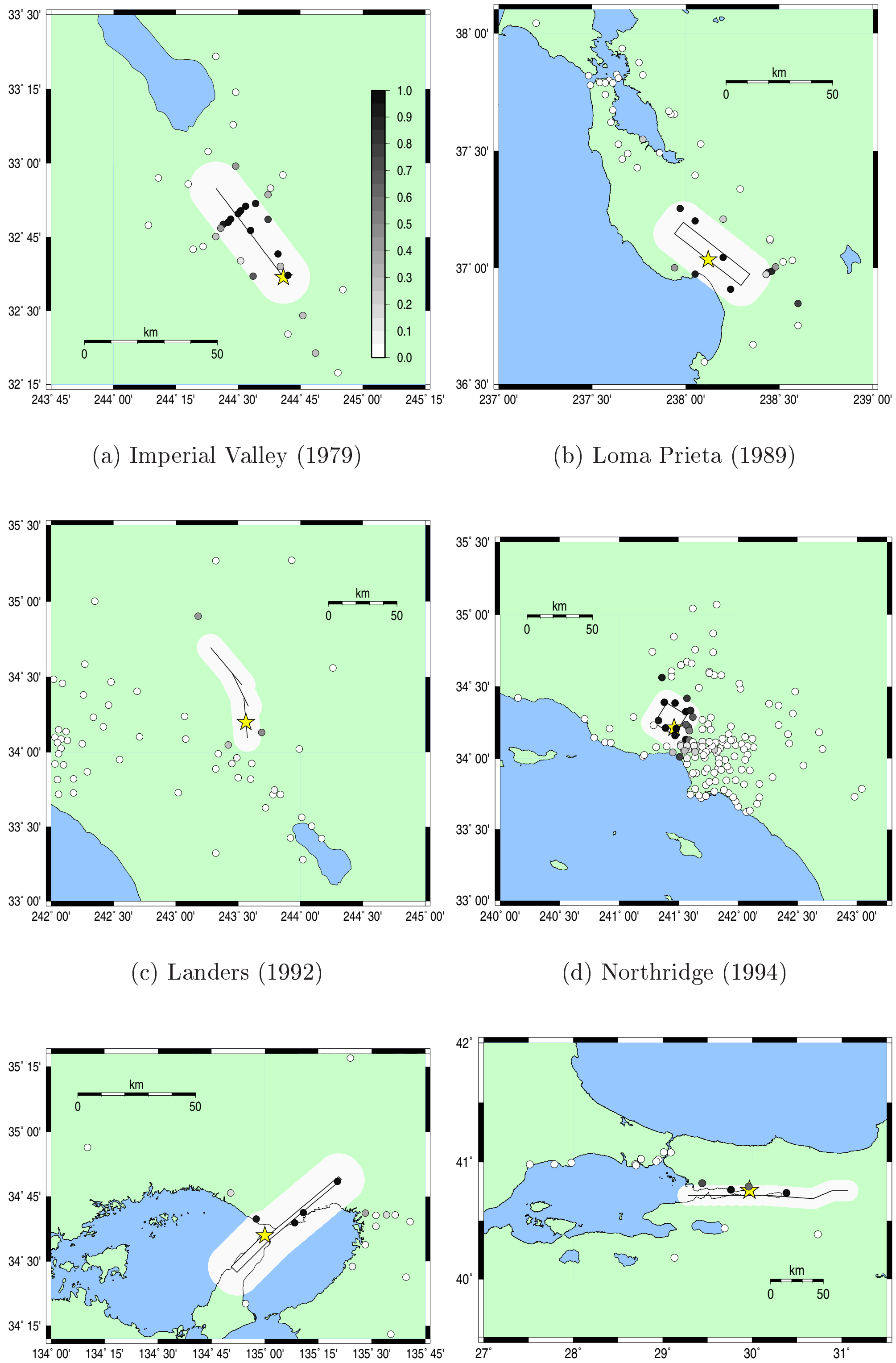

(a) Imperial Valley (1979)

(b) Loma Prieta (1989)

(c) Landers (1992)

(d) Northridge (1994)

(e) Hyogoken-Nanbu (1995)

(f) Izmit (1999)

Figure 5.10: Probabilities of near-source based on the optimal discriminant function obtained by the Bayesian approach. Darker marks have higher probability that the station is located at near-source. All stations in the figures use the same color code for scale. The symbols for the fault and epicenter are the same as in figure 5.2.

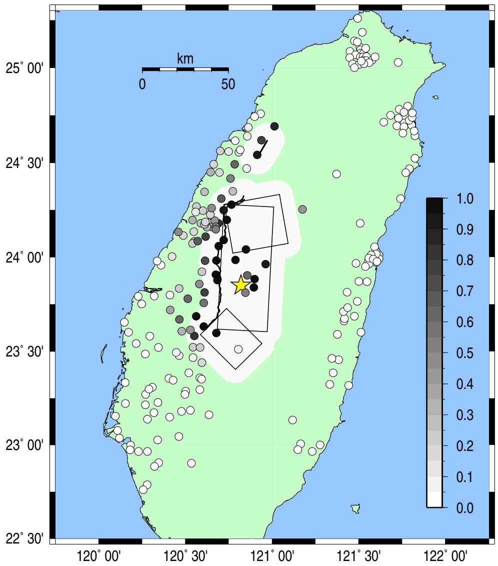

(g) Chi-Chi (1999)

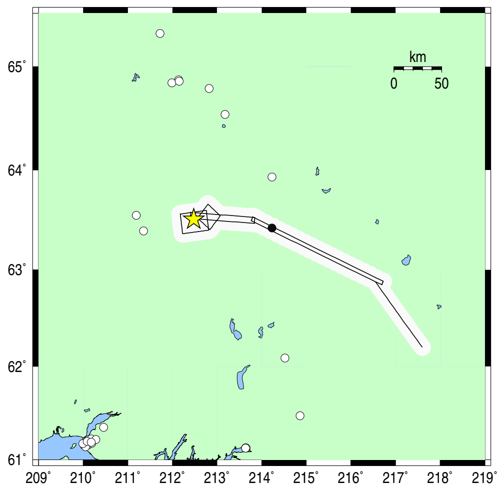

(h) Denali (2002)

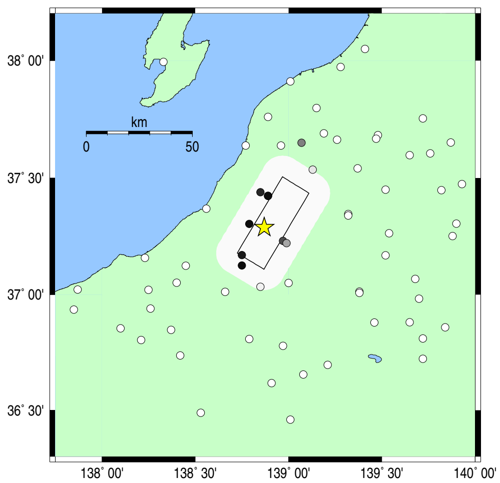

(i) Niigataken-Chietsu (2004)

Figure 5.10: Probabilities of near-source based on the optimal discriminant function obtained by the Bayesian approach (continued).

quakes.

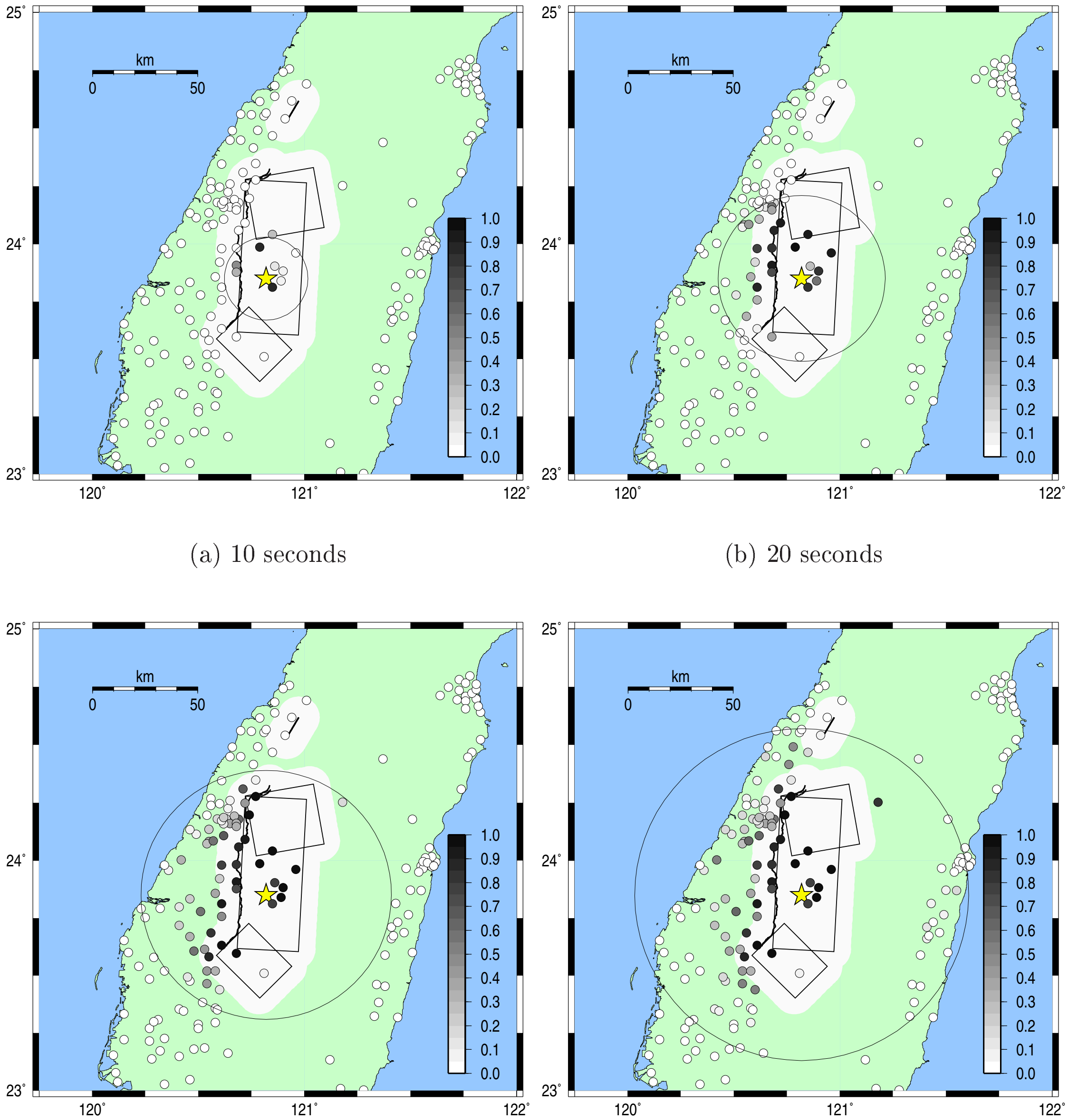

(a) 10 seconds

(b) 20 seconds

(c) 30 seconds

(d) 40 seconds

Figure 5.11: Snapshots of the probabilities of near-source for the Chi-Chi earthquake, based on the optimal discriminant function from the Bayesian approach. The large circle is the theoretical rupture front assuming the rupture velocity 2km/s.

Chapter 6

Estimating the Slip on the Fault from Low-Frequency Ground Motion

We developed a methodology to recognize the fault rupture geometry by incorporating the characteristics that high-frequency ground motions have stronger correlation with the fault rupture distance. However, it is difficult to predict the slip on the fault from high-frequency ground motions, since the near-source high-frequency ground motions saturate as a function of magnitude for large earthquakes. Therefore, we use low-frequency ground motions to determine the slip on the fault.

Low-frequency ground motion is important in a sense that it allows for the prediction of long-period seismic waves and the present value of slip on a rupture allows for a probabilistic prediction of additional rupture in the near future. Additionally, low-frequency ground motion increases exponentially as a function of magnitude, and is important to estimate seismic damage.

In this chapter, we propose a methodology to determine the slip on the fault that is compatible with both the observed low-frequency motions and also with the rupture geometry determined from high-frequency motions. We also create a methodology to predict the total length of the rupture propagation conditioned on the current slip size.

Currently, the displacement data is obtained from the double integration of strong motion records, and it is difficult to remove the linear trend from inertial seismometers in real-time analysis (Clinton, 2004). To determine the fault slip in real time, the future incorporation of real-time high-sample-rate GPS into early warning systems may be quite important.

Our method to recognize the slip on the fault in real time also works for tsunami warning because tsunami energy can be estimated by the slip on the fault. It is more effective for tsunami warning since the warning time is generally much larger than earthquake early warning.

6.1 Data

The strong motion data for Chi-Chi earthquake (September 20, 1999) are used for this analysis. This is the same dataset as the one in the near-source versus far-source classification analysis, and the data source is explained in section 5.1.1.

To obtain the real displacement data from strong motion records, we applied the following procedure. First, the DC offset of the accelerograms is corrected by subtracting the mean of the pre-event portion. The corrected accelerograms are integrated once to obtain the velocity records. Some velocity records have a linear trend due to either tilting, the response of the transducer to strong shaking, or problems in the analog-to-digital converter. Therefore, the baseline correction scheme explained in section 5.2.2 is applied to obtain appropriate velocity records. After time-domain integration of this corrected velocity, the approximated real displacements will be obtained. If the post-events displacement is not constant, the coefficients a_1 and a_2 in equation 5.1 are manually determined so that the post-events velocity is zero. In this way, approximated real displacement records are obtained.

This baseline correction scheme does not necessarily produce the real displacement records, since the scheme assumes the baseline shift of the acceleration occurs only once. Therefore, we compare the static displacement measured after the event with the GPS displacement data. The location of GPS stations are not the same as that of strong motion stations, but the displacement of the GPS station which is the nearest neighbor of the strong motion station is compared with the displacements

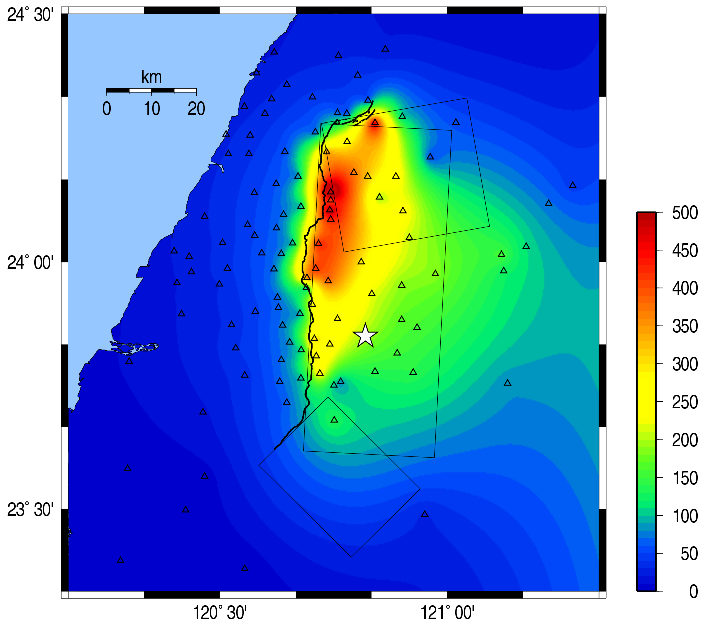

(a) Static displacements from GPS records. GPS stations are shown by open triangles.

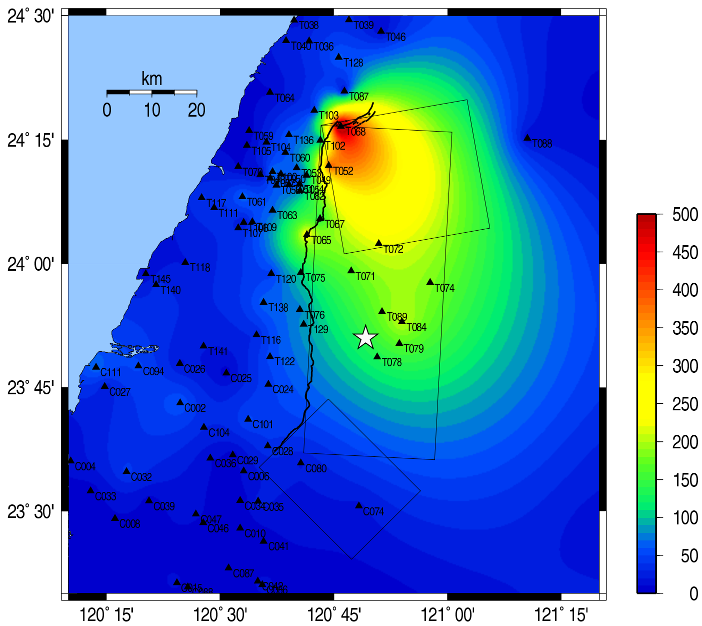

(b) Static displacements from strong motion records. Strong motion stations are shown by solid triangles.

Figure 6.1: Distribution of the static displacements for the Chi-Chi earthquake (EW component). The star symbol denotes the epicenter of the earthquake. The rectangular boxes display the map projection of the fault geometry proposed by Ji et al. (2003). The distribution of static displacements computed from strong motion records agrees well with the one from GPS displacements.

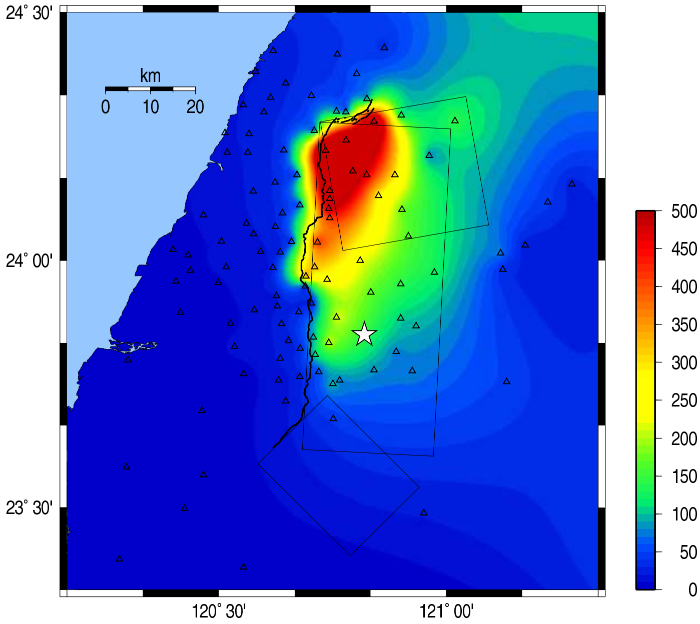

(a) Static displacements from GPS records.

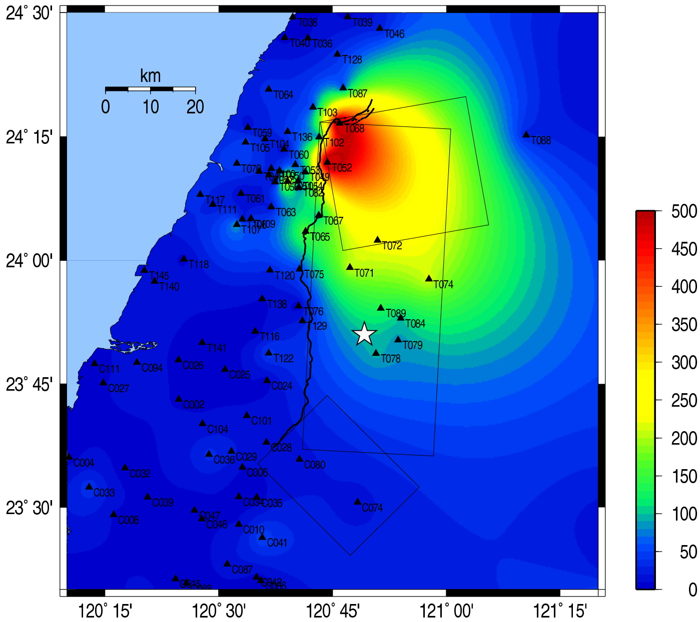

(b) Static displacements from strong motion records.

Figure 6.2: Distribution of the static displacements for the Chi-Chi earthquake (NS component). The symbols are in the same format as in figure 6.1.

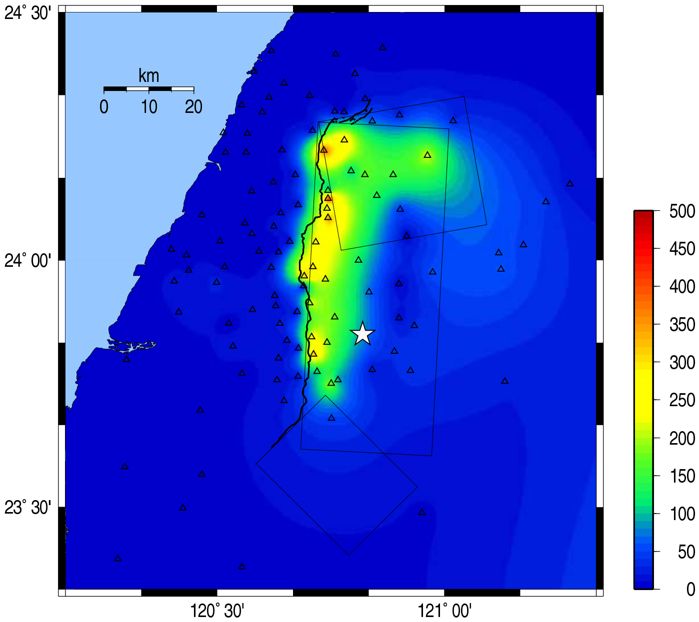

(a) Static displacements from GPS records.

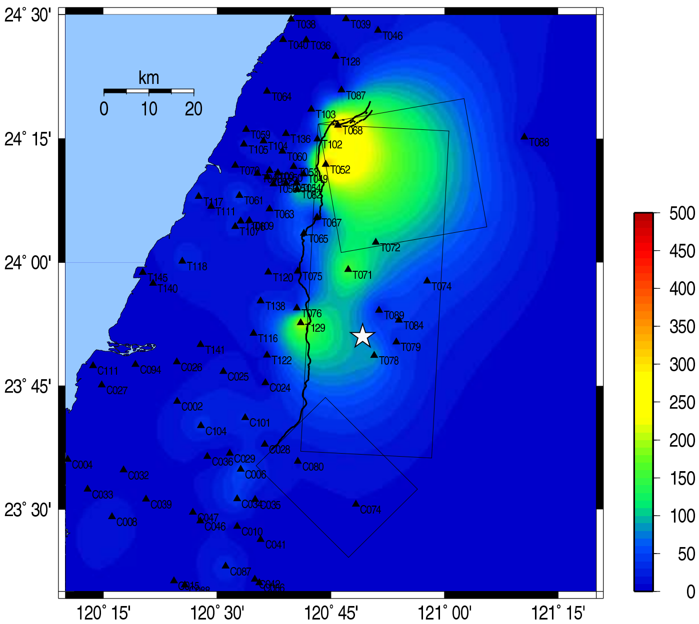

(b) Static displacements from strong motion records.

Figure 6.3: Distribution of the static displacements for the Chi-Chi earthquake (UD component). The symbols are in the same format as in figure 6.1.

obtained from double integration of strong motion records. Figures 6.1 – 6.3 show the comparison between the GPS displacement and static displacement computed from the strong motion records by applying the baseline correction scheme. The map for GPS displacement shows higher values on the hanging wall since there are more GPS stations than strong motion stations on the hanging wall. However, overall, the static displacement distribution computed from strong motion records agrees well with the GPS displacement and this suggests that our baseline correction scheme is reasonable.

6.2 Estimating the slip on the fault from low-frequency ground motion

6.2.1 Constructing a slip function as a function of fault distance

Aagaard et al. (2004) simulated near-source ground motions for five fault geometries with different combinations of fault dip and rake angles. Four of the simulated near-source peak ground displacements as a function of distance from the fault for scenarios with the shallow hypocenter are shown in figure 6.4. The average slip and fault area for scenarios across the different fault dip angles are constant. In figure 6.4, the value of maximum ground displacement normalized by the unit average slip is shown on the vertical axis. The peak ground displacement per unit slip is not significantly different for different fault scenarios, except the displacement for the strike-slip fault scenario (dip angle = 90°) is symmetric along the fault line and the displacement for the thrust fault scenario (dip angle = 45°, 60°, and 75°) is asymmetric and records larger amplitude on the hanging wall.

We fit an analytical function to this simulated ground displacement (x) as a function of fault distance (r). Using a bell-shape function $x(r) = x(0)/\sqrt{1 + (\alpha|r|)^{\beta}}$, we find α and β by minimizing the least-square errors between the simulated near-field

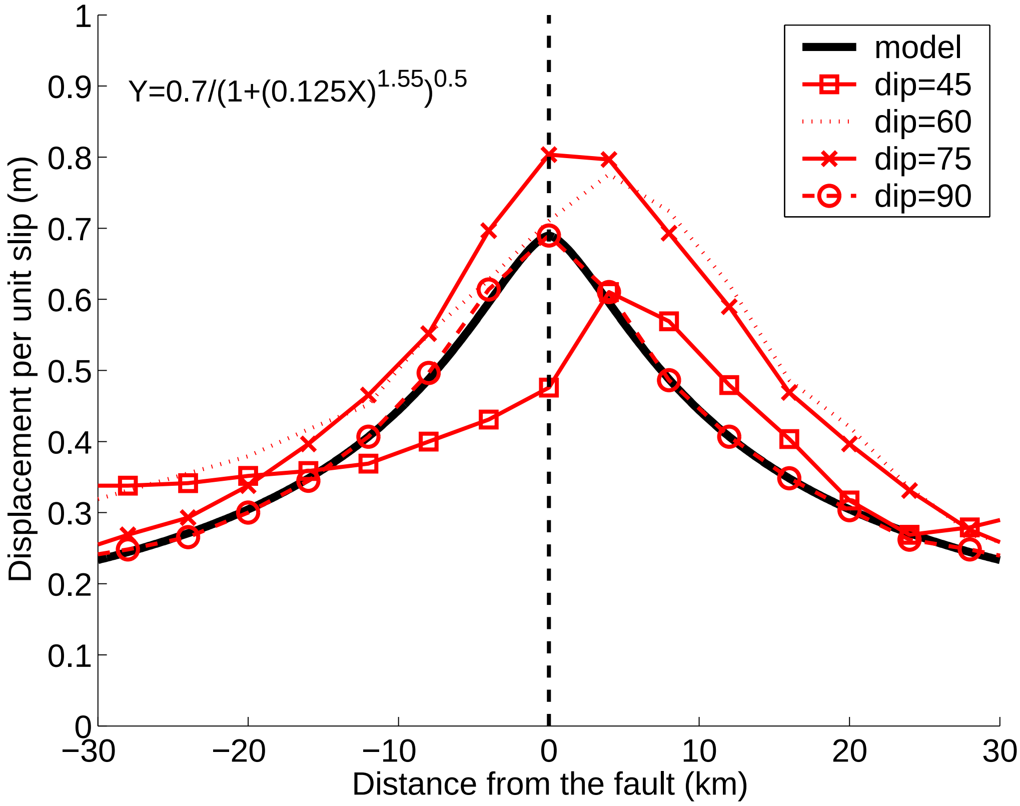

Figure 6.4: A displacement per unit slip as a function of fault distance obtained from ground motion simulations (Aagaard et al., 2004). An approximated curve for the strike-slip fault scenario (dip angle = 90°) is added in the thick line.

ground displacements and the bell-shape function. Assuming the ground displacement is proportional to the slip on the fault, the analytical function which approximates the simulated ground displacement is:

$$x(r) = \frac{0.7}{\sqrt{1 + (0.125|r|)^{1.55}}} \times slip. \tag{6.1}$$

For the proposed real-time analysis method, we back project the recorded displacement data onto the fault line to estimate the size of the slip on the fault. In the current state-of-the-art seismic network, the seismometer directly measuring the ground displacement, such as high-sampling GPS, is not as common as strong motion seismometer. We obtain the ground displacement by the double integration of the strong motion records or the single integration of the records of the broadband seismometer.

The location of the epicenter and the direction of the fault rupture are assumed to be estimated from the previous technique to recognize a rupture geometry (chapters 4 and 5). We define the fault line as a straight line on the epicenter oriented in the direction of the fault rupture, and the fault distance as the distance between the station and the fault line (see figure 6.5 as an example of calculating the fault distance). From equation 6.1, the slip on the fault line when the displacement (x) is recorded at the fault distance (r) is estimated by the following equation:

$$slip = \frac{x(r)}{0.7/\sqrt{1 + (0.125|r|)^{1.55}}}. \tag{6.2}$$

6.2.2 Estimating the slip on the fault and predicting the additional rupture extent

We estimated the slip on the fault of the Chi-Chi earthquake from the strong motion records and compared with the slip distribution computed it from the seismic waveform inversion (Ji et al., 2003). Figure 6.6 shows the slip distribution of the Chi-Chi earthquake (1999) obtained from the seismic waveform inversion (Ji et al., 2003).

The solid line in figure 6.7 shows the cross section of the slip distribution along AB which is identical to the fault line in figure 6.5. Figure 6.7 also shows the back projection of the observed ground displacement data onto the fault line after 10, 20, and 30 seconds after the origin time. Only the records of the stations where the rupture front arrived are shown in the figure. From the figure, we can see the back projection of the displacement records agrees with the slip distribution obtained from the waveform inversion to a first-order approximation. There is a large discrepancy at the north end of the fault line (40 km north from the epicenter). It shows that the most of the displacement records underestimate the slip on the fault and one station which significantly overestimate the slip on the fault. This is because there are many stations on the foot wall and few stations on the hanging wall of the fault for the Chi-

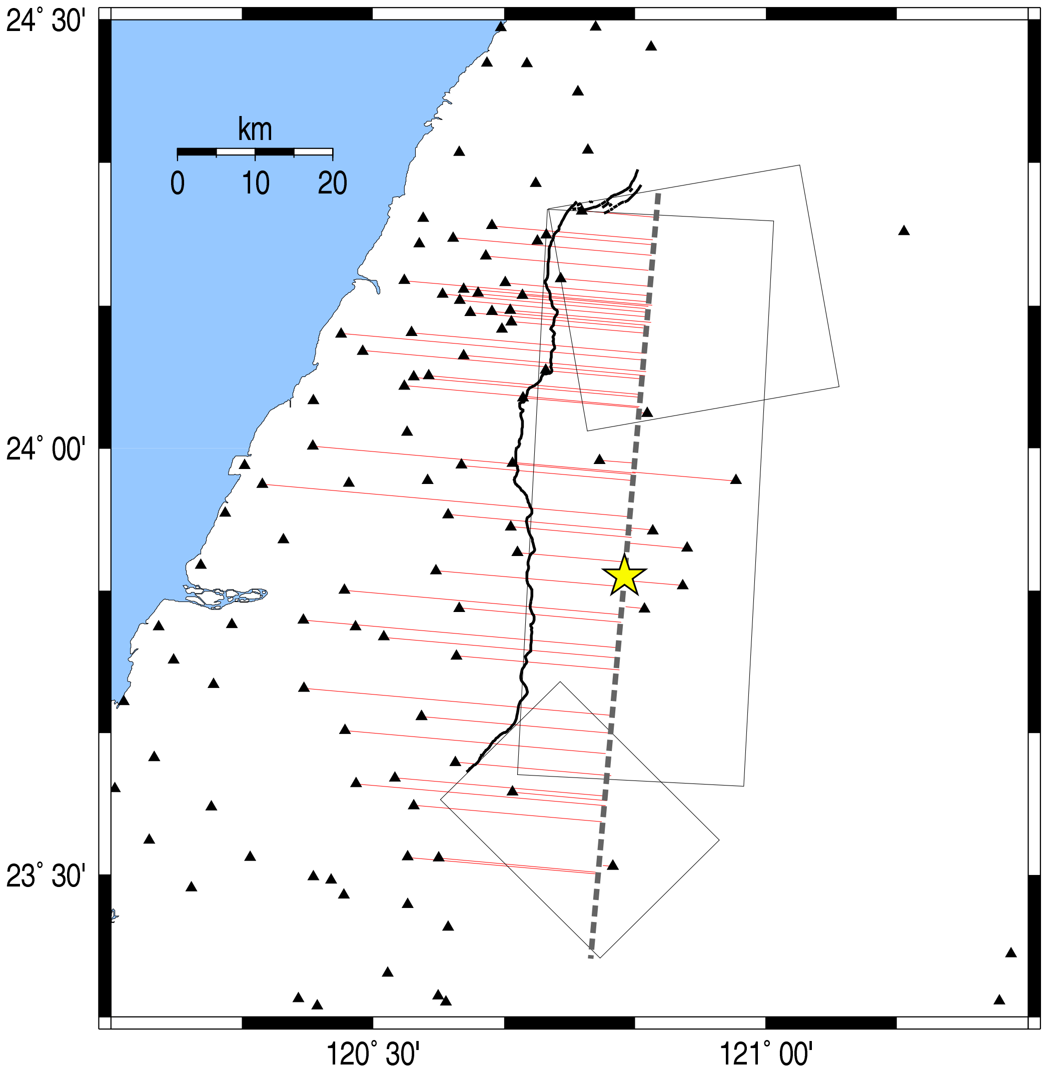

Figure 6.5: A slip on the fault can be obtained by backprojecting the displacement from the strong motion data onto the fault line shown as a thick broken line.

Chi earthquake. Additionally, we use the slip function which fits to the near-source ground motion simulation for strike-slip fault, while the Chi-Chi earthquake source is thrust fault and the slip on the fault is significantly asymmetric along the fault line.

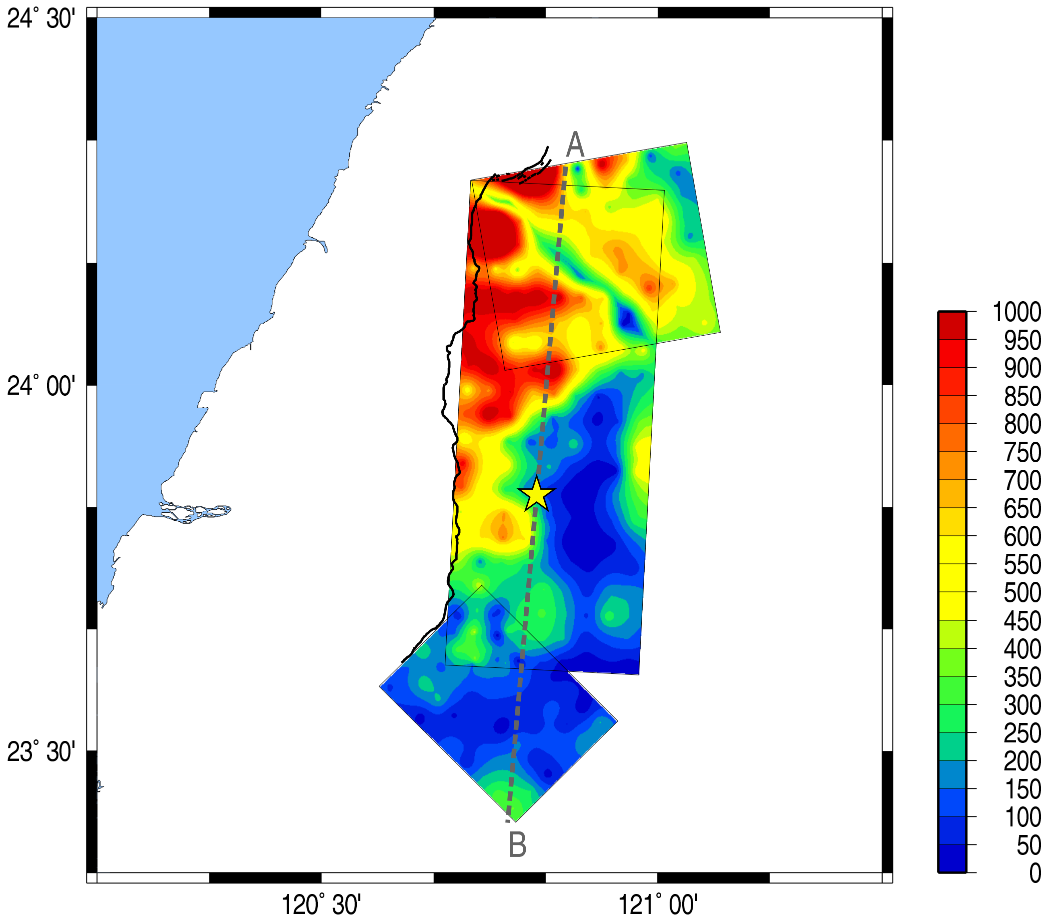

Figure 6.6: Slip distribution for the Chi-Chi earthquake proposed by Ji et al. (2003). The model consists three rectangular planes crossing in three dimension. The cross section along the fault line AB is shown in figure 6.7

6.3 Predicting the probability of the additional rupture extent

Given the current slip on the fault, what is the probability that the rupture length exceeds a certain number? To answer this question, we create a methodology to predict the total length of the rupture propagation conditioned on the current slip size. Liu-Zeng et al. (2005) constructed a methodology to generate simple 1-D models of spatially heterogeneous slip. By using this methodology, we compute the probability of the rupture length (L) conditioned on the current slip on the fault (D) in a statistic way.

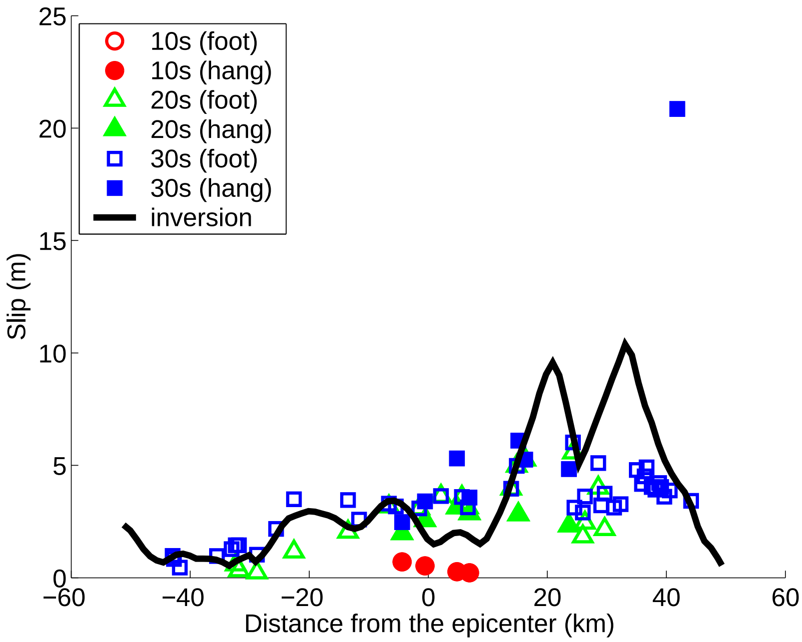

Figure 6.7: Cross section of the slip distribution in figure 6.6. The estimated slip from real-time displacement data are also shown. "Foot" and "hang" indicate stations on the footwall and hanging wall, respectively. The records from the stations on the hanging wall show higher value than that of footwall stations.

6.3.1 Generating 1-D slip models

In this section, we briefly discuss the basic procedures of the technique developed by Liu-Zeng et al. (2005).

Let $w(x)$ be white noise with mean zero and standard deviation one, and then $W(t)$ be a Fourier transform of $w(x)$.

$$W(k) = \mathcal{F}\{w(x)\} \tag{6.3}$$

Applying a low-pass filter $F(k)$ to $W(k)$,

$$Y(k) = W(k)F(k), \tag{6.4}$$

where $F(k) = k^{-\alpha}$, α=1.25 – 1.5 (Liu-Zeng et al., 2005). If α=1, applying the low-pass filter is equivalent to a single integration. If α=2, it is equivalent to a double

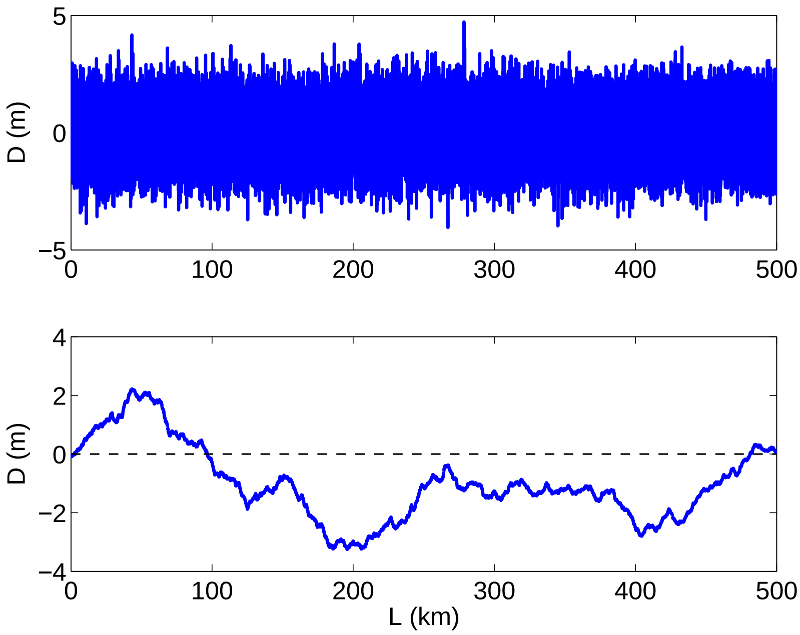

Figure 6.8: An example of the 1-D slip models. Top: an original white noise. Bottom: a parent series generated by the low-pass filtering of the white noise.

integration. Taking a inverse transform of $Y(k)$, a low-pass filtered white noise is obtained.

$$y(x) = \mathcal{F}^{-1}\{Y(k)\} \tag{6.5}$$

Figure 6.8 shows an example of the white noise $w(x)$ and low-pass filtered white noise $y(x)$. We call this generated series $y(x)$ the "parent series." We define the end of an individual rupture when the parent series crosses the zero line, and then take the absolute value of the individual series. In this way, each parent series is split into a set of earthquake slip models of varying length with approximately the same smoothness α. Taking a modulus of the parent series, the slip D as a function of position x is:

$$D(x) = D_0|y(x)|, \tag{6.6}$$

where D_0 is constant defined from the observation. The distance between adjacent

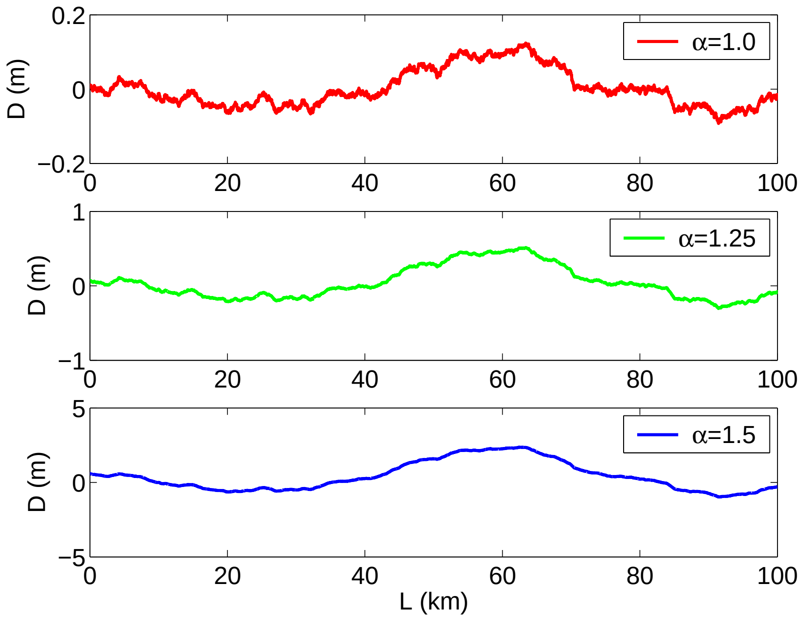

Figure 6.9: The effect of the low-pass filter with different order α on the slip models. Larger α can generate smoother series.

data points Δx is assumed to be $\Delta x = 10$ m.

6.3.2 Characteristics of the 1-D slip models

The order of the low-pass filter (α) can control the smoothness or roughness of the slip models. By definition of low-pass filter, α is the slope of its Fourier spectral amplitude with wave number. Therefore, as α increases, the applied filter removes more high-frequency components. Figure 6.9 shows generated parent series with three different orders of the low-pass filter. Applying the low-pass filter with smaller α, the generated series consists of much higher frequency component. If α of the low-pass filter is large, the generated series becomes smoother. The value of α controls not only the roughness of the slip model. A model with a rougher slip distribution (smaller α) has higher chance to cross the zero line. Therefore, models with smaller α will generate more short events.

Figure 6.10 shows the relationship of the average slip ($\bar{D}$) and the rupture length (L) of each model for three different α. The regression curves and regression equations

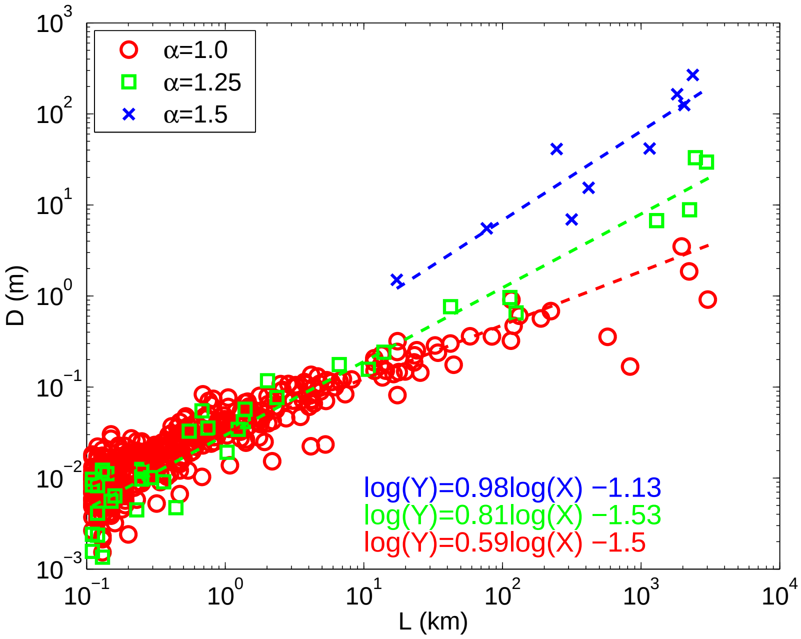

Figure 6.10: Plot for the average slip ($\bar{D}$) and rupture length (L) for the slip models with different α. Regression lines for each α are added in the figure. The parameter α controls the slope of the regression lines.

for each case are also added in the figure. The slope of the regression curves varies with different α, and the slip model with smaller α shows the steepest slope. This means the rougher slip distributions (smaller α) produce longer ruptures for a given average slip. That is because for a given slip, a rupture is more likely to terminate in a short distance.

The parameter α is determined so that the regression curve for $\bar{D}$ and L agrees with the observation. Figure 6.11 shows the $\bar{D}$ and L relationship of real earthquakes in a log-log plot. The strike-slip events from the dataset by Wells and Coppersmith (1994) and Liu-Zeng et al. (2005) are used in this figure. The trend of the regression line for non-interplate events and interplate events are similar, so the regression line for total dataset ($\log_{10}\bar{D} = 0.85\log_{10}L - 1.43$) is added in the figure. The slope of the regression curve for $\bar{D}$ and L scales with α (see figure 6.12), so the value of α which corresponds to the observed slope for $\log_{10}\bar{D}/\log_{10}L$ =0.85 is 1.33. The intersection of the regression line for $\bar{D}$ and L depends on α and the constant D_0 in equation 6.6,

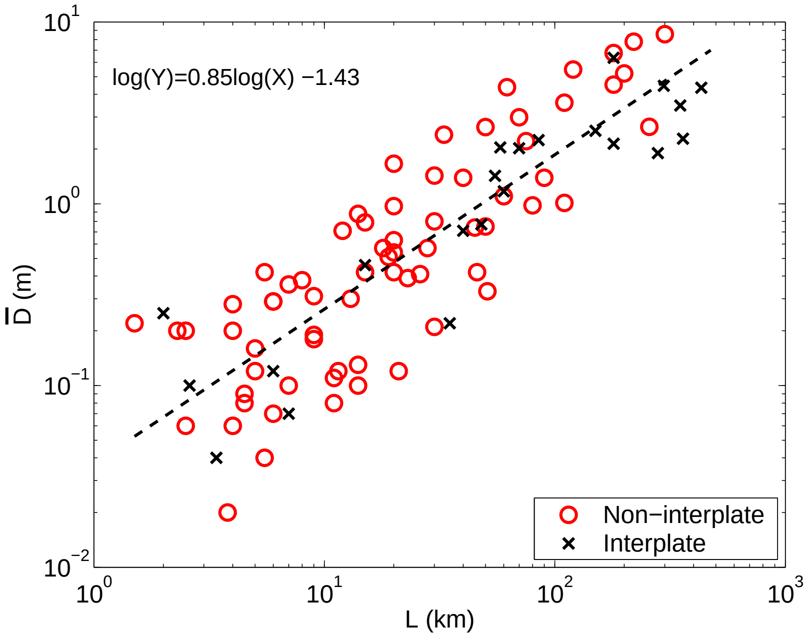

Figure 6.11: Plot for the average slip ($\bar{D}$) and rupture length (L) for the observed earthquake data in Wells and Coppersmith (1994) and Liu-Zeng et al. (2005).

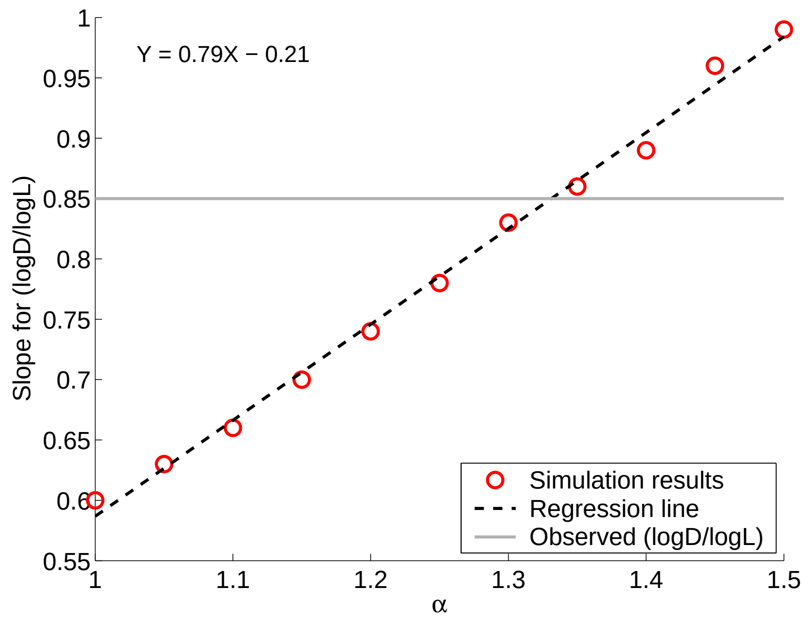

Figure 6.12: Plot for the slope of $\log \bar{D} / \log L$ and α. The value of α that corresponds to the observed slope (0.85) is 1.33.

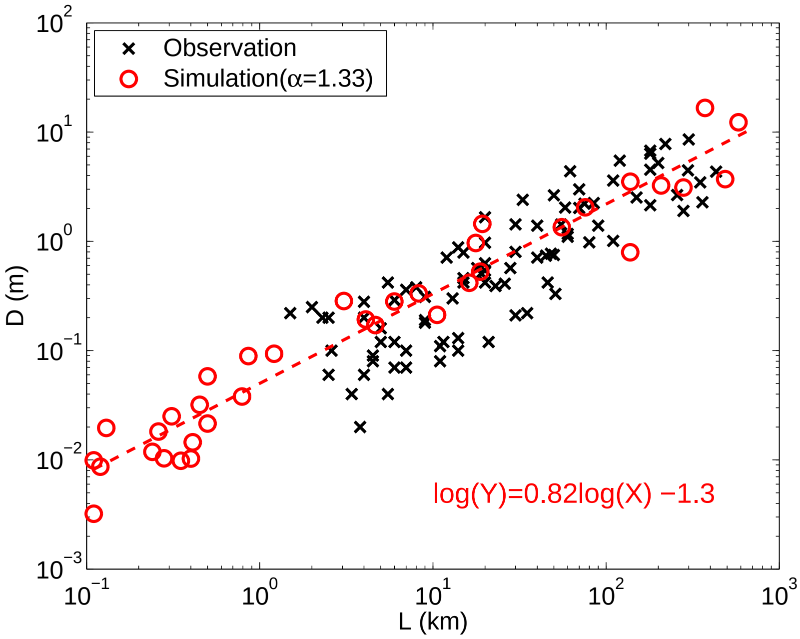

Figure 6.13: Plot for the average slip ($\bar{D}$) and rupture length (L) for the observed data and simulation results from the slip model with $\alpha = 1.33$.

and the value of D_0 which agrees with the observation is 0.02. Figure 6.13 shows $\bar{D}$ and L generated by the model with α=1.33 and D_0=0.02. The samples generated from models with these parameters agree with the real observations very well.

Figure 6.14 shows the comparison of the models with different numbers of the parent series (n). Even though the models with smaller n generate more short events, the slope of $\bar{D}$ and L does not change so much in the range of $n = 2^{18}, 2^{19}$ and 2^{20}. We conclude that the number of the parent series is not important to control the roughness of the models.

6.3.3 Statistical distribution of the additional rupture length

Using the Liu's method to generate 1-D slip models (Section 6.3.1), the statistical distribution of the rupture length conditioned on current slip on the fault is examined. First, we generated 1000 parent series with length 2^{20}, and 5254 models are obtained from the series. For each model, when the slip exceeds a certain value, the length between the current location and the location where the rupture terminates

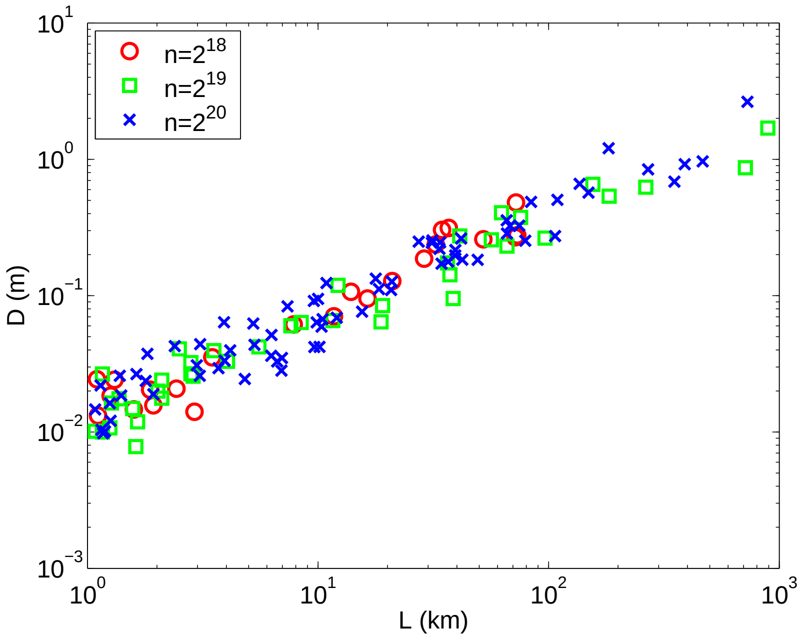

Figure 6.14: Plot for the average slip ($\bar{D}$) and rupture length (L) for the slip models with different parent series size n. The slope of $\bar{D}$ and L does not change so much in the range of $n = 2^{18}, 2^{19}$, and 2^{20}.

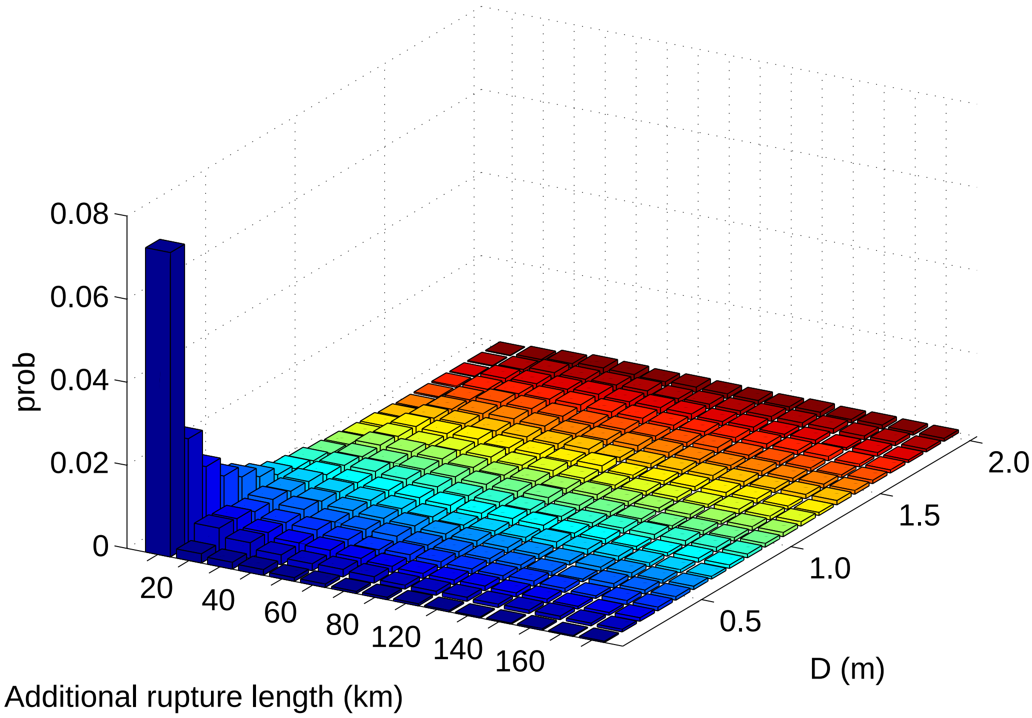

Figure 6.15: 3-D histogram of the additional rupture length (L_a) as a function of current slip (D).

is computed. We call this length the additional rupture length L_a, as opposed to the total rupture length of each model L. The statistical distribution of additional rupture length for different current slip sizes is shown in figure 6.15.

Figure 6.15 shows a histogram of additional rupture length conditioned on current slip on the fault. Here, the bin size of the histogram is 10 km. The figure shows that the rupture with small current slip has high probability that the additional rupture length is small and more likely to terminate in the near future. The 2-D plot of figure 6.15 is shown in figure 6.16 for later comparison.

Next, we try to describe the probability density for these samples by an analytical function. Using a Gaussian function as a kernel function (Silverman, 1986), the probability density can be estimated as a summation of Gaussian distributions. Given the samples $C = [c_1,\ c_2, \ldots,\ c_n]$, the probability density of the samples can be estimated by:

$$p(x) = \frac{1}{\sigma\sqrt{2\pi}}\frac{1}{n}\sum_{i=1}^{n}\exp\left(-\frac{(x-c_i)^2}{2\sigma^2}\right), \tag{6.7}$$

where n is the number of the samples and σ is a standard deviation of the kernel function. The σ controls the smoothness of the estimated density and we found the kernel function with constant $\sigma = 10$ estimates reasonably smooth distribution to approximate the original histogram. The estimated probability density is shown in figure 6.17, which is a very good approximation of the histogram in figure 6.16 .

The probability density estimated from the Gaussian kernel function is very accurate, but expensive to compute, since the function (equation 6.7) includes n exponential terms. Therefore, we try to approximate the probability density by using a single lognormal distribution.

Lognormal distribution is a probability distribution of any random variable whose logarithm is Normally distributed. The lognormal distribution has the probability density function (pdf):

$$p(x) = \frac{1}{x\sigma\sqrt{2\pi}} e^{-(\ln x - \mu)^2/2\sigma^2}. \tag{6.8}$$

The distribution is defined by two parameters: mean μ and standard deviation σ of the variable's logarithm. These two parameters are computed by fitting mode of the distribution (the value of the term that occurs the most often) and the probability density at the mode (peak value of the probability density). The mode of the log-normal distribution is $e^{\mu-\sigma^2}$ and the probability density at the mode is $\frac{1}{\sigma\sqrt{2\pi}} e^{-\mu+\sigma^2/2}$. The computed μ and σ for each slip size D are shown in figure 6.18. Since the relationship between μ and D seems logarithmic, a logarithmic trendline is added in the figure. The regression function is $\mu(D) = 1.16\ln(D) + 4.94$. On the other hand, the parameter σ does not show any dependence with D. Therefore, we select a constant $\sigma = 1.6$.

The lognormal distribution with parameters which are best fit to the probability density is shown in figure 6.19, which is a good approximation of the probability density shown in figure 6.17. The lognormal distribution with parameters $\mu(D) = 1.16\ln(D) + 4.94$ and $\sigma = 1.6$ is also shown in figure 6.20. The difference between figures 6.19 and 6.20 are very minor, so the equations to compute the μ and σ are reasonable and valid for the general case.

Figures 6.21 - 6.24 are enlarged graphs of figures 6.16 - 6.20. In those figures, we can see the slope of the approximated lognormal distribution around origin is much higher than that of kernel probability density. They also decay slower than that of probability density after the peak. However, it is important to express this kernel probability density with simpler expression for convenience, and the approximated lognormal distribution is close enough to express the kernel probability density.

From the probability density of the additional rupture length, we also compute the probability that the current rupture propagates more beyond a threshold value L_{thre} conditioned on the current slip size D. The probabilities for different L_{thre} are shown in figure 6.25. The figure shows for larger D, there is higher probability that the additional rupture length exceeds L_{thre}. Besides, the probability increases significantly for the D greater than 0.2 m. Therefore, if the slip size is less than 0.2 m at the beginning of the rupture, it is difficult to tell how far the rupture can propagate. Once the slip exceeds 0.4 m, there is higher probability that the rupture extends to a large event.

In summary, the probability density obtained from the simulations with 1-D slip models is expressed by:

$$p(x) = \frac{1}{\sigma\sqrt{2\pi}} \frac{1}{n} \sum_{i=1}^{n} \exp\left(-\frac{(x-c_i)^2}{2\sigma^2}\right), \tag{6.9}$$

where

$$\begin{aligned} n =& \text{number of the samples}, \\ c_i, i = 1, \ldots, n =& \text{samples}, \\ \sigma =& \text{a standard deviation of kernel function } (= 10). \end{aligned}$$

And the probability density function for the approximated lognormal distribution is:

$$p(x) = \frac{1}{x\sigma\sqrt{2\pi}} e^{-(\ln x - \mu)^2/2\sigma^2}, \tag{6.10}$$

where $\mu(D) = 1.16\ln(D) + 4.94$ and $\sigma = 1.6$.

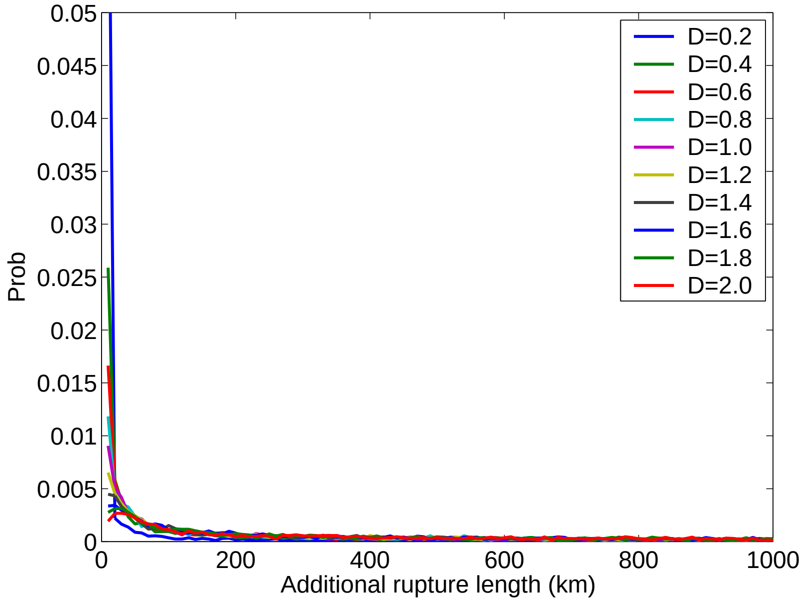

Figure 6.16: Histogram of the additional rupture length (L_a) as a function of current slip (D). The bin size of the histogram is 10 km.

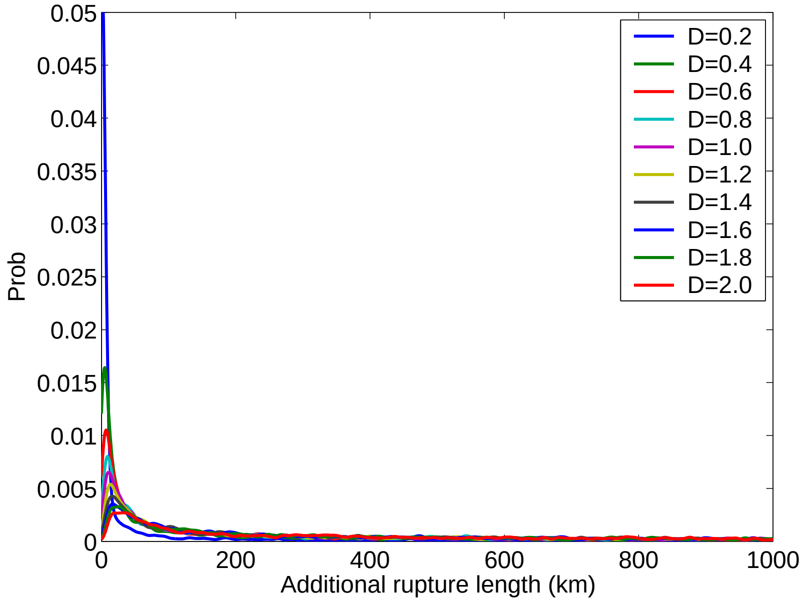

Figure 6.17: Probability density of the additional rupture length (L_a) as a function of current slip (D) by the kernel smoothing method.

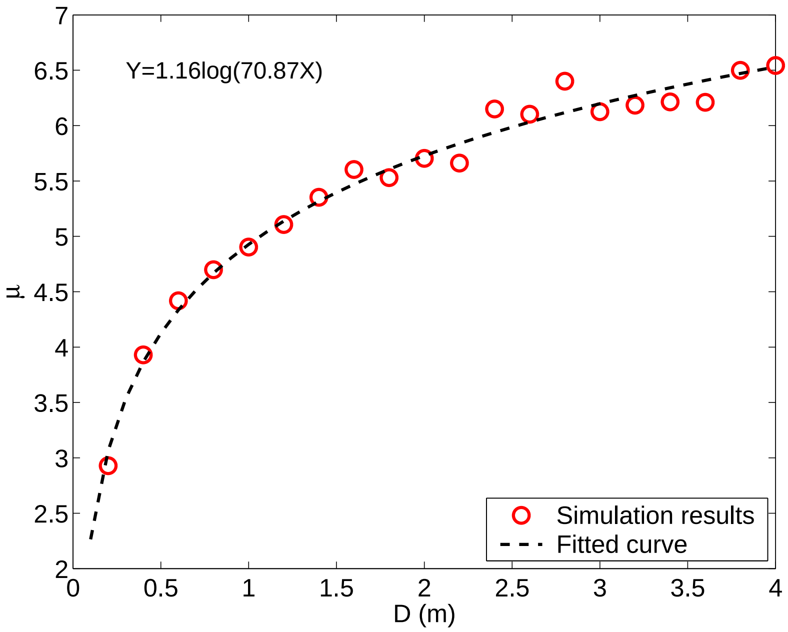

(a) Mean of lognormal distribution μ.

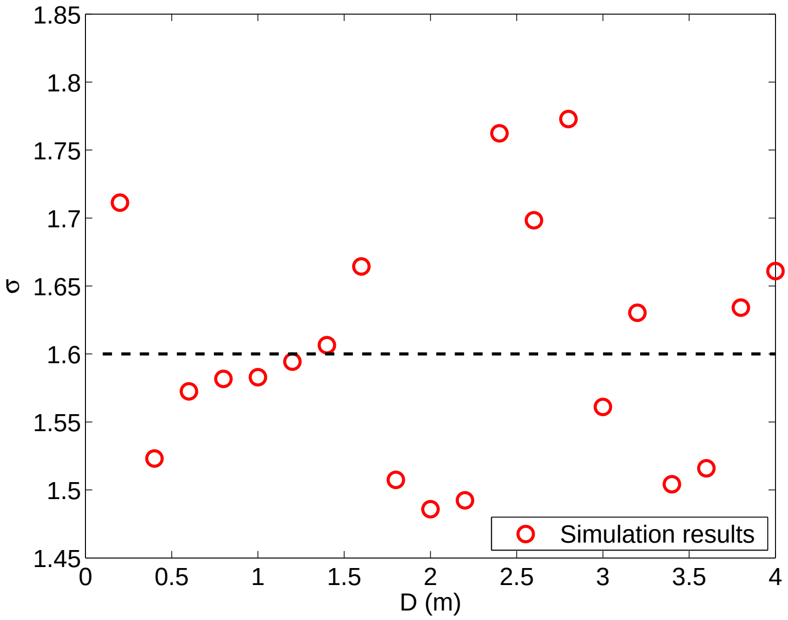

(b) Standard deviation of lognormal distribution σ.

Figure 6.18: The parameters μ and σ for the lognormal distribution which is an approximation of the probability density of the additional rupture length (L_a).

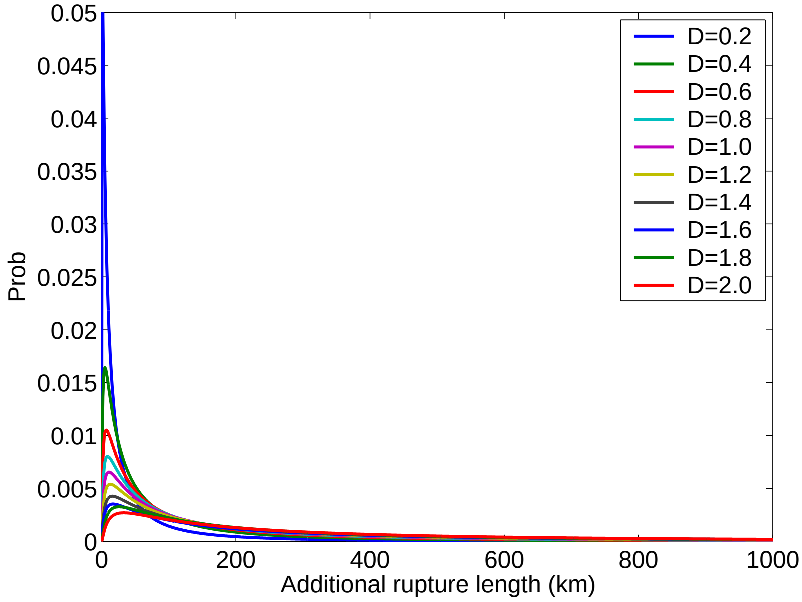

Figure 6.19: Probability density of lognormal distribution which is the approximation of the additional rupture length (L_a).

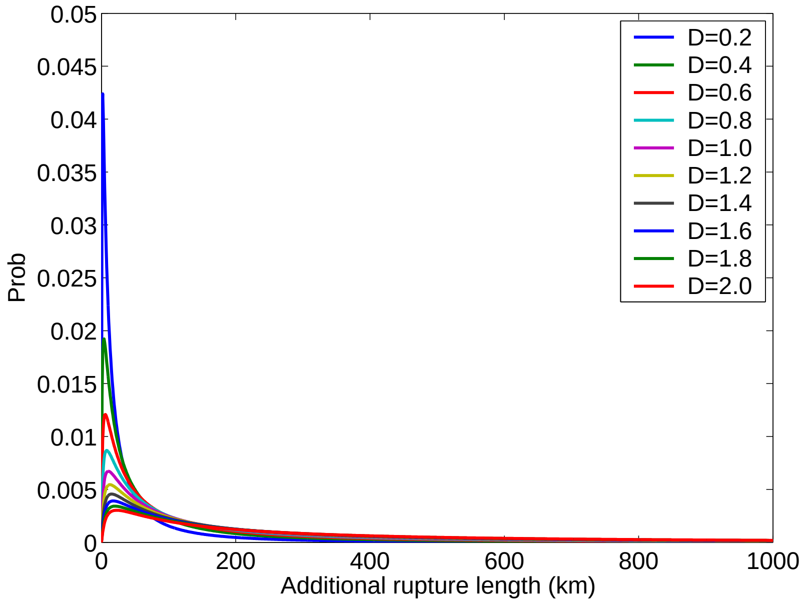

Figure 6.20: Probability density of lognormal distribution with mean from the formula $\mu(D) = 1.16 \ln(D) + 4.94$ and constant σ.

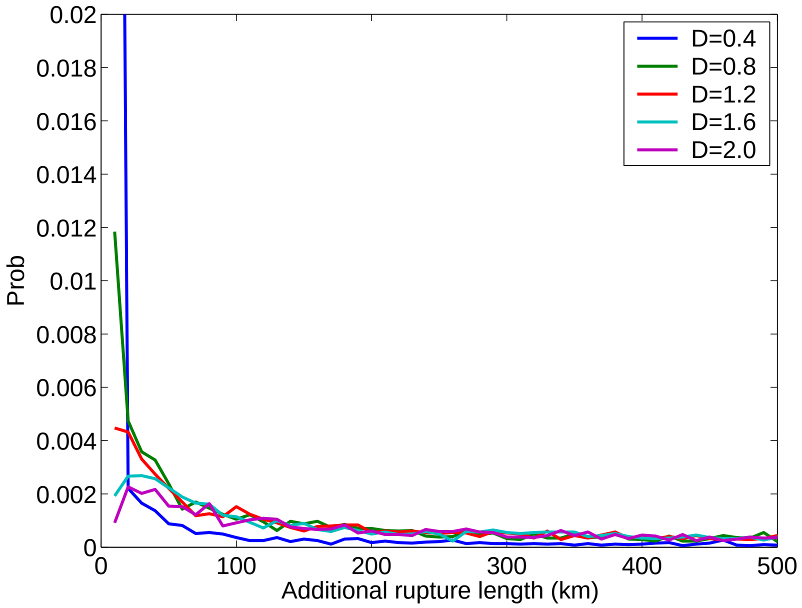

Figure 6.21: Histogram of the additional rupture length (L_a) as a function of current slip (D). The bin size of the histogram is 10 km.

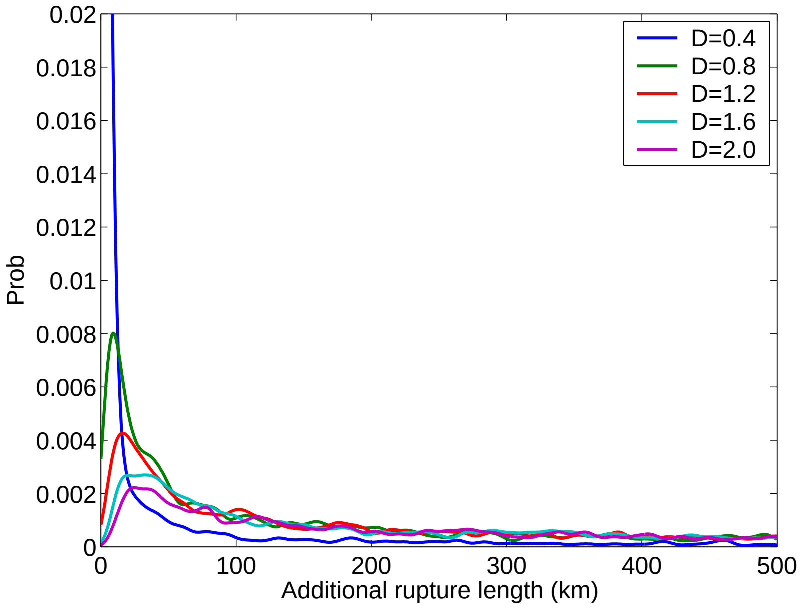

Figure 6.22: Probability density of the additional rupture length (L_a) as a function of current slip (D) by the kernel smoothing method.

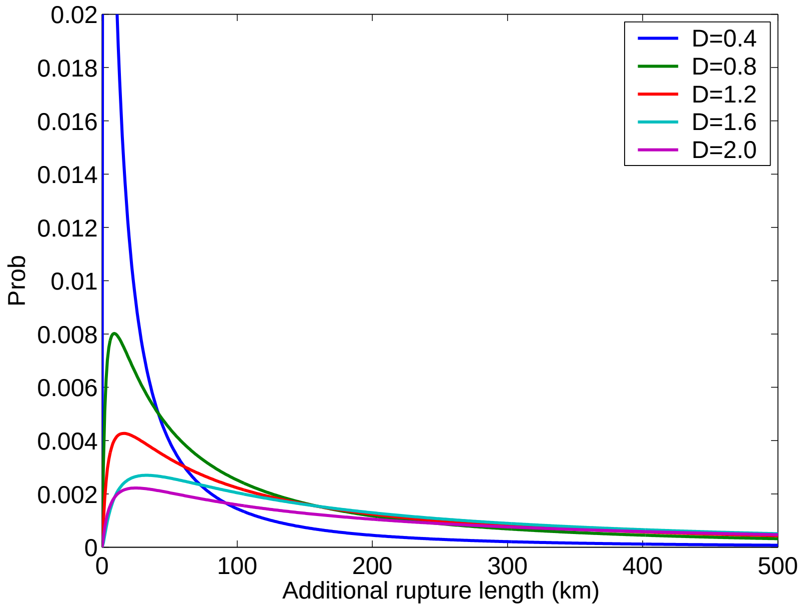

Figure 6.23: Probability density of lognormal distribution which is the approximation of the additional rupture length (L_a).

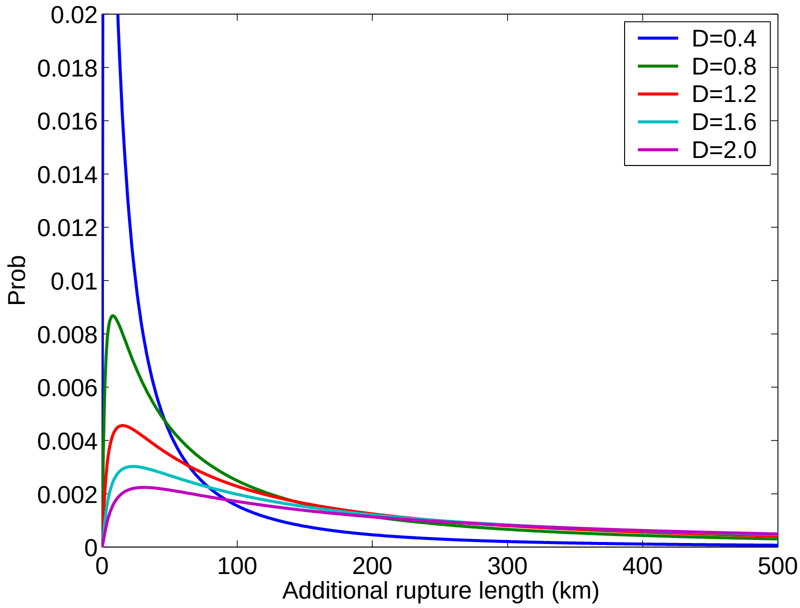

Figure 6.24: Probability density of lognormal distribution with mean from the formula $\mu(D) = 1.16\ln(D) + 4.94$ and constant σ.

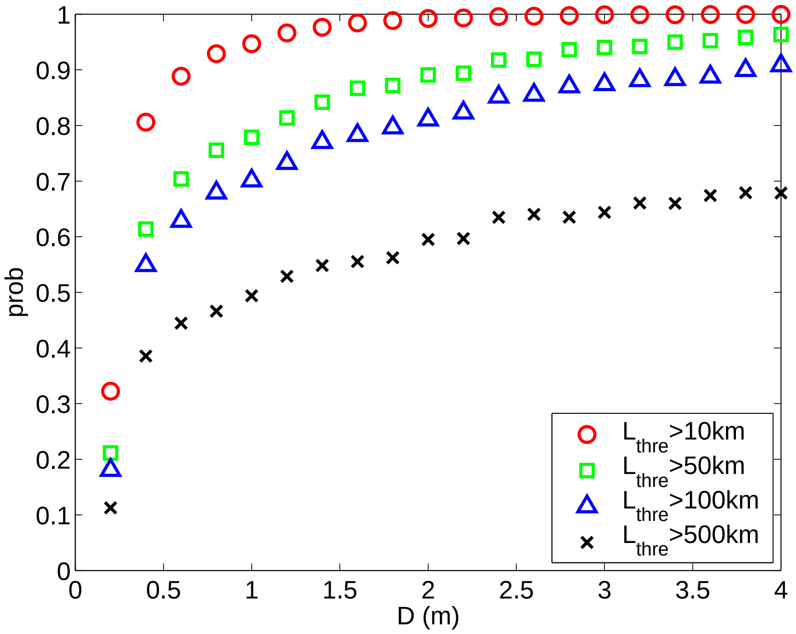

Figure 6.25: The probability that the additional rupture length exceeds a certain value conditioned on the current slip size D.

6.4 Summary

In this chapter, we propose a methodology to determine the slip on the fault that and predict the total length of the rupture propagation conditioned on the current slip.

In order to characterize a slip on the fault in real time, we construct an analytical function to estimate slip on the fault from observations of displacement away from the fault by using the result of a ground motion simulation (Aagaard et al., 2004). In real-time analysis, we back project the recorded displacement data onto the fault line scaled by the analytical function to estimate the size of the slip on the fault. The fault slip makes it possible to predict long-period seismic waves, which is important to estimate seismic damage.

This current size of the slip on the fault is used for a probabilistic prediction of additional rupture in the near future. We characterize the distribution of additional rupture length conditioned on the current slip on the fault for the ongoing rupture from the simulation with a 1-D slip model. The probability density of additional rupture length (L_a) can be approximated by a lognormal distribution conditioned on the current slip size (D).

$$p(L_a|D) = \frac{1}{x\sigma\sqrt{2\pi}} e^{-(\ln L_a - \mu(D))^2/2\sigma^2}, \tag{6.11}$$

where $\mu(D) = 1.16\ln(D) + 4.94$ and $\sigma = 1.6$.

The pdf shows the expectation of additional rupture length is longer as the current slip size is larger. This means a rupture with large current slip is more likely to continue propagating, and a rupture with small current slip tends to terminate shortly. However, the observation is not always the case: for example, rupture of Chi-Chi earthquake in figure 6.7 terminates right after the largest slip occurs at the north end of the fault. Since the mechanism of the rupture propagation is very complicated, it is difficult to predict the end of a rupture. The model proposed here is crude and may not agree with these observation completely, but the technique to generate pdf of additional rupture length from a slip model can apply to other slip models.

Chapter 7

Conclusions

Recently, according to advances in data analysis and an increased public perception of seismic hazards, the topic of early warning has attracted more research attention from seismologists and engineers. Earthquake early warning systems collect seismic data from an occurring event, analyze them quickly, and provide estimates for location and magnitude of the event.

Cua and Heaton developed the Virtual Seismologist (VS) method (Cua, 2005; Cua and Heaton, 2006). It is a Bayesian approach to seismic early warning designed for modern seismic networks, and proposed for small to moderate earthquakes with ruptures that can be approximately modeled as a point source. The VS algorithm uses an envelope attenuation relationship and the predominant frequency content from the first few seconds after the P-wave arrival. The advantage of the VS method is its capacity to assimilate different types of information that may be useful to find quick and reliable estimates of magnitude and location (Cua, 2005).

In order to construct an early warning system for large earthquakes, we characterize the rupture extent and the slip on the fault in real time and predict ground motions at a given site based on the current rupture configuration. Our strategy for large earthquakes is as follows:

- Characterize the present rupture extent from high-frequency ground motions.
- Characterize the present slip on the fault from low-frequency ground motions.
- Predict the final rupture extent from the on-going rupture.

- Estimate the ground motion at a given site based on the present rupture geometry.

The ground motions at a site could be different for different earthquakes of the same magnitude at the same distance, because of differences in source mechanisms, path effect, or site conditions. One of the most commonly used ground motion parameters is peak ground accelerations (PGA), and Campbell (1981) found this uncertainty of peak ground acceleration can be modeled using a lognormal distribution. In other words, the distribution of the amplitude of ground motions with constant magnitude and distance follows a lognormal distribution.

The statistical observations of high-frequency and low-frequency ground motions for large earthquakes show that the near-source high-frequency ground motion saturates as a function of magnitude for large earthquakes, and weakly depends on the magnitude. On the other hand, the low frequency ground motion has strong correlation with the magnitude of an earthquake.

1) Characterize the present rupture extent from high-frequency ground motions

We propose a new model to simulate high-frequency motions from earthquakes with large fault dimension: the envelope of high-frequency ground motion from a large earthquake can be expressed as a root-mean-squared combination of envelope functions from smaller earthquakes. We parameterize the fault geometry with an epicenter, a fault strike, and two along-strike rupture lengths, and find these parameters by minimizing residual sum of squares of errors between simulation and observed ground motion envelopes.

To provide the information on the spatial extent of rupture geometry, we present a methodology to estimate the fault dimension of an earthquake in real time by classifying seismic records into near-source or far-source records. We analyzes peak ground motions and finds the function that best classifies near-source and far-source records based on these parameters by Bayesian model class selection. This discriminant function is useful to estimate the fault rupture dimension in real time, especially for large earthquakes.

2) Characterize the present slip on the fault from low-frequency ground motions.

In order to characterize a slip on the fault in real time, we construct an analytical function to estimate slip on the fault from observations of displacements away from the fault by using the result of a ground motion simulation (Aagaard et al., 2004). In real-time analysis, we back project the recorded displacement data onto the fault line scaled by the analytical function to estimate the size of the slip on the fault. The fault slip makes it possible to predict long-period seismic waves, which is important to estimate seismic damage.

3) Predict the final rupture extent from the on-going rupture

This current size of the slip on the fault is used for a probabilistic prediction of additional rupture in the near future. We characterize the distribution of additional rupture length as a conditioned on the current slip on the fault for the ongoing rupture from the simulation with a 1-D slip model. The probability density of additional rupture length (L_a) can be approximated by a lognormal distribution conditioned on the current slip size (D):

$$p(L_a|D) = \frac{1}{L\sigma\sqrt{2\pi}} e^{-(\ln L_a - \mu(D))^2/2\sigma^2}, \tag{7.1}$$

where $\mu(D) = 1.16\ln(D) + 4.94$ and $\sigma = 1.6$.

4) Estimate the ground motion at a given site based on the present rupture geometry

In the current earthquake early warning system, the ground motion at a given site can be estimated by the velocity attenuation relationship as a function of magnitude and epicentral distance, and multiplying site amplification factors. There are implementation issues on this ground motion estimate, since the ground motion models for large earthquakes depends on rupture dimension and slip size, too. We found out that the high-frequency ground motion at a site can be expressed as a root-mean-squared combination of envelope functions from smaller earthquakes. However, this model does not work for velocity and displacement estimates since it relies on the random phase assumption of high frequency ground motions. Constructing ground motion models for low-frequency ground motions by considering the fault distance and slip size on the fault still remains as future work.

Bibliography

Aagaard, B., Hall, J., and Heaton, T. (2004). Effects of fault dip and slip rake angles on near-source ground motions: Why rupture directivity was minimal in the 1999 chi-chi, taiwan, earthquake. *Bulletin of the Seismological Society of America*, 94(1):155–170.

Abercrombie, R. and Mori, J. (1996). Occurrence patterns of foreshocks to large earthquakes in the western united states. *Nature*, 381:303–307.

Akkar, S. and Gülkan, P. (2002). A critical examination of near-field accelerograms from the sea of marmara region earthquakes. *Bulletin of the Seismological Society of America*, 92(1):428–447.

Allen, R. (2006). Probabilistic warning times for earthquake ground shaking in the san francisco bay area. *Seismological Research Letters*, 77(3):371–376.

Allen, R. and Kanamori, H. (2003). The potential for earthquake early warning in southern california. *Science*, 300(5620):786–789.

Baker, T., Granat, R., and Clayton, R. (2005). Real-time earthquake location using kirchhoff reconstruction. *Bulletin of the Seismological Society of America*, 95(2):699–707.

Bakun, W., Fischer, F., Jensen, E., and VanSchaack, J. (1994). Early warning system for aftershocks. *Bulletin of the Seismological Society of America*, 84(2):359–365.

Balassanian, S., Martirossyan, A., and Arzoumanian, V. (2003). Project of creation of an earthquake early warning system for armenia. In Zschau, J. and Küppers, A., editors, *Early Warning Systems for Natural Disaster Reduction*, pages 487–494. Springer.

Beck, J. and Katafygiotis, L. (1998). Updating models and their uncertainties. i: Bayesian statistical framework. *Journal of Engineering Mechanics*, 124(4):455–461.

Beck, J. and Yuen, K. (2004). Model selection using response measurements: Bayesian probabilistic approach. *Journal of Engineering Mechanics*, 130(2):192–203.

Boatwright, J. (1982). A dynamic model for far-field acceleration. *Bulletin of the Seismological Society of America*, 72(4):1049–1068.

Boatwright, J. and Boore, D. (1982). Analysis of the ground accelerations radiated by the 1980 livermore valley earthquakes for directivity and dynamic source characteristics. *Bulletin of the Seismological Society of America*, 72(6 A):1843–1865.

Boore, D. (2001). Effect of baseline corrections on displacements and response spectra for several recordings of the 1999 chi-chi, taiwan, earthquake. *Bulletin of the Seismological Society of America*, 91(5):1199–1211.

Boore, D. and Joyner, W. (1982). The empirical prediction of ground motion. *Bulletin of the Seismological Society of America*, 72(6B):S43–S60.

Boore, D., Joyner, W., and Fumal, T. (1993). Estimation of response spectra and peak accelerations from western north american earthquakes: An interim report. open-file report 93-509. *US Geological Survey*, page 70.

Brune, J. (1970). Tectonic stress and the spectra of seismic shear waves from earthquakes. *J Geophys Res*, 75(26):4997–5009.

Campbell, K. (1981). Near-source attenuation of peak horizontal acceleration. *Bulletin of the Seismological Society of America*, 71(6):2039–2070.

Clinton, J. (2004). *Modern Digital Seismology - Instrumentation, and Small Amplitude Studies in the Engineering World*. PhD thesis, California Institute of Technology.

Cooper, J. (1868). Letter to editor. San Francisco Daily Evening Bulletin. November 3, 1988 (as quoted in Nakamura and Tucker, 1988).

Cua, G. (2005). *Creating the Virtual Seismologist : developments in ground motion characterization and seismic early warning.* PhD thesis, California Institute of Technology.

Cua, G. and Heaton, T. (2006). *The Virtual Seismologist (VS) method: a Bayesian approach to earthquake early warning, in "Seismic early warning"*. Spring Heidelberg. in press.

Doi, K. (2003). Earthquake early warning system in japan. In Zschau, J. and Küppers, A., editors, *Early Warning Systems for Natural Disaster Reduction*, pages 447–452. Springer.

Erdik, M., Fahjan, Y., Ozel, O., Alcik, H., Mert, A., and Gul, M. (2003). Istanbul earthquake rapid response and the early warning system. *Bulletin of Earthquake Engineering*, 1(1):157–163.

Espinosa-Aranda, J., Jimenez, A., Ibarrola, G., and Alcantar, F. (1996). Results of the mexico city early warning system. *Proceedings of the 11th World Conference on Earthquake Engineering*, No.2132.

Espinosa-Aranda, J., Jimenez, S., Ibarrola, G., Alcantar, F., Aguilar, A., Inostroza, M., and Maldonado, S. (1995). Mexico city seismic alert system. *Seismological Research Letters*, 66(6):42–53.

Felzer, K. and Brodsky, E. (2006). Decay of aftershock density with distance indicates triggering by dynamic stress. *Nature*, 441(7094):735–738.

Fisher, R. (1936). The use of multiple measurements in taxonomic problems. *Annals of Eugenics*, 7(2):179–188.

Gull, S. (1988). Bayesian inductive inference and maximum entropy. In Erickson,

G. and Smith, C., editors, *Maximum Entropy and Bayesian Methods*, pages 53–74. Kluwer Academic Publishers.

Hanks, T. and Johnson, D. (1976). Geophysical assessment of peak accelerations. *Bulletin of the Seismological Society of America*, 66(3):959–968.

Hanks, T. and Mcguire, R. (1981). The character of high-frequency strong ground motion. *Bulletin of the Seismological Society of America*, 71(6):2071–2095.

Hartzell, S. and Heaton, T. (1983). Inversion of strong ground motion and teleseismic waveform data for the fault rupture history of the 1979 imperial valley, california, earthquake. *Bulletin of the Seismological Society of America*, 73(6 A):1553–1583.

Heaton, T. (1985). A model for a seismic computerized alert network. *Science*, 228(4702):987–990.

Heaton, T., Clayton, R., Davis, J., Hauksson, E., Jones, L., Kanamori, H., Mori, J., Porcella, R., and Shakal, T. (1996). The trinet project. *Proceedings of the 11th World Conference on Earthquake Engineering*, No.2136.

Heaton, T. and Hartzell, S. (1989). Estimation of strong ground motions from hypothetical earthquakes on the cascadia subduction zone. *Pacific Northwest, PAGEOPH*, 129:131–201.

Honda, R., Aoi, S., Morikawa, N., Sekiguchi, H., Kunugi, T., and Fujiwara, H. (2005). Ground motion and rupture process of the 2004 mid niigata prefecture earthquake obtained from strong motion data of k-net and kik-net. *Earth, Planets and Space*, 57:527–532.

Horiuchi, S., Negishi, H., Abe, K., Kamimura, A., and Fujinawa, Y. (2005). An automatic processing system for broadcasting earthquake alarms. *Bulletin of the Seismological Society of America*, 95(2):708–718.

Iwan, W., Moser, M., and Peng, C. (1985). Some observations on strong-motion earthquake measurement using a digital accelerograph. *Bulletin of the Seismological Society of America*, 75:1225–1246.

Ji, C., Choi, K., King, N., Larson, K., and Hudnut, K. (2004). Co-seismic slip history and early afterslip of the 2004 parkfield earthquake. *American Geophysical Union, Fall Meeting 2004, abstract*, pages S53D–04.

Ji, C., Helmberger, D., Wald, D., and Ma, K. (2003). Slip history and dynamic implications of the 1999 chi-chi, taiwan, earthquake. *Journal of Geophysical Research*, page 108(B9).

Joyner, W. and Boore, D. (1981). Peak horizontal acceleration and velocity from strong-motion records including records from the 1979 imperial valley, california, earthquake. *Bulletin of the Seismological Society of America*, 71(6):2011–2038.

Kanamori, H. (1993). Locating earthquakes with amplitude: Application to real-time seismology. *Bulletin of the Seismological Society of America*, 83(1):264–268.

Kanamori, H. (2005). Real-time seismology and earthquake damage mitigation. *Annual Review of Earth and Planetary Sciences*, 33(1):195–214.

Kanamori, H. and Hauksson, E. (1991). Terrascope and cube project at caltech. *EOS Transactions American Geophysical Union*, 72(50):564–564.

Kanamori, H., Hauksson, E., and Heaton, T. (1997). Real-time seismology and earthquake hazard mitigation. *Nature*, 390(6659):461.

Kanamori, H. and Jennings, P. (1978). Determination of local magnitude, m_l, from strong-motion accelerograms. *Bulletin of the Seismological Society of America*, 68(2):471–485.

Lee, W. and Espinosa-Aranda, J. (2003). Earthquake early-warning systems: Current status and perspectives. In Zschau, J. and Küppers, A., editors, *Early Warning Systems for Natural Disaster Reduction*, pages 409–423. Springer.

Lee, W., Shin, T., Kuo, K., Chen, K., and Wu, C. (2001). Cwb free-field strong-motion data from the 21 september chi-chi, taiwan, earthquake. *Bulletin of the Seismological Society of America*, 91(5):1370–1376.

Li, Y., Campbell, C., and Tipping, M. (2002). Bayesian automatic relevance determination algorithms for classifying gene expression data. *Bioinformatics*, 18(10):1332–1339.

Lindley, D. (1957). A statistical paradox. *Biometrika*, 44(1/2):187–192.

Liu, H. and Helmberger, D. (1985). The 23: 19 aftershock of the 15 october 1979 imperial valley earthquake: More evidence for an asperity. *Bulletin of the Seismological Society of America*, 75(3):689–708.

Liu-Zeng, J., Heaton, T., and DiCaprio, C. (2005). The effect of slip variability on earthquake slip-length scaling. *Geophysical Journal International*, 162(3):841–849.

Lockman, A. and Allen, R. (2005). Single-station earthquake characterization for early warning. *Bulletin of the Seismological Society of America*, 95(6):2029[unknown 2013]2039.

Ma, K., Wang, J., and Zhao, D. (1996). Three-dimensional seismic velocity structure of the crust and uppermost mantle beneath taiwan. *J Phys Earth*, 44(2):85–105.

MacKay, D. (1999). Introduction to monte carlo methods. In Jordan, M., editor, *Learning in graphical models*. MIT Press.

Metropolis, N., Rosenbluth, A., Rosenbluth, M., Teller, A., and Teller, E. (1953). Equation of state calculations by fast computing machines. *J Chem Phys*, 21:1087–1092.

Muto, M. (2006). *Application of Stochastic Simulation Methods to System Identification*. PhD thesis, California Institute of Technology.

Nakamura, Y. (1988). On the urgent earthquake detection and alarm system (uredas). *Proceedings of Ninth World Conference on Earthquake Engineering*, VII:673–678.

Nakamura, Y. (1996a). Real-time information systems for hazards mitigation. *Proceedings of the 11th World Conference on Earthquake Engineering*, No.2134.

Nakamura, Y. (1996b). Real-time information systems for seismic hazard mitigation uredas, heras and pic. *Quarterly Report of Railway Technical Research Institute (RTRI) Japan*, 37(3):112–127.

Nakamura, Y., Saita, J., Araya, T., and Sato, T. (2006). The fastest p-wave warning system freql, uredas and compact uredas with actual situations. *100th Anniversary Earthquake Conference Commemorating the 1906 San Francisco Earthquake.*

Nakamura, Y. and Tucker, B. (1988). Japan's earthquake warning system: Should it be imported to california. *California Geology*, 41(2):33–40.

Normile, D. (2004). Earthquake preparedness: Some countries are betting that a few seconds can save lives. *Science*, 306(5705):2178–2179.

Odaka, T., Ashiya, K., Tsukada, S. S., Ohtake, K., and Nozaka, D. (2003). A new method of quickly estimating epicentral distance and magnitude from a single seismic record. *Bulletin of the Seismological Society of America*, 93(1):526–532.

Papadimitriou, C., Beck, J., and Katafygiotis, L. (1997). Asymptotic expansions for reliability and moments of uncertain systems. *Journal of Engineering Mechanics*, 123(12):1219–1229.

Roberts, G., Gelman, A., and Gilks, W. (1997). Weak convergence and optimal scaling of random walk metropolis algorithms. *The Annals of Applied Probability*, 7(1):110–120.

Rydelek, P. and Pujol, J. (2004). Real-time seismic warning with a two-station subarray. *Bulletin of the Seismological Society of America*, 94(4):1546–1550.

Saita, J. and Nakamura, Y. (2003). Uredas: The early warning system for mitigation of disasters caused by earthquakes and tsunamis. In Zschau, J. and Küppers, A., editors, *Early Warning Systems for Natural Disaster Reduction*, pages 453–460. Springer.

Sambridge, M. (1999a). Geophysical inversion with a neighbourhood algorithm-i. searching a parameter space. *Geophysical Journal International*, 138(2):479–494.

Sambridge, M. (1999b). Geophysical inversion with a neighbourhood algorithm-ii. appraising the ensemble. *Geophysical Journal International*, 138(3):727–746.

Scholz, C. (1982). Scaling laws for large earthquakes: Consequences for physical models. *Bulletin of the Seismological Society of America*, 72(1):1–14.

Sekiguchi, H., Irikura, K., Iwata, T., Kakehi, Y., and Hoshiba, M. (1996). Minute locating of fault planes and source process of the 1995 hyogo-ken nanbu, japan, earthquake from the waveform inversion of strong ground motion. *J Phys Earth*, 44:473–487.

Sekiguchi, H. and Iwata, T. (2002). Rupture process of the 1999 kocaeli, turkey, earthquake estimated from strong-motion waveforms. *Bulletin of the Seismological Society of America*, 92(1):300–311.

Shin, T. and Teng, T. (2001). An overview of the 1999 chi-chi, taiwan, earthquake. *Bulletin of the Seismological Society of America*, 91(5):895–913.

Si, H. and Midorikawa, S. (1999). New attenuation relationships for peak ground acceleration and velocity considering effects of fault type and site condition. *Journal of Structural and Construction Engineering, AIJ*, 523:63–70. *(in Japanese).*

Silverman, B. (1986). *Density Estimation for Statistics and Data Analysis.* Chapman and Hall.

Simons, F., Dando, B., and Allen, R. (2006). Automatic detection and rapid determination of earthquake magnitude by wavelet multiscale analysis of the primary arrival. *Earth and Planetary Science Letters*, 250(1-2):214–223.

Sivia, D. (1996). *Data Analysis: A Bayesian Tutorial.* Oxford University Press.

Somerville, P. and Yoshimura, J. (1990). The influence of critical moho reflections on strong ground motions recorded in san francisco and oakland during the 1989 loma prieta earthquake. *Geophysical Research Letters*, 17(8):1203–1206.

Teng, T., Wu, L., Shin, T., Tsai, Y., and Lee, W. (1997). One minute after: Strong-motion map, effective epicenter, and effective magnitude. *Bulletin of the Seismological Society of America*, 87(5):1209–1219.

Toki, K., Irikura, K., and Kagawa, T. (1995). Strong motion records in the source area of the hyogoken-nambu earthquake, january 17, 1995, japan. *J Natural Disaster Science*, 16:23–30.

Toksöz, M., Dainty, A., and Bullitt, J. (1990). A prototype earthquake warning system for strike-slip earthquakes. *Pure and Applied Geophysics*, 133(3):475–487.

Tsuboi, S., Komatitsch, D., Ji, C., and Tromp, J. (2003). Broadband modeling of the 2002 denali fault earthquake on the earth simulator. *Physics of the Earth and Planetary Interiors*, 139(3):305–313.

Venables, W. and Ripley, B. (2002). *Modern Applied Statistics with S*. Springer.

Wald, D. (1996). Slip history of the 1995 kobe, japan, earthquake determined from strong motion, teleseismic, and geodetic data. *J Phys Earth*, 44:489–503.

Wald, D. and Heaton, T. (1994). Spatial and temporal distribution of slip for the 1992 landers, california, earthquake. *Bulletin of the Seismological Society of America*, 84(3):668–691.

Wald, D., Heaton, T., and Hudnut, K. (1996). The slip history of the 1994 northridge, california, earthquake determined from strong-motion, teleseismic, gps, and leveling data. *Bulletin of the Seismological Society of America*, 86(1B):S49–S70.

Wald, D., Helmberger, D., and Heaton, T. (1991). Rupture model of the 1989 loma prieta earthquake from the inversion of strong-motion and broadband teleseismic data. *Bulletin of the Seismological Society of America*, 81(5):1540–1572.

Wells, D. and Coppersmith, K. (1994). New empirical relationships among magnitude, rupture length, rupture width, rupture area, and surface displacement. *Bulletin of the Seismological Society of America*, 84(4):974–1002.

Wenzel, F., Oncescu, M. C., Baur, M., Fiedrich, F., and Ionescu, C. (2003). 25 seconds for bucharest. In Zschau, J. and Küppers, A., editors, *Early Warning Systems for Natural Disaster Reduction*, pages 471–478. Springer.

Wu, Y. and Kanamori, H. (2005a). Experiment on an onsite early warning method for the taiwan early warning system. *Bulletin of the Seismological Society of America*, 95(1):347–353.

Wu, Y. and Kanamori, H. (2005b). Rapid assessment of damage potential of earthquakes in taiwan from the beginning of p waves. *Bulletin of the Seismological Society of America*, 95(3):1181–1185.

Wu, Y., Shin, T., and Tsai, Y. (1998). Quick and reliable determination of magnitude for seismic early warning. *Bulletin of the Seismological Society of America*, 88(5):1254–1259.

Wu, Y., Yen, H., Zhao, L., Huang, B., and Liang, W. (2006). Magnitude determination using initial p waves: A single-station approach. *Geophysical Research Letters*, 33(5).

Yamada, M. and Heaton, T. (2006). Real-time estimation of fault rupture extent using envelopes of acceleration. *Bulletin of the Seismological Society of America. (submitted)*.

Yamada, M., Heaton, T., and Beck, J. (2006). Early warning systems for large earthquakes: Near-source versus far-source classification. *Bulletin of the Seismological Society of America. (submitted)*.

Zollo, A., Satriano, C., Lancieri, M., Lomax, A., Bobbio, A., Cantore, L., Convertito, V., Corciulo, M., Matteis, R. D., Crosta, M. D., Elia, L., Emolo, A., Iannaccone, G., Martino, C., Romeo, A., and Weber, E. (2006). Real-time estimation of earthquake location and magnitude for seismic early warning in campania region, southern italy. *100th Anniversary Earthquake Conference Commemorating the 1906 San Francisco Earthquake*.

Zschau, J., Isikara, M., Ergunay, O., Yalcin, M. N., and Erdik, M. (2003). Towards an earthquake early warning system for the megacity of istanbul. In Zschau, J. and Küppers, A., editors, *Early Warning Systems for Natural Disaster Reduction*, pages 433–440. Springer.

Appendix A

An Article in the *San Francisco Daily Evening Bulletin*

This is an article about the concept of seismic early warning system in the San Francisco Daily Evening Bulletin (Cooper, 1868).

> ... we are now obliged to look for some ... means of prognosticating [earthquakes] and I wish to suggest the following mode by which we may make electricity the means, perhaps, of saving thousands of lives in case of the occurrence of more severe shocks than we have yet experienced. It is well known that those shocks are produced by a wave-motion on the surface of the earth, the waves radiating from a center just as they do in water when a stone is thrown in. If this center happens to be far enough from [San Francisco], we may be easily notified of the coming wave in time for all to escape from dangerous buildings before it reaches us...
>
> A very simple mechanical contrivance can be arranged at various points from 10 to 100 miles from San Francisco, by which a wave of the earth high enough to do damage will start an electric current over the wires now radiating from this city and almost instantaneously ring an alarm bell, which should be hung in a high tower near the center of the city. This bell should be very large, of peculiar sound, and known to everybody as the *earthquake bell*. Of course, nothing but the distant undulation of the surface of the earth should ring it. This machinery would be self-

acting, and not dependent on the telegraph operators, who might not always retain presence of mind enough to telegraph at the moment or might sound the alarm too often.

Of course, there might be shocks the central force of which is too near this city to be thus protected but that is not likely to occur [often].

Appendix B

Peak Ground Motion Database

This chapter shows the dataset of the peak value of strong motion records used in chapters 3 and 5. The summary of the dataset is shown in table B.1. It consists of strong motion records of ten earthquake with magnitude greater than 6.0. Table B.2 is a list of the peak values of the strong motion records. The jerk, acceleration, velocity and displacement of EW, NS, srss horizontal, UD components are shown in the table.

Table B.1: Earthquake data set used for the near-source (NS) and far-source (FS) ground motion analysis. The left column is the earthquake ID number corresponding to the next table. Moment magnitude (M_w) is cited from Harvard CMT solution. The definition of the near-source station is a station with fault distance less than 10 km. The fault models are used as selection criteria to classify near-source stations.

No.	Earthquake	M_w	NS	FS	Total	Fault Model
1	Imperial Valley (1979)	6.5	14	20	34	Hartzell and Heaton (1983)
2	Loma Prieta (1989)	6.9	8	39	47	Wald et al. (1991)
3	Landers (1992)	7.3	1	112	113	Wald and Heaton (1994)
4	Northridge (1994)	6.6	17	138	155	Wald et al. (1996)
5	Hyogoken-Nanbu (1995)	6.9	4	14	18	Wald (1996)
6	Izmit (1999)	7.6	4	13	17	Sekiguchi and Iwata (2002)
7	Chi-Chi (1999)	7.6	42	172	214	Ji et al. (2003)
8	Denali (2002)	7.8	1	29	30	Tsuboi et al. (2003)
9	Parkfield (2004)	6.0	47	28	75	Ji et al. (2004)
10	Niigataken-Chuetsu (2004)	6.6	9	58	67	Honda et al. (2005)
	Total		147	623	770	

Table B.2: Peak values of the strong motion records for ten earthquakes. The first column is the earthquake ID number corresponding to the table B.1, and the sequencial number of the records. Station ID, Longitude and latitude of the station are shown the next column. NF is a binary near-source and far-source classification. NF is 1 if the station is near-source record, and 0 if far-source.

No.	ID	lon.	lat.	NF	Jerk (cm/s^3)				Acceleration (cm/s^2)				Velocity (cm/s)				Displacement (cm)			
					EW	NS	Hor.	UD	EW	NS	Hor.	UD	EW	NS	Hor.	UD	EW	NS	Hor.	UD
1-1	0117	−115.56	32.79	1	8205	9305	12406	18129	232	208	311	244	74.7	41.0	85.2	18.1	42.8	16.4	45.8	9.1
1-2	0286	−115.82	32.95	0	9146	4600	10238	3487	183	108	212	72	8.3	4.6	9.4	1.9	1.5	2.7	3.0	0.6
1-3	0412	−115.57	32.78	1	6341	6692	9219	3930	174	219	280	99	54.1	52.1	75.2	9.9	27.4	20.3	34.1	7.3
1-4	0724	−115.51	33.24	0	3040	2267	3792	2623	108	68	128	34	12.3	10.6	16.2	3.7	6.3	5.2	8.1	2.3
1-5	0931	−115.64	32.72	0	3499	4504	5703	3921	116	140	181	61	20.0	22.6	30.1	7.4	13.7	12.6	18.6	4.4
1-6	0952	−115.47	32.86	1	14733	23356	27615	24910	375	548	664	478	88.9	57.9	106.1	36.8	58.6	34.8	68.2	13.6
1-7	0955	−115.43	32.86	1	8585	10490	13555	15260	368	488	611	203	79.8	42.0	90.2	18.0	53.9	20.3	57.6	8.6
1-8	5028	−115.50	32.83	1	7531	7718	10783	32582	450	326	555	470	101.4	50.6	113.3	27.2	47.9	27.1	55.0	10.1
1-9	5051	−115.70	32.93	0	4694	3627	5932	5702	199	111	228	156	15.4	16.5	22.5	6.6	10.0	11.2	15.0	5.6
1-10	5052	−115.86	32.79	0	1808	1438	2310	1062	52	41	67	27	3.8	3.5	5.1	2.6	1.2	1.6	2.0	1.4
1-11	5053	−115.49	32.67	0	6343	7061	9491	8984	200	270	336	170	20.7	20.9	29.4	5.1	13.4	8.6	16.0	1.7
1-12	5054	−115.34	32.69	1	52190	70005	87318	104450	763	583	960	435	54.7	45.0	70.8	11.9	15.0	11.9	19.1	3.9
1-13	5055	−115.38	32.81	1	7440	5644	9338	13115	212	250	328	202	42.9	48.4	64.7	10.2	27.3	28.1	39.2	6.9
1-14	5056	−115.32	32.96	0	4783	6632	8177	3244	124	138	186	49	12.6	16.3	20.6	3.7	6.7	8.4	10.7	1.7
1-15	5057	−115.38	32.89	0	8713	10616	13734	8156	210	272	344	113	40.0	43.7	59.2	8.0	23.7	16.7	29.0	5.6
1-16	5058	−115.59	32.75	0	9937	11116	14910	6417	366	352	508	127	38.7	33.3	51.1	11.9	21.3	17.4	27.5	7.4
1-17	5059	−115.68	32.71	0	5364	3605	6463	2228	132	111	172	43	14.1	16.1	21.4	4.1	7.3	8.8	11.5	2.4
1-18	5060	−115.51	32.99	0	5807	6019	8363	8415	231	160	281	156	41.1	32.1	52.1	8.8	14.1	19.9	24.4	3.6
1-19	5061	−115.52	33.13	0	2201	4005	4570	2506	77	125	147	48	12.9	13.6	18.7	4.0	6.4	10.2	12.0	1.2
1-20	5066	−115.59	33.36	0	1635	1653	2325	617	127	114	171	37	15.7	12.0	19.7	4.0	2.2	2.5	3.4	1.1
1-21	5115	−115.37	32.92	0	13584	13619	19235	6673	372	307	483	103	26.5	30.8	40.7	6.4	17.9	13.1	22.2	4.4
1-22	5155	−115.45	32.77	1	4765	5194	7049	13108	291	311	426	247	94.6	70.2	117.8	28.7	40.8	26.7	48.8	8.4
1-23	5158	−115.49	32.84	1	15085	19803	24894	99299	447	332	557	1612	106.0	63.1	123.3	63.1	65.1	31.6	72.4	20.3
1-24	5159	−115.53	32.81	1	19563	16220	25413	24051	426	611	744	352	55.2	54.5	77.6	21.3	34.1	27.6	43.8	12.7
1-25	5165	−115.54	32.80	1	12918	11963	17606	39181	368	482	606	452	80.3	42.2	90.7	21.5	41.3	12.9	43.3	15.0
1-26	6604	−115.30	32.42	0	5850	7620	9607	14170	154	163	224	196	19.1	13.1	23.2	7.7	7.4	5.1	9.0	3.3
1-27	6605	−115.19	32.36	0	9490	16410	18956	13970	231	340	411	149	26.4	34.9	43.8	13.7	14.2	17.2	22.3	8.1
1-28	6610	−115.10	32.29	0	6900	8620	11041	5380	119	165	203	57	7.2	8.1	10.9	1.4	2.1	1.8	2.8	0.7
1-29	6616	−115.33	32.65	1	29310	27180	39973	16790	256	319	409	156	22.9	37.5	43.9	6.3	5.3	10.9	12.1	3.5
1-30	6618	−115.30	32.62	1	26390	41580	49248	149320	230	351	420	889	31.6	28.1	42.3	13.7	10.6	11.5	15.6	7.3

Table B.2: Continued.

No.	ID	lon.	lat.	NF	Jerk (cm/s^3)				Acceleration (cm/s^2)				Velocity (cm/s)				Displacement (cm)			
					EW	NS	Hor.	UD	EW	NS	Hor.	UD	EW	NS	Hor.	UD	EW	NS	Hor.	UD
1-31	6619	−115.44	32.62	1	36710	17360	40608	27770	435	238	496	328	33.4	21.2	39.6	10.0	8.7	7.2	11.3	2.8
1-32	6621	−115.24	32.48	0	7620	10090	12644	14940	251	262	363	211	25.4	22.2	33.7	5.7	7.3	8.7	11.3	2.3
1-33	6622	−115.08	32.57	0	5300	8310	9856	5310	145	184	234	72	8.5	12.4	15.0	3.6	2.6	3.4	4.2	1.6
1-34	11369	−115.62	33.04	0	2071	3539	4101	8538	74	110	133	84	23.5	23.5	33.2	7.0	15.6	9.9	18.5	2.5
2-1	47179	−121.64	36.67	0	3608	2357	4310	4162	110	88	141	100	16.1	10.9	19.5	6.9	6.3	6.9	9.3	3.1
2-2	47189	−121.40	36.75	0	1153	1591	1965	950	71	65	96	58	10.2	9.4	13.9	7.3	2.8	6.1	6.7	4.6
2-3	47377	−121.90	36.60	0	2037	2581	3288	1601	61	69	92	29	4.8	3.3	5.9	3.2	0.8	0.6	1.0	0.5
2-4	47379	−121.57	36.97	1	22524	21196	30929	11158	434	427	608	206	33.7	32.0	46.5	14.7	6.8	9.1	11.3	7.3
2-5	47380	−121.56	36.98	1	10193	8142	13046	14602	316	344	467	273	39.2	33.7	51.7	15.3	10.8	10.3	14.9	6.5
2-6	47381	−121.54	36.99	0	14190	19671	24255	25708	362	532	643	360	43.9	35.4	56.4	14.8	13.2	7.6	15.2	7.0
2-7	47459	−121.76	36.91	1	13173	6478	14680	18041	352	267	442	499	55.0	33.1	64.2	15.9	14.2	10.5	17.7	4.7
2-8	47524	−121.40	36.85	0	3768	6531	7539	6861	175	362	402	193	30.7	63.0	70.1	15.6	23.2	19.6	30.4	7.1
2-9	57007	−121.80	37.05	1	15571	12030	19677	18973	469	618	776	431	46.1	55.2	71.9	20.7	15.0	8.7	17.3	9.0
2-10	57064	−121.92	37.53	0	4078	3939	5670	3778	100	118	155	81	8.6	10.8	13.8	9.0	4.5	5.2	6.9	5.5
2-11	57066	−121.95	37.40	0	4777	4906	6847	5135	158	163	227	82	18.5	31.7	36.7	9.3	9.6	18.3	20.6	5.3
2-12	57180	−121.95	37.20	1	5559	4562	7192	4238	384	375	537	207	102.5	76.4	127.9	31.1	35.4	23.3	42.4	11.1
2-13	57191	−121.71	37.34	0	1809	1903	2626	1674	110	128	169	56	14.1	12.7	19.0	9.0	7.3	3.6	8.1	4.6
2-14	57217	−121.55	37.12	0	16234	6432	17462	3592	471	149	494	71	38.4	15.6	41.4	8.7	10.0	5.8	11.6	4.2
2-15	57382	−121.52	37.01	0	5170	8427	9886	5989	210	408	459	149	38.3	39.4	54.9	14.9	8.4	10.1	13.1	7.1
2-16	57383	−121.48	37.03	0	5220	5036	7253	4214	167	112	201	100	13.9	13.1	19.1	9.8	3.5	3.6	5.0	4.4
2-17	57504	−121.55	37.12	0	4464	5832	7344	3245	175	155	233	92	21.5	12.8	25.1	9.8	7.9	5.4	9.5	4.6
2-18	57563	−121.80	37.21	0	11210	11547	16093	15433	223	269	350	205	20.9	26.4	33.7	17.1	5.8	15.2	16.3	5.8
2-19	58043	−122.52	37.82	0	887	1798	2004	407	71	70	100	34	13.7	11.9	18.1	7.4	3.3	3.2	4.6	2.0
2-20	58133	−122.41	37.80	0	1613	1255	2044	727	91	51	104	32	10.4	7.1	12.5	4.2	4.1	1.9	4.5	1.9
2-21	58151	−122.39	37.79	0	1635	1994	2578	1027	89	79	118	28	11.5	7.3	13.6	3.8	3.8	2.7	4.7	2.0
2-22	58219	−122.06	37.66	0	2124	2824	3533	1422	83	73	110	44	7.3	5.6	9.2	4.6	3.8	3.3	5.0	3.3
2-23	58222	−122.46	37.79	0	3760	2037	4276	1218	195	98	218	56	33.5	13.4	36.0	11.5	7.9	3.6	8.6	3.0
2-24	58223	−122.40	37.62	0	5907	5387	7994	1959	326	231	399	63	29.1	26.3	39.2	5.5	6.6	5.5	8.6	2.3
2-25	58233	−122.36	37.53	0	2596	1854	3190	903	85	56	102	31	10.2	5.3	11.4	3.8	3.5	1.4	3.8	1.2
2-26	58375	−122.23	37.55	0	4326	3586	5619	2779	278	253	375	101	45.2	31.8	55.2	8.3	17.8	7.1	19.2	3.4

Table B.2: Continued.

No.	ID	lon.	lat.	NF	Jerk (cm/s^3)				Acceleration (cm/s^2)				Velocity (cm/s)				Displacement (cm)			
					EW	NS	Hor.	UD	EW	NS	Hor.	UD	EW	NS	Hor.	UD	EW	NS	Hor.	UD
2-27	58378	−122.31	37.49	0	2456	2467	3481	1419	85	154	175	60	14.1	17.2	22.2	6.2	5.1	5.3	7.4	2.8
2-28	58471	−122.25	37.88	0	1714	873	1924	502	114	48	124	38	22.0	8.5	23.6	4.3	5.1	2.2	5.6	1.6
2-29	58505	−122.34	37.94	0	2406	2073	3176	813	104	123	161	30	14.9	17.0	22.7	4.6	3.4	3.3	4.7	1.2
2-30	68003	−122.80	38.04	0	1983	1938	2773	453	100	158	187	55	16.3	18.6	24.7	6.5	3.4	3.9	5.1	1.3
2-31	47006	−121.57	36.97	1	17498	12329	21405	8722	349	310	467	153	29.2	22.9	37.1	12.7	7.0	7.5	10.3	7.0
2-32	47125	−121.95	36.97	1	12366	17513	21439	42672	391	463	606	500	31.5	36.4	48.2	19.0	6.6	10.0	12.0	5.8
2-33	57425	−121.43	37.03	0	8327	10832	13663	7301	314	206	376	101	16.5	16.5	23.3	5.4	3.7	2.6	4.5	2.8
2-34	58065	−122.03	37.26	1	10525	12397	16262	19499	316	494	587	353	44.6	41.5	60.9	26.6	27.4	12.2	30.0	13.2
2-35	58117	−122.37	37.83	0	3620	2437	4363	370	156	98	184	16	33.2	15.6	36.7	1.2	10.2	4.8	11.2	1.2
2-36	58127	−122.26	37.43	0	1740	1104	2061	865	80	79	113	49	15.2	15.1	21.4	6.6	6.3	6.4	8.9	2.5
2-37	58130	−122.43	37.74	0	1793	2114	2772	1036	111	96	147	42	14.2	10.5	17.7	6.9	3.4	2.6	4.3	1.9
2-38	58131	−122.43	37.79	0	721	909	1160	389	60	46	76	31	14.3	9.8	17.3	6.1	4.9	3.1	5.8	2.5
2-39	58132	−122.51	37.78	0	1109	1011	1500	631	106	73	129	61	21.0	11.4	23.9	7.7	5.2	3.8	6.4	2.0
2-40	58135	−122.06	37.00	0	12514	16536	20737	17567	402	433	591	325	21.6	21.7	30.7	12.2	6.4	6.8	9.3	7.3
2-41	58163	−122.36	37.81	0	1480	898	1731	609	66	28	72	27	14.7	4.5	15.4	4.0	3.8	1.7	4.2	1.2
2-42	58338	−122.23	37.82	0	1315	1745	2185	616	70	81	107	25	9.8	9.1	13.4	2.3	2.9	3.0	4.2	1.5
2-43	58373	−122.34	37.47	0	1210	1818	2184	1156	86	101	133	36	22.4	13.6	26.2	7.9	7.5	6.2	9.7	2.8
2-44	58393	−122.08	37.66	0	4110	4539	6123	4818	136	167	215	91	12.6	13.9	18.8	4.0	4.4	3.5	5.6	2.8
2-45	58498	−122.09	37.67	0	4410	6111	7536	2949	155	153	218	81	11.6	14.4	18.4	4.8	3.7	3.6	5.1	2.6
2-46	58539	−122.39	37.67	0	1850	2262	2922	1160	57	103	118	31	6.3	8.4	10.5	4.5	1.8	2.7	3.2	1.6
2-47	58596	−122.14	37.49	0	2054	2607	3319	3222	126	125	177	57	19.1	21.2	28.6	7.2	9.7	8.8	13.1	3.3
3-1	02	−117.94	33.72	0	979	832	1284	532	61	69	92	14	12.1	15.8	19.9	1.5	3.7	8.2	8.9	0.3
3-2	03	−118.52	34.21	0	602	568	827	379	35	40	53	16	14.4	16.5	21.9	4.5	8.2	16.8	18.7	2.0
3-3	04	−118.57	34.36	0	396	392	557	238	32	29	43	19	6.8	4.3	8.0	3.6	5.4	1.7	5.6	1.4
3-4	06	−118.42	34.22	0	507	615	797	433	26	37	45	20	6.5	16.6	17.9	5.1	2.8	18.6	18.8	2.3
3-5	07	−118.44	34.22	0	514	453	685	792	38	34	51	22	6.9	7.8	10.4	3.8	2.3	2.7	3.5	0.8
3-6	08	−118.37	34.24	0	358	360	508	280	23	17	29	12	3.2	2.9	4.3	1.1	0.6	0.6	0.8	0.2
3-7	12	−118.33	34.17	0	875	930	1277	793	55	62	82	24	6.9	11.2	13.2	4.1	2.4	2.7	3.6	1.1
3-8	18	−118.37	34.09	0	326	347	476	310	22	15	27	10	3.3	2.4	4.1	1.1	0.9	0.7	1.1	0.2
3-9	19	−118.09	34.09	0	570	553	794	404	35	48	60	20	11.3	14.3	18.2	6.0	7.8	14.0	16.0	3.2

Table B.2: Continued.

No.	ID	lon.	lat.	NF	Jerk (cm/s^3)				Acceleration (cm/s^2)				Velocity (cm/s)				Displacement (cm)			
					EW	NS	Hor.	UD	EW	NS	Hor.	UD	EW	NS	Hor.	UD	EW	NS	Hor.	UD
3-10	20	−118.30	34.05	0	396	584	706	249	25	34	42	15	7.3	7.0	10.1	3.1	5.4	1.9	5.7	1.1
3-11	21	−118.30	34.08	0	696	860	1106	351	31	40	50	15	5.4	3.8	6.6	2.3	1.3	1.1	1.7	0.5
3-12	22	−118.28	34.01	0	611	582	844	376	30	41	51	16	4.7	6.5	8.0	2.6	1.8	3.3	3.8	0.5
3-13	23	−118.29	33.98	0	745	750	1058	360	48	57	74	11	11.0	7.1	13.1	1.8	3.6	3.6	5.1	0.6
3-14	25	−118.23	34.00	0	606	644	885	483	33	35	49	20	8.5	8.6	12.1	2.3	5.6	3.5	6.6	0.6
3-15	32	−118.19	34.11	0	625	804	1018	401	27	37	46	16	3.9	4.1	5.6	2.5	1.0	1.0	1.4	0.5
3-16	33	−118.22	34.09	0	451	368	582	196	21	25	33	10	3.7	5.1	6.3	0.9	1.1	1.5	1.9	0.1
3-17	34	−118.24	34.12	0	631	619	884	450	33	43	54	20	5.1	5.7	7.7	3.1	1.2	1.6	2.0	0.8
3-18	40	−118.27	33.81	0	285	243	374	253	18	10	20	8	3.1	1.0	3.2	0.8	0.7	0.2	0.7	0.1
3-19	42	−118.41	33.78	0	201	270	337	223	9	11	14	9	0.6	0.7	1.0	0.7	0.1	0.2	0.2	0.1
3-20	45	−118.35	33.90	0	185	169	251	291	6	8	10	7	0.4	0.6	0.7	0.4	0.1	0.1	0.1	0.1
3-21	46	−118.39	33.89	0	407	371	550	295	32	23	40	13	5.0	4.9	7.0	2.2	1.7	2.1	2.7	0.8
3-22	48	−118.49	34.01	0	266	313	410	192	17	25	30	9	5.8	6.8	8.9	1.7	3.8	4.1	5.6	0.5
3-23	49	−118.55	34.04	0	268	304	406	152	13	11	17	4	1.3	1.2	1.7	0.6	0.3	0.3	0.4	0.1
3-24	51	−118.79	34.02	0	263	242	358	189	15	18	24	8	2.6	2.9	3.9	1.0	0.8	0.7	1.1	0.3
3-25	52	−118.70	34.15	0	229	365	431	221	13	18	22	12	2.2	3.1	3.8	1.3	1.0	0.8	1.3	0.3
3-26	56	−118.62	34.39	0	293	316	431	234	15	20	25	10	1.7	5.3	5.6	0.7	0.2	2.6	2.7	0.1
3-27	57	−118.43	34.42	0	258	250	359	483	13	13	19	10	1.7	1.3	2.1	0.8	0.4	0.2	0.5	0.2
3-28	58	−118.30	34.27	0	430	371	568	377	28	29	41	18	5.1	5.0	7.2	3.1	1.4	1.3	1.9	1.0
3-29	60	−118.25	34.24	0	538	406	674	517	24	29	38	13	3.0	6.1	6.8	1.7	0.7	1.1	1.3	0.4
3-30	61	−118.23	34.29	0	812	779	1125	804	24	27	36	16	3.0	3.1	4.4	2.7	0.7	0.9	1.1	1.0
3-31	62	−118.08	34.39	0	375	335	503	166	22	22	31	8	1.6	2.1	2.6	0.5	0.1	0.3	0.3	0.1
3-32	63	−118.23	34.20	0	1002	823	1296	859	67	41	79	27	4.6	4.9	6.7	2.1	0.7	1.1	1.3	0.6
3-33	65	−117.88	34.14	0	708	1211	1403	883	37	60	71	27	5.9	10.6	12.1	3.5	1.4	3.2	3.5	0.8
3-34	66	−118.02	34.09	0	504	467	687	533	41	34	53	19	12.1	7.0	14.0	4.8	8.5	3.1	9.1	1.3
3-35	67	−117.94	34.15	0	539	400	672	314	29	17	34	20	3.5	2.8	4.4	3.5	0.9	1.1	1.5	1.3
3-36	68	−117.87	34.08	0	731	851	1122	684	42	58	72	33	7.9	15.2	17.1	5.8	2.2	4.8	5.3	1.5
3-37	69	−117.97	34.10	0	310	317	443	370	24	32	40	18	8.6	8.2	11.9	3.8	5.3	5.1	7.3	1.3
3-38	70	−117.92	34.09	0	978	974	1380	820	45	64	78	28	8.6	15.5	17.7	5.7	2.1	9.4	9.6	2.3
3-39	71	−117.95	34.06	0	787	698	1052	793	43	52	68	24	16.2	8.9	18.5	5.3	12.9	2.4	13.2	2.3

Table B.2: Continued.

No.	ID	lon.	lat.	NF	Jerk (cm/s^3)				Acceleration (cm/s^2)				Velocity (cm/s)				Displacement (cm)			
					EW	NS	Hor.	UD	EW	NS	Hor.	UD	EW	NS	Hor.	UD	EW	NS	Hor.	UD
3-40	72	−117.92	34.03	0	591	670	893	440	42	34	54	22	10.7	8.7	13.8	2.9	5.4	4.9	7.3	0.8
3-41	73	−117.94	33.99	0	874	1051	1367	859	48	45	66	26	6.3	8.3	10.4	3.0	1.6	2.8	3.2	1.1
3-42	74	−117.97	33.92	0	609	647	888	884	44	39	59	26	9.8	10.3	14.3	2.0	3.0	3.9	5.0	0.7
3-43	77	−118.09	33.94	0	862	1067	1372	920	50	61	79	24	8.9	6.3	10.9	2.0	4.5	3.2	5.5	0.7
3-44	78	−118.20	33.90	0	1295	926	1592	674	64	61	88	19	12.9	12.4	17.9	1.2	3.9	5.2	6.5	0.3
3-45	79	−118.14	33.92	0	501	517	720	427	33	34	48	12	5.9	8.5	10.4	0.7	2.2	4.9	5.4	0.1
3-46	80	−118.18	33.88	0	1046	760	1293	796	59	48	76	20	11.2	9.6	14.7	1.5	4.6	4.1	6.2	0.4
3-47	81	−118.24	33.84	0	828	511	973	298	48	50	69	13	10.9	9.7	14.5	1.6	4.1	4.1	5.8	0.5
3-48	83	−118.04	33.73	0	1056	850	1356	349	59	52	79	12	13.0	9.0	15.8	1.1	4.8	5.2	7.1	0.3
3-49	84	−118.10	33.85	0	976	1080	1455	701	53	53	75	15	12.5	13.5	18.4	2.0	5.3	6.8	8.6	0.5
3-50	85	−118.01	33.79	0	682	606	912	141	33	46	57	3	6.8	8.8	11.2	0.2	3.3	4.9	5.9	0.1
3-51	86	−118.02	33.85	0	779	596	981	346	45	46	64	10	13.2	9.9	16.4	1.1	5.5	4.6	7.2	0.3
3-52	87	−117.90	33.92	0	604	638	879	668	41	41	58	18	11.6	8.8	14.5	3.2	7.2	5.6	9.1	1.3
3-53	88	−117.95	33.82	0	743	885	1156	656	37	48	61	17	10.4	11.9	15.8	3.6	3.9	8.0	8.9	1.3
3-54	89	−117.82	33.73	0	705	902	1145	597	40	40	56	15	12.4	8.1	14.8	3.1	6.6	2.3	7.0	1.1
3-55	90	−117.82	33.82	0	721	546	905	439	37	28	46	18	8.5	7.8	11.6	3.0	2.9	5.4	6.2	0.9
3-56	91	−118.36	34.05	0	387	394	553	185	37	26	45	9	15.2	4.8	16.0	1.9	7.8	2.6	8.2	0.7
3-57	93	−118.04	34.13	0	968	803	1257	723	51	48	70	23	11.8	8.6	14.6	3.6	6.8	3.4	7.6	1.3
3-58	94	−118.16	33.97	0	824	809	1155	469	46	34	57	14	13.2	4.2	13.9	1.0	4.2	1.4	4.4	0.3
3-59	95	−118.08	34.17	0	1377	1079	1750	813	60	52	79	27	6.5	6.6	9.2	2.6	1.8	2.3	2.9	0.5
3-60	99	−118.06	34.13	0	401	343	528	453	27	26	37	16	8.7	6.5	10.9	2.5	6.5	2.9	7.1	0.5
3-61	0637	−118.48	34.25	0	510	539	742	516	31	28	42	24	7.3	12.3	14.3	6.6	3.5	9.2	9.8	3.0
3-62	0655	−118.50	34.31	0	570	461	733	485	45	40	60	20	9.1	9.4	13.1	4.6	6.6	7.2	9.8	2.9
3-63	5068	−116.40	33.82	0	3979	8686	9554	10645	114	99	151	85	18.3	25.1	31.0	13.2	6.0	8.5	10.5	4.8
3-64	5069	−116.39	33.93	0	6266	6448	8991	6351	204	213	294	103	15.7	21.0	26.2	24.7	5.1	6.3	8.1	3.2
3-65	5071	−116.58	34.05	0	3377	5844	6750	15840	161	216	270	170	25.3	30.7	39.8	14.1	9.3	10.9	14.4	4.1
3-66	5072	−116.66	33.99	0	6208	5133	8055	8170	125	124	176	111	10.6	15.4	18.6	8.4	4.5	5.2	6.9	3.1
3-67	5075	−116.92	34.09	0	4072	4080	5764	8376	87	113	143	81	12.3	17.2	21.1	8.2	6.2	5.8	8.5	1.5
3-68	5294	−116.22	33.75	0	9972	5864	11568	4716	302	126	327	82	36.4	20.1	41.6	11.9	12.5	6.7	14.2	4.9
3-69	5295	−116.55	33.93	0	5224	3852	6491	6685	137	137	194	99	30.0	25.5	39.4	21.8	7.5	5.9	9.5	3.9

Table B.2: Continued.

No.	ID	lon.	lat.	NF	Jerk (cm/s^3)				Acceleration (cm/s^2)				Velocity (cm/s)				Displacement (cm)			
					EW	NS	Hor.	UD	EW	NS	Hor.	UD	EW	NS	Hor.	UD	EW	NS	Hor.	UD
3-70	11591	−115.83	33.42	0	1236	1906	2272	930	56	99	114	46	8.7	12.5	15.2	5.6	5.5	4.9	7.4	2.7
3-71	11613	−115.91	33.50	0	2006	2502	3207	1717	130	116	174	53	17.6	14.3	22.7	8.0	10.3	7.1	12.5	4.1
3-72	11625	−115.99	33.56	0	2091	2362	3155	1586	114	115	162	37	18.1	9.7	20.5	6.2	13.4	3.9	14.0	5.0
3-73	11628	−115.98	33.28	0	4049	3151	5130	1136	122	150	193	23	10.5	12.1	16.0	3.5	5.7	4.3	7.2	1.4
3-74	12025	−116.50	33.83	0	2761	3537	4487	6873	87	74	115	106	13.8	11.1	17.7	6.7	5.7	5.3	7.8	2.4
3-75	12026	−116.16	33.72	0	1926	2606	3240	2390	107	102	148	41	15.1	9.5	17.8	6.6	7.5	4.6	8.8	3.6
3-76	12149	−116.51	33.96	0	3282	5010	5989	6974	151	167	225	164	20.8	19.2	28.3	9.9	8.0	7.9	11.3	3.7
3-77	12168	−116.68	33.32	0	1931	1928	2729	1833	43	46	63	37	2.0	2.1	2.8	1.7	0.5	0.5	0.7	0.5
3-78	12331	−116.98	33.73	0	3568	3718	5153	3163	95	80	124	61	5.8	5.5	8.0	2.9	2.2	1.2	2.5	1.2
3-79	12543	−116.22	33.72	0	2170	3386	4022	2876	85	81	117	53	30.3	13.2	33.1	8.7	18.2	6.6	19.4	4.7
3-80	12624	−116.28	33.63	0	2127	2194	3056	1919	40	48	62	21	3.9	2.5	4.6	1.9	2.0	1.0	2.2	0.9
3-81	12626	−116.08	33.43	0	1230	1710	2106	1342	44	44	62	23	4.9	2.7	5.6	2.1	2.1	1.3	2.5	0.8
3-82	12630	−116.68	33.89	0	4077	6463	7641	4904	48	51	70	39	3.8	2.5	4.6	2.5	2.7	1.2	3.0	1.1
3-83	13122	−117.71	33.87	0	1388	1217	1846	995	51	50	71	25	4.6	6.9	8.3	2.2	2.2	3.2	3.9	0.9
3-84	13123	−117.45	33.95	0	1715	1886	2549	2172	40	42	58	39	3.1	3.0	4.3	1.7	1.4	1.4	2.0	0.7
3-85	14196	−118.28	33.91	0	591	669	893	369	34	42	54	15	10.5	15.6	18.8	4.8	10.3	17.0	19.9	4.6
3-86	14368	−118.17	33.92	0	727	801	1082	678	39	50	64	16	11.3	18.3	21.5	6.4	8.6	21.4	23.0	4.7
3-87	14403	−118.26	33.93	0	877	594	1059	400	41	41	58	13	12.1	14.1	18.5	5.3	11.4	16.9	20.4	3.9
3-88	21081	−115.74	34.56	0	5077	3680	6271	5486	143	113	182	88	20.0	18.4	27.1	10.9	9.7	9.3	13.4	4.0
3-89	22074	−116.82	34.90	0	4187	4924	6463	7370	240	149	282	133	51.3	29.6	59.3	12.9	36.7	25.2	44.5	5.0
3-90	22161	−116.01	34.02	0	3267	3890	5080	2613	59	79	98	39	4.8	3.7	6.1	3.2	3.5	2.2	4.2	1.8
3-91	22170	−116.31	34.13	1	5250	4069	6642	9157	278	268	387	178	42.7	27.2	50.6	15.0	11.8	7.9	14.2	6.2
3-92	22561	−116.94	34.24	0	5702	6366	8546	6190	162	188	248	79	7.6	14.0	15.9	4.1	3.0	9.9	10.4	1.4
3-93	23522	−117.29	34.10	0	2810	2815	3978	3740	95	84	126	69	13.2	15.7	20.5	4.7	5.6	7.7	9.6	1.4
3-94	23525	−117.75	34.06	0	1425	1288	1920	1173	43	66	78	34	8.5	12.8	15.4	2.8	3.6	6.4	7.3	1.2
3-95	23572	−117.66	34.23	0	1746	1641	2396	2154	42	40	58	30	3.9	7.8	8.7	2.3	2.1	7.4	7.7	2.0
3-96	23573	−117.54	34.31	0	3168	2998	4361	3743	81	80	113	55	6.5	11.4	13.1	3.4	2.3	7.7	8.0	1.7
3-97	23583	−117.31	34.41	0	2078	1829	2768	2788	64	58	86	55	12.4	13.1	18.0	5.4	7.2	8.6	11.2	2.9
3-98	23584	−117.91	34.46	0	1018	1549	1854	1574	38	57	68	29	5.3	5.7	7.8	4.9	3.6	4.5	5.8	1.8
3-99	23585	−117.73	34.59	0	1517	2194	2667	1132	33	32	46	20	3.2	5.5	6.4	4.9	2.6	4.7	5.4	2.1

Table B.2: Continued.

No.	ID	lon.	lat.	NF	Jerk (cm/s^3)				Acceleration (cm/s^2)				Velocity (cm/s)				Displacement (cm)			
					EW	NS	Hor.	UD	EW	NS	Hor.	UD	EW	NS	Hor.	UD	EW	NS	Hor.	UD
3-100	23590	−117.74	34.38	0	903	803	1208	1240	38	46	60	28	5.5	10.1	11.5	3.0	3.2	6.6	7.3	1.7
3-101	23595	−117.98	34.49	0	661	958	1164	1064	24	38	45	23	5.3	6.9	8.7	4.3	3.8	4.8	6.1	2.2
3-102	23597	−117.52	34.47	0	3663	3364	4973	3870	95	84	127	62	7.6	9.7	12.3	5.2	3.1	7.5	8.1	2.6
3-103	23598	−117.58	34.17	0	1822	1322	2251	1081	75	66	100	37	8.7	9.6	13.0	3.0	3.5	6.8	7.6	1.5
3-104	24400	−118.18	34.04	0	1171	947	1506	510	63	42	76	20	7.6	15.5	17.3	4.1	5.6	15.8	16.8	2.9
3-105	24436	−118.53	34.16	0	696	1353	1521	572	42	65	77	25	5.3	9.4	10.8	2.6	3.0	5.8	6.5	1.1
3-106	24575	−118.39	34.66	0	1336	1145	1760	774	60	48	77	21	4.7	7.4	8.8	3.4	1.3	2.8	3.1	1.5
3-107	24577	−116.68	35.27	0	3517	3724	5122	2467	120	111	164	55	16.4	9.5	18.9	5.5	18.3	3.7	18.7	3.5
3-108	24592	−118.17	34.05	0	1357	1393	1944	785	57	55	79	32	7.4	11.5	13.7	4.2	3.9	11.8	12.4	2.3
3-109	24605	−118.20	34.06	0	867	982	1310	448	42	40	58	21	6.7	9.5	11.7	3.8	3.4	10.9	11.4	2.4
3-110	24611	−118.25	34.06	0	588	717	927	395	31	31	43	19	7.0	10.9	13.0	3.9	3.6	9.0	9.7	2.6
3-111	24612	−118.27	34.04	0	367	414	553	292	34	26	43	17	7.2	10.2	12.5	3.5	6.1	11.8	13.2	2.5
3-112	32075	−116.07	35.27	0	3703	2946	4732	2565	106	104	148	55	9.4	10.9	14.4	4.9	5.5	6.9	8.9	3.8
3-113	33083	−117.65	35.00	0	1856	2297	2954	1186	88	117	146	53	9.6	12.8	16.0	5.0	3.8	7.0	8.0	2.7
4-1	03	−118.52	34.21	1	12835	11220	17048	39102	319	444	547	785	42.9	60.6	74.3	39.1	11.9	20.3	23.5	9.3
4-2	06	−118.42	34.22	1	7438	9030	11699	16158	430	262	504	279	40.9	23.3	47.0	16.4	8.9	6.7	11.2	4.5
4-3	09	−118.41	34.19	1	7690	10331	12879	14031	248	296	386	256	31.6	25.2	40.4	11.6	13.0	9.2	16.0	5.4
4-4	11	−118.11	33.99	0	4254	4656	6306	2962	120	163	203	76	7.8	11.0	13.5	4.3	2.0	2.6	3.3	0.8
4-5	13	−118.44	34.13	1	11126	10830	15527	11597	477	434	645	313	69.2	57.2	89.8	19.7	11.9	17.7	21.4	5.5
4-6	14	−118.41	34.13	0	15911	16152	22673	12181	434	577	722	278	27.9	29.8	40.8	23.5	4.2	9.0	10.0	6.5
4-7	15	−118.48	34.09	1	6320	3685	7316	6510	207	176	272	136	18.3	29.4	34.6	6.8	3.7	6.0	7.0	1.2
4-8	16	−118.43	34.09	0	5578	5858	8088	9642	257	273	375	158	26.3	17.0	31.3	8.6	5.1	3.4	6.2	1.8
4-9	17	−118.38	34.11	0	4459	5466	7055	3820	102	156	186	90	11.1	14.5	18.2	4.5	1.4	3.0	3.3	0.7
4-10	18	−118.37	34.09	0	5436	4703	7188	7161	132	245	278	139	14.0	28.1	31.4	11.8	4.7	5.4	7.2	3.5
4-11	19	−118.09	34.09	0	6057	6347	8773	3487	234	135	270	65	12.6	9.2	15.6	4.9	2.1	2.3	3.1	1.5
4-12	20	−118.30	34.05	0	2245	3923	4520	1446	96	167	192	48	14.9	12.2	19.3	5.6	4.9	3.4	5.9	1.3
4-13	21	−118.30	34.08	0	7055	12743	14566	5899	322	409	521	81	29.8	25.2	39.0	7.3	4.2	4.2	5.9	1.3
4-14	22	−118.28	34.01	0	7081	5607	9032	3261	246	271	366	97	25.4	19.9	32.3	4.8	3.7	1.8	4.1	1.1
4-15	32	−118.19	34.11	0	4347	5562	7059	4199	129	155	201	98	11.6	8.4	14.4	5.6	1.9	2.2	3.0	2.0
4-16	33	−118.22	34.09	0	5518	4046	6842	4108	204	151	254	76	15.4	10.2	18.4	4.4	2.5	2.9	3.8	1.1

Table B.2: Continued.

No.	ID	lon.	lat.	NF	Jerk (cm/s^3)				Acceleration (cm/s^2)				Velocity (cm/s)				Displacement (cm)			
					EW	NS	Hor.	UD	EW	NS	Hor.	UD	EW	NS	Hor.	UD	EW	NS	Hor.	UD
4-17	34	−118.24	34.12	0	4483	5032	6739	3839	241	167	293	109	25.3	14.7	29.2	10.5	3.0	3.2	4.4	1.9
4-18	40	−118.27	33.81	0	2779	2251	3577	1327	94	90	130	48	7.3	5.2	9.0	3.3	1.7	1.6	2.3	0.6
4-19	44	−118.33	33.74	0	2290	2621	3480	1767	121	150	193	72	7.8	10.8	13.3	4.4	1.7	1.4	2.2	0.9
4-20	45	−118.35	33.90	0	3246	5531	6413	2838	77	140	160	49	11.7	8.9	14.7	4.9	3.2	3.6	4.8	0.9
4-21	46	−118.39	33.89	0	4198	3356	5374	2450	120	155	196	79	10.6	18.8	21.6	7.1	5.9	2.5	6.4	2.3
4-22	47	−118.43	33.96	0	2161	2774	3516	2512	68	139	155	51	16.6	15.4	22.6	9.8	8.1	3.5	8.9	3.8
4-23	49	−118.55	34.04	0	5817	10181	11726	7466	188	438	476	157	14.0	40.4	42.8	15.1	4.0	6.6	7.7	4.4
4-24	51	−118.79	34.02	0	513	424	666	287	24	18	29	12	3.4	3.3	4.7	1.5	1.0	0.7	1.2	0.5
4-25	53	−118.61	34.21	1	13331	10048	16694	23192	343	381	513	410	39.7	64.2	75.5	14.4	10.0	16.7	19.5	4.4
4-26	54	−118.43	34.00	0	13349	15044	20113	4969	324	433	541	101	29.4	22.3	36.9	10.3	7.1	4.1	8.2	4.3
4-27	55	−118.67	34.26	1	16262	18166	24381	18950	503	713	873	341	46.2	52.3	69.8	13.6	6.3	6.6	9.1	2.8
4-28	56	−118.62	34.39	1	4140	3427	5375	8492	411	348	539	281	117.2	60.9	132.1	28.9	52.5	19.2	55.9	7.6
4-29	57	−118.43	34.42	0	18793	10379	21469	8171	447	389	592	280	37.9	43.8	57.9	18.5	9.4	11.3	14.7	6.9
4-30	58	−118.30	34.27	0	3451	3332	4797	5899	151	127	198	175	16.2	15.7	22.6	9.8	4.7	4.8	6.7	1.9
4-31	59	−118.30	34.20	0	2785	4973	5700	2971	107	153	186	81	10.7	13.0	16.9	2.8	2.2	2.9	3.6	0.9
4-32	60	−118.25	34.24	0	6496	4710	8023	4279	201	137	243	104	12.0	11.8	16.8	6.0	2.2	1.7	2.8	1.2
4-33	61	−118.23	34.29	0	5871	9938	11543	8448	162	242	291	149	11.2	12.3	16.6	5.6	2.4	2.2	3.2	1.3
4-34	63	−118.23	34.20	0	11234	14486	18332	6145	167	330	370	121	10.9	20.0	22.8	6.9	2.6	5.9	6.5	1.5
4-35	65	−117.88	34.14	0	1459	2489	2885	1309	45	89	100	46	3.5	5.1	6.2	3.4	0.7	1.2	1.4	0.8
4-36	66	−118.02	34.09	0	4078	4287	5917	2622	123	155	198	57	11.2	9.6	14.8	2.8	3.6	2.8	4.6	0.8
4-37	67	−117.94	34.15	0	1933	1239	2296	1288	78	26	83	47	4.8	2.4	5.4	3.2	0.8	0.5	0.9	1.0
4-38	68	−117.87	34.08	0	1250	1529	1975	1485	71	64	96	55	5.3	6.5	8.3	4.4	1.0	2.2	2.4	1.0
4-39	69	−117.97	34.10	0	3168	2839	4254	1777	132	92	161	42	7.7	5.6	9.6	2.7	1.6	1.9	2.5	1.4
4-40	70	−117.92	34.09	0	1754	2366	2945	1955	80	100	128	43	8.2	4.8	9.5	4.1	2.2	1.2	2.5	1.7
4-41	71	−117.95	34.06	0	1859	1667	2497	2376	64	62	89	43	4.6	7.3	8.6	3.6	1.4	1.6	2.1	0.8
4-42	72	−117.92	34.03	0	2126	1967	2897	1209	114	92	147	45	8.4	8.0	11.6	4.1	1.1	2.0	2.2	0.8
4-43	73	−117.94	33.99	0	1572	1969	2519	1267	47	74	88	38	6.3	6.0	8.7	2.6	1.4	1.5	2.0	0.6
4-44	74	−117.97	33.92	0	4175	2142	4693	1480	198	105	224	57	10.2	9.9	14.2	2.6	1.9	1.6	2.5	0.6
4-45	75	−118.03	34.02	0	1193	1540	1947	594	43	73	85	22	3.1	7.0	7.7	2.0	0.7	1.2	1.4	0.3
4-46	77	−118.09	33.94	0	4045	3955	5657	2186	129	131	184	51	10.2	8.4	13.2	3.2	3.5	2.1	4.0	0.5

Table B.2: Continued.

No.	ID	lon.	lat.	NF	Jerk (cm/s^3)				Acceleration (cm/s^2)				Velocity (cm/s)				Displacement (cm)			
					EW	NS	Hor.	UD	EW	NS	Hor.	UD	EW	NS	Hor.	UD	EW	NS	Hor.	UD
4-47	78	−118.20	33.90	0	4570	2816	5368	1604	117	82	142	41	9.4	7.8	12.2	4.0	2.8	2.3	3.6	0.8
4-48	79	−118.14	33.92	0	3430	3313	4769	2669	139	156	209	54	10.3	10.2	14.4	5.2	2.2	2.2	3.1	1.2
4-49	81	−118.24	33.84	0	3027	3944	4972	2212	85	85	120	41	8.4	7.6	11.3	2.2	2.4	1.5	2.9	0.7
4-50	82	−118.27	33.74	0	3576	5118	6244	1145	145	179	230	49	14.5	14.9	20.8	3.5	2.5	2.8	3.7	1.8
4-51	83	−118.04	33.73	0	2266	2077	3074	777	74	87	114	18	7.7	6.1	9.9	1.6	1.6	2.0	2.6	0.3
4-52	84	−118.10	33.85	0	3668	5094	6277	3823	119	129	176	61	9.8	12.0	15.5	2.8	2.3	1.9	3.0	0.6
4-53	86	−118.02	33.85	0	4545	2548	5211	892	147	92	173	29	11.1	8.9	14.2	1.9	1.8	2.0	2.7	0.7
4-54	87	−117.90	33.92	0	2210	2093	3044	1255	100	95	138	37	6.8	5.9	9.0	3.2	1.7	1.0	2.0	0.5
4-55	88	−117.95	33.82	0	1648	1822	2457	1230	65	72	97	40	6.9	6.4	9.4	2.3	1.7	1.3	2.1	0.5
4-56	89	−117.82	33.73	0	1828	1664	2472	1199	66	70	96	24	4.8	4.1	6.3	2.2	1.5	0.9	1.7	0.5
4-57	90	−117.82	33.82	0	1243	1144	1689	715	43	37	57	27	3.7	2.4	4.4	2.0	1.3	0.8	1.5	0.5
4-58	91	−118.36	34.05	0	11558	8323	14243	2954	420	433	604	98	43.4	38.0	57.6	8.4	6.2	7.0	9.3	1.6
4-59	93	−118.04	34.13	0	3213	3347	4639	2758	112	87	142	52	9.0	6.7	11.2	3.6	2.2	2.6	3.4	0.9
4-60	94	−118.16	33.97	0	2685	2823	3896	1748	62	98	116	51	8.4	7.3	11.1	4.3	1.8	1.7	2.5	1.1
4-61	95	−118.08	34.17	0	6358	4901	8028	4834	186	256	316	145	12.8	13.4	18.5	8.3	2.9	2.5	3.8	2.8
4-62	96	−118.29	34.02	0	2771	4766	5513	4594	63	131	145	229	7.8	10.7	13.2	20.0	1.8	2.3	3.0	3.9
4-63	99	−118.06	34.13	0	3456	2394	4204	2623	90	88	126	83	8.0	8.7	11.8	4.6	1.6	1.9	2.5	1.2
4-64	0141	−118.30	34.12	0	13053	8551	15604	8070	282	163	326	137	29.8	13.5	32.7	10.2	3.7	2.2	4.3	1.8
4-65	0634	−118.07	33.92	0	2111	1962	2882	2120	55	86	102	45	7.9	8.1	11.3	3.7	3.5	2.7	4.4	1.8
4-66	0638	−118.46	34.06	0	3732	4328	5715	10683	162	184	245	136	19.0	21.5	28.7	8.4	6.8	5.2	8.6	2.5
4-67	0757	−118.48	34.10	1	24208	9299	25932	15391	455	258	523	155	31.3	25.8	40.5	8.0	4.6	5.1	6.8	1.7
4-68	5030	−117.99	34.52	0	4786	7068	8536	3177	121	163	203	78	11.3	8.6	14.2	5.7	2.6	1.6	3.0	1.5
4-69	5080	−118.69	34.08	0	11108	16413	19819	13671	161	180	242	121	10.9	10.2	14.9	5.9	2.4	4.0	4.6	1.9
4-70	5081	−118.60	34.08	0	7303	12992	14904	17248	192	327	379	189	12.7	15.9	20.4	8.9	2.2	4.9	5.3	2.7
4-71	5082	−118.45	34.05	0	9170	11619	14801	10282	250	252	355	160	36.2	20.3	41.5	10.5	9.5	5.5	11.0	3.8
4-72	5106	−118.12	33.78	0	1968	1756	2637	1601	67	63	92	32	8.7	5.9	10.5	5.5	3.1	1.7	3.5	1.7
4-73	5108	−118.71	34.23	1	13045	11179	17180	13929	279	228	360	148	17.5	17.6	24.8	13.7	4.6	6.9	8.2	2.7
4-74	5129	−118.16	34.00	0	4342	6570	7875	3543	154	260	302	82	13.2	19.4	23.5	5.7	3.9	2.1	4.5	1.5
4-75	5243	−118.38	33.90	0	4326	5675	7135	3625	120	185	220	84	12.6	14.3	19.1	7.0	5.1	2.9	5.9	2.1
4-76	5288	−118.02	33.70	0	3100	2956	4284	878	110	117	161	20	16.4	10.6	19.5	4.5	2.5	3.1	3.9	1.1

Table B.2: Continued.

No.	ID	lon.	lat.	NF	Jerk (cm/s^3)				Acceleration (cm/s^2)				Velocity (cm/s)				Displacement (cm)			
					EW	NS	Hor.	UD	EW	NS	Hor.	UD	EW	NS	Hor.	UD	EW	NS	Hor.	UD
4-77	5296	−118.13	34.14	0	6712	6605	9417	5290	143	161	215	103	10.0	13.4	16.7	5.6	2.7	2.1	3.4	1.7
4-78	5466	−117.84	33.68	0	2146	1902	2867	1409	102	68	123	32	9.4	7.8	12.3	2.5	2.1	1.5	2.6	0.9
4-79	12673	−116.96	33.79	0	661	1980	2087	1689	22	97	100	79	3.7	7.6	8.5	8.1	1.2	1.9	2.2	1.6
4-80	13122	−117.71	33.87	0	2726	1028	2913	2506	98	24	101	102	5.8	1.6	6.0	7.6	0.4	0.2	0.5	0.8
4-81	13123	−117.45	33.95	0	1937	726	2068	1746	58	21	61	62	2.7	2.3	3.5	3.1	0.3	0.5	0.6	0.5
4-82	13160	−117.90	33.63	0	1465	313	1498	999	60	17	62	40	5.2	2.3	5.6	4.3	1.8	0.8	1.9	1.9
4-83	13197	−118.00	33.66	0	1288	1233	1783	1930	68	18	71	89	5.7	2.3	6.2	5.4	1.5	0.8	1.7	1.5
4-84	13610	−117.93	33.62	0	1579	513	1660	1783	79	19	82	103	7.3	2.1	7.6	7.1	2.4	0.9	2.5	1.9
4-85	13660	−117.02	33.73	0	696	838	1090	978	27	45	52	63	2.0	4.7	5.1	4.5	0.2	0.6	0.6	0.6
4-86	14159	−118.31	33.72	0	2133	1682	2716	2199	93	69	116	99	6.6	2.9	7.2	5.5	1.1	0.3	1.1	0.5
4-87	14196	−118.28	33.91	0	2905	2283	3694	4212	99	54	113	89	10.2	2.7	10.6	7.0	3.1	1.1	3.2	2.1
4-88	14242	−118.19	33.84	0	2415	2110	3207	1979	68	38	78	63	8.1	2.6	8.6	4.8	2.8	1.1	3.0	2.1
4-89	14368	−118.17	33.92	0	7720	7178	10541	5366	174	129	216	218	9.9	3.5	10.5	12.7	3.5	1.2	3.7	1.9
4-90	14403	−118.26	33.93	0	4984	2403	5533	4381	194	56	202	139	15.8	2.7	16.0	13.2	3.6	1.4	3.8	3.2
4-91	14404	−118.40	33.75	0	1363	1822	2275	1308	53	42	68	71	3.4	1.8	3.8	5.0	0.9	0.4	1.0	0.7
4-92	14405	−118.36	33.79	0	2659	1069	2865	2184	113	40	120	104	8.8	2.0	9.1	5.7	1.2	0.5	1.3	0.9
4-93	14560	−118.20	33.77	0	1220	810	1464	1929	36	22	42	50	4.9	2.1	5.3	4.0	1.6	0.6	1.7	1.3
4-94	14578	−118.08	33.76	0	1822	2825	3361	2093	36	82	90	60	2.1	6.9	7.2	5.7	1.4	2.2	2.6	2.1
4-95	23497	−117.57	34.10	0	1586	1101	1931	2016	45	32	55	71	3.2	2.0	3.8	3.8	0.7	0.3	0.7	0.5
4-96	23542	−117.29	34.07	0	1850	1155	2181	1657	94	43	103	83	6.5	2.6	7.0	5.9	1.1	0.5	1.2	1.0
4-97	23572	−117.66	34.23	0	2764	1549	3168	2852	68	36	77	78	4.3	2.2	4.8	3.8	0.3	0.4	0.5	0.6
4-98	23573	−117.54	34.31	0	1246	903	1538	1430	41	21	46	41	3.2	1.3	3.4	2.9	0.6	0.2	0.6	0.5
4-99	23574	−117.66	34.37	0	2510	1892	3143	1548	59	33	67	46	3.7	2.0	4.2	3.7	0.5	0.2	0.5	0.4
4-100	23590	−117.74	34.38	0	776	1032	1291	1151	36	33	49	55	3.5	2.9	4.5	5.0	0.9	0.3	0.9	0.7
4-101	23595	−117.98	34.49	0	1693	1880	2530	1429	59	35	69	71	6.3	2.2	6.7	6.0	1.5	0.5	1.6	1.3
4-102	23597	−117.52	34.47	0	1575	1037	1886	1391	56	35	66	46	4.0	2.3	4.6	5.0	1.3	0.5	1.4	1.0
4-103	23598	−117.58	34.17	0	1409	744	1593	1796	50	25	56	70	5.8	2.2	6.3	4.1	0.6	0.4	0.7	0.5
4-104	23672	−117.32	34.18	0	569	1968	2049	1025	20	67	70	33	1.5	4.0	4.3	2.8	0.3	0.7	0.8	0.3
4-105	24047	−118.33	34.49	0	6138	2616	6672	6888	137	84	161	148	12.4	6.7	14.1	18.3	2.8	1.5	3.2	2.6
4-106	24055	−118.24	34.60	0	3496	3944	5270	2325	90	95	131	144	10.4	11.5	15.5	14.9	3.0	2.1	3.6	2.4

Table B.2: Continued.

No.	ID	lon.	lat.	NF	Jerk (cm/s^3)				Acceleration (cm/s^2)				Velocity (cm/s)				Displacement (cm)			
					EW	NS	Hor.	UD	EW	NS	Hor.	UD	EW	NS	Hor.	UD	EW	NS	Hor.	UD
4-107	24087	−118.44	34.24	1	9328	30716	32101	8898	337	541	638	302	39.4	17.4	43.0	22.7	8.7	6.9	11.1	9.7
4-108	24088	−118.38	34.29	1	5176	7079	8769	8025	295	177	344	424	31.1	14.1	34.1	50.8	10.9	4.7	11.9	8.7
4-109	24092	−118.21	34.87	0	1098	854	1391	2234	39	23	45	74	3.5	1.4	3.7	4.6	0.8	0.3	0.9	0.4
4-110	24157	−118.36	34.01	0	7403	3538	8205	7660	234	89	251	164	14.9	8.4	17.1	17.3	6.2	3.3	7.0	5.4
4-111	24207	−118.40	34.33	1	59557	58000	83133	59156	1205	1554	1966	1260	49.1	54.5	73.3	104.0	7.8	6.3	10.0	16.7
4-112	24207	−118.40	34.33	1	18936	6362	19976	13751	407	180	445	426	44.8	16.2	47.6	30.7	5.9	2.6	6.5	5.0
4-113	24271	−118.43	34.67	0	2089	3239	3854	2300	75	97	123	85	9.5	7.0	11.8	9.4	2.8	2.7	3.9	3.3
4-114	24272	−118.56	34.61	0	6930	6123	9247	5008	221	78	235	155	13.5	3.6	14.0	8.7	2.9	3.1	4.3	4.2
4-115	24278	−118.64	34.56	0	17168	6496	18356	9424	557	213	596	504	51.8	12.3	53.3	52.1	11.1	4.6	12.0	13.7
4-116	24279	−118.53	34.39	1	19864	16952	26114	14717	572	537	785	578	74.7	30.7	80.8	95.6	19.2	10.5	21.9	25.9
4-117	24283	−118.88	34.29	0	5273	8347	9873	4745	143	286	320	189	6.6	20.5	21.5	20.0	3.1	5.0	5.9	3.9
4-118	24303	−118.34	34.09	0	8987	10501	13822	12154	227	139	266	381	18.3	9.8	20.8	22.2	4.8	2.6	5.4	3.5
4-119	24305	−118.24	34.59	0	2157	2284	3142	3067	72	49	87	87	7.1	6.8	9.8	7.8	1.7	1.8	2.5	1.5
4-120	24306	−118.24	34.60	0	2159	1440	2595	2716	62	57	84	89	7.2	7.1	10.1	7.5	2.0	1.9	2.8	1.5
4-121	24307	−118.24	34.60	0	2004	1988	2823	2693	104	50	115	83	8.1	6.9	10.6	8.5	1.9	1.8	2.6	1.9
4-122	24308	−118.24	34.60	0	2380	1363	2743	1670	56	47	73	78	8.0	7.9	11.2	8.6	2.2	1.9	2.8	1.8
4-123	24309	−118.24	34.60	0	5210	2544	5797	3601	174	61	185	128	14.3	8.2	16.5	9.9	2.1	1.5	2.6	1.2
4-124	24310	−118.36	34.76	0	1949	1583	2511	1133	67	28	73	45	4.3	3.6	5.5	3.4	2.1	2.2	3.0	2.5
4-125	24389	−118.42	34.06	0	6649	7232	9824	5931	251	113	275	217	20.9	8.7	22.7	25.1	6.2	2.8	6.8	5.8
4-126	24396	−118.80	34.01	0	3051	3753	4836	2814	127	85	153	92	8.4	4.3	9.4	9.2	2.0	1.0	2.2	2.0
4-127	24399	−118.06	34.22	0	4811	3792	6126	6265	131	87	157	229	5.4	2.9	6.2	7.6	0.5	0.6	0.8	0.7
4-128	24400	−118.18	34.04	0	11754	4498	12585	13785	348	110	365	400	14.6	4.3	15.2	30.8	4.4	1.6	4.6	2.7
4-129	24401	−118.13	34.12	0	4414	3796	5822	7406	122	88	151	148	7.9	3.8	8.8	6.6	1.1	0.7	1.3	1.1
4-130	24436	−118.53	34.16	1	74693	41614	85503	51510	1745	1028	2025	971	109.7	72.5	131.5	77.9	21.5	17.5	27.7	24.8
4-131	24461	−118.15	34.07	0	3486	1546	3813	2869	99	45	109	78	10.9	4.2	11.7	4.9	2.4	1.2	2.7	1.6
4-132	24469	−118.48	34.65	0	3566	2914	4605	2331	82	52	97	56	6.2	4.1	7.4	6.5	1.9	2.7	3.3	3.2
4-133	24475	−118.21	34.74	0	1479	2232	2678	2185	63	47	78	80	5.3	4.0	6.6	7.0	1.3	0.8	1.5	1.4
4-134	24514	−118.44	34.33	1	12925	25450	28544	31897	593	525	792	827	77.4	19.1	79.7	128.9	19.9	7.6	21.3	35.3
4-135	24521	−118.14	34.58	0	2772	1685	3244	2579	65	40	77	60	8.4	4.0	9.3	7.4	1.8	1.3	2.2	2.1
4-136	24523	−118.48	34.65	0	2877	1665	3324	945	62	41	74	36	5.3	3.7	6.5	3.1	2.0	3.0	3.6	2.1

Table B.2: Continued.

No.	ID	lon.	lat.	NF	Jerk (cm/s^3)				Acceleration (cm/s^2)				Velocity (cm/s)				Displacement (cm)			
					EW	NS	Hor.	UD	EW	NS	Hor.	UD	EW	NS	Hor.	UD	EW	NS	Hor.	UD
4-137	24538	−118.49	34.01	0	28643	10815	30617	14973	866	228	895	363	41.0	14.2	43.4	25.1	13.2	4.5	13.9	8.2
4-138	24575	−118.39	34.66	0	4043	4085	5747	4175	112	48	122	152	8.1	4.6	9.3	7.3	1.9	2.3	3.0	2.1
4-139	24576	−118.20	34.58	0	2035	2804	3465	908	59	43	73	43	5.5	4.7	7.2	3.9	1.2	1.3	1.8	1.0
4-140	24586	−118.54	34.85	0	660	1863	1976	914	68	46	82	55	13.1	7.2	14.9	9.9	6.5	3.8	7.6	5.6
4-141	24592	−118.17	34.05	0	14568	5977	15747	8899	310	132	337	258	14.0	7.6	15.9	12.8	2.3	1.6	2.8	3.1
4-142	24605	−118.20	34.06	0	5328	10839	12078	7971	117	483	497	210	6.4	31.1	31.7	10.7	1.3	2.5	2.8	2.6
4-143	24607	−118.56	34.57	0	10635	8104	13371	6284	253	115	278	171	11.9	4.5	12.7	11.8	5.4	3.8	6.6	3.7
4-144	24611	−118.25	34.06	0	6159	4964	7910	4894	180	95	204	124	20.0	4.6	20.5	13.9	2.7	1.3	3.0	3.4
4-145	24612	−118.27	34.04	0	3611	2507	4396	3745	183	64	193	101	14.2	5.3	15.2	12.2	2.2	1.6	2.7	3.6
4-146	24644	−118.72	34.74	0	1474	1613	2185	1296	97	43	106	89	8.8	6.4	10.9	12.2	4.1	3.5	5.4	3.5
4-147	24688	−118.44	34.07	0	11286	8397	14067	20131	272	261	377	465	21.8	9.6	23.8	22.2	3.6	3.3	4.9	6.4
4-148	25091	−119.85	34.42	0	1209	1086	1625	2094	68	38	78	76	6.7	3.0	7.3	7.0	1.6	0.7	1.8	1.6
4-149	25147	−119.12	34.11	0	4102	2341	4723	5339	141	63	154	174	16.2	4.3	16.7	13.1	2.7	1.0	2.8	2.1
4-150	25148	−119.07	34.11	0	4806	3190	5768	3296	219	66	228	132	19.0	3.3	19.3	10.2	1.9	0.5	2.0	1.4
4-151	25281	−119.21	34.15	0	1766	2665	3197	2221	36	84	92	101	4.6	9.6	10.7	11.3	2.3	5.4	5.9	6.5
4-152	25282	−119.08	34.21	0	2690	2525	3690	2066	122	48	131	118	10.8	4.9	11.9	11.7	3.8	1.2	4.0	2.9
4-153	25340	−119.29	34.28	0	961	581	1123	1276	53	25	58	74	7.9	5.1	9.4	12.0	2.4	2.9	3.8	3.1
4-154	34093	−118.18	35.07	0	1156	1207	1671	847	52	26	58	37	4.0	1.8	4.4	4.5	0.4	0.3	0.5	0.7
4-155	34237	−118.38	35.04	0	1407	1193	1845	1524	58	25	63	49	3.4	2.0	3.9	3.1	0.4	0.5	0.6	0.5
5-1	ABN	135.52	34.64	0	7228	6557	9759	12711	226	213	310	115	24.8	21.3	32.6	6.2	7.9	9.2	12.1	2.6
5-2	CHY	135.66	34.44	0	5982	3998	7195	5188	108	91	141	76	4.9	5.2	7.1	2.4	1.0	2.0	2.3	0.9
5-3	FKS	135.47	34.69	0	7485	3114	8106	12772	211	179	276	191	29.8	31.0	43.0	9.6	13.2	15.5	20.3	5.0
5-4	MRG	135.57	34.68	0	7851	7228	10672	9499	125	210	244	162	24.6	27.0	36.6	6.1	9.6	10.8	14.4	2.7
5-5	SKI	135.47	34.56	0	18156	6178	19178	6459	182	149	235	95	15.7	15.9	22.3	6.6	8.0	10.8	13.4	3.5
5-6	TDO	135.41	34.48	0	6520	8523	10731	10757	190	290	347	129	14.7	24.4	28.5	5.9	8.6	6.9	11.1	2.5
5-7	YAE	135.61	34.68	0	2167	2136	3043	6806	144	154	211	128	21.8	21.2	30.4	7.0	9.2	9.3	13.1	3.4
5-8	aida	134.17	34.94	0	879	508	1016	673	36	20	42	30	2.4	-	3.4	1.6	1.8	-	2.5	1.1
5-9	awaj	134.91	34.34	0	2909	7418	7968	1501	162	200	257	53	11.7	-	16.5	5.9	3.3	-	4.7	3.6
5-10	hegu	135.68	34.65	0	643	546	843	398	20	21	29	13	2.5	-	3.6	1.9	2.4	-	3.4	1.2
5-11	kak	134.84	34.76	0	9631	8818	13058	8068	318	235	395	168	27.5	20.4	34.2	10.2	9.6	6.2	11.4	3.2

Table B.2: Continued.

No.	ID	lon.	lat.	NF	Jerk (cm/s^3)				Acceleration (cm/s^2)				Velocity (cm/s)				Displacement (cm)			
					EW	NS	Hor.	UD	EW	NS	Hor.	UD	EW	NS	Hor.	UD	EW	NS	Hor.	UD
5-12	kob	135.18	34.69	1	9028	14150	16785	10431	617	818	1025	332	75.8	92.4	119.5	40.6	18.6	18.0	25.8	10.6
5-13	koya	135.59	34.22	0	1520	1175	1921	620	46	50	68	21	2.7	2.9	4.0	1.8	1.6	2.9	3.3	1.4
5-14	nis	134.96	34.66	1	11392	11182	15963	11811	455	474	657	380	41.8	44.3	60.9	24.1	14.2	10.6	17.7	6.1
5-15	osa	135.52	34.68	0	1444	1141	1840	2343	66	81	104	65	65.9	80.9	104.3	64.5	8.0	8.6	11.7	3.1
5-16	tat	135.14	34.65	1	21608	14120	25812	14402	657	606	893	279	122.0	122.7	173.0	20.5	31.4	34.9	47.0	6.8
5-17	taz	135.34	34.81	1	18990	11646	22277	16572	601	684	910	418	88.8	66.7	111.1	33.8	16.7	23.5	28.9	8.3
5-18	wach	135.40	35.28	0	278	561	626	296	21	16	26	14	3.0	-	4.3	3.1	1.3	-	1.9	2.1
6-1	ATS	28.69	40.98	0	3748	5237	6440	4199	186	253	314	80	35.3	37.6	51.6	10.7	19.2	27.2	33.3	8.5
6-2	BRS	29.13	40.18	0	733	834	1110	1005	53	44	69	25	9.5	8.6	12.8	6.9	6.2	3.9	7.3	4.2
6-3	BTS	27.98	40.99	0	2918	2087	3587	623	99	87	132	24	11.7	11.2	16.2	4.0	3.8	9.3	10.0	3.6
6-4	CNA	28.76	41.02	0	3955	5139	6485	3064	132	177	221	58	10.3	16.8	19.7	7.3	4.4	12.0	12.8	5.1
6-5	FAT	28.95	41.02	0	10559	14307	17782	15881	162	190	249	132	15.2	18.9	24.3	8.8	8.8	11.7	14.6	6.7
6-6	IST	29.09	41.08	0	1782	1175	2135	1328	59	42	73	35	9.6	7.7	12.2	5.8	7.7	5.3	9.3	5.7
6-7	KMP	28.93	41.00	0	4150	4358	6018	4224	128	107	167	83	14.3	18.4	23.2	10.2	10.2	10.3	14.5	6.1
6-8	SKR	30.38	40.74	1	-	28717	40612	20561	-	399	564	254	-	80.2	113.5	42.6	-	61.9	87.5	23.2
6-9	TKR	27.52	40.98	0	721	745	1036	263	32	33	46	10	5.8	3.2	6.7	1.3	4.8	1.9	5.2	0.6
6-10	YKP	29.01	41.08	0	1086	964	1453	964	36	41	54	27	7.2	9.2	11.7	6.1	3.9	7.0	8.1	5.9
6-11	YPT	29.76	40.76	1	10010	8081	12865	17065	230	322	396	241	88.4	88.3	124.9	31.7	55.7	52.4	76.5	20.9
6-12	cek	28.70	40.97	0	2496	3092	3973	2476	88	115	145	49	15.0	11.9	19.2	5.5	8.3	8.3	11.8	4.0
6-13	erg	27.79	40.98	0	2770	2159	3512	1745	99	88	132	55	13.2	14.1	19.3	7.1	4.6	8.5	9.6	5.4
6-14	gbz	29.44	40.82	1	8095	9169	12231	20366	141	262	297	192	47.2	44.4	64.8	33.0	34.3	44.1	55.9	8.9
6-15	gyn	30.73	40.39	0	8175	8048	11472	10192	117	136	179	128	14.3	13.1	19.4	17.3	6.1	5.1	7.9	11.9
6-16	izn	29.69	40.44	0	3510	5282	6341	7452	121	90	151	80	28.0	23.3	36.4	7.7	17.6	10.7	20.6	5.2
6-17	izt	29.96	40.79	1	11082	9150	14371	13825	222	166	277	145	58.9	35.5	68.7	15.0	21.5	14.7	26.0	10.7
7-1	C002	120.41	23.72	0	2168	3424	4053	5667	108	135	173	96	43.2	56.0	70.8	17.8	38.7	57.5	69.3	16.8
7-2	C004	120.17	23.60	0	2138	1974	2910	2452	95	93	133	39	21.6	14.7	26.1	6.0	15.5	13.5	20.6	4.9
7-3	C006	120.55	23.58	1	8583	8464	12054	12905	348	351	495	211	60.0	42.8	73.7	21.7	25.5	14.5	29.3	12.4
7-4	C008	120.27	23.49	0	3768	3125	4896	4441	126	117	172	72	30.6	23.3	38.4	11.6	17.6	14.5	22.8	9.4
7-5	C010	120.54	23.47	0	6879	6490	9457	10482	221	171	279	139	18.6	24.4	30.7	10.2	5.0	9.1	10.4	6.0
7-6	C012	120.15	23.33	0	1256	1525	1976	987	52	61	80	29	12.6	15.0	19.6	9.1	9.6	12.1	15.4	7.8

Table B.2: Continued.

No.	ID	lon.	lat.	NF	Jerk (cm/s^3)				Acceleration (cm/s^2)				Velocity (cm/s)				Displacement (cm)			
					EW	NS	Hor.	UD	EW	NS	Hor.	UD	EW	NS	Hor.	UD	EW	NS	Hor.	UD
7-7	C014	120.58	23.30	0	3080	5638	6424	1705	224	255	339	98	24.1	23.4	33.6	11.5	6.8	4.4	8.1	4.3
7-8	C015	120.41	23.36	0	3095	3439	4627	1077	141	149	205	33	23.7	24.0	33.7	7.0	6.6	13.4	14.9	4.4
7-9	C016	120.15	23.22	0	2602	2408	3545	1107	97	105	143	45	13.8	16.2	21.3	10.7	10.5	14.5	17.9	7.1
7-10	C017	120.27	23.22	0	1241	1241	1755	942	51	54	74	29	17.0	17.1	24.1	5.9	9.6	17.5	20.0	5.8
7-11	C019	120.48	23.18	0	1316	1705	2154	822	50	64	82	23	5.7	6.0	8.2	4.3	4.2	3.3	5.4	4.2
7-12	C022	120.46	23.05	0	1480	942	1755	733	64	44	77	23	7.0	5.4	8.8	4.4	6.3	5.6	8.4	4.6
7-13	C023	120.28	22.97	0	912	927	1301	598	46	58	74	18	7.3	8.4	11.2	5.5	4.5	8.5	9.7	6.4
7-14	C024	120.61	23.76	1	5730	6065	8344	5898	276	162	320	141	51.3	43.1	67.0	47.0	36.8	33.9	50.1	33.9
7-15	C025	120.51	23.78	0	5359	8506	10053	8924	159	152	220	170	51.1	32.9	60.8	37.7	35.5	28.3	45.4	31.4
7-16	C026	120.41	23.80	0	3086	1735	3540	4390	76	66	101	70	41.5	26.3	49.1	24.2	36.0	22.6	42.5	16.3
7-17	C027	120.25	23.75	0	1328	1902	2320	3625	54	51	74	46	20.4	15.7	25.7	8.0	15.9	13.5	20.9	5.7
7-18	C028	120.61	23.63	1	43593	42600	60952	41021	624	750	976	335	63.0	83.8	104.9	30.5	20.9	21.2	29.8	15.4
7-19	C029	120.53	23.61	1	4594	4606	6505	6209	283	233	367	158	35.1	39.9	53.1	17.7	12.2	30.4	32.8	11.4
7-20	C032	120.29	23.58	0	1771	2345	2938	3637	86	73	113	62	26.8	19.7	33.3	7.9	18.5	14.9	23.7	6.0
7-21	C033	120.22	23.54	0	1699	1460	2240	1615	68	59	90	34	19.6	17.7	26.4	8.5	14.5	13.8	20.1	7.0
7-22	C034	120.54	23.52	0	4905	4860	6905	4127	243	294	381	91	34.6	44.9	56.7	16.0	10.1	16.7	19.6	7.9
7-23	C035	120.58	23.52	0	13781	8231	16052	3625	246	244	346	106	44.3	30.8	53.9	17.8	11.2	11.6	16.2	6.2
7-24	C036	120.48	23.61	0	7357	6269	9666	6627	267	200	333	104	41.6	44.1	60.6	14.1	22.6	34.4	41.1	9.8
7-25	C039	120.34	23.52	0	1986	2572	3249	2106	114	97	149	38	24.2	24.8	34.7	11.3	12.0	16.2	20.2	7.1
7-26	C041	120.60	23.44	0	9295	10946	14360	5359	297	630	697	123	20.3	37.3	42.5	9.7	7.1	8.9	11.4	6.1
7-27	C042	120.58	23.36	0	1412	1783	2274	1328	98	65	117	63	14.5	10.5	18.0	8.7	6.5	7.6	10.0	4.0
7-28	C046	120.46	23.48	0	5156	7226	8877	3924	143	186	235	80	20.7	20.9	29.4	7.7	8.7	9.0	12.5	5.8
7-29	C047	120.45	23.49	0	5159	5204	7328	3918	165	178	243	83	23.1	26.7	35.3	14.7	12.8	10.1	16.3	8.9
7-30	C052	120.50	23.29	0	1555	2632	3057	1032	84	151	172	40	11.2	14.9	18.6	7.1	6.5	6.0	8.9	6.0
7-31	C054	120.31	23.31	0	1591	1723	2345	1364	93	94	132	33	17.8	17.9	25.2	8.0	12.2	13.5	18.2	5.4
7-32	C055	120.27	23.27	0	1809	2318	2940	2064	97	88	131	40	16.4	27.3	31.9	7.1	10.4	18.4	21.1	7.1
7-33	C057	120.41	23.15	0	1113	1436	1816	550	39	53	65	21	6.5	6.5	9.2	4.3	4.2	4.4	6.1	5.8
7-34	C058	120.32	23.17	0	1531	6388	6569	1029	47	57	74	25	10.9	14.2	17.9	5.0	5.3	10.8	12.0	4.2
7-35	C063	120.34	23.03	0	825	1029	1319	467	58	65	87	26	7.8	9.1	12.0	5.8	4.2	7.1	8.3	4.6
7-36	C065	120.34	22.91	0	1483	1376	2023	634	114	93	147	29	17.2	13.2	21.6	5.1	6.3	7.6	9.9	6.4

Table B.2: Continued.

No.	ID	lon.	lat.	NF	Jerk (cm/s^3)				Acceleration (cm/s^2)				Velocity (cm/s)				Displacement (cm)			
					EW	NS	Hor.	UD	EW	NS	Hor.	UD	EW	NS	Hor.	UD	EW	NS	Hor.	UD
7-37	C067	120.18	23.00	0	1391	1062	1750	957	57	57	81	21	9.4	11.9	15.1	5.6	6.1	8.1	10.1	6.4
7-38	C069	120.18	22.97	0	909	837	1236	598	43	38	58	25	10.7	9.3	14.2	5.2	6.2	7.2	9.5	6.8
7-39	C070	120.23	22.97	0	658	634	914	467	38	47	61	17	9.4	12.7	15.8	5.2	5.3	8.4	9.9	5.9
7-40	C074	120.81	23.51	1	2787	4642	5414	2237	229	157	278	98	32.3	21.2	38.6	14.9	14.3	9.1	17.0	8.2
7-41	C079	120.53	23.19	0	861	1089	1388	610	42	50	65	28	5.5	6.6	8.6	4.5	4.7	3.6	5.9	4.4
7-42	C080	120.68	23.60	1	22191	24536	33083	19703	792	842	1156	716	108.2	93.6	143.1	40.6	17.7	35.8	39.9	17.2
7-43	C081	120.50	23.27	0	981	969	1379	490	53	44	69	26	9.1	9.5	13.2	6.0	5.8	6.0	8.3	5.5
7-44	C086	120.59	23.35	0	1902	2249	2946	1208	99	202	225	50	17.9	18.1	25.4	8.6	6.6	8.1	10.4	4.3
7-45	C087	120.52	23.38	0	3146	4115	5180	1507	132	125	182	55	10.2	14.3	17.6	7.6	5.5	5.9	8.1	4.5
7-46	C088	120.43	23.35	0	3996	4713	6179	1962	148	207	255	42	17.9	20.4	27.1	8.5	7.2	10.6	12.8	5.1
7-47	C093	120.15	23.65	0	2094	2393	3179	2662	53	65	83	36	19.8	14.3	24.4	5.9	14.4	13.3	19.6	5.5
7-48	C094	120.32	23.79	0	1690	1690	2390	2766	64	53	83	41	24.5	19.2	31.1	14.0	20.6	17.7	27.1	9.0
7-49	C099	120.28	23.14	0	1002	1002	1417	718	61	51	79	27	14.1	18.4	23.2	8.5	7.8	13.3	15.4	5.9
7-50	C100	120.34	23.23	0	1630	1974	2560	778	66	60	89	28	11.1	17.1	20.4	5.8	6.4	12.4	14.0	4.5
7-51	C101	120.56	23.69	1	12346	11006	16540	8613	333	390	513	162	66.6	108.3	127.1	27.9	43.8	75.7	87.5	21.7
7-52	C104	120.46	23.67	0	3409	4980	6035	3903	143	177	228	130	55.5	53.1	76.8	32.4	41.4	47.0	62.6	21.7
7-53	C107	120.29	23.30	0	2557	2079	3295	1690	101	92	136	40	20.1	17.3	26.5	8.9	12.6	14.1	18.9	6.1
7-54	C111	120.23	23.79	0	2228	2826	3599	2901	58	85	103	42	19.6	11.4	22.7	9.0	19.2	10.0	21.7	6.5
7-55	C114	120.12	23.04	0	957	1151	1497	628	54	47	71	15	16.3	14.2	21.6	8.4	15.3	15.6	21.9	6.0
7-56	C115	120.10	23.15	0	1047	1525	1850	523	48	61	77	13	13.5	15.8	20.8	6.8	13.3	13.6	19.0	6.4
7-57	C116	120.11	23.08	0	1600	1510	2200	643	63	51	81	19	15.0	20.5	25.4	7.1	14.4	20.0	24.6	7.5
7-58	H002	121.51	23.60	0	1151	1271	1715	1107	51	89	102	32	9.4	12.7	15.8	7.1	4.5	6.0	7.5	5.2
7-59	H005	121.41	23.66	0	3439	2542	4277	2363	144	132	195	50	11.7	18.0	21.5	7.6	5.7	5.5	7.9	4.3
7-60	H006	121.42	23.67	0	2153	1989	2931	3484	90	85	124	61	7.8	8.0	11.2	7.0	5.5	4.9	7.4	4.8
7-61	H009	121.62	23.99	0	1735	2153	2765	3039	84	101	131	39	16.6	14.1	21.8	11.3	11.4	11.6	16.3	7.8
7-62	H011	121.59	24.00	0	2261	1866	2932	1998	87	97	130	37	19.4	25.1	31.7	8.5	11.2	8.9	14.3	8.6
7-63	H013	121.59	23.98	0	3804	2094	4342	2680	140	111	179	61	29.8	24.3	38.4	8.9	14.1	8.4	16.4	7.0
7-64	H014	121.60	23.97	0	1842	2058	2762	1842	102	89	135	39	21.1	25.2	32.9	9.9	11.8	9.0	14.8	6.6
7-65	H015	121.55	23.98	0	2213	1806	2857	2022	104	70	126	51	14.0	14.0	19.8	10.0	8.9	5.7	10.5	6.1
7-66	H016	121.56	23.97	0	1555	1448	2125	3242	101	82	130	50	15.7	13.8	20.8	10.9	8.5	5.2	10.0	7.0

Table B.2: Continued.

No.	ID	lon.	lat.	NF	Jerk (cm/s^3)				Acceleration (cm/s^2)				Velocity (cm/s)				Displacement (cm)			
					EW	NS	Hor.	UD	EW	NS	Hor.	UD	EW	NS	Hor.	UD	EW	NS	Hor.	UD
7-67	H017	121.54	23.95	0	1806	2608	3172	1723	81	83	116	49	11.4	9.5	14.9	9.3	7.0	4.2	8.1	7.0
7-68	H019	121.61	23.98	0	2548	2333	3455	1998	126	133	183	47	18.3	20.1	27.2	10.6	11.2	11.9	16.3	6.2
7-69	H020	121.43	23.81	0	2728	2608	3774	2405	57	67	87	52	10.5	8.9	13.8	8.3	4.9	3.6	6.1	6.9
7-70	H027	121.59	24.06	0	2177	1926	2907	1723	120	92	152	37	15.8	12.4	20.1	7.2	7.7	5.7	9.6	6.0
7-71	H028	121.60	24.02	0	2787	2309	3619	3505	101	85	132	49	15.2	14.5	21.0	8.5	9.0	9.1	12.8	7.8
7-72	H031	121.49	23.77	0	2237	1543	2718	2297	91	98	134	70	17.9	17.2	24.9	14.6	7.0	5.5	8.9	10.9
7-73	H032	121.41	23.71	0	8924	7118	11415	4355	150	108	185	87	12.6	8.4	15.2	8.7	6.2	4.3	7.5	5.3
7-74	H033	121.47	23.69	0	2010	2464	3180	1603	162	164	230	51	19.8	16.5	25.7	8.6	7.4	7.5	10.6	8.2
7-75	H034	121.38	23.59	0	4199	4510	6162	1436	134	139	193	66	11.9	10.7	16.0	8.0	4.7	4.0	6.1	4.4
7-76	H035	121.44	23.73	0	3828	3804	5397	5060	77	72	106	52	12.0	6.9	13.9	8.8	5.0	5.2	7.2	5.9
7-77	H037	121.38	23.45	0	1974	1699	2604	1316	108	124	164	78	13.0	23.3	26.6	12.7	4.6	8.6	9.7	5.4
7-78	H038	121.34	23.46	0	969	1364	1673	1053	36	57	67	40	7.8	9.2	12.0	6.5	5.0	4.9	7.0	3.2
7-79	H039	121.35	23.38	0	1137	1460	1850	718	81	74	110	39	11.1	14.9	18.6	7.6	4.1	4.0	5.7	5.3
7-80	H045	121.74	24.31	0	3724	4920	6170	1914	123	186	223	71	15.9	31.9	35.6	9.3	5.8	7.3	9.3	5.9
7-81	H048	121.57	24.01	0	2991	2318	3784	2482	122	166	206	53	20.0	22.4	30.0	11.3	10.4	11.3	15.4	6.5
7-82	H049	121.56	24.00	0	2243	1944	2968	1705	98	84	129	37	19.9	22.2	29.9	8.1	11.1	8.3	13.9	7.3
7-83	H050	121.58	23.99	0	2632	2318	3507	2034	90	92	129	53	15.0	10.3	18.2	9.0	8.1	5.3	9.7	6.4
7-84	H051	121.55	23.87	0	3439	4755	5869	2348	165	149	223	50	21.4	20.7	29.8	11.4	5.9	5.5	8.1	9.6
7-85	H055	121.33	23.32	0	1107	1331	1731	733	87	85	121	61	19.4	14.6	24.3	8.6	6.3	5.2	8.2	6.6
7-86	H056	121.51	24.18	0	3326	4139	5310	2034	102	106	147	59	8.8	10.7	13.8	7.8	7.2	7.2	10.2	6.8
7-87	H058	121.48	23.97	0	3756	3732	5295	2740	92	114	146	57	10.9	10.3	15.0	8.2	5.2	3.6	6.3	6.6
7-88	H059	121.50	23.87	0	6257	3134	6998	2871	135	118	180	53	14.7	15.5	21.4	9.9	4.7	3.9	6.1	8.5
7-89	HWA2	121.61	23.98	0	2584	2381	3513	2070	129	132	185	48	18.9	19.9	27.4	11.0	11.4	11.7	16.4	6.5
7-90	I003	121.78	24.80	0	1092	852	1385	568	57	71	91	18	20.2	18.7	27.5	7.6	17.0	12.1	20.9	7.5
7-91	I005	121.81	24.70	0	1271	987	1609	449	69	79	105	25	19.9	15.4	25.2	10.8	18.1	11.7	21.5	10.1
7-92	I006	121.83	24.64	0	1585	1406	2119	493	77	68	103	37	13.3	14.6	19.7	10.8	8.5	7.2	11.1	7.7
7-93	I008	121.76	24.71	0	1480	912	1739	957	77	56	96	33	18.8	15.0	24.0	10.0	14.7	11.8	18.9	9.4
7-94	I012	121.73	24.78	0	1077	1137	1566	673	81	61	101	27	17.5	18.2	25.2	9.5	8.9	7.9	11.9	9.0
7-95	I013	121.73	24.74	0	2901	4396	5267	1062	134	147	199	40	29.5	21.5	36.5	11.9	13.5	9.2	16.4	9.2
7-96	I014	121.72	24.69	0	1181	1062	1588	434	60	62	86	28	11.7	12.9	17.5	10.0	9.6	7.7	12.3	9.7

Table B.2: Continued.

No.	ID	lon.	lat.	NF	Jerk (cm/s^3)				Acceleration (cm/s^2)				Velocity (cm/s)				Displacement (cm)			
					EW	NS	Hor.	UD	EW	NS	Hor.	UD	EW	NS	Hor.	UD	EW	NS	Hor.	UD
7-97	I016	121.68	24.75	0	927	972	1343	748	79	71	106	37	16.4	12.8	20.8	7.6	8.1	7.0	10.7	8.0
7-98	I021	121.64	24.71	0	957	1077	1441	1062	60	69	91	27	11.7	8.3	14.4	11.3	7.0	5.9	9.1	8.7
7-99	I027	121.76	24.69	0	1627	1531	2234	670	103	67	123	22	17.7	15.4	23.5	5.0	7.2	11.3	13.4	4.4
7-100	I041	121.79	24.72	0	987	1062	1450	733	100	62	117	23	29.2	21.5	36.3	11.3	22.5	17.9	28.7	8.0
7-101	I044	121.76	24.66	0	1286	1256	1798	1032	80	70	106	29	24.2	16.5	29.3	10.3	14.6	9.0	17.1	7.9
7-102	I048	121.76	24.77	0	1645	1540	2253	1047	89	75	116	30	22.4	24.4	33.1	10.2	14.7	16.9	22.4	8.9
7-103	I055	121.81	24.74	0	1391	1735	2223	568	75	68	101	25	29.3	23.5	37.6	12.9	23.2	20.0	30.6	7.8
7-104	I056	121.81	24.76	0	1077	2348	2583	942	69	64	95	23	32.5	30.9	44.9	10.2	29.1	25.5	38.6	8.4
7-105	I059	121.82	24.67	0	1690	1660	2369	808	62	70	93	30	14.8	14.0	20.4	8.9	11.2	8.8	14.2	10.3
7-106	I061	121.83	24.52	0	613	822	1026	643	52	49	72	25	7.4	10.2	12.6	7.2	6.9	7.2	10.0	6.5
7-107	I062	121.79	24.47	0	1660	1555	2275	1525	81	72	108	47	10.5	12.4	16.2	8.5	6.4	7.2	9.6	5.2
7-108	I066	121.77	24.45	0	1944	2153	2901	1525	95	74	121	53	11.6	12.0	16.6	12.0	6.1	7.7	9.9	5.9
7-109	I067	121.37	24.44	0	6125	6783	9139	5551	195	168	257	94	11.8	18.7	22.1	12.5	5.7	12.2	13.4	8.8
7-110	K001	120.64	23.16	0	852	598	1041	822	43	22	48	40	6.1	6.1	8.6	7.5	2.9	6.2	6.8	5.3
7-111	K010	120.28	22.79	0	323	335	465	227	32	31	44	11	11.5	14.9	18.8	5.1	8.9	14.5	17.0	6.6
7-112	K011	120.26	22.76	0	634	778	1003	407	56	54	78	14	12.2	13.4	18.1	5.3	10.0	11.6	15.3	6.5
7-113	K020	120.54	22.90	0	742	790	1083	395	54	75	93	19	13.0	16.3	20.9	5.0	5.2	4.0	6.5	4.2
7-114	K085	120.32	22.89	0	628	822	1035	329	50	52	72	23	9.0	13.7	16.4	7.9	6.9	8.0	10.6	5.9
7-115	N001	121.44	23.32	0	808	763	1111	613	94	61	112	39	15.6	9.3	18.1	9.8	6.7	5.4	8.6	6.4
7-116	N041	121.12	23.13	0	1929	1869	2686	1346	79	64	102	39	7.1	6.2	9.4	4.5	5.3	2.5	5.9	3.9
7-117	N042	121.28	23.00	0	867	1256	1526	808	57	56	81	20	5.7	7.6	9.4	5.8	4.8	2.4	5.4	4.8
7-118	N044	121.17	23.01	0	628	613	878	493	49	55	74	32	9.7	9.9	13.8	5.6	6.2	5.6	8.3	3.3
7-119	N045	121.15	22.98	0	419	523	670	479	39	33	51	16	9.4	8.4	12.6	3.9	5.2	4.1	6.6	2.6
7-120	N046	121.23	22.97	0	1585	972	1859	718	112	65	129	19	9.5	7.7	12.2	5.4	5.4	2.1	5.8	4.5
7-121	P003	121.45	25.09	0	1655	2327	2855	1385	127	106	165	43	28.9	31.0	42.4	11.2	14.0	13.5	19.5	7.5
7-122	P005	121.51	25.11	0	1684	1909	2546	1203	127	81	151	24	31.1	20.8	37.4	6.7	10.3	7.7	12.8	6.2
7-123	P006	121.51	25.10	0	795	842	1158	741	99	68	120	31	20.3	13.6	24.5	6.9	8.8	6.2	10.8	5.7
7-124	P007	121.51	25.08	0	1134	724	1345	847	105	72	127	29	20.1	16.7	26.1	7.8	9.3	5.9	11.0	6.1
7-125	P008	121.53	25.08	0	1970	2927	3528	973	73	59	95	18	20.6	15.4	25.7	5.9	11.5	9.4	14.8	6.0
7-126	P010	121.48	25.07	0	1076	1056	1508	1256	115	86	144	27	26.9	26.2	37.5	6.3	11.7	10.4	15.6	6.8

Table B.2: Continued.

No.	ID	lon.	lat.	NF	Jerk (cm/s^3)				Acceleration (cm/s^2)				Velocity (cm/s)				Displacement (cm)			
					EW	NS	Hor.	UD	EW	NS	Hor.	UD	EW	NS	Hor.	UD	EW	NS	Hor.	UD
7-127	P012	121.51	25.06	0	842	716	1105	1046	96	54	110	28	19.2	15.3	24.5	6.4	9.4	6.3	11.3	7.0
7-128	P013	121.53	25.06	0	991	720	1224	766	87	75	115	24	21.5	16.4	27.0	7.4	9.5	7.3	12.0	6.9
7-129	P014	121.54	25.06	0	1436	908	1699	921	107	69	127	28	28.5	18.3	33.9	7.6	10.2	8.4	13.2	6.4
7-130	P017	121.45	25.05	0	1943	1586	2507	1189	111	97	147	34	24.3	28.6	37.5	11.4	14.5	15.6	21.3	8.7
7-131	P020	121.53	25.04	0	619	748	971	840	60	66	89	32	21.8	14.2	26.0	7.4	10.6	9.2	14.0	7.1
7-132	P021	121.54	25.04	0	1747	2034	2681	954	98	99	140	36	29.9	18.0	34.9	7.5	10.7	6.8	12.7	7.0
7-133	P024	121.47	25.02	0	684	874	1109	721	62	76	98	23	16.8	20.0	26.1	7.8	15.2	11.1	18.8	8.6
7-134	P026	121.50	25.02	0	967	983	1378	2025	77	69	104	49	14.7	13.8	20.2	7.8	11.9	8.4	14.6	7.1
7-135	P032	121.47	25.00	0	2357	1627	2864	1137	108	112	156	57	23.8	19.5	30.8	9.9	12.1	9.1	15.1	8.3
7-136	P066	121.52	25.19	0	467	718	856	371	49	71	86	21	8.6	12.8	15.4	4.5	8.5	7.2	11.2	4.8
7-137	P075	121.73	25.03	0	1122	1122	1586	673	81	49	95	24	10.8	8.9	14.0	5.8	7.6	5.1	9.1	7.5
7-138	P083	121.49	25.26	0	837	658	1065	508	36	61	71	18	13.7	16.1	21.1	7.0	17.3	9.0	19.5	6.0
7-139	P088	121.58	25.04	0	1320	1655	2117	930	89	115	145	42	16.9	16.8	23.9	8.3	7.2	5.2	8.9	7.4
7-140	P089	121.56	25.03	0	723	667	984	391	42	39	58	23	9.2	7.4	11.8	7.7	8.5	6.1	10.5	8.0
7-141	P090	121.59	25.06	0	1404	931	1684	711	136	88	162	29	32.7	19.2	37.9	7.1	8.9	5.8	10.6	5.8
7-142	P094	121.48	25.14	0	836	616	1038	461	63	83	104	29	16.2	16.8	23.3	9.2	9.3	7.3	11.9	7.3
7-143	P095	121.49	25.14	0	3706	3294	4958	1960	138	92	166	47	30.0	17.8	34.9	7.3	8.9	5.5	10.4	7.0
7-144	P097	121.53	25.02	0	628	643	899	404	72	81	108	23	14.0	18.3	23.1	8.6	11.6	8.8	14.5	8.3
7-145	P098	121.54	25.10	0	1176	956	1516	874	62	55	83	26	13.7	9.0	16.4	5.2	8.5	5.4	10.1	5.4
7-146	P100	121.51	25.04	0	838	823	1174	735	56	85	102	23	15.6	13.6	20.7	7.8	10.4	8.2	13.3	6.9
7-147	T015	120.93	24.76	0	3613	2548	4421	2668	128	122	177	66	40.3	25.0	47.5	15.8	47.6	25.8	54.2	13.5
7-148	T029	120.75	24.56	0	5670	6185	8391	3051	155	194	248	62	38.1	51.2	63.8	20.5	42.6	40.4	58.7	21.8
7-149	T031	120.70	24.56	0	1531	2799	3191	2512	113	123	166	65	55.7	46.9	72.8	26.9	51.0	34.1	61.4	23.4
7-150	T033	120.86	24.69	0	4235	5060	6599	3924	154	181	238	73	41.6	24.3	48.1	15.1	48.5	18.8	52.0	13.1
7-151	T034	120.86	24.64	0	5503	3098	6315	3972	248	103	268	70	43.7	24.1	49.9	12.7	46.5	20.8	50.9	10.5
7-152	T035	120.79	24.62	0	2393	2871	3737	2680	116	114	163	60	34.6	29.5	45.4	17.9	38.2	19.0	42.7	13.1
7-153	T036	120.70	24.45	0	2369	2369	3350	2058	134	122	182	61	57.9	47.1	74.7	21.6	60.4	48.0	77.2	19.8
7-154	T038	120.66	24.49	0	4570	5838	7414	4115	142	143	201	66	56.2	38.5	68.1	32.2	55.2	42.8	69.8	27.5
7-155	T039	120.78	24.49	0	4163	6245	7505	7417	193	136	236	122	54.8	56.9	79.0	50.6	56.3	39.3	68.6	46.5
7-156	T040	120.65	24.45	0	4139	3039	5135	5228	159	122	200	79	57.0	47.0	73.9	18.0	54.2	52.7	75.6	17.2

Table B.2: Continued.

No.	ID	lon.	lat.	NF	Jerk (cm/s^3)				Acceleration (cm/s^2)				Velocity (cm/s)				Displacement (cm)			
					EW	NS	Hor.	UD	EW	NS	Hor.	UD	EW	NS	Hor.	UD	EW	NS	Hor.	UD
7-157	T042	120.81	24.55	0	9355	5024	10619	3685	248	208	323	82	36.9	36.6	52.0	19.5	44.5	23.8	50.5	20.1
7-158	T045	120.91	24.54	1	18710	21330	28373	37372	463	512	690	353	49.3	46.4	67.7	21.2	36.4	14.4	39.1	12.2
7-159	T046	120.85	24.47	1	3242	3075	4468	4187	140	116	182	97	28.6	25.4	38.2	32.9	37.2	21.3	42.8	28.8
7-160	T047	120.94	24.62	1	12597	23603	26754	14296	292	399	495	261	42.2	35.8	55.3	22.3	32.8	21.1	39.0	18.8
7-161	T048	120.59	24.18	0	4055	5551	6874	3374	117	176	211	97	36.3	47.4	59.7	25.2	29.8	52.9	60.7	20.1
7-162	T049	120.69	24.18	1	10683	8745	13806	8434	273	242	365	178	56.9	59.3	82.2	27.1	48.5	41.7	64.0	19.1
7-163	T050	120.63	24.18	1	3768	4044	5527	2883	143	128	192	87	40.0	43.5	59.1	43.2	30.1	47.1	55.9	26.8
7-164	T051	120.65	24.16	1	5467	8242	9891	5635	157	231	279	110	51.2	40.3	65.1	30.5	39.8	44.2	59.4	22.8
7-165	T052	120.74	24.20	1	6962	7728	10402	11975	349	439	560	194	180.7	220.0	284.7	169.0	154.8	139.8	208.6	114.0
7-166	T053	120.67	24.19	1	8266	3649	9036	4929	225	132	261	121	42.9	44.0	61.5	32.5	38.2	42.0	56.8	17.9
7-167	T054	120.68	24.16	1	3948	5312	6618	7034	143	190	238	133	45.9	45.3	64.6	29.7	49.1	35.2	60.4	21.8
7-168	T056	120.62	24.16	1	4450	3709	5793	3685	154	140	208	117	41.4	40.3	57.8	40.7	38.7	46.6	60.5	27.8
7-169	T057	120.61	24.17	0	5898	8817	10607	2273	111	100	150	81	40.7	49.4	64.0	34.0	30.7	49.4	58.2	22.4
7-170	T059	120.56	24.27	0	2596	2261	3443	1651	157	162	225	64	52.2	53.9	75.0	13.9	56.5	51.9	76.7	12.1
7-171	T060	120.64	24.23	1	4139	3003	5114	3350	197	101	221	86	36.7	42.8	56.4	28.4	34.0	44.6	56.1	19.6
7-172	T061	120.55	24.14	0	2919	6077	6742	3948	133	154	204	86	41.1	37.9	55.9	27.6	37.2	30.4	48.0	25.8
7-173	T063	120.62	24.11	1	8350	3326	8988	7309	179	130	222	133	44.2	82.4	93.5	57.4	48.0	58.8	75.9	37.3
7-174	T064	120.61	24.35	0	1555	2153	2656	1794	109	113	157	82	42.6	56.1	70.4	32.0	50.1	56.0	75.1	22.5
7-175	T065	120.69	24.06	1	13159	15600	20409	6998	774	563	958	258	132.1	92.9	161.5	68.7	99.4	58.0	115.1	47.1
7-176	T067	120.72	24.09	1	12717	11269	16992	12334	489	313	580	231	97.8	55.8	112.6	50.1	51.8	31.8	60.8	25.8
7-177	T068	120.77	24.28	1	12992	20720	24456	14894	501	362	618	519	280.9	291.3	404.6	228.7	159.3	252.7	298.7	131.4
7-178	T070	120.54	24.20	0	6520	4319	7820	5766	249	157	294	76	45.9	60.0	75.5	35.9	35.2	54.6	65.0	25.1
7-179	T071	120.79	23.99	1	21772	29297	36501	27251	518	639	822	416	70.1	82.8	108.5	59.3	34.3	36.0	49.7	28.9
7-180	T072	120.85	24.04	1	16844	23196	28667	16198	465	371	595	275	87.6	69.3	111.8	38.9	29.1	30.2	42.0	25.4
7-181	T074	120.96	23.96	1	22682	23268	32494	20600	586	368	692	270	70.2	49.0	85.6	24.9	27.4	17.5	32.5	14.5
7-182	T075	120.68	23.98	1	18291	9331	20534	10432	325	257	415	224	116.1	37.0	121.8	50.0	69.4	25.9	74.1	23.2
7-183	T076	120.68	23.91	1	27969	23268	36382	16844	340	420	540	275	69.1	63.2	93.6	32.8	32.8	33.2	46.7	17.0
7-184	T078	120.85	23.81	1	21138	14320	25532	11221	440	302	534	171	43.3	32.3	54.0	19.4	22.2	8.8	23.9	13.5
7-185	T079	120.89	23.84	1	25625	18375	31532	22909	580	417	714	384	67.4	31.5	74.4	22.9	14.6	15.4	21.2	13.8
7-186	T082	120.68	24.15	1	5407	5204	7505	4701	221	182	287	129	51.6	43.3	67.4	35.0	50.6	40.4	64.8	27.4

Table B.2: Continued.

No.	ID	lon.	lat.	NF	Jerk (cm/s^3)				Acceleration (cm/s^2)				Velocity (cm/s)				Displacement (cm)			
					EW	NS	Hor.	UD	EW	NS	Hor.	UD	EW	NS	Hor.	UD	EW	NS	Hor.	UD
7-187	T084	120.90	23.88	1	16916	13829	21849	13638	989	423	1076	312	116.2	54.1	128.2	29.8	41.1	23.7	47.5	17.2
7-188	T087	120.77	24.35	1	1890	1962	2724	1830	119	112	163	91	43.6	44.2	62.1	58.5	48.7	24.9	54.7	53.9
7-189	T088	121.18	24.25	1	36690	35446	51015	19464	509	515	724	224	13.3	36.5	38.8	12.9	6.1	18.8	19.8	9.4
7-190	T089	120.86	23.90	1	10097	11090	14998	13315	348	225	414	190	45.4	34.9	57.3	21.7	19.6	20.0	28.0	14.2
7-191	T095	121.01	24.69	1	13590	30996	33844	21772	367	685	776	251	48.6	49.2	69.2	22.9	41.4	21.0	46.4	16.7
7-192	T098	120.90	24.74	0	3505	2919	4561	2979	104	98	142	48	45.6	27.1	53.0	17.3	48.6	25.8	55.1	12.2
7-193	T100	120.62	24.19	0	2931	4067	5013	4534	108	111	155	84	40.6	43.1	59.2	39.7	30.5	49.0	57.7	29.6
7-194	T102	120.72	24.25	1	3541	2835	4536	3864	298	169	343	173	87.0	71.7	112.7	68.0	75.2	41.4	85.9	34.0
7-195	T103	120.71	24.31	1	3780	3948	5466	12729	126	149	196	142	68.5	22.4	72.1	60.9	63.1	14.5	64.8	48.0
7-196	T104	120.60	24.25	0	2381	1902	3047	2512	101	87	134	90	30.9	48.2	57.3	24.3	35.1	44.7	56.8	17.7
7-197	T105	120.56	24.24	0	2046	2429	3175	2440	111	124	167	61	32.6	42.5	53.6	23.6	35.8	40.7	54.2	16.5
7-198	T106	120.55	24.08	0	4953	4725	6845	5922	157	122	199	116	40.5	39.3	56.4	23.3	40.0	28.5	49.2	22.8
7-199	T107	120.54	24.07	0	2381	3517	4247	3409	128	144	192	94	34.0	46.2	57.4	25.6	34.3	31.9	46.9	25.4
7-200	T109	120.57	24.09	0	4498	3685	5815	8936	149	159	218	133	55.0	56.0	78.5	23.7	46.2	34.7	57.8	22.5
7-201	T111	120.49	24.11	0	2787	3158	4212	3350	125	94	156	77	52.9	31.7	61.7	23.4	49.5	33.7	59.8	20.9
7-202	T116	120.58	23.86	0	4402	6364	7739	4965	185	133	228	119	39.7	52.8	66.1	34.6	35.1	35.1	49.6	26.9
7-203	T117	120.46	24.13	0	2010	1878	2751	4809	121	113	166	90	56.4	57.9	80.8	22.8	43.5	42.2	60.6	17.5
7-204	T118	120.42	24.00	0	2740	2704	3849	7644	116	92	148	100	29.7	35.1	46.0	18.7	22.4	34.2	40.9	20.6
7-205	T120	120.61	23.98	1	7812	8350	11435	11317	223	193	295	167	62.6	34.8	71.6	35.5	34.1	32.6	47.2	24.2
7-206	T122	120.61	23.81	1	11736	8362	14410	24213	207	256	329	236	44.6	42.8	61.8	40.9	35.5	27.7	45.0	36.3
7-207	T128	120.76	24.42	0	2787	2775	3934	5180	141	163	216	90	62.0	62.2	87.8	44.6	74.3	46.1	87.4	39.7
7-208	T129	120.68	23.88	1	40961	25708	48360	8207	983	611	1157	335	68.1	54.9	87.5	37.5	38.9	25.4	46.5	19.2
7-209	T131	120.82	24.57	0	2464	2656	3623	2393	118	123	170	54	37.9	39.1	54.4	19.3	37.5	31.6	49.0	16.7
7-210	T136	120.65	24.26	1	2916	2482	3829	3365	167	171	239	112	43.3	52.9	68.4	33.4	55.7	43.3	70.6	25.2
7-211	T138	120.60	23.92	1	5937	5772	8280	4710	202	207	290	110	33.3	38.5	50.9	25.7	24.2	25.8	35.4	19.8
7-212	T140	120.36	23.96	0	1824	2288	2926	3978	71	53	89	68	24.1	21.6	32.4	19.3	21.8	19.0	28.9	17.0
7-213	T141	120.46	23.83	0	4187	1615	4488	4621	86	89	124	107	46.0	28.4	54.1	25.2	37.1	22.2	43.3	22.2
7-214	T145	120.34	23.98	0	1959	1884	2718	2363	70	60	92	52	24.6	19.8	31.6	19.2	26.3	20.3	33.2	16.9
8-1	2723	−146.36	61.13	0	297	220	370	167	9	9	13	6	2.7	2.1	3.4	2.0	3.6	1.9	4.1	1.7
8-2	2767	−147.18	64.79	0	871	673	1101	454	42	30	52	15	5.5	4.2	6.9	2.7	1.7	2.1	2.7	1.4

Table B.2: Continued.

No.	ID	lon.	lat.	NF	Jerk (cm/s^3)				Acceleration (cm/s^2)				Velocity (cm/s)				Displacement (cm)			
					EW	NS	Hor.	UD	EW	NS	Hor.	UD	EW	NS	Hor.	UD	EW	NS	Hor.	UD
8-3	2784	−146.35	61.13	0	271	243	364	271	26	21	34	12	4.6	3.0	5.5	2.2	3.8	2.1	4.3	1.8
8-4	2797	−147.85	64.86	0	1883	1408	2351	1539	108	63	125	40	8.9	5.3	10.4	3.4	2.3	1.8	2.9	1.5
8-5	8016	−149.86	61.19	0	452	367	582	109	21	16	26	6	3.0	2.5	3.9	1.5	2.1	1.7	2.7	0.7
8-6	8017	−149.95	61.20	0	221	198	296	134	16	18	24	10	3.7	4.2	5.6	1.8	2.6	2.9	3.9	0.7
8-7	8019	−149.54	61.35	0	238	229	330	86	5	6	8	4	1.9	1.2	2.2	1.1	1.6	0.9	1.8	1.3
8-8	8022	−147.86	64.87	0	1552	1344	2053	1708	85	69	109	47	7.1	6.3	9.5	3.7	2.2	2.4	3.2	1.9
8-9	8024	−149.89	61.18	0	240	226	329	94	10	14	17	5	2.5	2.4	3.4	1.1	2.1	2.3	3.1	0.6
8-10	8027	−149.89	61.16	0	232	222	321	163	13	12	18	6	2.7	2.5	3.7	1.8	2.2	2.2	3.1	0.7
8-11	8030	−149.81	61.18	0	168	160	232	89	10	9	13	5	2.2	1.9	2.9	1.3	1.8	1.7	2.4	0.9
8-12	8034	−146.36	61.13	0	99	143	174	85	6	6	9	6	2.7	2.2	3.5	2.1	3.5	1.9	4.0	1.6
8-13	8036	−149.97	61.18	0	172	253	306	101	12	22	26	8	3.4	4.0	5.2	1.5	2.4	3.0	3.9	0.7
8-14	8037	−149.98	61.16	0	193	299	356	203	14	19	24	7	3.6	4.3	5.6	1.1	2.4	2.8	3.7	0.7
8-15	8038	−149.88	61.22	0	168	174	242	123	17	18	25	8	3.1	4.2	5.2	1.6	2.2	2.5	3.3	0.9
8-16	8039	−149.95	61.14	0	420	380	567	154	20	20	29	8	3.8	3.3	5.0	1.3	2.2	3.4	4.1	0.7
8-17	CARL	−148.81	63.55	0	4637	3251	5663	3863	98	86	130	70	7.6	10.4	12.8	8.5	3.3	4.0	5.2	2.8
8-18	FA02	−148.01	64.85	0	1665	1285	2103	1189	47	40	62	24	5.4	3.0	6.1	3.8	2.0	2.0	2.8	2.5
8-19	K202	−149.82	61.22	0	204	208	292	138	11	12	16	7	2.8	2.9	4.0	1.3	1.8	1.8	2.5	0.9
8-20	K203	−149.72	61.22	0	177	149	232	99	8	9	12	5	2.5	1.9	3.1	1.1	1.8	1.6	2.4	1.0
8-21	K204	−150.01	61.18	0	233	227	325	187	13	11	17	7	4.6	3.4	5.7	1.7	2.3	2.7	3.5	0.9
8-22	K205	−149.91	61.20	0	238	232	333	153	16	15	21	7	3.0	3.2	4.4	1.7	2.1	2.8	3.5	0.7
8-23	K206	−149.82	61.19	0	224	297	372	114	10	11	14	5	2.2	2.3	3.2	1.3	1.9	2.2	2.9	0.9
8-24	PS07	−148.28	65.31	0	235	234	332	206	18	17	24	10	3.4	3.2	4.7	1.7	1.7	2.1	2.7	1.4
8-25	PS08	−146.82	64.54	0	1277	1621	2063	1567	46	35	58	24	5.3	4.3	6.8	3.1	2.4	3.0	3.8	2.7
8-26	PS09	−145.77	63.93	0	4156	3279	5294	4655	73	55	91	52	12.5	11.7	17.1	9.8	9.4	8.2	12.4	3.9
8-27	PS10	−145.77	63.42	1	5542	9273	10803	11842	330	290	440	233	113.7	64.0	130.4	52.0	44.3	33.8	55.7	24.4
8-28	PS11	−145.48	62.09	0	4054	3777	5541	2138	70	85	110	32	10.0	15.9	18.8	9.0	11.0	12.9	16.9	8.8
8-29	PS12	−145.14	61.48	0	972	712	1205	670	38	34	51	23	5.4	5.6	7.8	5.1	3.8	3.5	5.2	3.0
8-30	R109	−148.65	63.40	0	1646	1880	2499	1618	59	107	122	48	6.2	12.9	14.3	5.7	3.4	3.8	5.2	2.8
9-1	1575	−121.40	36.85	0	128	146	194	76	14	11	18	6	3.2	3.2	4.5	1.7	1.7	1.3	2.2	0.7
9-2	1747	−120.36	36.14	0	1966	1206	2306	1242	78	44	89	27	6.0	5.8	8.4	3.9	2.6	1.7	3.1	1.2

Table B.2: Continued.

No.	ID	lon.	lat.	NF	Jerk (cm/s^3)				Acceleration (cm/s^2)				Velocity (cm/s)				Displacement (cm)			
					EW	NS	Hor.	UD	EW	NS	Hor.	UD	EW	NS	Hor.	UD	EW	NS	Hor.	UD
9-3	1748	−119.73	36.74	0	107	55	120	146	5	3	6	5	0.4	0.3	0.5	0.2	0.2	0.1	0.2	0.0
9-4	1797	−121.40	36.89	0	64	112	129	47	9	10	14	5	3.3	2.8	4.3	1.5	1.5	1.2	1.9	0.6
9-5	1840	−119.78	36.77	0	123	113	167	108	7	5	9	4	0.5	0.4	0.7	0.2	0.2	0.2	0.3	0.0
9-6	35219	−119.45	35.40	0	113	130	172	170	6	10	12	6	1.0	1.1	1.5	0.5	0.2	0.2	0.3	0.1
9-7	36138	−120.43	35.90	1	4904	3810	6210	6237	271	297	402	135	39.3	47.4	61.6	9.6	10.1	11.5	15.3	2.2
9-8	36153	−120.46	35.21	0	930	658	1140	456	20	12	23	9	0.6	0.8	1.0	0.6	0.1	0.1	0.1	0.1
9-9	36176	−120.53	35.92	0	12344	14942	19381	10179	258	297	394	246	18.2	19.6	26.8	8.7	5.2	4.1	6.7	2.2
9-10	36177	−120.47	35.97	1	7967	6461	10257	3452	352	224	418	93	23.7	12.1	26.6	8.3	6.2	3.0	6.9	2.9
9-11	36227	−120.33	35.70	1	8785	7432	11507	9700	245	228	334	169	18.6	11.8	22.0	7.0	2.7	1.3	3.0	0.8
9-12	36228	−120.29	35.73	1	10994	10462	15176	11440	593	362	695	182	63.3	44.1	77.2	14.3	11.2	7.2	13.3	3.6
9-13	36229	−120.40	35.64	0	3729	4749	6039	2113	74	83	111	40	6.7	4.1	7.9	2.9	0.7	1.0	1.2	0.7
9-14	36230	−120.26	35.75	1	19116	18203	26396	13703	455	465	650	183	22.6	22.3	31.8	5.7	3.5	2.1	4.0	1.0
9-15	36407	−120.31	35.76	1	15224	15421	21670	11188	581	803	991	256	62.5	80.7	102.0	9.9	9.3	10.9	14.4	2.6
9-16	36408	−120.34	35.80	1	15988	18637	24555	26887	363	382	528	372	22.5	19.7	29.9	11.8	3.7	2.6	4.5	1.8
9-17	36410	−120.30	35.73	1	10900	10851	15380	6117	314	554	637	156	28.0	38.3	47.5	9.7	5.0	7.4	8.9	1.2
9-18	36411	−120.31	35.72	1	14151	11127	18002	6786	565	503	757	146	31.6	27.0	41.6	10.0	5.2	4.2	6.7	1.7
9-19	36412	−120.32	35.71	1	9874	7336	12301	10562	293	275	402	111	26.5	16.6	31.3	5.0	4.4	3.1	5.3	1.6
9-20	36414	−120.40	35.84	1	2215	3484	4129	4275	129	105	167	68	16.5	13.6	21.4	4.5	3.4	1.6	3.8	1.1
9-21	36415	−120.38	35.82	1	8956	6304	10952	3777	146	139	202	68	9.9	7.4	12.4	2.6	2.0	1.6	2.6	0.9
9-22	36416	−120.39	35.81	1	7399	13404	15310	5247	157	265	308	91	14.5	9.8	17.5	3.6	1.7	1.9	2.6	0.6
9-23	36419	−120.29	35.79	1	24705	29660	38601	14912	665	793	1035	299	34.6	38.6	51.8	15.9	5.9	4.0	7.1	1.8
9-24	36420	−120.41	35.80	1	32185	23222	39688	10259	665	409	781	162	23.2	15.7	28.0	4.4	3.1	2.8	4.2	1.2
9-25	36421	−120.35	35.84	1	10253	8396	13252	5910	159	204	259	89	7.7	10.4	13.0	3.9	1.4	1.8	2.3	0.8
9-26	36422	−120.28	35.81	1	9416	7961	12330	10868	177	180	253	121	12.5	9.8	15.9	4.2	2.2	1.5	2.7	1.0
9-27	36427	−120.89	35.27	0	569	348	667	345	13	10	16	8	1.0	0.9	1.3	0.5	0.2	0.2	0.2	0.1
9-28	36431	−120.40	35.87	1	12457	10793	16482	7021	224	249	335	145	18.6	21.6	28.5	7.4	4.7	4.8	6.7	1.6
9-29	36432	−120.51	35.74	0	4528	3840	5937	2862	103	98	142	83	4.3	4.4	6.1	2.2	0.8	1.2	1.5	0.9
9-30	36433	−120.44	35.79	1	27373	22161	35219	7045	377	305	485	86	12.6	7.7	14.8	3.0	2.1	1.6	2.7	0.9
9-31	36434	−120.48	35.77	0	9064	8956	12743	3833	243	171	297	55	7.7	7.0	10.4	2.7	1.3	1.3	1.8	1.0
9-32	36437	−120.27	35.83	1	8019	10866	13505	3794	188	195	271	47	8.6	9.7	13.0	3.0	2.3	2.5	3.4	0.9

Table B.2: Continued.

No.	ID	lon.	lat.	NF	Jerk (cm/s^3)				Acceleration (cm/s^2)				Velocity (cm/s)				Displacement (cm)			
					EW	NS	Hor.	UD	EW	NS	Hor.	UD	EW	NS	Hor.	UD	EW	NS	Hor.	UD
9-33	36439	−120.33	35.87	1	9010	4615	10123	3806	199	103	224	59	12.1	7.1	14.1	2.3	2.5	1.5	2.9	0.7
9-34	36440	−120.56	35.89	1	6033	8449	10382	8961	154	179	237	157	10.6	10.5	15.0	4.3	3.0	2.8	4.1	1.1
9-35	36441	−120.60	35.86	0	4461	4084	6047	5061	112	98	149	97	9.0	7.8	11.9	3.4	3.2	2.4	3.9	1.1
9-36	36443	−120.44	35.88	1	2809	3268	4309	5013	148	94	176	77	24.0	14.2	27.9	3.5	6.2	4.4	7.6	1.0
9-37	36445	−120.48	35.92	1	4487	6182	7639	5960	139	224	264	135	23.0	18.3	29.3	11.4	6.9	5.6	8.9	3.1
9-38	36446	−120.55	35.91	1	4817	3186	5776	3625	98	86	131	71	6.1	7.8	9.9	3.4	2.2	2.1	3.0	1.1
9-39	36447	−120.51	35.93	1	16759	10413	19731	7866	507	375	631	120	27.6	17.7	32.8	6.8	3.4	3.2	4.7	1.0
9-40	36448	−120.50	35.93	1	5818	6716	8886	4495	161	131	208	104	18.3	11.4	21.6	6.0	5.2	4.0	6.5	1.9
9-41	36449	−120.38	35.88	1	26384	16561	31151	16453	536	487	724	246	20.2	16.6	26.2	9.1	2.1	2.0	2.9	2.2
9-42	36450	−120.25	35.77	1	13150	32617	35168	16278	503	735	890	245	23.5	27.8	36.4	5.7	2.7	2.6	3.8	0.8
9-43	36451	−120.34	35.68	0	6846	11627	13493	7467	228	369	434	128	11.8	18.1	21.6	5.4	2.0	2.2	3.0	0.6
9-44	36452	−120.27	35.74	1	12241	9705	15621	9687	418	337	537	236	40.3	39.1	56.2	9.8	8.2	7.0	10.8	1.9
9-45	36453	−120.40	35.90	1	32491	60011	68242	34664	450	903	1009	403	15.3	26.0	30.2	10.2	1.9	1.9	2.7	3.0
9-46	36454	−120.42	35.86	1	9269	9160	13031	9850	171	178	247	109	24.4	8.5	25.8	5.0	4.9	2.0	5.3	1.0
9-47	36455	−120.48	35.96	1	9351	12330	15475	5383	260	284	385	174	29.5	25.8	39.2	13.7	8.1	4.7	9.3	2.8
9-48	36456	−120.46	35.91	1	43945	25082	50599	21935	1286	528	1390	547	82.8	42.3	93.0	23.5	15.8	7.6	17.6	4.6
9-49	36510	−120.17	35.71	0	3147	2730	4166	1537	100	76	125	32	6.5	7.1	9.6	2.5	1.0	1.1	1.4	0.6
9-50	36529	−120.36	35.88	1	4885	4236	6466	3934	241	191	307	70	14.6	11.5	18.6	4.7	2.1	1.7	2.7	1.5
9-51	36535	−120.00	35.66	0	5149	7226	8873	4334	156	190	245	72	7.0	6.8	9.7	2.5	1.0	0.8	1.3	0.5
9-52	36712	−120.72	35.56	0	1125	1077	1557	847	37	34	50	19	2.1	2.2	3.1	1.0	0.4	0.5	0.6	0.2
9-53	37737	−121.12	35.59	0	233	222	322	148	9	10	13	5	0.6	0.8	1.0	0.3	0.1	0.1	0.2	0.0
9-54	46174	−120.71	36.19	1	368	504	624	442	22	27	35	16	3.2	4.6	5.6	3.5	1.7	1.6	2.3	1.0
9-55	46175	−120.59	36.03	1	3248	6461	7231	3521	207	341	399	105	25.8	52.5	58.5	8.6	7.4	7.4	10.5	1.8
9-56	47125	−121.95	36.97	0	277	305	411	142	8	10	13	4	0.6	0.7	0.9	0.3	0.1	0.1	0.1	0.0
9-57	47136	−121.78	36.25	0	235	336	410	239	7	8	11	5	0.5	0.7	0.9	0.3	0.1	0.1	0.1	0.1
9-58	47179	−121.64	36.67	0	199	257	325	309	10	11	15	7	1.4	1.6	2.2	0.6	0.4	0.4	0.6	0.2
9-59	47216	−121.78	36.81	0	177	188	258	163	10	11	15	6	2.1	1.2	2.4	1.0	0.5	0.5	0.7	0.2
9-60	47232	−121.13	36.21	0	2000	2812	3451	4903	58	44	73	59	3.1	2.5	3.9	1.4	0.4	0.4	0.5	0.1
9-61	47460	−121.24	36.32	0	1230	1024	1601	1602	32	23	40	21	2.1	1.8	2.8	0.8	0.3	0.5	0.6	0.2
9-62	47524	−121.40	36.85	0	222	178	285	320	10	13	17	5	2.1	3.0	3.6	1.2	0.8	1.1	1.3	0.4

Table B.2: Continued.

No.	ID	lon.	lat.	NF	Jerk (cm/s^3)				Acceleration (cm/s^2)				Velocity (cm/s)				Displacement (cm)			
					EW	NS	Hor.	UD	EW	NS	Hor.	UD	EW	NS	Hor.	UD	EW	NS	Hor.	UD
9-63	47762	−121.63	36.70	0	169	189	253	122	16	11	20	5	1.7	1.8	2.5	0.6	0.3	0.5	0.6	0.1
9-64	61022	−120.54	35.95	1	5824	5700	8149	3259	160	146	216	87	8.5	9.2	12.6	4.7	2.7	3.3	4.2	0.9
9-65	DFU	−120.42	35.94	1	11967	16610	20472	12574	289	366	466	171	15.1	13.9	20.5	9.0	3.3	1.7	3.7	2.0
9-66	EFU	−120.42	35.89	1	23969	29082	37687	14486	312	384	494	192	26.7	25.9	37.2	7.4	7.1	5.1	8.7	1.7
9-67	FFU	−120.49	35.91	1	29822	23653	38063	21584	448	373	583	215	17.5	11.1	20.7	6.7	3.0	2.8	4.0	1.5
9-68	GFU	−120.35	35.83	1	10389	9237	13901	8959	168	136	216	116	6.0	5.7	8.3	2.1	1.0	1.1	1.5	0.6
9-69	JFU	−120.43	35.94	1	44427	29030	53071	20444	487	609	780	301	30.2	25.6	39.6	9.6	4.6	2.7	5.4	1.9
9-70	KFU	−120.20	35.71	0	8738	7771	11694	12730	144	167	220	159	6.1	10.7	12.3	4.4	1.0	1.9	2.1	0.3
9-71	MFU	−120.50	35.96	1	6310	8970	10967	4167	181	402	441	108	26.0	29.4	39.3	8.4	8.2	6.7	10.6	2.4
9-72	PHOB	−120.48	35.87	1	15383	9903	18295	11940	269	251	367	171	22.5	19.6	29.8	9.2	5.0	3.8	6.3	1.4
9-73	RFU	−120.25	35.62	1	1948	1942	2751	3742	45	47	65	53	1.8	3.1	3.6	1.7	0.3	0.4	0.5	0.3
9-74	VFU	−120.53	35.92	1	12080	8032	14507	9496	184	256	315	145	16.9	22.4	28.1	6.3	3.8	4.5	5.9	1.7
9-75	WFU	−120.51	35.81	0	22457	17785	28647	10001	335	183	382	167	9.9	5.8	11.4	4.4	1.0	1.5	1.8	0.4
10-1	FKS021	139.87	37.65	0	2742	5700	6326	1144	103	135	170	22	6.6	4.5	8.0	1.5	1.7	2.6	3.1	0.7
10-2	FKS022	139.65	37.60	0	4387	5041	6682	4602	148	132	198	71	7.7	9.6	12.3	3.2	1.6	2.2	2.7	1.0
10-3	FKS023	139.93	37.47	0	1352	1114	1752	940	62	51	80	17	4.7	4.6	6.6	1.6	2.0	1.5	2.5	1.0
10-4	FKS025	139.90	37.31	0	2855	3450	4478	2321	59	50	77	44	2.5	1.9	3.1	1.5	1.0	0.9	1.3	0.7
10-5	FKS026	139.54	37.26	0	7255	5068	8849	6031	132	111	173	60	4.7	3.6	5.9	3.7	1.8	1.3	2.2	1.2
10-6	FKS027	139.68	37.07	0	6990	6326	9428	3288	84	70	109	33	1.4	1.7	2.2	3.0	0.7	1.0	1.3	1.5
10-7	FKS028	139.32	37.35	0	9252	6429	11266	11436	167	141	219	123	12.3	12.1	17.3	4.3	3.1	3.1	4.4	1.3
10-8	FKS029	139.38	37.01	0	11551	14292	18376	6367	172	215	275	70	3.6	3.6	5.1	2.8	1.1	0.7	1.2	1.6
10-9	FKS030	139.52	37.45	0	6553	10413	12304	4124	98	145	175	50	5.4	4.4	6.9	2.3	1.8	1.7	2.5	1.2
10-10	FKSH01	139.72	37.75	0	4300	3837	5763	1786	59	49	77	17	1.5	2.6	3.0	0.9	0.8	0.9	1.2	0.7
10-11	FKSH03	139.76	37.61	0	2353	2517	3445	2191	79	101	128	53	6.9	4.8	8.4	3.1	1.5	1.8	2.4	1.0
10-12	FKSH04	139.82	37.45	0	5187	2035	5572	1592	95	41	104	21	2.7	2.8	3.9	1.9	1.6	1.7	2.3	1.4
10-13	FKSH05	139.88	37.25	0	3056	2629	4031	2174	67	60	90	26	2.3	3.0	3.8	1.4	1.0	0.9	1.4	0.8
10-14	FKSH06	139.52	37.17	0	7319	5694	9273	6677	147	126	194	76	4.2	4.6	6.2	3.4	1.6	1.0	1.9	1.7
10-15	FKSH07	139.38	37.01	0	10731	17377	20423	10275	101	149	180	90	2.8	2.5	3.8	2.6	1.0	0.6	1.2	1.6
10-16	FKSH21	139.32	37.34	0	19418	9751	21729	13091	362	247	438	137	18.8	15.6	24.4	5.0	3.1	1.8	3.5	1.1
10-17	GNM002	138.97	36.78	0	17211	19606	26089	17473	279	341	441	195	7.0	6.4	9.4	3.1	1.1	1.2	1.7	1.7

Table B.2: Continued.

No.	ID	lon.	lat.	NF	Jerk (cm/s^3)				Acceleration (cm/s^2)				Velocity (cm/s)				Displacement (cm)			
					EW	NS	Hor.	UD	EW	NS	Hor.	UD	EW	NS	Hor.	UD	EW	NS	Hor.	UD
10-18	GNM003	139.08	36.66	0	19772	26288	32894	8373	293	359	463	126	6.8	8.7	11.1	3.4	1.4	1.8	2.3	1.7
10-19	GNM007	139.01	36.46	0	2970	3770	4800	1462	52	82	97	39	3.2	3.3	4.6	1.8	2.2	1.7	2.7	1.1
10-20	GNMH07	139.21	36.70	0	7315	5514	9160	7448	103	69	124	65	2.5	2.2	3.3	2.1	1.3	1.7	2.2	1.6
10-21	GNMH08	138.53	36.49	0	389	433	582	267	15	13	19	8	3.4	3.3	4.8	1.3	2.2	2.1	3.0	0.7
10-22	GNMH09	138.91	36.62	0	1186	1406	1840	699	20	25	32	8	1.7	1.8	2.5	1.5	0.9	1.4	1.6	1.3
10-23	NGN001	138.37	36.85	0	1933	2213	2938	1610	78	74	107	34	8.1	5.7	9.9	3.6	3.1	1.3	3.3	1.5
10-24	NGN002	138.21	36.80	0	3417	2922	4496	1011	101	114	152	34	5.2	5.8	7.8	3.4	2.5	3.1	4.0	1.8
10-25	NGN003	138.42	36.74	0	3631	4840	6051	2563	70	93	117	29	3.2	2.5	4.1	1.2	0.7	0.8	1.1	0.7
10-26	NIG003	138.33	38.00	0	4840	4382	6529	4009	76	89	117	41	3.4	4.3	5.5	1.3	2.1	2.0	2.9	0.5
10-27	NIG008	139.41	38.05	0	2653	2796	3854	2354	53	47	71	26	2.4	2.3	3.3	1.2	1.2	1.3	1.7	0.9
10-28	NIG010	139.01	37.91	0	3450	2818	4454	1321	104	69	124	34	8.1	7.7	11.2	2.4	5.2	4.8	7.1	1.7
10-29	NIG011	139.15	37.80	0	1657	1338	2130	661	57	55	79	17	6.3	7.4	9.7	2.7	4.2	4.2	5.9	1.6
10-30	NIG012	139.48	37.68	0	22084	11263	24790	3376	291	237	375	63	15.1	16.3	22.2	3.8	2.6	3.4	4.3	1.3
10-31	NIG013	138.89	37.76	0	4669	2405	5252	1242	129	95	161	39	12.2	13.6	18.2	4.4	6.4	8.1	10.3	2.4
10-32	NIG014	138.96	37.64	0	2137	3801	4360	3777	96	118	152	76	14.9	14.8	21.0	7.0	8.0	7.0	10.6	3.2
10-33	NIG015	139.19	37.69	0	3638	3074	4763	2133	79	67	103	29	3.8	5.1	6.3	2.6	1.7	2.2	2.8	1.5
10-34	NIG016	138.77	37.64	0	3611	4513	5780	1648	86	103	134	37	5.6	6.3	8.4	2.4	2.9	2.2	3.7	1.6
10-35	NIG017	138.85	37.44	1	20586	15758	25925	18012	369	468	596	331	21.6	49.0	53.5	15.7	14.1	15.6	21.0	4.8
10-36	NIG018	138.56	37.37	0	4639	4850	6711	3125	144	98	174	76	31.3	14.0	34.3	6.6	9.2	4.7	10.3	4.7
10-37	NIG019	138.79	37.30	1	39122	27548	47848	73872	1308	1147	1740	820	170.7	130.0	214.6	34.3	31.1	18.0	35.9	13.3
10-38	NIG020	138.97	37.23	1	18744	23183	29813	22737	407	521	662	312	30.6	32.4	44.6	12.3	8.5	11.8	14.5	5.8
10-39	NIG021	138.75	37.13	1	44384	71142	83852	27738	850	1716	1914	564	44.5	51.0	67.7	13.4	6.0	10.1	11.8	5.2
10-40	NIG022	138.85	37.03	1	12139	10519	16063	8634	342	342	483	127	20.0	21.0	29.0	3.9	3.9	4.8	6.2	1.4
10-41	NIG023	138.66	37.01	0	11115	12164	16477	3551	275	397	483	86	26.2	25.0	36.2	10.2	4.8	6.9	8.4	5.4
10-42	NIG024	138.45	37.12	0	9373	7205	11822	2704	218	240	324	55	9.4	13.3	16.3	3.8	4.3	3.8	5.8	2.9
10-43	NIG025	138.23	37.16	0	2917	2983	4172	1159	200	190	276	38	18.1	16.3	24.3	2.9	3.6	2.3	4.2	2.1
10-44	NIG026	138.25	37.02	0	1959	2692	3329	1271	78	71	106	18	4.2	3.7	5.6	2.7	2.2	3.0	3.7	2.0
10-45	NIG027	137.87	37.02	0	2899	2125	3594	1135	61	58	84	16	1.8	2.5	3.1	1.1	1.1	1.1	1.5	0.9
10-46	NIG028	138.89	37.42	1	33284	65947	73870	27991	706	870	1121	436	67.6	66.3	94.7	25.0	12.0	14.7	18.9	8.0
10-47	NIGH01	138.89	37.42	1	21865	31770	38567	20851	655	818	1048	375	64.6	59.8	88.0	27.5	12.1	14.7	19.0	7.9

Table B.2: Continued.

No.	ID	lon.	lat.	NF	Jerk (cm/s^3)				Acceleration (cm/s^2)				Velocity (cm/s)				Displacement (cm)			
					EW	NS	Hor.	UD	EW	NS	Hor.	UD	EW	NS	Hor.	UD	EW	NS	Hor.	UD
10-48	NIGH05	139.28	37.97	0	3260	3837	5035	1532	88	93	128	17	4.3	5.6	7.1	1.9	3.3	2.5	4.1	1.3
10-49	NIGH06	139.07	37.65	0	7198	8939	11476	6292	410	357	543	205	29.1	36.8	46.9	12.7	3.3	4.0	5.2	1.7
10-50	NIGH07	139.26	37.66	0	8433	5179	9896	4462	128	115	172	50	3.5	3.3	4.8	1.8	0.8	1.7	1.9	1.2
10-51	NIGH08	139.47	37.67	0	7804	5569	9587	4245	140	126	188	59	9.9	10.9	14.7	4.0	2.4	5.0	5.5	1.4
10-52	NIGH09	139.13	37.54	0	17092	17885	24739	27925	390	368	537	245	17.8	14.9	23.3	5.6	2.8	3.0	4.1	1.6
10-53	NIGH10	139.37	37.54	0	8859	8082	11992	6496	131	214	251	99	7.8	11.4	13.8	3.3	1.5	2.2	2.7	1.3
10-54	NIGH11	138.75	37.17	1	30584	26406	40406	28540	588	454	743	325	56.2	36.1	66.8	12.7	12.3	10.8	16.3	4.7
10-55	NIGH12	138.99	37.22	1	15530	21580	26587	38015	345	410	536	325	21.1	20.9	29.7	9.1	7.8	6.0	9.8	4.1
10-56	NIGH13	138.40	37.05	0	3163	2193	3849	1496	84	67	107	28	5.6	5.6	7.9	3.3	2.1	2.6	3.3	2.8
10-57	NIGH15	139.00	37.05	0	12812	24317	27486	8154	183	243	304	119	9.1	7.2	11.6	5.3	1.7	2.6	3.1	2.1
10-58	NIGH16	137.85	36.94	0	1586	1594	2249	1671	30	29	41	18	1.1	1.2	1.7	0.6	0.4	0.9	1.0	0.4
10-59	NIGH17	138.10	36.85	0	856	980	1301	634	52	67	85	39	6.4	5.3	8.3	3.4	2.3	1.7	2.8	1.5
10-60	NIGH18	138.26	36.94	0	3082	2804	4167	1049	110	96	146	44	6.0	8.9	10.7	3.4	3.8	3.4	5.1	2.4
10-61	NIGH19	138.79	36.81	0	3736	4536	5876	3008	75	72	103	33	2.3	3.2	3.9	1.9	1.4	0.8	1.6	1.2
10-62	TCG003	139.72	36.81	0	1766	1715	2461	298	52	47	70	5	2.3	1.6	2.8	0.4	0.6	0.8	1.0	0.3
10-63	TCG009	139.72	36.72	0	3224	2278	3947	3048	120	86	148	61	4.4	4.4	6.2	1.5	0.9	0.9	1.2	0.6
10-64	TCGH07	139.46	36.88	0	7213	7191	10186	8740	100	160	189	74	2.7	4.2	5.0	1.9	1.1	0.8	1.4	1.7
10-65	TCGH08	139.65	36.88	0	2373	2459	3417	2072	43	51	67	28	2.0	2.3	3.1	1.6	0.7	0.8	1.1	1.0
10-66	TCGH09	139.84	36.86	0	1858	1584	2441	1101	31	28	42	21	1.6	1.5	2.2	1.6	0.9	0.8	1.2	1.3
10-67	TCGH17	139.70	36.98	0	6378	5714	8563	4652	66	53	85	38	1.6	1.3	2.0	1.5	0.9	0.7	1.1	1.1